Investigation of manganese as a radioprotective agent in human cancers

by Thomas E. Lockwood

Thesis submitted in fulfilment of the requirements for the degree of

Doctor of Philosophy: Science

under the supervision of Dist. Prof. Philip Doble and Dr. David Bishop

University of Technology Sydney

Faculty of Science

May 25, 2022

Certificate of Authorship

I, Thomas Edward Lockwood, declare that this thesis is submitted in fulfilment of the requirements for the award of Doctor of Philosophy: Science, in the Faculty of Science at the University of Technology Sydney. This thesis is wholly my own work unless otherwise referenced or acknowledged. In addition, I certify that all information sources and literature used are indicated in the thesis. This document has not been submitted for qualifications at any other academic institution. This research is supported by the Australian Government Research Training Program.

Signature: Production Note: Signature removed prior to publication.

Date: May 25, 2022

Acknowledgements

I would like to acknowledge the following people for their care and advice throughout my PhD, firstly my supervisors Dist. Prof. Philip Doble and Dr. David Bishop. Since convincing me that analytical chemistry was the best chemistry in my undergraduate courses, Philip has been an excellent font of knowledge and occasional castigation. David has taught me all I know about ICP (not an indictment on him) and, more importantly, how to make a passably drinkable home brew.

Our Germans, Dr. David Clases and Dr. Raquel González de Vega for teaching me the arcane ways of single-particle ICP–MS and standard creation, and for being great people. Technical wizards Anthea Harris, Dayanne Mozaner Bordin and Alex Angeloski for training, acquisition of forbidden goods and keeping all the instruments running, even after I had used them.

Fellow monkeys Mika Westerhausen, Jake Violi and David Gertner. Mika has always been a great guide in all things physics, biology and places to drink. Jake and Daz are great friends and always up for arguing about chromatography and mass specs.

My fellow PhDs: Ana Chiaravalle, Brooke Mansell, Ciara Devlin, Dylan Johnson, Edward York, Eda Arslan, Minh Nguyen, Monique, Prashina Singh, Sarah Meyer and all the rest. You all made it possible to work long days, knowing there was beer, climbing or coffee at the end.

Finally, thank you to Siobhan Peters for her constant love and support, and to my family and friends for listening to me rant about chemistry and pretending to care.

List of Publications

- Lockwood, T. E.; Westerhausen, M. T.; González de Vega, R.; Röhnelt, A.; Bishop, D. P.; Cole, N.; Doble, P. A.; Clases, D. Low background mould-prepared gelatine standards for reproducible quantification in elemental bio-imaging. *The Analyst* **2019**, *144*, 6881–6888.
- Clases, D.; González de Vega, R.; Funke, S.; Lockwood, T. E.; Westerhausen, M. T.; Taudte, R. V.; Adlard, P. A.; Doble, P. A. Matching sensitivity to abundance: high resolution immuno-mass spectrometry imaging of lanthanide labels and endogenous elements in the murine brain. *Journal of Analytical Atomic Spectrometry* **2020**, *35*, 728–735.
- Bishop, D. P.; Westerhausen, M. T.; Barthelemy, F.; Lockwood, T.; Cole, N.; Gibbs, E. M.; Crosbie, R. H.; Nelson, S. F.; Miceli, M. C.; Doble, P. A.; Wanagat, J. Quantitative immuno-mass spectrometry imaging of skeletal muscle dystrophin. *Scientific Reports* **2021**, *11*, DOI: 10.1038/s41598-020-80495-8.
- Lockwood, T. E.; Westerhausen, M. T.; Doble, P. A. Pew2: Open-Source Imaging Software for Laser Ablation–Inductively Coupled Plasma–Mass Spectrometry. *Analytical Chemistry* **2021**, *93*, 10418–10423.
- González de Vega, R.; Goyen, S.; Lockwood, T. E.; Doble, P. A.; Camp, E. F.; Clases, D. Characterisation of microplastics and unicellular algae in seawater by targeting carbon via single particle and single cell ICP-MS. *Analytica Chimica Acta* **2021**, *1174*, 338737.
- Lockwood, T. E.; González de Vega, R.; Clases, D. An interactive Python-based data processing platform for single particle and single cell ICP-MS. *Journal of Analytical Atomic Spectrometry* **2021**, DOI: 10.1039/d1ja00297j.
- González de Vega, R.; Lockwood, T. E.; Xu, X.; Gonzalez-deVega, C.; Scholz, J.; Horstmann, M.; Doble, P.; Clases, D. Analysis of Ti and Pb-based Particles in the Aqueous Environ-ment of Melbourne (Australia) via single particle ICP-MS. *Analytical and Bioanalytical Chemistry* **2022**, submitted for publication.

Abstract

Manganese complexes are effective and catalytic scavenges of $O_2^{\bullet -}$, mimicking the behaviour of superoxide dismutase (SOD). These complexes even replace typical SOD in certain extremophile bacteria, providing resistance to huge doses of radiation. Recently, manganese concentrations have been shown to correlate with inferred radiotherapy resistance in human tumours. Radiation plays an important role in the treatment of cancer, but there is still no reliable way to predict an individual tumour's response to therapy. Imaging of manganese in tumours using laser ablation–inductively coupled plasma–mass spectrometry (LA–ICP–MS) could provide a novel way of predicting radioresistance and informing treatments, but currently implemented methods have some significant shortcomings. Measurement of manganese using ICP–MS is difficult due to the low concentrations in tissues and high background from polyatomic interferences. Existing LA–ICP–MS image processing software usually falls into one or more of the following categories: hard to use, limited in compatibility or unverifiable due to a closed-source nature. This thesis addresses these shortcomings by developing low-background standards and open-source software for both single cell (sc) and LA–ICP–MS. These new tools are then used to interrogate the metal contents of skin, testis, pancreas and brain tumours, and compare them to the inferred radioresistance of the cancers. Radioresistance is also investigated in a breast cancer cell model using ultraviolet (UV) radiation as a gamma surrogate.

Moulds were used to reproducibly prepare gelatine standards with controllable thickness, and surface characteristics that were improved over traditional methods. To prepare the standards: heated gelatine was pipetted into laboratory-made and commercial moulds, dried, frozen, de-moulded and dehydrated. When compared with traditional gelatine and homogenised tissue standards, the new standards had improved analytical figures of merit. Background signals for transition metals were reduced by removing endogenous elements from the gelatine using a chelating resin.

Open-source LA–ICP–MS imaging software was created using modern design and visualisation philosophies, minimising errors in data interpretation. The new software was compatible with data

collected using ICP–MS from common vendors, and implemented calibration, drift correction, spike filtering, segmentation, overlays and an image calculator. Documentation and a simple graphical user interface eases adoption, contributes to ease of use and maximises productivity.

Transition metals were quantified in tissue microarrays of testis, skin and pancreatic cancer. Concentrations of Mn, Fe, Cu and Zn all correlated with the inferred resistance of the tumours. These correlations also existed in normal testis, skin and pancreatic tissues. In testis tumours with different inferred radiosensitivities, seminoma and nonseminomatous germ cell tumours, only Cu correlated with resistance.

Concentrations of metals were quantified in glioblastoma and meningioma, brain tumours with vastly different patient outcomes. Glioblastoma contained significantly more Cu than benign (grade I) meningioma, but similar concentrations of other transition metals. Previous studies have noted raised serum Cu in patients with glioblastoma and this could be linked to tumour angiogenesis. Concentrations of Mn were increased in grade II over grade I meningioma, but did not reach significance.

To aid in the investigation of single-cellular Mn concentrations software was developed for single particle (sp) and scICP–MS analysis, with multiple methods of thresholding and calibration. The code is open-source, highly vectorised and could process 10×10^6 points in 19 ms. The software was demonstrated using the analysis of TiO_2 nano particles in water, LA–spICP–MS of micro-plastics in soil and the measurement of C fixation in algae.

The radioprotective properties of inorganic Mn^{2+} were investigated using UV radiation and a breast cancer cell model. Toxicity of $MnCl_2$ was determined, with an median lethal dose of 1.2 mmol L^{-1} in 1 % fetal calf serum (FCS), an order of magnitude lower than in 10 % FCS. Cells were treated with 10 and 100 µmol L^{-1} $MnCl_2$ for 24 h before exposure to 0 to 400 J m^{-2} UV-C radiation. Similar viabilities were observed across the range of treatments; Mn had no protective effects. Uptake of Mn from the media was determined using acid digestion and scICP–MS with similar results, although low signal prevent accurate quantification via scICP–MS in untreated cells. Multi-modal distributions of Mn was observed in treated cells, information that was lost when digestion was performed.

The tools created during this thesis will assist in future investigations of manganese and radioresistance. The primary limitation of imaging Mn via LA–ICP–MS, standards with insufficient limits of detection, has been solved and the new software will accelerate LA and scICP–MS analyses. Further experiments with large sample sizes and radiotherapy patient outcomes are required to definitively conclude if manganese complexes contribute to tumour radioresistance.

Contents

List of Figures

List of Tables

Abbreviations

ANOVA analysis of variance

BDD boron-doped diamond

CD133 prominin-1

CD30 tumour necrosis factor receptor superfamily member 8

CNS central nervous system

CRM certified reference material

CSC cancer stem cell

DAB 3,3'-diaminobenzidine

DMEM Dulbecco's Modified Eagle Medium

DNA deoxyribonucleic acid

DSB double-strand break

FCS fetal calf serum

FFPE formalin-fixed paraffin-embedded

FITC fluoresein isothiocyanate

GUI graphical user interface

H&E haematoxylin and eosin

HIF1 hypoxia inducible-factor 1

HPF high-power field

HRP horseradish peroxidase

ICP inductively coupled plasma

IHC immunohistochemistry

LA laser ablation

LD_{50} median lethal dose

LED light-emitting diode

LOD limit of detection

MRN MRE11-RAD50-NBS1

MS mass spectrometry

NBT nitro blue tetrazolium

NHEJ non-homologous end joining

NP nano particle

NSGCT nonseminomatous germ cell tumour

PAM polyacrylamide

PBS phosphate buffered saline

PFS progression free survival

PMMA poly(methyl methacrylate)

PNC particle number concentration

PTFE poly(tetrafluoroethylene)

RGB red-green-blue

ROI region of interest

ROS reactive oxygen species

RSD relative standard deviation

sc single cell

SEC size-exclusion chromatography

SIMS secondary ion mass spectrometry

SOD superoxide dismutase

sp single particle

TBS tris-buffered saline

TMA tissue microarray

TOF time-of-flight

UV ultraviolet

XOD xanthine oxidase

Chapter 1

Introduction

Cancer is one of the most common causes of death globally and treatments often rely on the use of radiotherapy. Radiotherapy exposes tumours to a controlled dose of ionising radiation in an attempt to destroy the cancerous cells. However, some tumours have or develop a resistance to radiation treatment, limiting its effectiveness. The mechanisms of tumour radioresistance remain poorly understood and there is no universal diagnostic for determining the potential resistance of an individual tumour. Manganese has been identified as the source of radioresistance in several extremeophile bacteria[1] and recently, manganese concentrations have been associated with the radioresistance in tumours.[2] By using bio-imaging and the simulation of radiotherapy it may be possible to determine if manganese is truly responsible for the varying resistance to radiation seen in tumours.

1.1 Cancer

In 2016 cancer accounted for 22 % of all deaths worldwide.[3] Cancer is the name given to a range of diseases characterised by the uncontrolled growth of cells. This uncontrolled growth often leads to invasion of the surrounding tissue and the formation of solid masses of cancerous tissue called tumours. Cancerous cells can also break off an initial tumour and travel through lymphatic or blood vessels to distant sites, a process known as metastasis.[4] Cancers are classified both by the region of the body in which they develop and the type of cell from which they originated. Some examples are *-blastoma* for cancers originating in precursor cells, *-carcinoma* for those originating in skin or the tissue that lines organs. In 2012 five cancers: lung, breast, colorectal, prostate and stomach accounted for half of all new diagnoses and with the addition of liver cancer, half of all deaths.[5]

Environmental factors are suspected to cause upwards of 90 % of cancers, with the rest caused by genetics. Exposure to these factors, known as 'carcinogens', causes damage to the genome and may lead to the formation of a cancerous tumour. Carcinogens include: mutagenic chemicals, some infectious diseases and ionising radiation. Poor diet, obesity and insufficient physical inactivity are also risk factors for the development of cancer.[6]

1.1.1 Diagnosis and histology

Histology, the microscopic analysis of cells and tissue, remains the only tool for definitive diagnosis of cancer. A physical exam, blood test or imaging technique may lead a physician to suspect a tumour and, if it is suspected to be cancerous, then a small biopsy is removed, sectioned, stained with dyes and viewed by a pathologist under a microscope. General stains such as haematoxylin and eosin (H&E) improve contrast and pattern recognition by highlighting structural features within the tissue. Abnormalities in the properties and distributions of cells and tissue are used to provide a diagnosis and possibly a grading. H&E is often sufficient to distinguish between normal and cancerous tissue, such as those in Figure 1.1.

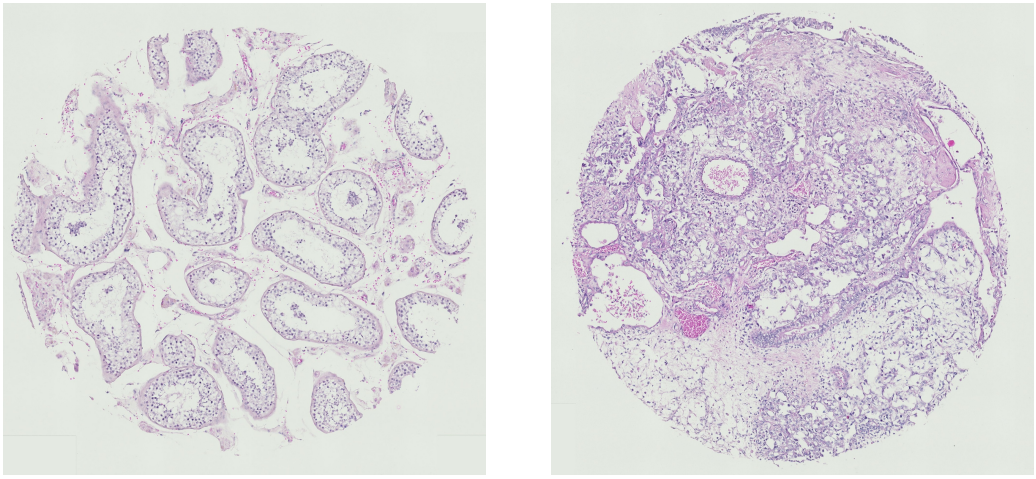

Figure 1.1. Tissue microarray cores of H&E stained normal (left) and cancerous (right) testicular tissues. The structure of the cancerous tissue is much less defined due to unrestricted growth.

A pathologist may also use immunohistochemistry (IHC) to aid in the diagnosis of both the type and stage of a tumour. IHC uses dyes coupled to antibodies that bind to antigens within the biopsy and can be used to detect the up- or down-regulation of cancer specific markers.[7] Detection of markers such as human epidermal growth factor receptor 2 in breast cancer[8] and tumour necrosis factor receptor superfamily member 8 (CD30) in testis tumours[9] can directly affect the prognosis and treatment of

a tumour. Histology and IHC also play an important role in cancer research, where they are used to identify novel markers used in diagnosis. High throughput of samples is achieved using automation and by using tissue microarrays (TMAs) containing many small tissue sections.[10]

Once a cancer has been diagnosed it will be treated with chemotherapy, radiotherapy, surgery or a combined regimen. While surgery is effective at destroying or removing large tumours and the surrounding invaded tissues, it is usually performed in combination with chemo- or radiotherapy to destroy any cancer cells remaining post-surgery.[11]

1.1.2 Radiotherapy

Around half of all cancer patients will receive some form of radiotherapy during their treatment, making it a crucial part of an effective response to cancer.[12] Radiotherapy uses controlled doses of radiation to destroy or impede the growth of cancerous cells and is used in both a curative and palliative way. Modern radiotherapy can precisely deliver beams of electrons or x-rays in the megavolt range (4 to 20 MV) using robotically controlled linear accelerators and collimators. Use of larger charged particle beams also allows for control of the depth at which the maximum dose of radiation is delivered.[13,14] Both of these techniques deliver large amounts of radiation to a tumour while minimising exposure of the surrounding healthy tissue.

Exposure of biological material to radiation causes damage both 'directly' and 'indirectly'. Indirect damage occurs via the formation of various reactive oxygen species (ROS), particularly hydroxyl radicals ($HO^{\bullet}$). While short-lived, $HO^{\bullet}$ react indiscriminately with molecules in the cell, oxidising them and causing damage.[15] In the presence of oxygen both $HO^{\bullet}$ and the solvated electron (e_{aq}^{-}) can react to form peroxides and superoxide ($O_2^{\bullet -}$) (eqs. 1.1 and 1.2).[16] Direct damage is caused by the interaction of photons with deoxyribonucleic acid (DNA) causing damage in the form of single- and double-strand breaks (DSBs). Typically exposure amounting to 1 Gy of ionising radiation will result in 1000 single- and 35 DSBs per cell.[17,18] While the number of DSBs are relatively small they are the most toxic DNA lesions and can lead to cell death if left un-repaired.[19]

$$2\,HO^{\bullet} \longrightarrow H_2O_2 \tag{1.1}$$

$$e_{aq}^{-} + O_2 \longrightarrow O_2^{\bullet -} \tag{1.2}$$

The first step in DSB repair is binding of the MRE11-RAD50-NBS1 (MRN) complex, signalling to the cell that repair is required, followed by recruitment of the relevant damage-repair proteins, ataxia telangiectasia mutated (ATM) and ATM- and Rad3-Related. These proteins also activate and phosphorylate substrates such as checkpoint kinase 1 and checkpoint kinase 2, leading to the arrest of the cell cycle to provide time for repair.[20] In response to signalling by MRN several of DNA repair pathways are activated, the major ones being non-homologous end joining (NHEJ) and homologous repair. In the major mammalian repair pathway, (NHEJ) binding of the X-ray repair cross complementing 5 complex to the break site recruits and activates the catalytic repair subunit DNA-dependent protein kinase.[21] This then phosphorylates a variety of targets which repair the broken DNA ends.[22] Inhibition of the DNA damage repair pathways or the accumulation of an un-repairable amount of DNA damage will induce cell death via the activation of normal cell death pathways and lead to apoptosis of the cell.[23]

1.1.2.1 Oxygen as a radiosensitiser

It has long been known that the effects of ionising radiation on cells is greatly reduced in the absence of oxygen. Initially this was thought to be due to lower metabolic rates leading to a reduced damage-repair response.[24] Later experiments introducing oxygen a fraction of a second before irradiation showed that this was not the case and led to the theory that oxygen can 'fix' radiation induced DNA damage, preventing chemical restoration.[25] This theory postulates that the DNA radical formed after irradiation reacts with oxygen with high affinity producing a peroxy radical and making damage permanent (Figure 1.2).

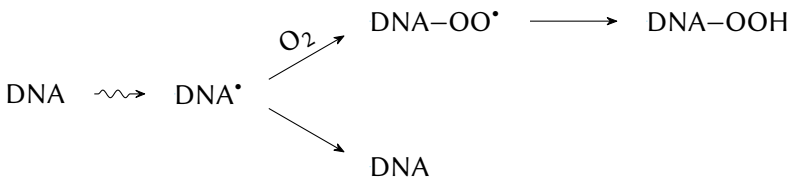

Figure 1.2. Mechanism of the oxygen fixation hypothesis. Damage to the DNA is made chemically irreversible via reaction with oxygen.

This process correlates with differing responses to radiation in varying oxygen concentrations but is only applicable to the chemical repair of DNA. If the biological and enzymatic mechanisms of DNA repair are unaffected then chemical restorability would not be relevant to radiation lethality. At least one study of *Escherichia coli* has demonstrated that under the same conditions the maximum dose

required to reduce survival was strain dependant.[26] As oxygen fixation would not be strain dependant it could not account for this variability and another mechanism of oxygen radiosensitisation must also be present.

1.1.2.2 Protein damage

The prevailing theory on how radiation kills cells is by damaging DNA through both direct and indirect damage, however there is increasing evidence that this is not the case.[27] The amount of DSBs caused by a given amount of radiation is similar across both radioresistant and radiosensitive cells (around 0.004 DSB/Gy/Mbase–pair) despite very different survival outcomes.[28] As such, radioresistant bacteria such as *Deinococcus radiodurans* can survive several thousand times more γ-radiation than radiosensitive bacteria yet suffers a similar number of DSBs.[1] In contrast, the restriction endonuclease *Bam*HI is inactivated by 150 Gy in aerobic conditions in the presence of Fe^{2+} but can survive irradiation to 4 kGy when exposed anaerobically.[1] These results suggest that protein damage is the source of the observed radiosensitisation in oxygen rich environments.

Irradiation of water in the presence of oxygen will generate $O_2^{\bullet -}$ as well as H_2O_2 and while both are unable to oxidise the amino acids of proteins they still cause significant damage. The negatively charged $O_2^{\bullet -}$ is electrostatically attracted to the metal centres of certain proteins where it binds and oxidises them. Enzymes containing a [4 Fe – 4 S] cluster have been shown to be damaged by $O_2^{\bullet -}$, releasing Fe^{2+} in the process.[29] This iron is then free to take part in Fenton reactions and produce highly oxidising $HO^{\bullet}$ directly at the active site of the enzyme and throughout the cell.[30] A number of DNA repair enzymes contain these clusters and would therefore be targeted during radiation exposure, explaining oxygen's ability to cause radiosensitisation.[31–33] This is supported by results showing proteome carbonylation (indicative of protein damage) is inversely proportional to cell survival in bacteria.[34]

1.1.3 Radioresistance

Tumours such as glioma, pancreatic cancer (adenocarcinoma) and melanoma are typically radioresistant, with radiation therapy providing no improvement in patient outcomes.[35,36] Others, such as testis and prostate cancer, are almost universally radiosensitive.[37,38] Survival of human cancer cell lines to treatment with radiation also correlates with the observed radiosensitivities of tumours, suggesting that some cells are intrinsically radioresistant.[39] In addition to these inferred resistances there also exists variation within tumour types.

There is no universal factor for predicting radioresistance, however the size of a tumour does affect the required radiation dose. Current approaches use genetics,[40] proteomics[41] and metabolomics[42] to try to individualise radiation dosage, however the value of these approaches is questionable given the heterogeneity of cancer cells.[43] Heterogeneity of cell population is also seen even within tumours and increases during tumour growth.[44] While the cause of varying radioresistance between, and within, different types of cancers is currently unknown there are a number of theories for the underlying mechanisms of radioresistance.

It should be noted that the most convincing theories for cancer radioresistance involve similar mechanisms; there is a reduction of oxygen in tumours and an increase in ROS during radiotherapy. The most radioresistant regions of tumours are found in hypoxic tissue, typically located adjacent to necrotic tissues.[45] This makes separating the individual mechanisms from one another difficult as well as confounding determination of the underlying causes.

1.1.3.1 Cancer stem cells

The cancer stem cell (CSC) theory postulates that a small number (0.0001 to 0.1 %) of tumour cells possess the capacity for unregulated growth and can reform a tumour after treatment. The CSCs are inherently radioresistant and survive radiotherapy, becoming selectively enriched after treatment. Stem cells in a variety of tumours have been shown to have an increased DNA repair capacity,[46–48] although the mechanisms are not well understood. Levels of ROS are lower in normal stem cell tissues to allow for increased metabolism and this appears to be the case in CSCs as well.[49]

While there is strong evidence that some cancers (such as leukaemia,[48] brain[46] and colon[50]) follow a CSC model, where a small number of identifiable cells able to form tumours, other cancers do not.[51] When CSCs are killed in targeted therapies tumours can adapt and resume their previous rate of growth, leading to very little clinical benefit.[50] Tumourigenic cells were found to still be present in leukaemia patients in complete remission following treatment with a tumourigenic inhibitor.[52] These results suggest that either insufficient identification and differentiation of CSCs or that their presence is not related to clinical outcomes.

A study by Quintana et al.[53] demonstrated that modification of assay conditions used to detect CSCs can dramatically affect their occurrence. Using immunocompromised mice during xenotransplantation of human melanoma cells raised the rate of cells able to reform a tumour to 25 %. This discovery coupled with the difficulty in defining what CSCs are and how to differentiate them from normal cells

led to an alternative theory where cancers cells undergo genetic change over time leading to a wide variety of heterogeneous cells.[51] From this heterogeneous pool of cells those with the requisites for radioresistance can survive treatment and multiply. If this is the case, then then CSCs could not account for the increased radioresistance of some tumours and another mechanism must be present.

1.1.3.2 Hypoxia

The abnormal structure of blood vessels within solid tumours and consequential reduced blood flow causes regions with extremely low oxygen levels.[54] These regions, dominated by necrotic tissue (Figure 1.3), are 100 to 150 µm from blood vessels or approximately the distance oxygen can diffuse through living tissue.[55] Adjacent to the necrotic tissue are regions of reduced oxygen where cells are still viable and these 'hypoxic cells' have been found to have greatly increased resistance to radiation.[24]

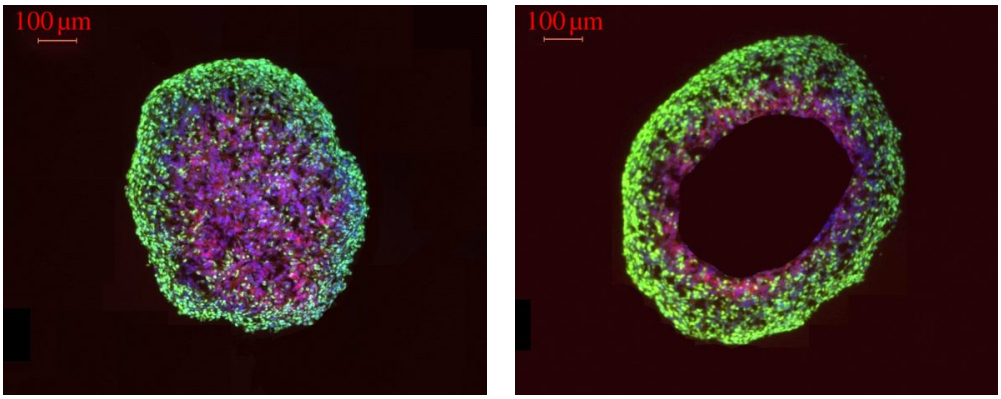

Figure 1.3. Tumour spheroids showing the development of hypoxia and necrosis at four (left) and six (right) days. Tissues were stained for live (green) and hypoxic (red) cells. Necrosis is visible in the centre of the spheroid at six days.[56]

Oxygen is a known radiosensitiser (Section 1.1.2.1) and its presence dramatically changes the yields of certain ROS during the irradiation of water.[23] Without the production of $O_2^{\bullet -}$ direct and in-direct damage to DNA would be able to be repaired, as fixation or protein damage would not occur. Efforts have been made to reduce hypoxia in tumours prior to radiotherapy by placing patients in hypobaric chambers but blockages commonly found in tumours prevented re-oxygenation taking place.[57] Additionally, inefficient delivery of nutrients to tumours lead to cycling oxygen demand providing periods for the re-oxygenation of tissue.[54] Irradiation of the tumour itself has also been shown to reduce hypoxia.[45] Following irradiation most of the surviving cells will be hypoxic due to their increased ionising radiation resistance, however normal aerobic:hypoxic ratios are re-established within a few hours. The most likely cause for this being reduced oxygen demand[45] or fluctuating blood flow.[58]

Of recent interest is the hypoxia inducible-factor 1 (HIF1) transcription factor, a promoter of many genes involved in: aerobic metabolism, antiogenisis (the formation of new blood vessels), protection against oxidative damage and cell mobility.[45] When the partial pressure of oxygen falls below 10 mmHg, or during periods of oxidative stress, the activity of HIF1 increases. H_2O_2 stabilises the HIF1α subunit and induces HIF1 related expressions, and when a Mn porphyrin superoxide dismutase (SOD) mimetic was added to irradiated cells HIF1 was inhibited.[59,60] As SODs remove $O_2^{\bullet -}$ and form H_2O_2 it would appear that both ROS play a role in HIF1 activity. Following irradiation HIF1 protein levels increase, despite subsequent re-oxygenation of the tumour, due to increased ROS and could explain the survival of tumours following intense chemo- or radiotherapy.[60,61]

While all tumours have a reduced oxygen level compared to the tissue from which they originated, hypoxia can't account for the variances seen in cancer cell lines.[62] Hypoxia definitely contributes to the radioresistant nature of tumours but it alone does not adequately explain the differences in radioresistance found between certain types of cancer.

1.1.3.3 Upregulation of ROS scavengers

The indirect damage caused by ROS to both DNA and the associated repair mechanisms is well established.[23] One possible mechanism of tumour radioresistance is the upregulation of endogenous ROS scavengers such as SODs, catalases and peroxidases both prior to and following exposure to radiation. Cancerous cells show an increased level of oxidative stress due to several factors, including increased ROS generation and consequently may overexpress ROS-scavenging enzymes.[63]

In general, tumour cells have normal or lowered cytosolic CuZnSOD activity when compared with normal cells.[64] Traditionally radioresistant tumours such as those of the brain,[65,66] thyroid[67] and colon[68] have all been shown to have increased MnSOD content over normal tissues and gene transfer studies have shown MnSOD to have a direct role in radioprotection.[69] And while MnSOD content has also been shown to be increased in mesothelioma cell lines neither it nor CuZnSOD levels were correlated with radiosensitivity.[70] In fact, a study of 46 different cell lines and tissues found no relationship between response to radiation and the content of any of the antioxidant enzymes.[71]

1.1.3.4 Upregulation of DNA repair mechanisms

The expression of genes within cancer cells has been shown to change following radiotherapy, possibly indicating a mechanism for radioresistance.[72,73] While there are hundreds of genes involved in the repair of DNA[74] only a few have been found to be upregulated in radioresistant cancers.[75–77] Upregulation of these genes is usually dependant on the type of tumour and therapies aiming at increasing these genes have yielded little clinical results.[43] One possible cause is the amount of genetic diversity found within tumours, with distinct sub-populations of cells and up to 24 % of the tumour mass consisting of cells with their own distinct genome.[78] Upregulation of a gene in one cell population would not represent the entire tumour and could therefore not be used to infer radioresistance.

1.1.3.5 Manganese complexes

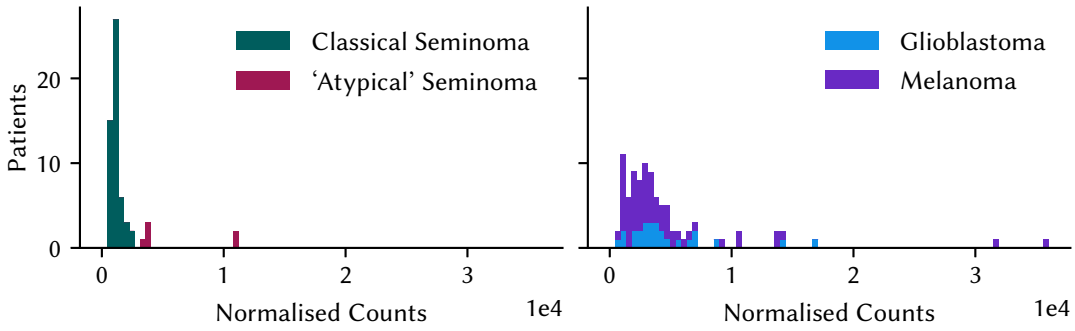

Figure 1.4. Concentrations of manganese correlated with the clinically-inferred radioresistance of tumours. Atypical seminoma had higher Mn than classical seminoma and the highest Mn was found in melanomas and glioblastomas.[2]

Tumours, even those of the same type, vary significantly in their response to radiotherapy. One possible cause of tumour radioresistance that remains relatively unexplored is the ROS scavenging ability of Mn^{2+} complexes. If this was the case, then radioresistant tumours would contain all the elements required to form scavenging complexes (Section 1.2) and radiosensitive ones would not.

Manganese, along with zinc and rubidium, is preferentially taken up by certain tumours leading to high concentrations and possibly the conditions required for the formation of ROS scavenging Mn^{2+} complexes.[79] It is already known from melanoma survival data that melanin is radioprotective, however the mechanism remains unknown.[36,80,81] Melanin is a chelator of transition metals and spatial determination of these metals shows increased Mn where melanin is present.[2]

A study of 359 samples of seven different types of cancerous tumours and healthy organs demonstrated a direct association between concentrations of Mn and documented radioresistance (Figure 1.4). Classically radiosensitive (testis) tumours had the lowest levels of Mn while those with clinically-inferred radioresistance such as glioblastomas and melanomas had the highest. Levels of other metals (Cu, Zn and Fe) showed no such association. Further, atypical seminoma that display a level of radioresistance had higher levels of Mn that the classical, radiosensitive seminoma.[2] While this is study demonstrated a strong association between Mn concentrations and resistance to radiation it could not rule out other proposed mechanisms of radioresistance.

The formation of radioprotective Mn complexes also requires the presence of carbonate or orthophosphate anions and free organic acids. At phosphate concentrations of less than $50\,\mathrm{mmol\,L^{-1}}$ formation of the protective complex is inhibited.[82] Phosphate has been shown to be higher in radioresistant tumours[83] and to increase following radiotherapy, most likely due to cell necrosis.[84] Interstitial phosphate is also associated with tumour growth rates and tumours have about twice the interstitial phosphate as normal tissues.[85] The formation of complexes also requires a low pH however this is commonly found within the tumour micro-environment, especially near hypoxic cells.[83]

Necrosis is associated with poor prognosis in tumours and typically arises from poor oxygen permeability.[55,86] The necrotic 'core' of tumours is adjacent to the most radioresistant cells of a tumour and as cells in the core die they will release their contents making them available for uptake by the nearby live cells.[87] These cells will therefore have an ample supply of the amino acids and peptides required to form ROS scavenging complexes. This availability of material correlates with the radioresistance of cancerous cells found near necrotic zones.

1.1.4 Cancer specific responses

The underlying mechanisms of inter- and intra-tumour radioresistance remain unknown and categorisation of tumour resistance is based on their type, location and size. The maximum dose that can be delivered to a tumour is limited by surrounding tissues and doses have been tuned over the decades to balance complete eradication of the tumour while limiting the damage to surrounding healthy tissue. Glioblastoma are resistant brain tumours usually situated deep within sensitive brain tissue,[19] melanoma are variably resistant[88] and seminoma are almost universally sensitive. Typical radiotherapy doses are correlated with inferred resistance of tumours (Table 1.1); a higher dose is required to treat a more radioresistant tumour.

Table 1.1. Accumulated dose for radiotherapy clinical trials involving glioblastoma, meningioma, seminoma, melanoma and pancreatic cancer.

	Dose (Gy)	Patients	Reference
Glioblastoma	60	24	[89]
	40 – 60	562	[90]
Meningioma	57	190	[91]
(atypical)	61	27	[92]
Melanoma	48	234	[93]
	30 – 36	139	[94]
Seminoma	20 – 30	625	[95]
	20 – 30	885	[96]
	30 – 36	94	[38]
Pancreatic Cancer	71	44	[97]
	61	81	[98]

1.1.4.1 Glioblastoma

Glioblastoma multiforme (WHO grade IV astrocytoma) is the most common primary brain tumour and is treated using a combination of surgery, radiotherapy and chemotherapy. Due to the inherent radioresistance of glioblastoma the delivered radiotherapy dose has been increasingly escalated as new technology has permitted better targeting, increasing survival.[19] Current combined chemo- and radiotherapy treatments offer a median progression free survival (PFS) of five months,[90] after which most patients suffer recurrence of the tumour and face limited treatment options. Recurrent glioblastoma is characterised by increased chemo-[99] and radioresistance[100] and while re-irradiation sometimes used to treat recurrent tumours it comes with a serious risk of radiation toxicity.[101]

1.1.4.2 Meningioma

Meningiomas are a relatively common malignancy of the meninges, the tissue covering the brain. The majority (70 to 90 %) of meningioma are benign (WHO grade I) and usually actively monitored instead of being treated. Depending on their location and rate of growth these benign tumours can still cause debilitating symptoms that warrant surgery. Radiotherapy is also used to treat meningioma, particularly in cases where the tumour location makes resection difficult.[91] Combined treatments are particularly effective and Soyuer et al.[102] found radiotherapy improved 5 year PFS from 38 to 91 %. Atypical meningioma (WHO grade II and III) has a worse prognosis and high recurrence rate and are

treated with radiotherapy following surgical removal.[92] Resistance to radiotherapy in atypical cases is common and PFS is reduced to only 48 %.

1.1.4.3 Pancreatic cancer

Pancreatic adenocarcinoma is highly malignant, presents late and has a poor prognosis with a median survival time of three to six months from diagnosis. Less than 20 % of tumours are resectable, the only curative option, and even these cases often result in local or distant recurrence.[97] Non-resectable tumours are treated with chemo- and radiotherapy but survival rates have not significantly improved in the last decade.[103] High radiation doses are required to treat pancreatic cancer as it is intrinsically radioresistance and its location deep in the abdomen, surrounded by radiosensitive organs, makes radio toxicity common.[98]

1.1.4.4 Melanoma

Melanoma are tumours with both a propensity for metastasis and resistance to chemo- and radiotherapy and thus have a very poor prognosis. Both melanoma tumours[104] and cell lines[105] have highly variable responses to radiation, but radiotherapy is still recommended in a majority of cases.[106] Skin pigmentation is associated with both the onset of melanoma[107] and possibly with its resistance to radiotherapy.[108] Brożyna et al.[36] found that amelanomic tumours have a significantly better median survival time after radiotherapy, 21.4 months versus 6.6 months for pigmented tumours. Melanin scavenges free radicals, toxins and consumes oxygen, resulting in a hypoxic tumour environment. It is also a powerful chelator of metal ions and melanin and metal distributions are closely colocalised.[2,15] However, studies in epithelial and melanoma cell lines showed that melanin alone does not have an effect on radiosensitivity.[108,109] Both of these studies cultured cells in alpha minimum essential medium, a media that is devoid of transition metal containing inorganic salts. A combination of melanin and inorganic ions may be required to induce radioresistance.

1.1.4.5 Seminoma & NSGCTs

Most testis cancers are germ cell tumours, classified as either seminoma or nonseminomatous germ cell tumours (NSGCTs). NSGCTs are then further divided into embryonal carcinoma, yolk sac tumours, teratoma or a mixed presentation. Seminoma are usually slow growing and respond well to treatment, both radio- and chemotherapy.[110] But a small number of seminoma present with a high mitotic

count (>3 per high-power field (HPF)) and are classified as anaplastic. These 'atypical' seminoma were historically associated with a worse prognosis.[111] However, more recent data has failed to confirm this association[112,113] and both normal and anaplastic seminoma have a similar response to radiotherapy.[114,115] The anaplastic classification is also contested as they may simply be seminoma with high proliferative activity.[116] In contrast, NSGCTs are well established as more aggressive then seminoma, and have a poor response to radiotherapy.[117,118] A review of clinical trials found that the recurrence of tumours following radiotherapy was 3.7 and 11.1 % for seminoma and NSGCT respectively.[119] NSGCTs are usually differentiated from seminoma using IHC as they express CD30, a tumour necrosis factor that is usually not present in seminoma.[9]

1.2 Manganese chemistry

Manganese(II) is an effective scavenger of $O_2^{\bullet -}$ (eq. 1.3) and in the presence of certain anions can form a redox cycling complex.[120]

$$Mn^{2+} + O_2^{\bullet -} \longrightarrow Mn^{3+} + O_2 \tag{1.3}$$

Anions such as pyro- and ortho-phosphate stabilise MnO_2^{+}, a short-lived transient product of the oxidation, and drive the reaction allowing stoichiometric removal of $O_2^{\bullet -}$.[120] In the case of ortho-phosphate, disproportionation of the MnO_2^{+} occurs (eqs. 1.4 and 1.5), regenerating the Mn^{2+} complex and making the process truly catalytic .[121] While there are a number $O_2^{\bullet -}$ scavenging Mn-complexes only orthophosphate and carbonate demonstrate the ability to catalytically remove $O_2^{\bullet -}$ at physiologically relevant concentrations and pH. Both orthophosphate and carbonate complexes have been shown to remove $O_2^{\bullet -}$ during irradiation without producing Mn^{3+}, the product of non-catalytic reactions.[82]

$$Mn^{2+}\text{–L} + O_2^{\bullet -} \rightleftharpoons MnO_2^{+}\text{–L}^{\bullet -} \tag{1.4}$$

$$2\,MnO_2^{+}\text{–L}^{\bullet -} \xrightarrow[H^+]{} 2\,Mn^{2+}\text{–L} + H_2O_2 + O_2 \tag{1.5}$$

In addition to removing $O_2^{\bullet -}$, Mn-carbonate complexes can catalytically disproportionate H_2O_2 to form H_2O and O_2.[122] The reaction is similar to that of an Fe^{3+} catalysed Fenton reaction however no damaging $HO^{\bullet}$ are produced. Catalytic efficiency of the complex can also be improved by substituting for one HCO_3^{-} ligand for an amino acid.[123] Despite this, Anjem et al.[124] have shown that the rate of removal of H_2O_2 by even high concentrations of Mn^{2+} complexes is still several magnitudes

lower than those achieved by the catalase enzymes found in normal cells. The formation of these complexes is also disrupted by the presence of orthophosphate, a likely candidate for the Mn^{2+} catalysed disproportionation of $O_2^{\bullet -}$.[122]

The use of manganese as a defence against ROS by cells was first demonstrated by Archibald and Fridovich.[120] *Lactobacillus plantarum* bacteria were shown to be able to survive aerobic conditions despite lacking the SOD enzymes usually responsible for scavenging and removing the ROS formed by aerobic respiration. Milli-molar concentrations of Mn were used by the bacterium in place of the normal micro-molar levels of MnSOD and FeSOD found in other bacteria.

In 2004 Daly[125] identified manganese as a potential factor in the radiation resistance of *D. radiodurans*, an extremophile bacterium capable of surviving large doses of ionising radiation. Ratios of intra-cellular Mn to Fe were far higher in *D. radiodurans* than in radiosensitive bacteria and resistance to radiation was concentration-dependant on $MnCl_2$ supplied via growth media. Those grown in the presence of Mn were shown to release H_2O_2, suggesting its removal by Fe redox cycling was limited.[1] And bacterium grown in the absence of Mn were rendered susceptible to radiation induced protein damage.[1] Neither Cu, Fe or Zn were capable of forming protective complexes in the same manner as Mn.

Extracts from *D. radiodurans* were shown to provide radioresistance to cells that were typically sensitive to radiation with the survival of both *E. coli* and human lymphoblastoid Jurkat T cells improved significantly when grown in the extract. These extracts were both ultra-centrifuged and ultra-filtrated to remove molecules >1 kDa proving that small Mn^{2+} complexes were responsible for resistance and not MnSODs.[126] Extracts were found to be highly enriched in nucleosides, amino acids and peptides; these antioxidant molecules provide protection against damage caused by $HO^{\bullet}$.[127] Following these initial findings and the analysis of the *D. radiodurans* ultra-filtrate it was hypothesised that complexes of Mn^{2+}, phosphate and small organic molecules were responsible.[128] Nucleosides are capable of complexing with manganese[129] however these complexes alone were found to be less radioprotective than the *D. radiodurans* homogenates. Given that a large proportion of the intra-cellular Mn appeared to be bound to peptides, one based on the most abundant amino acids in the ultra-filtrate was synthesised.[126]

Synthesised manganese decapeptide complexes provided a similar level of γ-radiation protection as the *D. radiodurans* homogenate. The complex protected DNA repair enzymes exposed to 60 kGy and accumulated in human Jurkat T cells, however DNA itself remained unprotected.[126] The decapeptide was found to be non-toxic in mammals and mice treated with the complex survived exposure to 9.5 Gy, usually lethal to 63 % of individuals after 30 days.[130] However amino acids vary in their ability to

scavenge $HO^{\bullet}$ and thus protect cells from radiation, the damage to sulphur containing amino acids is even reversible.[127] Knowing this Berlett and Levine[131] were able to synthesise an even more protective peptide. A hexapeptide made using the most protective amino acids (histidine and methionine) increased the required radiation dose for 50 % inactivation of glutamine synthetase from 2 kGy to 112 kGy while the original decapeptide only achieved protection to 33 kGy.

The Mn^{2+} centre is substitutionally labile, making analysis of complexes in situ in radioresistance organisms difficult.[132] While the exact nature of the complexes formed by manganese is unknown, such complexes can play a role in protection of cells from ionising radiation. The most likely candidate for such a complex involves an acidic anion, such as orthophosphate or carbonate and an organic component such an amino acid or peptide. This would provide protection from protein oxidising $O_2^{\bullet -}$ and potentially from H_2O_2 as well. Therefore, to be radioresistant a cell must contain a significant amount of Mn^{2+}, acidic anions and free or peptide-bound amino acids.

1.3 Reactive oxygen species

ROS are a group of oxygen containing compounds with high reactivity and toxicity. They are primarily generated in vivo by aerobic metabolism and, in the context of radiotherapy, via the radiolysis of water. Organisms have evolved several mechanisms for removing ROS, principally enzymes such as SODs (for removal of $O_2^{\bullet -}$) as well as catalases and peroxidases (for removal of H_2O_2).[133] There are a number of different types of ROS, the most biologically important of which are covered here.

$HO^{\bullet}$ is short-lived (10^{-9} s in vivo), extremely reactive and will react with surrounding molecules forming peroxide (eq. 1.1) and organic radicals. In the presence of oxygen e_{aq}^{-} can react to form $O_2^{\bullet -}$ (eq. 1.2) and organic peroxides.[16] Peroxides and $O_2^{\bullet -}$ are more stable than $HO^{\bullet}$ and can persist for a relatively long time (Figure 1.5), several seconds in the absence of scavengers.[134] Due to its high reactivity the majority of ROS induced damage following radiation exposure is caused by $HO^{\bullet}$. This damage is non-targeted and all components of a cell such as DNA, ribonucleic acid, lipids and proteins are oxidised.[23]

Unlike $HO^{\bullet}$, the damage from $O_2^{\bullet -}$ is limited to certain molecules. DNA is insensitive to $O_2^{\bullet -}$ and superoxide is unable to oxidise amino acids, but it can still cause significant damage to proteins.[1] The negative charge also prevents $O_2^{\bullet -}$ from easily crossing phospholipid membranes causing it to build up in irradiated cells.[135]

Peroxides such as H_2O_2 are the most stable of the ROS and can freely diffuse out of cells so damage is usually limited. However, in the presence of free iron peroxides can take part in Fenton reactions (eqs. 1.8 and 1.9) and produce highly damaging $HO^\bullet$ at the site of the iron. Nucleic acids bind iron well and as such DNA is a target of Fenton-related damage and due to the presence of iron at the binding sites of many proteins peroxides can selectively damage these proteins as well.[29] The damaging nature of these radicals make it important for organisms to both carefully store transition metals and to remove H_2O_2.

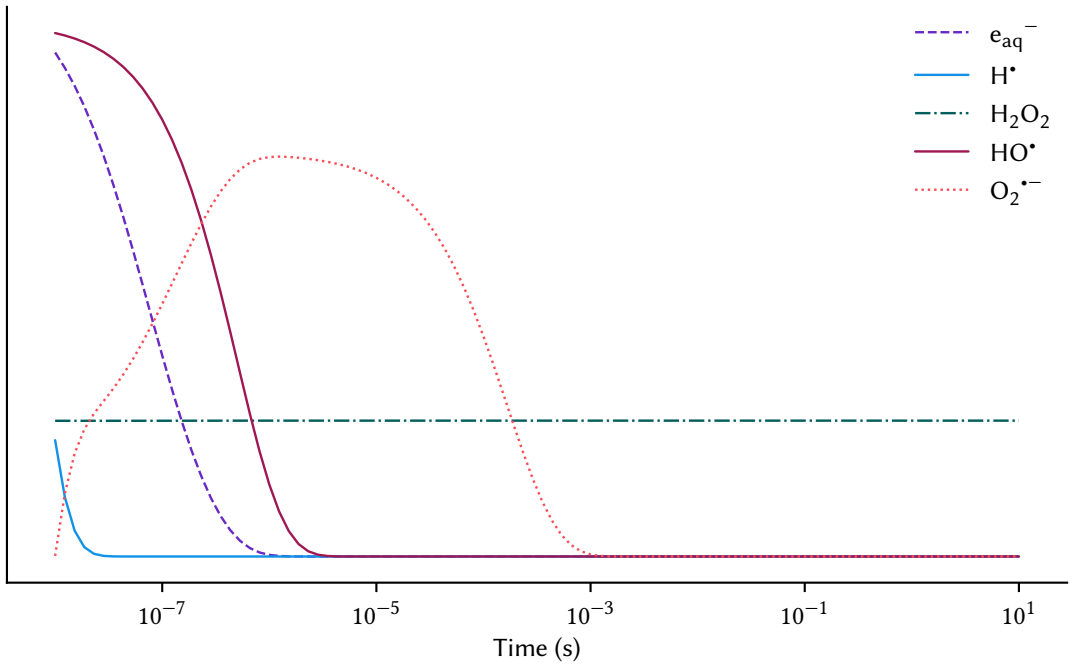

Figure 1.5. Relative concentrations of the major ROS resulting from the irradiation of a cell. Kinetics data from Buxton et al.[136] was used, assuming an intracellular oxygen concentration of 250 µmol L^{-1}. $HO^\bullet$ is assumed to react with cell contents and $O_2^{\bullet-}$ removed by µmol L^{-1} level SODs.[137]

1.3.1 Generation of ROS

The majority of ROS are unstable, degrading soon after their creation so the study of their effects requires in situ generation. Radiolysis of water is most commonly used and most accurately simulates the environment during radiotherapy, however it requires a potentially dangerous γ-radiation source and will always produce a mixture of ROS. There are a variety of other ways to selectively produce different ROS allowing for the study of their effects individually.

1.3.1.1 Radiolysis of water

Water is the major constituent of living cells and when exposed to high energy ionising radiation, such as during radiotherapy, electrons are ejected from their orbitals (Figure 1.6) resulting in the creation of free radicals known as ROS.[15]

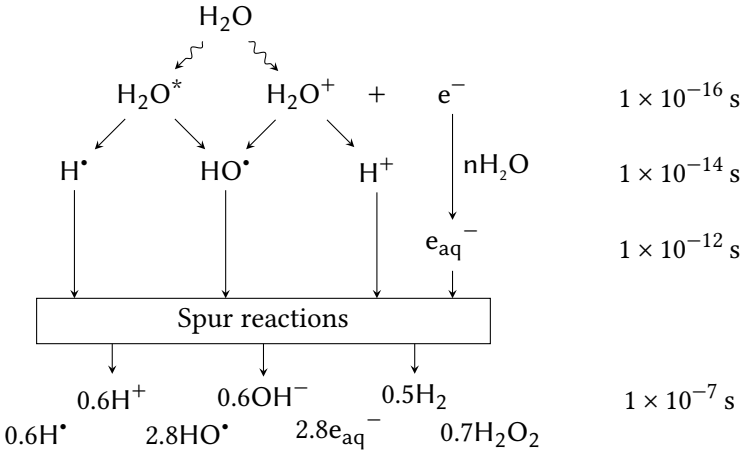

Figure 1.6. Reactions arising from the radiolysis of water and expected ROS yields. *G*-values are reported with units of 10^{-7} mol J^{-1}.

It is also possible to produce ROS with other, less energetic, sources of radiation. Ultraviolet (UV) light and H_2O_2 has been used to remove organic contaminants and disinfect water via the production of $HO^{\bullet}$ as in eq. 1.6.[138] Photogeneration of $HO^{\bullet}$ is also possible using nitrite (eq. 1.7) and the formation rate can be a magnitude greater than when using H_2O_2. Nitrite also absorbs at a higher wavelength (λ_{max} = 355 nm) than H_2O_2 allowing for more commonly available UV light sources to be used.[139]

$$H_2O_2 \xrightarrow{h\nu} 2\,HO^{\bullet} \tag{1.6}$$

$$NO_2^- + H_2O \xrightarrow{h\nu} HO^{\bullet} + NO + OH^- \tag{1.7}$$

Specific wavelengths of visible and infra-red light can also be used to generate $HO^{\bullet}$ and H_2O_2 in oxygenated water although the amounts generated are small.[140]

1.3.1.2 Chemical

Many transition metal ions can promote the production of free radicals by donating electrons. Fe^{2+} is capable of catalysing the disproportionation of H_2O_2 via a Fenton reaction, where Fe^{2+} is first reduced to Fe^{3+} (eq. 1.8) and then oxidised (eq. 1.9), releasing highly reactive free radicals.

$$Fe^{2+} + H_2O_2 \longrightarrow Fe^{3+} + OH^- + HO^\bullet \tag{1.8}$$

$$Fe^{3+} + H_2O_2 \longrightarrow Fe^{2+} + H^+ + HOO^\bullet \tag{1.9}$$

While using a solution of H_2O_2 is common, it is more efficient to supply the peroxide gradually. One method is the use of metal peroxides, insoluble salts that slowly decomposes in water to form H_2O_2. The gradual release limits disproportionation and loss of H_2O_2 and can be controlled by altering solution pH.[141] The chemistry behind the Fenton reaction is well understood and it has been used in numerous studies on the biological impacts of ROS, particularly $HO^\bullet$.[142,143]

Production of $O_2^{\bullet -}$ is most effective using the enzyme xanthine oxidase (XOD) in the presence of hypoxanthine. XOD catalyses the reduction of oxidation of hypoxanthine to xanthine and then uric acid forming $O_2^{\bullet -}$ and H_2O_2 (eq. 1.10).[144]

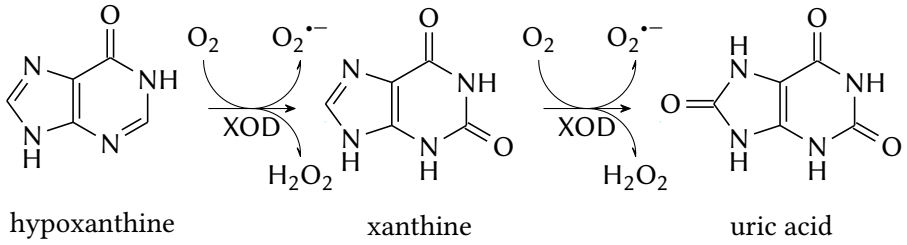

hypoxanthine xanthine uric acid (1.10)

In the presence of transition metals the XOD will become inactivated due to damage resulting from the production of $HO^\bullet$.

1.3.1.3 Electrochemical

Oxidative electrochemistry is primarily used for organic synthesis and the incineration of organic pollutants in water and is therefore focused on the production of $HO^\bullet$. Discharge of an electrode results in the formation of hydroxyl radicals adsorbed to its surface as in eq. 1.11.

$$M + H_2O \longrightarrow M(^\bullet OH) + H^+ + e^- \tag{1.11}$$

Depending on the type of electrode used these radicals then react with the metals surface or are free to oxidise organics in solution (eq. 1.12).[145]

$$M(^{\bullet}OH) + R \longrightarrow M + RO^{\bullet} + H^{+} + e^{-} \tag{1.12}$$

The efficiency of the process is highly dependent on the electrode materials used. Active electrodes will interact strongly with the adsorbed $HO^{\bullet}$ and produce oxygen, wasting energy. Because of this, non-active electrodes such as metal oxides (PbO_2, SnO_2 and TiO_2) are preferred, however these electrodes tend to have poor electrochemical stability.[146] A new material, boron-doped diamond (BDD), retains the high oxygen overpotential (electric potential required to form oxygen) of the materials (2.7 V) while significantly improving on their stability.[147]

Diamond is an extremely poor conductor of electricity making it an odd choice for an electrode material, however dopants can dramatically change the properties of diamond. The addition of $>10^{20}$ cm^{-3} atoms of boron to diamond increases its conductivity substantially giving it metal like properties.[148] BDD electrodes are usually created using chemical vapour deposition of carbon onto a conductive substrate and can have current efficiencies as high as 90 %.[146] The surface finish and termination dramatically change the electrochemical properties of BDD and an O-terminated electrode is recommended due to its increased stability over H-terminated electrodes. BDD can also be used to produce small amounts of other ROS like H_2O_2 and O_3 however the efficiency is very low.[147]

Noble metals are the most efficient catalysts for the generation of H_2O_2 from the electrolysis of water however their scarcity and cost makes other, more common materials attractive.[149] Carbon electrodes can achieve near 100 % efficiency in a basic environment and are capable of maintaining a solution at 7 % w/w H_2O_2.[150] Unfortunately the pH required is far higher than would be found within a cellular environment making them unsuitable for mimicking the formation of H_2O_2 in vivo. Careful growth of the carbon can allow for a lower level of H_2O_2 to be maintained at a range of pH values and newer nitrogen-doped carbon nano-structures allow for efficiencies to be as high as 98 %.[151,152] Also promising for the production of H_2O_2 are atomically dispersed noble metal electrodes. These reduce the required quantity of metal per electrode to less than 5 % while retaining high efficiency and selective H_2O_2 production.[153]

1.3.2 Detection of ROS

Measuring the concentration of ROS is an important step in understanding their biological impacts. Many of the techniques used are derived from those used by food chemists in the measurement of antioxidant capacity and typically involve the competitive oxidisation of a fluorescence or colourimetric probe.[154] These methods are rarely quantitative or specific to a single ROS and instead measure the total antioxidant capacity of substances.[155] There are however several methods of accurately quantifying the individual ROS both in vivo and -vitro.

1.3.2.1 Spectroscopy

There have been many colorimetric, chemiluminescence and fluorescence reagents successfully used for the detection of the different ROS, with common examples listed in Table 1.2. These reagents react with one or more ROS producing an observable change in absorbance (colorimetric), a release of light (chemiluminescence) or re-emission of absorbed light (fluorescence). A specific wavelength is monitored using a spectrophotometer and the change in intensity correlated to the concentration of the ROS.

Given the high reactivity of $HO^{\bullet}$ most chemicals that exhibit a change in colour or fluoresce on oxidation can be used. Both salicylic acid[145] and terephthalic acid[156] are cheap, commonly available examples with good $HO^{\bullet}$ specificity. If $HO^{\bullet}$ is not being quantified a spin-trap such as mannitol,[140] dimethylsulfoxide[1] or *tert*-butyl alcohol[136] may be used to reduce its interaction with other probes.

Tetrazolium salts such as nitro blue tetrazolium (NBT) are colorimetric reagents used to detect and quantify $O_2^{\bullet -}$. These dyes are reduced to highly absorbing formazans by $O_2^{\bullet -}$ and have been used to assay $O_2^{\bullet -}$ and SOD in living cells.[157] While NBT is the most readily available dye, its formazan is water insoluble and where water solubility of the formazan is required another salt such as 3-(4,5-Dimethylthiazol-2-yl)-5-(3-carboxymethoxyphenyl)-2-(4-sulfophenyl)-2H-tetrazolium or 2,3-Bis-(2-methoxy-4-nitro-5-sulfophenyl)-2H-tetrazolium-5-carboxanilide must be used.[158] Luminol and lucigenin can be used as fluorescent probes for detecting $O_2^{\bullet -}$ although they are not recommended for detection in vivo.[159] Other luciferins such as Cypridina luciferin analogue and Methyl-CLA have better biological compatibilities and are more active at physiological pH.[160,161]

'Persistent' radicals such as $ABTS^{\bullet +}$ are commonly used and measure an antioxidant's ability to quench radicals via transfer of electrons and can be used for the detection of H_2O_2. However, these radicals are non-specific and will also react with organic peroxides and other ROS.[155] More specific

probes require horseradish peroxidase (HRP) or a similar peroxidase to catalyse their oxidation by H_2O_2, but HRP will still react with several organic peroxides.[162] Other probes such as neocuproine use transition metal catalysts and will therefore suffer from interference in the presence of additional transition metals.

1.3.2.2 Electrochemical

Functionalisation of an electrode with certain compounds will allow for the immobilisation of proteins on the electrodes surface. These proteins can then be reduced by ROS and reoxidised at the electrodes surface, generating a detectable current.[163] One of the earliest examples of this was the production of an $O_2^{\bullet -}$ detecting electrode by Eddowes and Hill.[164] An Au electrode was coated with 4,4′-bipyridyl and then cytochrome *c* was covalently bound to its surface. Simplified production consists of simply incubating the electrode in solutions of the required coating and protein, allows detection down to 10 nmol L^{-1} and has been proven in a variety of in vitro experiments.[165] The most sensitive and specific sensors for $O_2^{\bullet -}$ use immobilised CuZnSOD. These sensors can have fast response times, detection limits in the low nmol L^{-1} region and are linear over a range of several hundred µmol L^{-1}.[166]

Similar techniques can also be used to create electrodes specific to other radical species. Electrochemical deposition of polypyrrole and HRP onto glassy carbon was used to create an electrode with a detection limit of 100 nmol L^{-1} H_2O_2.[167] Prussian Blue can be deposited in a similar manner to create an array of nano-electrodes, enabling a µg L^{-1} (10 nmol L^{-1}) detection limit and linearity to 10 mmol L^{-1}.[168]

Table 1.2. Common colorimetric, chemiluminescence and fluorescent methods for the detection of e_{aq}^-, $HO^\bullet$, H_2O_2 and $O_2^{\bullet -}$.

	Probe	Absorbance	LOD	Notes	Reference
e_{aq}^-	*Direct*	λ=720 nm; ϵ=19000[a]	nmol L^{-1}		[136]
$HO^\bullet$	*Direct*	λ=225 nm; ϵ=540[a]	µmol L^{-1}		[136]
	Br^-	λ=360 and 700 nm; ϵ=12000[a]	µmol L^{-1}	Acidic conditions	[169]
	Terephthalic acid	λ_{ex}=315 nm, λ_{em}=425 nm	nmol L^{-1}	High specificity	[156]
	Benzoic acid	λ=272 nm; ϵ=930[a]	nmol L^{-1}	Forms salicyclic acid	[170, 171]
	Salicyclic acid	λ_{ex}=305 nm, λ_{em}=450 nm	nmol L^{-1}		[172]
	Proxyl fluorescamine	λ_{ex}=404 nm, λ_{em}=490 nm	nmol L^{-1}	Reacts with $CH_3^\bullet$	[173]
H_2O_2	*Direct*	λ=200 nm; ϵ=189[a]	mmol L^{-1}		[16]
	ABTS	λ=415 nm; ϵ=3600[a]	µmol L^{-1}	Non-specific	[155]
	Amplex red	λ_{ex}=563 nm, λ_{em}=587 nm	pmol L^{-1}	Buffer to pH 7.4; HRP catalyst	[174]
	Leuco crystal violet	λ=596 nm; ϵ=87000[a]	µmol L^{-1}	$ROO^\bullet$ interferences; pH 4.5; HRP cataylst	[175]
	2,7-Dichloro-dihydro-fluorescein	λ_{ex}=498 nm, λ_{em}=522 nm	nmol L^{-1}	Non-specific	[176]
	p-Hydroxyphenyl-acetic acid	λ_{ex}=317 nm, λ_{em}=414 nm	nmol L^{-1}	pH > 8.5; stable; HRP catalyst	[177]
	Scopoletin	λ_{ex}=350 nm, λ_{em}=460 nm	pmol L^{-1}	pH 4.5, pH 10 buffer; HRP catalyst	[178]
	Luminol	λ_{em}=425 and 470 nm	nmol L^{-1}	high pH; promotes $O_2^{\bullet -}$ production	[159]
	Neocuproine + Cu^{2+}	λ=460 nm; ϵ=8400[a]	nmol L^{-1}	Transition metal interferences	[179]

Continued on next page

Table 1.2. Common colorimetric, chemiluminescence and fluorescent methods for the detection of e_{aq}^-, $HO^\bullet$, H_2O_2 and $O_2^{\bullet-}$. (Continued)

	Probe	Absorbance	LOD	Notes	Reference
	3,3'-diamino-benzidine	λ=575 nm; ϵ=140000[a]	nmol L^{-1}	HRP catalyst; $O_2^{\bullet-}$ with Mn^{2+}	[180]
	diphenyl-1-pyrenyl-phosphine	λ=358 nm; ϵ=28000[a]	pmol L^{-1}	Lipid soluble	[181]
$O_2^{\bullet-}$	*Direct*	λ=243 nm; ϵ=2350[a]	µmol L^{-1}	pK_a=4.69	[16]
	SOD	*Detection of H_2O_2*	µmol L^{-1}	Transition metal interferences	[137]
	Cytochrome *c* + Fe^{3+}	λ=555 nm; ϵ=21000[a]	µmol L^{-1}	Transition metal, H_2O_2 interferences	[144]
	NBT	λ=530 nm; ϵ=25400[a]	µmol L^{-1}	ϵ pH dependant; lipid soluble	[157]
	MTS	λ=490 nm; ϵ=26900[a]	nmol L^{-1}	ϵ pH dependant; water soluble	[158]
	XTT	λ=470 nm; ϵ=21600[a]	µmol L^{-1}	ϵ pH dependant; water soluble	[158]
	Hydroethidine	λ_{ex}=520 nm, λ_{em}=610 nm	µmol L^{-1}	H_2O_2 interference	[182]
	Luminol	λ_{em}=425 and 470 nm	nmol L^{-1}	high pH; promotes $O_2^{\bullet-}$ production	[159]
	Lucigen	λ_{em}=425 and 470 nm	nmol L^{-1}	high pH; promotes $O_2^{\bullet-}$ production	[160]
	CLA	λ_{em}=380 nm	pmol L^{-1}	$^1O_2$ interferences	[161]
	MCLA	λ_{em}=460 nm	pmol L^{-1}	$^1O_2$ interferences	[160]

[a] $mol^{-1}\,L^{-1}\,cm^{-1}$

1.4 Elemental Bio-imaging

Many biological processes rely of the presence of trace metals with deficiency or surplus of these metals causing a wide variety of problems. Protein active sites usually contain a metal ion with approximately half of all enzymes requiring metal cofactors to be active.[183] Metals are distributed non-uniformly within cells and tissues making spatial measurements of metal levels important for providing insights in the role these elements play in normal biological function and disease. Bio-imaging has demonstrated that Parkinson's disease is correlated with increased Fe in certain parts of the brain,[184] provided new tools for immunology[185] and even provided insights into the dietary evolution of primates.[186]

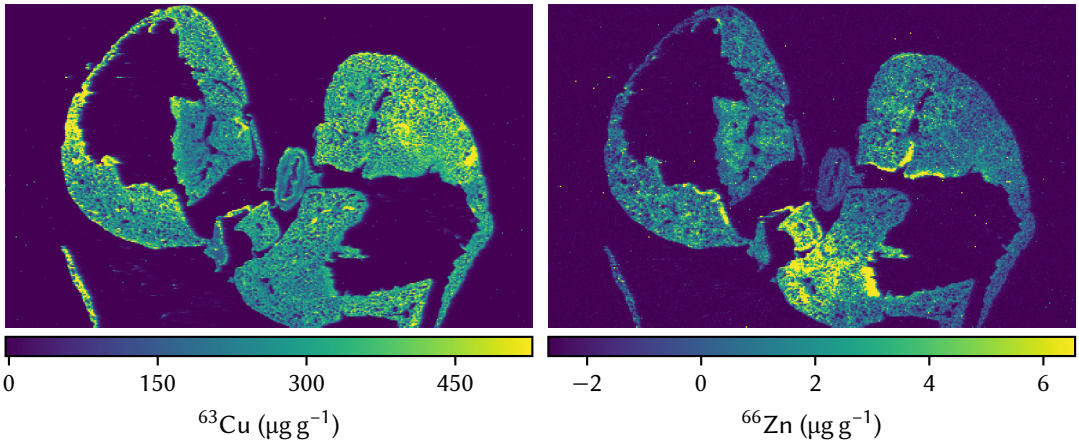

Figure 1.7. Concentrations of ^{63}Cu and ^{66}Zn in a mouse lung section.

The three major bio-imaging categories: X-ray fluorescence, metal-selective sensors and mass spectrometry (MS) based techniques all have their own advantages and disadvantages. X-ray fluorescence methods such as X-ray photoelectron spectroscopy are non-destructive, have high spatial resolution (<50 nm) and may be used to map multiple elements in a single scan.[187] Sensitivity is typically in the μg g^{-1} range but as high as the ag per pixel range, however this requires a synchrotron radiation source making it prohibitively expensive.[188] Metal-sensor based techniques apply a metal-specific fluorescent probe to samples which are then observed using optical microscopy. While the technique requires a suitable sample permeable probe it is non-destructive and allows imaging of metals within living cells.[187]

The MS imaging techniques, secondary ion mass spectrometry (SIMS) and laser ablation–inductively coupled plasma–MS (LA–ICP–MS), are destructive. SIMS uses an ion beam directed at a samples surface

to eject low-mass secondary ions which are then analysed by an MS. While it has excellent sensitivity and spatial resolution (500 nm when using a Bi_3^+ ion beam[187]) it suffers from severe matrix effects and requires extensive sample preparation.[189] The ion beam also has limited penetration of the sample limiting quantification to the surface of samples.[187]

1.4.1 LA–ICP–MS

The high spatial resolution of LA (<10 µm) combined with the sub $\mu g\, g^{-1}$ sensitivity of ICP–MS make it an excellent technique for precise mapping of trace elements in tissue. While LA–ICP–MS has been used in the earth and material sciences for more than 40 years it wasn't applied to biological materials until the 1990s.[190,191] A high powered, focused laser is used to ablate the sample, creating a plume of particulate matter. These particles are then transported by a gas to the ICP–MS where they are ionised, filtered and detected. Typically 193, 213 and 266 nm Nd:YAG solid-state or 193 nm ArF gas excited dimer lasers are used due to their high energy and short pulse durations.[192] Laser flux will determine the quantity of material ablated by each pulse and must be great enough to ensure a sufficient signal but remain below the roll-off point, where large particles with low transport efficiency are formed.[193] Cutting edge LA instruments use pulse widths in the fs region, minimising the transfer of heat into the sample and thus reducing roll-off and damage to the adjacent material.[194]

The quality of the data produced by an LA–ICP–MS system depends on several laser parameters. The laser radius (spotsize), speed of the laser and MS acquisition time (f_{MS}) will determine the resolution of the image produced. Typically, these are set so the pixel aspect ratio of the image is equal (eq. 1.13), although this can also be done later during image processing.[195]

$$\frac{\text{spotsize} \cdot f_{MS}}{\text{speed}} = 1 \tag{1.13}$$

Issues can arise when LA–ICP–MS parameters are misconfigured, leading to increased noise or imaging artefacts. To avoid this the laser pulse frequency (f_{LA}) and total MS dwell time need to be synchronised to ensure that each integration performed by the MS corresponds to a known integer of laser pulses, as in eq. 1.14.

$$f_{LA} = \mathbb{Z}^+ \cdot f_{MS} \tag{1.14}$$

Alternatively the integration time can be made large enough that any noise arising from non-synchronisation is negligible.[196]

Most ICP systems use a single quadruple MS however the use of ICP–triple-quadrupole mass spectrometry is increasing as they become more readily available. Both systems use a reaction cell were ions collide or interact with a collision or reaction gas. The sensitivity of some elements can be improved using H_2 or He as a collision gas during ICP–MS analysis. Introduction of collision gasses removes polyatomic interferences such as those in Table 1.3 and can more than double signal-to-noise ratios.[197] Analysis of Mn should always be performed using a collision / reaction gas as it has high background due to atmospheric nitrogen, $^{40}Ar^{15}N^+$.

Table 1.3. Common polyatomic interferences. Adapted from May and Wiedmeyer.[198]

Isotope	Abundance (%)	Interference
^{55}Mn	100.0	$^{40}Ar^{14}N^1H^+$, $^{39}K^{16}O^+$, $^{40}Ar^{15}N^+$, $^{38}Ar^{17}O^+$, $^{36}Ar^{18}O^1H^+$, $^{38}Ar^{16}O^1H^+$, $^{23}Na^{32}S^+$
^{56}Fe	91.7	$^{40}Ar^{16}O^+$, $^{40}Ca^{16}O^+$, $^{40}Ar^{15}N^1H^+$, $^{38}Ar^{18}O^+$, $^{38}Ar^{17}O^1H^+$
^{63}Cu	69.1	$^{31}P^{16}O_2{}^+$, $^{40}Ar^{23}Na^+$, $^{23}Na^{40}Ca^+$, $^{40}Ca^{16}O^1H^+$, $^{36}Ar^{12}C^{14}N^1H^+$
^{64}Zn	48.9	$^{32}S^{16}O_2{}^+$, $^{31}P^{16}O_2^1H^+$, $^{48}Ca^{16}O^+$, $^{32}S_2{}^+$, $^{31}P^{16}O^{17}O^+$, $^{34}S^{16}O_2{}^+$, $^{36}Ar^{14}N_2{}^+$
^{66}Zn	27.8	$^{34}S^{16}O_2{}^+$, $^{33}S^{16}O_2^1H^+$, $^{32}S^{16}O^{18}O^+$, $^{32}S^{17}O_2{}^+$, $^{33}S^{16}O^{17}O^+$, $^{32}S^{34}S^+$, $^{33}S_2{}^+$

Proteins are also able to be quantified using LA–ICP–MS using an IHC approach (Figure 1.8). A polymer is chelated with a rare-earth metals and then bound to an antibody with an affinity to the epitope of choice. The sample is then incubated with the tagged probe, and it binds to the region of interest, allowing imaging of the metals and thus of the epitope.[7] Using this approach Giesen et al.[199] were able to image three breast cancer markers simultaneously and later expanded the number of tags, imaging 32 proteins and protein modifications at once.[200]

1.4.1.1 LA–ICP–MS data processing

Most MS imaging (MSI) techniques have a large library of dedicated, open software for the reduction of data into parsable formats and images.[201] This is not the case for LA–ICP–MS, where the only full featured processing platforms are expensive, closed source commercial products. Due to a historical lack of vendor interest, the data produced by ICP–MS instruments coupled to LA systems are rarely in a readable format and must undergo some form of manual processing. In a typical pre-processing pipeline, the separate data files produced for each laser spot or scan line are reduced and stacked to form a single image for each acquired element. There is no universal format for ICP–MS data and as

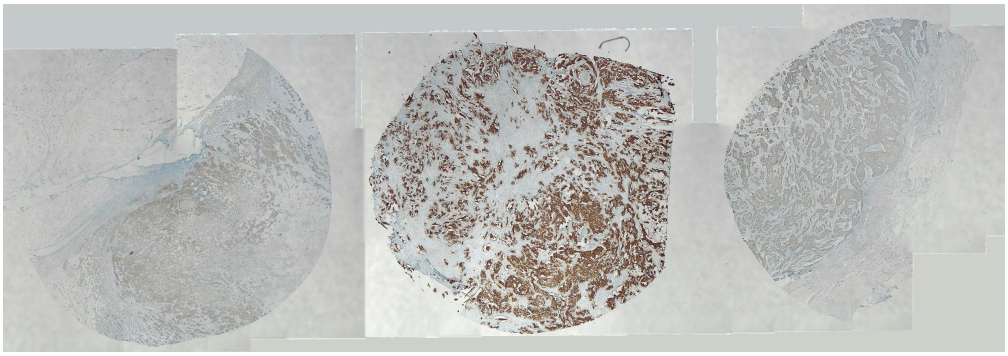

(a) DAB/HRP stain

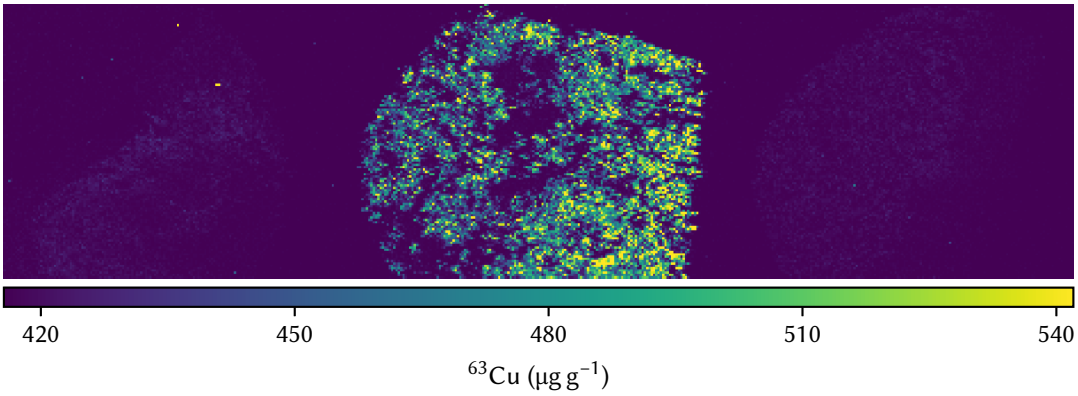

(b) LA–ICP–MS quantification

Figure 1.8. HER2 expression in breast cancer biopsies scored 0, 3+, 1+ (left to right), visualised using colourimetric (a) and LA–ICP–MS (b) IHC techniques. Over-expression of HER2 influences a cancers growth-rate and likelihood of spreading.

such a custom data conversion pipeline is required for each instrument vendor or even type.[202] Current processing software creates a large time burden on users with the pre-formatting of data often taking longer than the actual data acquisition.[203]

1.4.2 Calibration standards

One of the biggest challenges in quantifying biological matrices using LA–ICP–MS is the production of appropriate matrix-matched standards. Given the mass-dependant nature of ICP–MS absolute quantification requires that standards have both the same density and ablation characteristics as the tissue being analysed. Previous studies have used a range of materials including: certified reference material (CRM),[204] polymers,[205] homogenised tissue,[197,206–210] agarose gels[211] and gelatine.[212] While a variety of CRMs exist that allowing for accurate calibration they often are not available in a suitable format or in the required concentration range. This leads laboratories to develop their own, fit for purpose, calibration standards as in Table 1.4.

Table 1.4. Calibration standards used for LA–ICP–MS analysis of ^{55}Mn in biological tissues.

Standard material	Sample matrix	LOQ (µg g^{-1})	Reference
Chicken breast	Mouse brain	0.96[a]	[213]
Mouse brain	Mouse brain	2.35	[208]
Sheep brain	Mouse brain	0.55	[197]
Bone meal (CRM)	Human teeth	0.1 [a]	[214]
Sol-gel	*None*	2.7	[215]
Mouse brain	Mouse brain	1.2 [a]	[216]
Glass (NIST610; CRM)	Foraminifera shells	[b]	[217]
Agarose gel	*None*	[b]	[211]

[a] Lowest reported value as no LOQ provided.
[b] Values normalised.

1.4.2.1 Homogenised tissue

The most obvious sources for a matrix-matched standard is the matrix itself. Calibration standards can be prepared by homogenising tissue similar to the sample matrix and spiking it with known amounts of analytes.[208] The standards are then accurately quantified by digesting a small amount of the original

tissue homogenate and measuring it using solution-nebulisation ICP–MS.[208] A number of different biological tissues have been used previously the selection of which is dependent on the desired properties and must be carefully matched with those of the sample being analysed.[204,209,213]

While spiked and homogenised tissue standards closely match the samples, they are laborious to prepare and require handling biological material.[212] Additionally, tissues typically already contain metals which can make them unsuitable for the analysis of low concentrations. The matrix-matched brain tissue used in the widely followed protocol by Hare et al.[208] was found to contain (10.3 ± 6.9), (31.0 ± 18.0), (160 ± 55) and (10.7 ± 4.4) $\mu g\,g^{-1}$ of Cu, Fe, Mg and Zn respectively, making accurate quantification below these levels impossible.

1.4.2.2 Polymers and gels

Spin coated application of poly(methyl methacrylate) (PMMA) solutions allows for the creation of a thin film coating with uniform thickness. By doping PMMA solutions with ^{66}Zn and ^{63}Cu Austin et al.[205] prepared standards for the quantification of these metals in soft tissue. However, PMMA has lower internal standard accuracy than tissue homogenate and cracks when stored at 4 °C leading to decreased uniformity.[211]

Agarose gels have also been used to create calibration standards for LA–ICP–MS. A buffered gel (75 mg in 10 g water) was spiked with 69 elements and pipetted onto a glass slide. This produced a layer 30.0 ± 2.4 µm thick and recoveries of the elements were satisfactory.[211] However no comparison to tissues or reference materials was made and only the centre portion of the gel was flat enough to be useful for calibration.

1.4.2.3 Gelatine

Gelatine is an attractive alternative to homogenised tissues as it is a simpler matrix and retains similar density and ablation characteristics to tissue.[210,218] Only certain cations (Al^{3+}, Cr^{3+}, Fe^{3+}, Ce^{3+}, La^{3+}, Zr^{4+}) will exhibit cross-linking with the gelatine and thus be immobilised.[219] For other elements careful preparation protocols must be followed to avoid a ‘coffee stain’ effect (concentration of the spiked elements at the gelatine boundaries) caused by chromatographic effects. The setting temperature must be controlled to minimise temperature differentials across the gel and a 10 % w/v gelatine concentration should be used.[212] Alternatively a chelating agent such as EDTA may be added to assist in immobilisation.

There are several ways of preparing gelatine standards including: dripping liquid gelatine onto a slide,[212] slicing frozen gelatine to a certain thickness using a cryotome[218] and setting the gelatine in a prefabricated mould. The initial and final thickness also must be determined as a typical 10 % gelatine solution will dehydrate and shrink to around 10 % of its original depth.[220]

One issue with using gelatine is high background levels of Mn, around 150 ng g^{-1}. A cation exchange resin can be added to the gelatine to chelate Mn and then removed via centrifugation. This nearly eliminates the Mn background and can be used to reduce levels of other metals as well.[221]

1.4.3 Internal Standards

Even when matrix-matched standards are prepared correctly they still cannot account for the heterogeneity within tissues. Varying density, thickness and composition will affect the ablation of tissue, therefore altering the apparent concentration. To compensate for this, metals are commonly quantified against elements that are distributed homogeneously throughout tissues.[204] Differential isotopes elements have been used successfully: ^{43}Ca in teeth,[214] ^{32}S in hair and both ^{31}P and ^{13}C in tissue.[206] ^{13}C is the most commonly used internal standard for tissues due to its ubiquitous occurrence and the ability to account for variations in sample humidity.[222] However a review of the use of in-matrix internal standards found that ^{13}C had different ablation characteristics to many transition metals, possibly making it unsuitable for their quantification.[223]

1.5 Single cell experiments

The catalytic removal of ROS by manganese complexes was first observed as a defence mechanism in anaerobic bacteria.[120] Since then it has been observed in extremeophile bacteria,[125] yeast,[135] and coral.[224] Measurement of the bulk elemental properties of a population of cells is a simple process: digest a known amount of cells and quantify the elements using solution nebulisation ICP–MS. However this obscures cell to cell variations and thus gives no information about the elemental distributions within a population. A relatively new technique, single particle ICP–MS (spICP–MS), has the potential to simultaneously count cells and quantify their elemental contents.

When a dilute solution of particles is introduced into an ICP–MS they are delivered into the plasma and ionised into discrete clouds of particles. When operating the instrument with a low dwell time it is possible to detect these clouds as transient peaks, and integrate them to produce an intensity

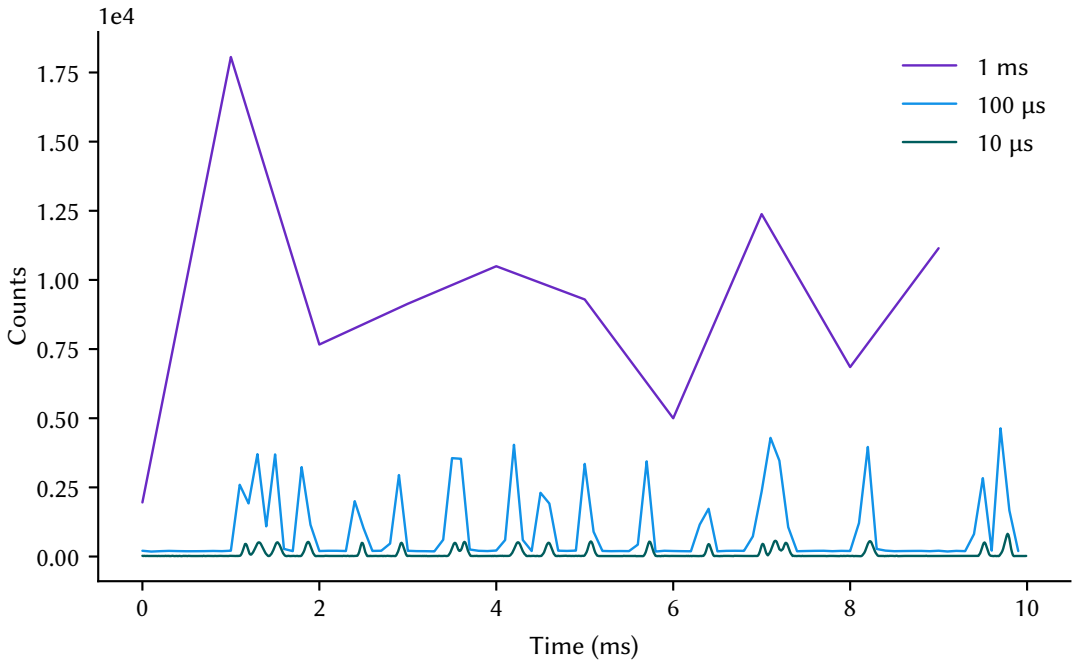

Figure 1.9. Simulated signals of the same data collected using different acquisition times. Lower dwell times improve signal-to-noise.

per detected particle. The ion cloud of a single nano particle (NP) is 300 to 1000 µs and acquisition frequencies of greater than 1000 Hz are required.[225] In general, higher acquisition frequencies increase signal-to-noise ratios and better resolve individual particles (Figure 1.9). Detection and measurement of several thousand particles produces a distribution of their elemental contents and can be used as a statistical base to calculate properties such as their size and mass.[226]

Mass cytometry uses IHC with lanthanide-tagged antibodies and an ICP–time-of-flight (TOF) instrument to measure antigens in single cells.[227] Unlike the quadruple instruments typically used in spICP–MS, a TOF can collect multiple elements simultaneously but has significantly reduced sensitivity. The low sensitivity limits the application of these instruments to measurement of elements with high ionisation efficiencies and low backgrounds. Additionally, many endogenous elements fall below the lower mass range (89 m/z) used by mass cytometry specific instruments and are unable to be measured. Endogenous elements such as Mn can be measured with sufficient sensitivity by applying the principles of spICP–MS to individual cells, a technique known as single cell ICP–MS (scICP–MS).

1.5.1 Investigations of Mn using scICP–MS

The intra-cellular concentrations of Mn have been investigated using scICP–MS several times, usually in association with other elements or as a response to an induced stress. Early studies measuring Mn simply fail to report concentrations determined by scICP–MS at all, indicative of measurement issues.[228–230] Wang et al.[231] examined the distribution of ^{55}Mn within HeLa, A549 and 16HBE cells using NH_3 as a reaction gas to increase signal resolution, however no limit of detection (LOD) was reported. There were also discrepancies between reported data points and mean concentrations, and the distribution of Mn in cells was Poisson, indicating a failure to isolate true signals from the ionic background. These issues are carried over to their latest paper as well, although they were able to show that the detected cells had a multi-modal distribution.[232] Such distributions suggest subpopulations of cells with different levels of Mn that would be unidentifiable using digestion and solution ICP-MS. Manganese was measured in yeast cells by Liu et al.[233] by scICP–MS and solution ICP-MS with LODs of 0.01 fg/cell. A dwell time of 0.1 ms was required to adequately separate the signal from the background. Using LA–scICP–MS, Löhr et al.[234] measured Mn in leukaemia cells but only 6 % of measured cells where above the LOD.

Signal intensities for Mn are an issue with low intra-cellular concentrations and high LODs. The LOD is typically defined using the blank + 3σ criterion but in the context of scICP–MS can lead to underestimation of the LOD and a large number of falsely detected cells. For a Gaussian signal the 3σ criterion will omit 0.27 % of events. The scICP–MS analysis of a blank with a 0.1 ms dwell time for 60 s will therefore lead to 1.62×10^3 false detections. More informed approaches use a higher σ level or a different method of defining the LOD, such as Poisson statistics.[235–237]

1.6 Thesis aims

Investigations of manganese and radioresistance requires specialised and dedicated analytical methods. High quality quantitative data is needed to determine the thresholds of resistance in tumours, guide future treatment regimens and probe the underlying biological mechanisms of antioxidant defence. Specifically, there are no fit-for-purpose LA–ICP–MS calibration standards capable of quantifying low levels of Mn, and a paucity of data reduction and processing options for both LA–ICP–MS and scICP–MS. This thesis will address these shortcomings by developing and implementing novel scICP–MS and LA–ICP–MS tools and methods. The specific aims and their objectives are:

Aim 1. To develop reproducible matrix-matched standards for accurate quantification of manganese in biological samples.

a) Manufacture of gelatine based standards with controllable chemical and physical properties.
b) Development of a method to reduced endogenous elemental backgrounds.
c) Evaluation of the suitability of new standards for quantification of tumour sections.

Aim 2. To develop open-source software tools to aid in ICP–MS analysis.

a) Creation of a library of processing algorithms and tools for calibration, calculations and artefact correction.
b) Development of open-source LA–ICP–MS data reduction and image processing software.
c) Development of open-source spICP–MS data reduction and analysis software.
d) Demonstration of the suitability of the software.

Aim 3. To investigate the relationship between manganese and inferred radio-resistance in tumour TMAs and sections.

a) Collection of tumour TMAs and section images using LA–ICP–MS.
b) Investigation of similar tissues with differing radiosensitivities.
c) Comparison of manganese concentrations with known cancer biomarkers determined using immunohistochemistry.
d) Comparison of segmentation methods with the goal of implementing an automated analysis pipeline.

Aim 4. To investigate the antioxidant effect of inorganic manganese using a breast cancer cell model.

a) Determination of the toxicity of manganese in the cell model and optimal treatment conditions.
b) Creation of a UV treatment method to assess the toxicity of different UV wavelengths.
c) Confirmation of the protective effect of manganese complexes when the cell model is exposed to ionising radiation.
d) Development of a scICP–MS method capable of characterising cell populations and quantifying intracellular manganese.

Chapter 2

Low Background Laser Ablation Standards

Quantification of elements in biological standards requires appropriate matrix-matched calibration standards. Current calibration standard technologies are chemically and physically heterogeneous and contain endogenous elements. These factors limit their ability to quantify elements, particularly those with low natural abundances in tissue such as manganese. This chapter addresses Aim 1 by detailing the manufacture and characterisation of low-background gelatine standards using both commercial and laboratory prepared moulds. The thickness, surface properties and robustness of the new standards are compared against cyro-section gelatine and tissue homogenate, and a method for lowering gelatine background using a metal chelator is presented. Mould-prepared standards had improved accuracy and precision while being easier to prepare and more reproducible than those prepared traditionally.

2.1 Introduction

LA–ICP–MS was first applied to biological tissues in 1994 by Wang et al.[191] and is now routinely used to measure the spatial distribution of elements in tissue. It is often considered the gold standard for spatial quantification of elements in biological tissues due to its high dynamic range and species- and matrix-independent ionisation and detection. Recent advances in immunohistochemistry have since extended the applicability of LA–ICP–MS to the investigation of bio-molecules.[238] Consistent ablation with a pulsed laser is dependent on the sample matrix and while internal standardisation approaches[239,240] and improvements in sampling techniques[241] have contributed to improved precision and accuracy[242] they can be time consuming and difficult to perform correctly. Instrumental drift also influences quantification and becomes particularly pronounced when long acquisition times are

required.[243] Nevertheless, spatially resolved quantification provides invaluable insights into biological processes and this has encouraged extensive investigations into a variety of accurate calibration and quantification procedures.[242,244]

The heterogeneous nature of biological tissues often preclude the use of certified reference materials and laboratories are required to prepare and characterise custom standards.[208,245] Most calibration approaches suggest matrix-matching to simulate the chemical and physical environment of a sample, in an attempt to guarantee consistent ablation characteristics, aerosol formation, atomisation and ionisation.[242,246] Unfortunately the application of matrix-matched standards is limited as the resulting matrices are unable to fully mimic the heterogeneous characteristics of biological tissues. One common approach to creating reference standards includes the homogenisation of easily obtainable tissues from domesticated animals to match the target tissue. This homogenate is then spiked with aliquots of elements before being homogenised again, frozen and sectioned to their desired thickness. Cross-quantification by solution ICP–MS analysis of the digested standard is then used to determine elemental concentrations.[208] A variety of approaches have been published reporting the preparation of materials to simulate brain,[208] eye,[247,248] tumour tissue,[249,250] liver[251,252] and teeth.[214] The processing required to produce tissue standards (specifically homogenisation and cryotome sectioning) causes deformation and variations in thickness, as discussed by Dorph-Petersen et al.[253] The tedious preparation and susceptibility towards systematic errors has encouraged the investigation of other standard materials.

Hydrocolloid gels such as gelatine or agarose[211] are an increasingly popular calibration standard material for biological tissues. Similarities in the gel and tissue composition mitigate many of the problems associated with animal tissue homogenates.[210,212,215,246] Three major methods for the fabrication of gelatine standards are described in literature: pipetted films,[254] spotted droplets[212] and cryo-sections.[255] However these techniques are associated with heterogeneous elemental distributions and poor standard topography due to elemental discrimination, surface tensions, “coffee-stain” effects, and cutting artefacts. Šala et al.[212] found that careful control of gelatine drying allows the fabrication of highly homogeneous standards suitable for biological tissue.

Endogenous elements present in tissue gelatine and other naturally derived standards place a lower limit on the usable calibration range. Trace elements that may be down-regulated by a biological response are therefore unable to be accurately quantified when the reference tissues used contain these elements. There has been little investigation into the elemental background of commonly used standard materials but a number of alternative polymers have been used. Both thin films of PMMA[205] and

acetonitrile-butadiene-styrol terpolymers[256] have been used as reference standards for LA–ICP–MS. Fabrication of standards from non-naturally derived materials should contain less endogenous elements but due to structural differences compared with tissue they may have significantly different ablation characteristics. An alternative to synthetic materials is to simply remove the endogenous metals from natural matrices using solid-liquid extraction methods.[257]

This chapter details methods for preparation of low-background gelatine standards using both commercial and laboratory-made moulds. The optimal gelatine source and concentration are discussed with regard to their physical properties and endogenous elemental make-up, and an extraction method that can mitigate high elemental backgrounds is presented. We demonstrate the simple, repeatable control of dimensions and surface properties of mould produced standards and contrast this with traditional standards of tissue and cyro-sectioned gelatine. The improved calibration characteristics of the low-background gelatine standards is proven through their analytical figures of merit.

2.2 Materials and methods

2.2.1 Tissue standard preparation

Male mouse C57/Bl6 lungs were harvested under Animal Care and Ethics protocol number 15-104-FINMH at the Florey Institute of Neuroscience and Mental Health (Melbourne, Australia). Animals were euthanised with an overdose of sodium pentobarbitone ($100\,mg\,kg^{-1}$) and perfused with 30 mL of warmed (37 °C) $0.1\,mol\,L^{-1}$ phosphate buffered saline (PBS), pH 7.4. Male wild-type (C57BL/6J) muscle tissues were purchased from Jackson Laboratories (Bar Harbor, ME, USA) and the quadriceps muscle was dissected under guidelines established by the Institutional Animal Care and Use Committee at the University of California, Los Angeles (ARC #2000-029-61D). Seastar baseline 67 to 70 % nitric acid and 30 to 32 % H_2O_2 obtained from Choice Analytical (Thornleigh, Australia) were used for all standards and tissue digestions. Mouse brain standards were prepared as previously described by Hare et al.[208] using mouse tissues harvested from control animals which were euthanised under a material transfer agreement between the Florey Institute and University of Technology Sydney.

2.2.2 Gelatine standard preparation

Gelatines from bovine bone, porcine skin and cold fish skin were purchased from Sigma Aldrich (Castle Hill, Australia) and gelatine from calf skin from Polysciences, Inc. (Warrington, PA). A 10 % m/v

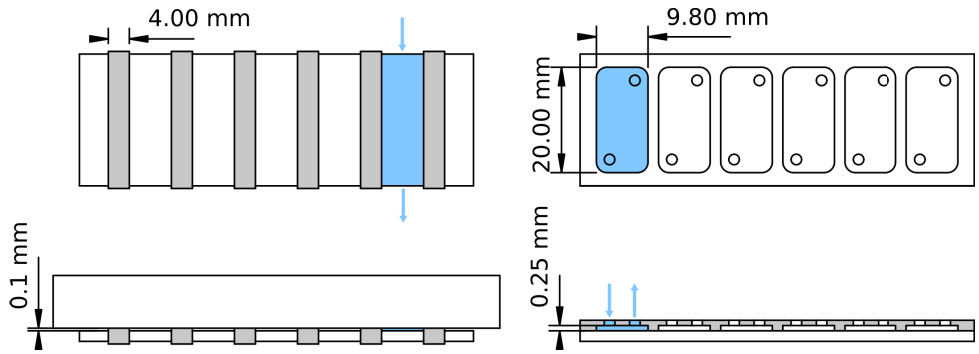

Figure 2.1. Schematic of the laboratory-made mould (left) and commercial HybriWell™ sealing system (right). Thickness of the custom mould can be adjusted by using multiple layers of PTFE tape. Blue arrows indicate the gelatine flow path.

solution of each gelatine was prepared by dissolving gelatine powder in a buffering solution composed of 100 mmol L^{-1} Tris-HCl (pH 7.4), 10 mmol L^{-1} EDTA and 1 % w/w polyethylene glycol–400 (Sigma Aldrich) in milli-Q water (Arium Pro Vf, Sartorius; Goettingen, Germany). This buffering solution helps maintain the integrity of the gelatine at high metal concentrations. Nitrate hydrate salts of Mn, Cu and Zn were diluted with the buffer solution and spiked into the gelatine solution at concentrations of 0, 1, 5, 10, 15 and 30 µg mL^{-1} respectively.

Commercial Grace Bio-Labs HybriWell™ sealing systems (0.8 mm × 20 mm × 0.25 mm; Sigma Aldrich) were used with microscope slides to manufacture 25 µm thick gelatine standards. Gelatine was heated to 54 °C until liquid then pipetted into a pre-heated mould as illustrated in Figure 2.1 and immediately frozen at −20 °C for 15 min. The mould was then removed and the frozen gelatine standards were dried overnight at room temperature. While freezing was vital to obtain homogeneous elemental distributions and to remove the mould without damaging the standard, longer freezing times were found to induce cryo-artefacts such as holes and uneven surfaces. The final thickness of the standards was 25 µm as drying reduced the mass and thickness of the standards 10-fold.

For cross-quantification of standards, liquid gelatine was pipetted in polypropylene tubes and weighed after drying overnight. Digestion was achieved shaking the solidified gelatine aliquot in 1 mL of 20 % nitric acid for 20 min followed by dilution. All gelatine standards were analysed in triplicate to calculate averages and standard deviations. Various gelatine standards thicknesses were produced with laboratory prepared moulds by using commercial poly(tetrafluoroethylene) (PTFE) tape (Bush branded) (100 µm) as a spacer between a PTFE block and glass microscope slide. The resulting gaps were filled from the side with heated liquid gelatine as shown in Figure 2.1 and subsequently frozen and dried as per the commercial moulds. Multiple layers of the 100 µm Teflon tape could be used to manufacture gelatine

standards with thicknesses of any multiple of 10 µm and the thickness could further be controlled by varying the gelatine content.

Cross-linking of gel solutions was performed using caffeic acid, formaldehyde or a 25 % glutaraldehyde solution (Sigma Aldrich).

2.2.3 Polymer standard preparation

Standards of various concentrations polyacrylamide (PAM) standards were prepared from stock solutions of 500 mg mL^{-1} acrylamide and 20 mg mL^{-1} N,N'-methylenebisacrylamide (Sigma Aldrich). Polymerisation of acrylamide gel solutions was initiated using by adding 2 mg mL^{-1} ammonium persulphate and 2 mL mL^{-1} tetramethylethylenediamine. UV–curing gels were created using commercial nail polishes. Gels were spiked with oil based metal standards (Conostan; Choice Analytical), then cured under a 310 nm light for 15 min.

2.2.4 Endogenous element extraction

Naturally abundant elements were removed from the gelatine via solid–liquid extraction with non-buffered water to avoid buffer components interfering with the extraction. 200 mg of gelatine was weighed and dissolved in 1000 µL of water, heated to 54 °C, and spiked with chelating resins. Various resins were investigated: Amberlyst 15 (H), Amberlite CG50 (H) and Amberlite IR120 (Na) were purchased from Sigma Aldrich and Bio-Rex 70 and Chelex 100 were purchased from Bio-Rad (Gladesville, Australia). The resins were added to liquid gelatine standards and gently shaken for an hour at 40 °C before being separated by centrifugation in a Centrifuge 5702 (Eppendorf; Macquaire Park, Australia) operated at 2000 rpm for 2 min. The supernatant was diluted with a two times concentrated buffer solution to produce a 10 % buffered gelatine standard, which was then filled into the mould.

2.2.5 Topography

Brain tissue samples were homogenised and cryo-sectioned at 10 µm. After cryo-sectioning, thickness and surface topography were compared against those of the gelatine standards and representative samples using a DektaXT Profilometer (Bruker, Billerica, MA) operated at room temperature. Gelatine standards were kept overnight to allow drying to ensure repeatable 10-fold thickness reduction. A 2 µm stylus with a force of 1 µN was used to scan standards with a lateral resolution of 0.33 µm over the full lengths of the standards.

Two-dimensional height maps of brains were created using parallel scans spaced at 200 µm intervals both horizontally and vertically. Spacing was achieved by ablating marker holes into the glass surrounding the brain sections.

2.2.6 Instrumentation

Cross-quantification of standards was performed on an Agilent 7500cx-series ICP–MS (Mulgrave, Australia) equipped with a micromist™ concentric nebuliser (Glass Expansion; West Melbourne, Australia) and a Scott type double pass spray chamber cooled to 2 °C for sample introduction. Helium was employed as collision gas to reduce polyatomic interferences. For tissue homogenate, three aliquots (approximately 50 mg) of spiked homogenate were weighed and digested in a Milestone ML1200 microwave digester (In Vitro Scientific; Noble Park North, Australia) in 4 mL concentrated nitric acid and 1 mL H_2O_2 then subsequently diluted. For gelatine standards approximately 12 mg of dried gelatine was dissolved in 5 mL of 2 % nitric acid.

Characterisation of lanthanide-labelled antibodies was performed using size-exclusion chromatography (SEC)–ICP–MS, as per Clases et al.[258] Briefly, 10 µL of a dilute solution of labelled antibodies was injected and separated on a Waters ACQUITY SEC column (1.7 µm, 4.6 mm × 300 mm; Rydalmere, Australia) using a 0.1 mol L^{-1} ammonium acetate buffer. The sulphur and lanthanide content were measured using post-column isotope dilution analysis on an Agilent 8900 series ICP–MS. A spike solution containing ^{34}S and natural abundances of Eu and Er was introduced at 0.0263 mL min^{-1}. Mass shifts from the oxygen reaction gas were used to measure SO^+ and ErO^+, removing interferences.

2.2.7 LA–ICP–MS analysis

A NWR193 Laser Ablation System operated at 40 Hz (Kenelec Scientific; Frenchs Forest, Australia) was coupled to an Agilent Technologies 7700-series for LA–ICP–MS experiments. Laser and ICP–MS parameters were set to those outlined by Lear et al.[195] to obtain square pixels that represent the same dimensions of the standard. The laser fluence was set to 0.5 J cm^{-2}, beam diameter to 35 µm and scan speed to 140 µm s^{-1}. Average values, standard deviations and figures of merit were calculated following the ablation of 4 lines with a length of 2 mm producing approximately 230 data points per standard.

2.3 Results and discussion

2.3.1 Topography and thickness characterisation

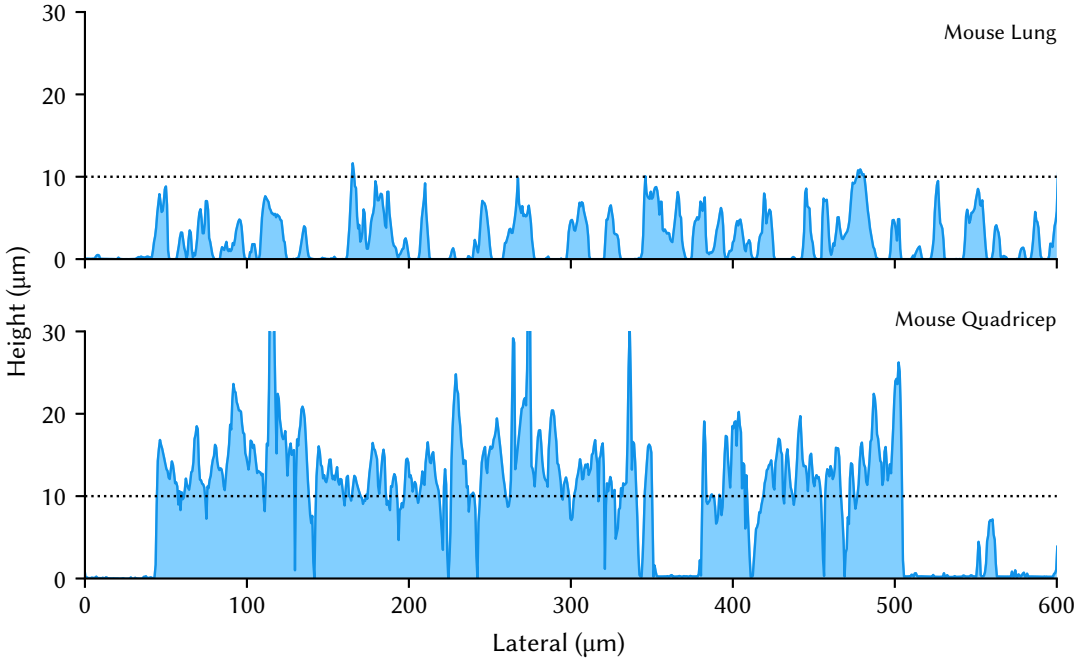

Figure 2.2. Thickness and roughness of cryosectioned tissue, a dotted line indicates the desired thickness.

In order to investigate the topographical characteristics of tissue two representatives were chosen, mouse lung and mouse muscle. These tissues are known to have heterogeneous distributions of elements and complex physical structures. It can be seen from the data in Figure 2.2 that cyro-sectioning produced highly heterogeneous surfaces with incorrect thicknesses. Thicknesses were 49 and 126 % of the expected values for lung and quadriceps tissue with relative standard deviations (RSDs) of 67 and 46 %. The cryo-sectioning of a homogenised brain standard and gelatine standard also resulted in slices of incorrect thickness with largely rough surfaces. Here thicknesses and deviations of 67 ± 35 % and 74 ± 10 % were recorded for the tissue and gelatine. The high shear forces that occur during sectioning induce surface artefacts and increased the thickness at the margins of the sections substantially. Accuracy is also impacted by drying effects of the gelatine standard which undergoes significant shrinking. In case of a 10 % gelatine material, shrinking will reduce standard thickness by approximately 90 %. The results in Figure 2.2 as well as previous work by Dorph-Petersen et al.[253] demonstrates that use of a cryotome to prepare thin sections below 50 µm inevitably induces artefacts that may influence elemental distributions. Preparation of matrix-matched standards to mimic the properties of these tissue would lead to highly

heterogeneous physical structure and elemental distributions, properties that are highly undesirable in reference standards. Therefore it is suggested that a material with similar ablation characteristics to tissue (such as gelatine;[212] Figure 2.4) is formed into standards in a way that produces a smooth and flat surface with a homogeneous distribution of elements.

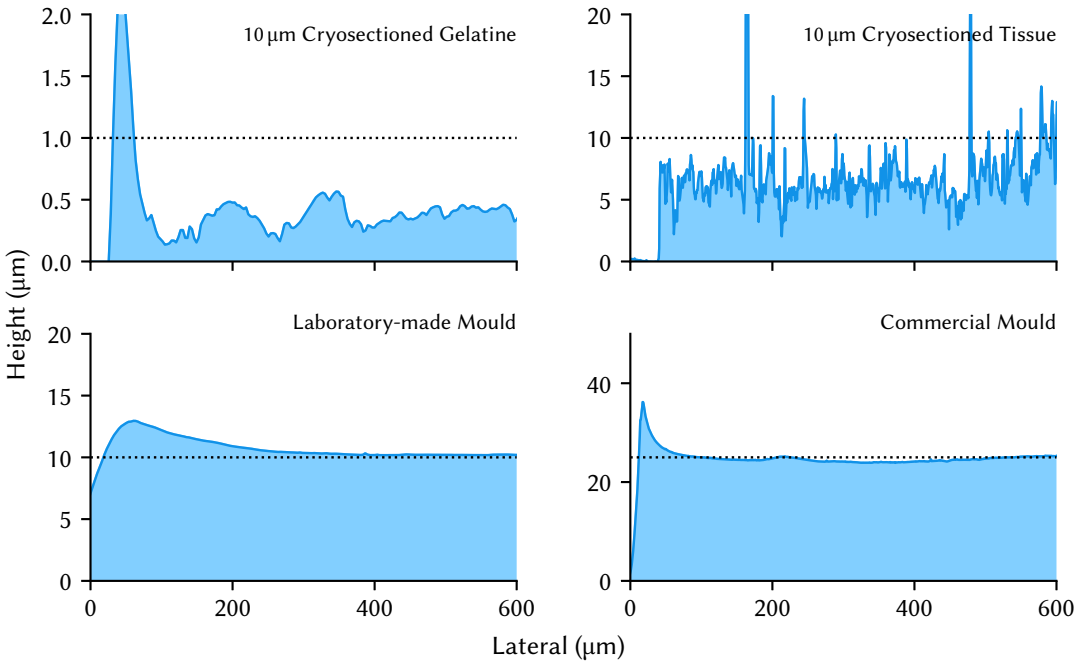

Figure 2.3. Profiles of sectioned and mould produced standards, the sectioned gelatine was cut at 10 µm. All gelatine standards exhibited drying artefacts in a 100 µm margin of their edge.

Thin films of gelatine can be dried reproducibly to produce defined and highly homogeneous layers with thicknesses in the lower µm range. Results in Figure 2.3 show thin film gelatine prepared using a cryotome and both commercial and laboratory made moulds. Thicknesses of the mould-produced films were very close to the expected values (95 to 103 %) with low RSDs (2 to 6 %) while the cryosectioned standard was 40 ± 30 % of the desired thickness. Only the margins (approximately 100 µm) of the mould-prepared standards appeared to contain drying artefacts, typically seen as an increased thickness. While this area should be avoided when ablating it only reduces the usable area of produced standards by a small amount. The precise control of thickness and surface finish surface increases calibration precision by decreasing variations during ablation of the gelatine. It is clear from this data that cryosectioning results in a rough surface finish and is therefore poorly suited for the production of calibration standards. In contrast both the mould-prepared standards demonstrated a fine control of thickness and superior flatness.

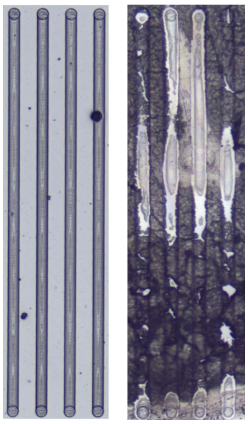

(a) Image of the lines ablated in gelatine (left) and tissue.

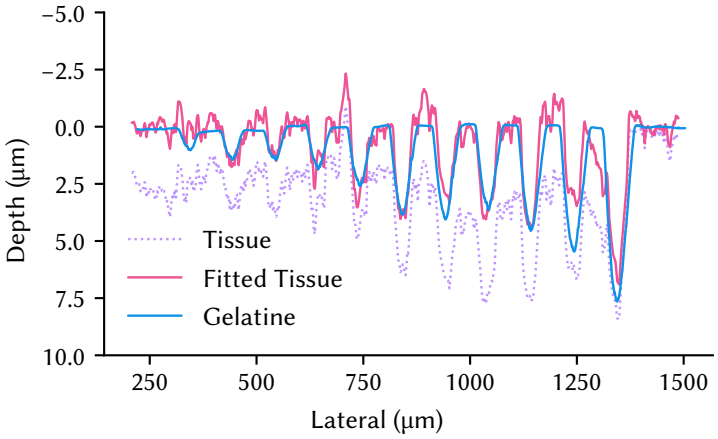

(b) Comparison of the ablation depths in gelatine and tissue.

Figure 2.4. Ablation depths in both gelatine and homogenised brain tissue standards at a range of laser powers. Ablation characteristics were similar as seen in (b). Tissue profilometric data was fitted to the gelatine using a polynomial curve to aid in comparison.

To investigate the ablation characteristics of the new and old standards they were ablated with 11 laser scan lines of increasing power (0.02 to 3.52 J cm^{-2}). Initial observations seemed to show differences in the ablation characteristics but subsequent profilometric measurements determined them to be very similar Figure 2.4b. Depths of ablation in both standards increased linearly with laser power however high laser powers caused crater formation in the homogenised tissue standard. These craters could potentially impact neighbouring scan lines if spacing closely together.

2.3.2 Calibration and backgrounds

The material characteristics of the moulded gelatine standards is apparent in their improved linearity and sensitivity. This was demonstrated by monitoring Mn, Cu and Zn during ablation of four scan lines on both the homogenised tissue and gelatine standards (Table 2.1). The high heterogeneity of the tissue standards results in signal deviation at each calibration level (Figure 2.5), reducing the LODs for all elements and extending their usable calibration range. The lower backgrounds of Cu and Zn also contribute to lower detection limits however the high concentration of Mn in the gelatine demonstrates that materials still have to be chosen carefully to avoid issues with specific metals.

Due to issues with bovine gelatine containing high background concentrations of specific metals a number of other gelatine sources were investigated. Various metals were quantified in triplicate using solution ICP–MS and are reported in Table 2.2. Both fish and porcine gelatines contained lower concentrations of all tested metals however fish gelatine solutions do not solidify at room temperature

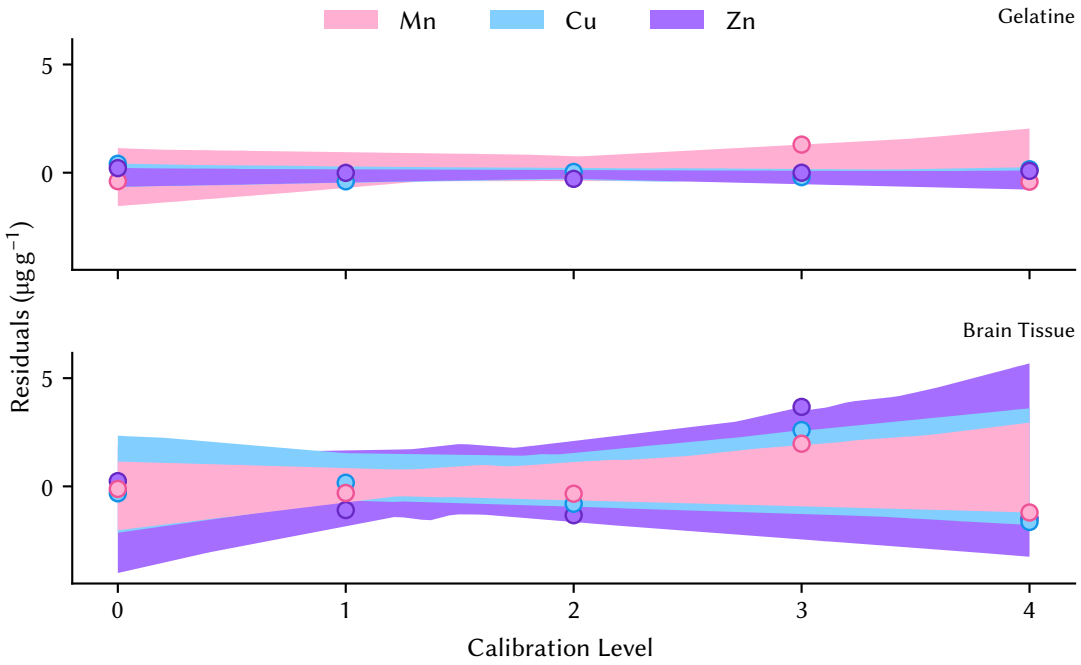

Figure 2.5. Residuals of the calibration curves produced from the gelatine and tissue standards.

Table 2.1. Characterisation of the gelatine and homogenised brain tissue standards using LA–ICP–MS. Each calibration level was determined via cross-quantification using solution ICP–MS

	Gelatine			Tissue		
	Mn	Cu	Zn	Mn	Cu	Zn
Slope (counts·g µg^{-1})	4750	630	518	2600	244	570
Intercept (counts)	2130	−182	52.5	1300	−610	1950
LOD (µg g^{-1})	2.54	1.09	0.63	4.09	5.54	7.50
Linearity (r^2)	0.9976	0.9980	0.9989	0.9963	0.9940	0.9929

without addition of a cross-linking agent. If cross-linked gels lose their ability to revert to a liquid on heat, making any cross-linked gel single use only. To further lower background concentrations a range of ion exchange resins were added to the porcine gelatine. These resins contain metal ion binding functional groups that exhibit different affinities for ions based on their size and charge. By adding them to the gelatine a loosely bound ion (Na^+ or H^+) is released into the gel and ions with a higher affinity are removed.[257] Care should be taken when using H^+ bound or carboxylic based resins as the addition or removal of H^+ will affect the pH of the gel, potentially reducing its strength and preventing it from setting. Some elements were actually increased during chelation, possibly due to metals already bound to the resins or contamination during extraction. These elements could be reduced by implementing an additional resin cleaning step before chelation. All metals, with the exception of zinc, were significantly reduced by one or more resin demonstrating the ability for resins to reduce natural background levels in standards, a critical requirement for analysis of trace elements. The chelating resins in Table 2.2 represent many of the commonly available resin functional groups and a good reference for resin selection when a specific element is being targeted.

Table 2.2. Background concentrations (pg g^{-1}) of various gelatines and their reduction using chelating resins.

	^{24}Mg	^{55}Mn	^{56}Fe	^{58}Ni	^{63}Cu	^{66}Zn
Bovine	40 600±400	2100 ±10	54 500±300	338 ± 9	530 ± 9	1200±120
Fish	260± 30	8 ± 4	910± 50	7 ±11	120 ±10	110±110
Porcine	4500±200	33 ± 6	1300±100	17 ±11	70 ±40	300±170
Amberlite IR120+	2± 3[a]	6 ± 0.3[a]	1300±200	20.0± 1.1[b]	46 ± 9	69± 55
Amberlite CG50	160± 19[a]	7 ± 8 [a]	1000±300	14 ± 2 [a]	260 ± 5 [b]	90± 80
Bio-Rad Bio-Rex 70	10± 20[a]	0.4± 0.7[a]	780± 60[a]	43 ± 6 [b]	76 ± 4	35± 43
Amberlyst 15	140± 50[a]	0.6± 0.7[a]	670± 20[a]	4.5± 1.2[a]	28.0± 1.5[a]	30± 60
Bio-Rad Chelex 100	90± 50[a]	0.6± 1.1[a]	660± 80[a]	26 ± 6	18 ± 5 [a]	80± 80

[a] Significantly lower as determined by *t*-test (α=0.05).
[b] Significantly higher.

2.3.3 Polymer standards

Materials from natural sources will inevitably contain endogenous elements that could affect calibration quality and thus quantification. Synthetic materials could offer a low background alternative to the naturally sourced gels discussed above. Several synthetic materials were investigated to determine

their suitability as calibration standards for elemental bio-imaging. Initial tests with PAM were positive however the gel films tended to peel off slides, ruining the flat surface required Figure 2.6. Concentrations of acrylamide from 2 to 40 % with a cross-linker concentration of 0 to 4 % were tested, with higher percentage, moderately crosslinked gels performing best. However even these gels would crack when dried and exposed to the low pressures in the laser ablation chamber during evacuation and the use of PAM was abandoned.

The second synthetic material trialled was a polyurethane UV-curing resin. These resins do not mix with the aqueous salt or acid metal standards usually used to spike the calibration matrix and produce different calibration levels. Instead, oil based microwave plasma atomic emission spectroscopy metal standards were used, however the relatively low concentration of the standards limited the maximum calibration range. Standards were moulded in a HybriWell on a glass slide then inverted under a 310 nm lamp to cure. Unfortunately, the cured UV gel had a different ablation characteristic to tissue, rendering it unsuitable for use as a calibration standard matrix.

(a) Polyacrylamide. **(b)** Polyacrylamide after drying. **(c)** UV cured resin.

Figure 2.6. Images of the standards produced using acrylamide and urethane polymers in commercial moulds. The polyacrylamide standards peeled off the glass slide (b) due to drying induced stresses.

2.3.4 Gelatine height-map

External standards can normalise for variations in sampling and instrument response but cannot account for heterogeneity within a sample. Variations arise in bio-imaging due to intra- and inter-sample variations in thickness, density and composition. Previous attempts at normalising these variations used an endogenous element such as or a pseudo-internal standard. Endogenous elements such as ^{31}P[206] or ^{13}C[222] suffer from poor signal-to-noise and are rarely distributed homogeneously. The most common form of pseudo-internal standardisation involves placing a sample over or under a thin film of material spiked with a rare earth element, which are then completely ablated.[205] This method provides no detail on the thickness, density or composition of the sample.

To definitively quantify a sample using LA–ICP–MS you must know the thickness of the material at each pixel location. The simplest way to do this would be to create a 2D map of the sample prior to ablation using a non-destructive technique such as profilometry. However, this is extremely time consuming if using a contact profilometer or requires an expensive optical profilometer, something not found in a bio-imaging laboratory. It should be possible to calculate the thickness of a tissue by first coating it in a known amount of spiked gelatine, then measuring the signal produced. Areas of high sample thickness will have less gelatine, demonstrated in Figure 2.7, and thus lower signal.

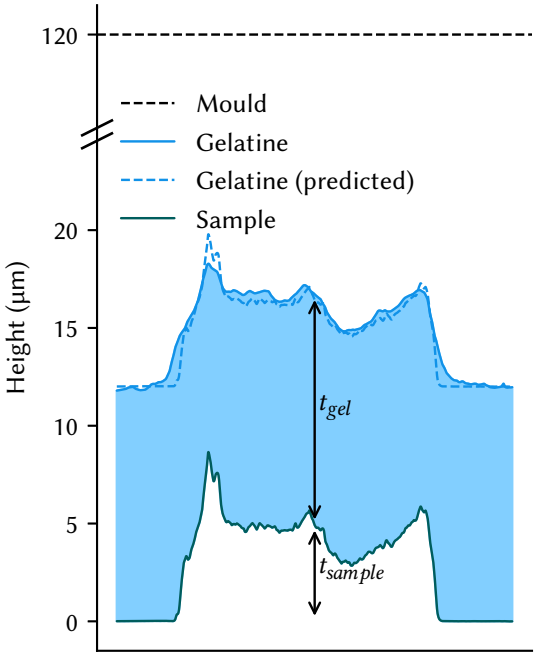

$$t_s = t_m - t_g / f_s \tag{2.1}$$

$$t_s = \frac{t_m - I/\bar{I}_S}{f_s} \tag{2.2}$$

Figure 2.7. Calculation of the height of a brain sample using a moulded gelatine coating.

To demonstrate the technique a brain sample was profiled, coated in 10 % gelatine using a 0.12 mm HybriWell and profiled again. Sample height t_s was calculated for all pixels using equations eqs. 2.1 and 2.2 and the known thickness of the mould (t_m) and gelatine shrinkage factor f_s. The gelatine thickness t_g was determined from the signal of a spiked element over the sample I and in areas with no sample I_S. This technique only required the collection of a single additional element and could easily be implemented in current LA–ICP–MS methods. However, small errors from imperfections in the gelatine are multiplied and cause large over- and underestimations of the samples thickness. Despite the gelatine in Figure 2.7 having only a 1 % mean difference from the predicted value, the mean error in calculated sample thickness was 69 %.

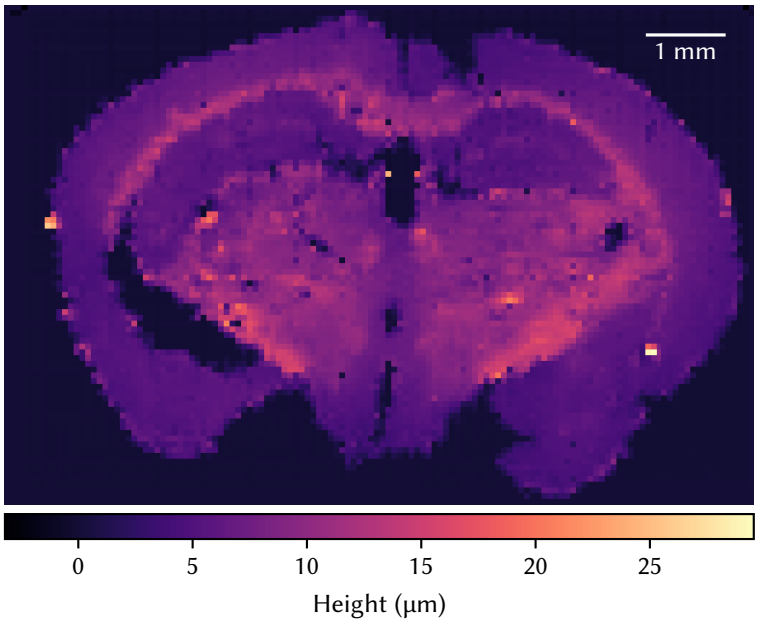

Figure 2.8. Height map produced by interpolating a series of 79 1D profilometric measurements. Measurements were taken at 200 µm intervals in both the x and y directions.

In an effort to decrease the magnitude of the errors a new technique for creating much thinner gelatine was developed. A mould template was cut out of 50 µm thick 3M 467 transfer tape, adhered to a glass slide and covered with a TODO film. Heated gelatine was then flowed into the mould using capillary action, frozen at −80 °C and allowed to dry. To track the errors produced over an entire sample using the new moulds required the creation of an accurate height-map. This height-map was produced by 'scanning' a sample using a 1D contract profilometer in orthogonal directions and is shown in Figure 2.8. Once the profilometic measurements were made a python script was used to interpolate

them to the same 75 µm pixel size used in the LA–ICP–MS images. Interpolation had the additional benefit of 'smoothing over' measurement artefacts from dust or vibrations.

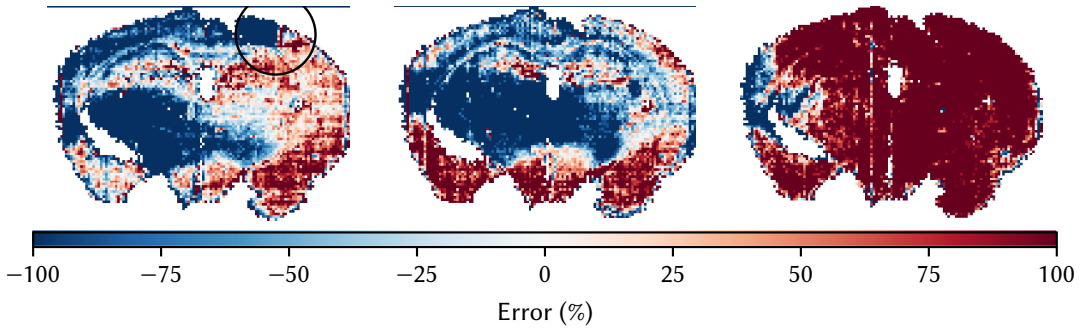

Figure 2.9. Errors in the gelatine produced height maps in three separate brain sections. Drying forces and small deviations in the gelatines surface lead to large errors in the produced map.

Errors in the predicted height across three brain sections (Figure 2.9) were large. Large stresses occur in gelatine as it dries and result in small deformations and rippling. While it may be possible to reduce the stresses using a temperature controlled oven to slow the drying process[219] the magnification of error is inherent to the method. Reducing the amount of drying by using a higher percent gelatine is also possible but slows the ablation of the sample due to the increased amount of material. Complete ablation of a sample coated in 10 µm of gelatine will require double the amount of time as the sample alone. The large error and growing complexity of this method make it unsuitable for use in its current form.

2.4 Conclusion

The analysis of the mouse lung and muscle tissues demonstrated the complex requirements of matrix-matched calibration standards. Preparation of standards from homogenised tissue resulted in poor precision, accuracy and reproducibility. Using gelatine as a matrix mimicked the most important physical and chemical properties of the tissue sections while allowing fast, easy and repeatable standard production. Preparation of the gelatine in moulds further improved the standards surface characteristics and offered increased control over their final thickness. This new method of production led to improved ablation characteristics, demonstrated by the increased accuracy, precision and linearity when compared to tissue standards. When trace analysis is required the natural background of biological materials can reduce the calibration range of standards and therefore standard materials must be carefully chosen. Various gelatine materials were quantified to determine the optimal material for use when low

backgrounds are required and chelating resins were employed to further reduce backgrounds. All five resins reduced elemental backgrounds further improving the LODs and dynamic calibration ranges of standards. The methods for production of gelatine films presented in this thesis improve upon those currently used for LA–ICP–MS standard preparation. The ease of manufacture, improved properties and high reproducibility of these standards have the potential to greatly improve intra- and inter-laboratory comparability.

Chapter 3

LA–ICP–MS Imaging Software

Open-sourced software is a key component of the mass spectrometry imaging field, where transparency in data processing is vital. However, options for LA–ICP–MS data conversion and processing are limited with published software either no longer available, undocumented, failing to support multiple instruments or limiting access to the code used to interpret data. The chapter describes Pew² an LA–ICP–MS specific feature-rich open-source image processing software that is compatible with common ICP–MS vendors. The software is fast, easy to use, and adheres to modern visualization philosophies that minimize data interpretation errors and image anomalies. The features of Pew² addressed Aim 2 and were used throughout this thesis.

3.1 Introduction

The high sensitivity of LA–ICP–MS makes it the preferred technique for imaging trace elements in biological tissues. Since the seminal paper of Gray[190] there has been significant improvements in the speed, sensitivity and resolution of LA–ICP–MS imaging with growing utility for medical, life science, environmental, geoscience and food safety applications.[242,259–262] However, there has been sporadic development of data reduction software with no open-source option available. While a large library of software does exist for the conversion and analysis of MSI data,[201] very few of these programs focus on LA–ICP–MS data specifically (Table 3.1). These are confined to specific vendor file formats,[203] require purchase of an expensive commercial license[263,264] or are closed-source.[265] This is partially driven by a lack of vendor support for LA–ICP–MS imaging.

Table 3.1. Published software for LA–ICP–MS data processing. Most software is no longer available and has poor vendor support.

Program	Import Formats	Availability	Reference
ELAI VBA script	Pre-formatted	Unavailable	[266]
HDIP	Multiple	Commercial	[263]
IMAGENA	Pre-formatted	Unavailable	[267]
iQuant2	Pre-formatted	Unavailable	[265]
LA-ICP-MS Image Tool	Pre-formatted	Open-source	[268]
LA-iMageS	PerkinElemer	Open-source	[203]
Iolite	Multiple	Commercial	[264]
MapIT! MATLAB script	Pre-formatted	Open-source	[269]
RecSegImage-LA	Pre-formatted	Open-source	[270]

Initially LA–ICP–MS data was collected in a spot-wise manner, similar to other MSI techniques, where images were constructed via integration of signal peaks produced by ablation of a grid of individual spots.[271] In contrast, most LA–ICP–MS methods today use continuous collection of individual lines. The laser is usually configured to continuously ablate a line such that each MS acquisition window forms a single pixel of an image. Typically, the laser scan speed, spot diameter and MS acquisition time are set for equal aspect pixels.[272] The separate spots or lines must then be combined to form a complete image. Quantitative imaging is possible by simultaneously or consecutively sampling material of a known concentration. A calibration curve is constructed by plotting signal intensities against concentrations and samples quantified by comparison to a line of best fit. This combination of spatially resolved and quantified elemental imaging provides in depth analysis of biological systems normally only possible by multiple techniques.

Each ICP–MS vendor and instrument stores and exports data in different formats, usually with little consideration for imaging applications. Consequently, vendor exports require pre-processing prior to examination of data using external imaging software.[203] Time spent manually pre-processing data files is often longer than analysis time, a problem that increases exponentially with data size and is further multiplied when each instrument requires a separate process. Most available software does little to assist users in importing data, mainly due to the complexities to support a large variety of file formats. Only closed-source commercial product software platforms natively supports more than one vendor format.[263,264]

Open sourcing software provides many benefits and enables users to collaborate and build upon existing software. In the field of bioimaging one such example is FIJI, an image processing package based on ImageJ. FIJI has a fully open development stream and ubiquitous usage in literature.[273] Public visibility of code allows users to verify implemented algorithms that ensures confidence in performance and outputs. This code visibility allows users to contribute features such as support for new vendors and instruments. Open sourcing also provides opportunities for other developers to maintain the software if the original designer abandons the project. This is seen extensively with published LA–ICP–MS software where many programs fail to receive meaningful updates a year after publication and lack support for newly released instruments or formats.

The usual scientific publication model relies on peer review to ensure quality, robust interpretation, and appropriate reporting of results and conclusions. However, this is not true of un-reviewable closed commercial software. Open-source software usage is the future of research with large entities such as CERN moving to a totally open-source framework in order to improve collaborative efficiency.[274] This model would be particularly valuable for the growing field of LA–ICP–MS imaging, which is finding ever increasing applications in many diverse areas of endeavour.

User experience and documentation of features contribute to software's ease of use and facilitates widespread adoption. This is true for software in all fields and is an educational pillar for computer science and software engineering courses.[275] Documentation accelerates acceptance of new features and techniques as software development progresses with research. Documentation is not common in LA–ICP–MS imaging software, inhibiting widespread implementation, and preventing use of full feature sets. Current LA–ICP–MS programs also fail to adhere to unbiased visualisation philosophies, potentially leading to misidentification and obfuscation of data.[276] Despite a large amount of research into visualisation methods, the majority of published ICP–MS imaging software default to misleading rainbow colour-maps.[277] The non-uniformity in perceptual contrast of these colour-maps can introduce apparent artifacts and lead to incorrect interpretations.[278] These issues can be completely negated by using a perceptually uniform colour-map.

Image processing is often used to improve the clarity of experimental data to better communicate results. Displaying regions of interest (ROIs), signal overlaps and the removal of instrumental anomalies all simplify the interpretation of data. Segmentation[279] and ratiometric analysis[206] of LA–ICP–MS images have been used to identify structural features and filters such as numerical inversion of blur[280]

and Richardson-Lucy deconvolution[281] have been used to remove system artefacts. These tools are quickly becoming essential for LA–ICP–MS imaging applications.

This work discusses the development of a novel LA–ICP–MS imaging program 'Pew²', that addresses the shortcomings of current software and to simplifies the import and conversion of spot-wise and line-by-line acquired quantitative data. The new software is an open-source, python-based implementation using 'NumPy',[282] with a cross-platform Qt5 graphical user interface (GUI) implemented using 'PySide2'. A low-level python library 'pewlib' has been made available for creation of python scripts for batch conversion of data and processing. Features of the program are demonstrated using real and simulated data.

3.2 Materials and methods

3.2.1 LA–ICP–MS analysis

To demonstrate the use of Pew² a human pancreatic adenocarcimoa TMA core (US Biomax; Rockville, MD) was imaged using a NWR193 laser ablation system (Kenelec Scientific; Frenchs Forest, Australia) coupled to an Agilent Technologies 8900 ICP–MS (Mulgrave, Australia). The laser was operated at 40 Hz with a 10 µm beam diameter and scan speed of 40 µm s^{-1}. Laser fluence was 0.4 J cm^{-2}. A total acquisition time of 0.25 s was used to produce square image pixels. Quantification of the tissue was performed using gelatine calibration standards prepared as per Lockwood et al.[221]

3.2.2 Software design

Pew² was written in python using the 'NumPy' and 'PySide2' libraries and is available on GitHub[i]. NumPy is a powerful array programming library that efficiently accesses and computes multidimensional data.[282] Image processing operations in Pew² take advantage of NumPy's vectorisation to ensure performant code and enable analysis of large datasets, such as those produced by time-of-flight instruments. A modern, cross-platform Qt5 based graphical user interface (GUI) is implemented using PySide2, the official python bindings for Qt. The wide availability of both these libraries mean that Pew² can be compiled on modern operating systems, maximising its availability. A python library

[i] Pew²: https://github.com/djdt/pewpew

'pewlib'[ii] that implements the import and export of data as well as basic data processing, is also available. This library can be used to easily load data for use into python scripts, allowing further processing and batch operations.

3.3 Results and discussion

3.3.1 Visualisation

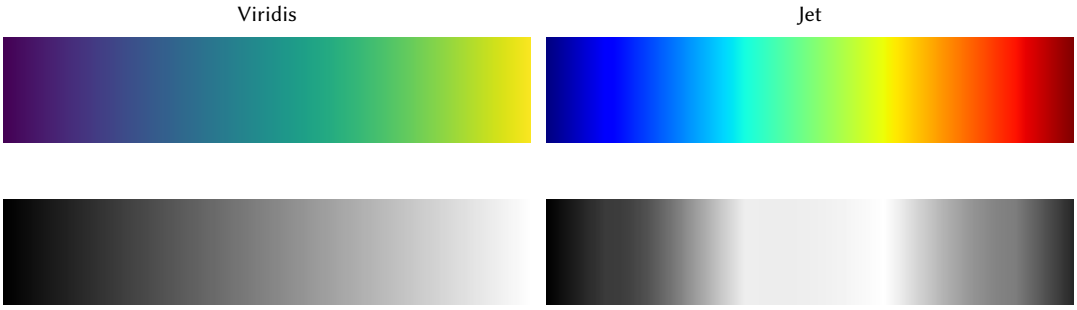

Figure 3.1. Comparison of colour-maps Viridis and Jet and their Lab colour lightness channels (bottom row). The sharp changes in contrast of Jet can introduce perceptual artefacts when interpreting images.

The primary focus of any LA–ICP–MS imaging program is the visualisation of data. Trends and features in images are determined from false-colour representations of MS signals and the interpretation of this colouring should therefore be clear.[277] Commonly used rainbow colour maps have non-uniform colour gradients and low contrast features that occupy a small region of the colour-map increasing the possibility of misinterpretation due to sharp transitions in contrast and improper grouping, apparent in Figure 3.1. Pew² implements a range of colour-maps where the change in perceived colour is uniform across the entire map. These colour maps alleviate any risk of misinterpretation allowing for transparent depictions of MS signals.

3.3.2 Data Import

Pew² is suitable for direct import of a variety of vendor formats of both sample and calibration data according to the workflow shown in Figure 3.2, avoiding the need for data pre-processing for the most common instruments. Drag-and-drop importation of raw Agilent batches (MassHunter G7200B or later), PerkinElmer Elan 'XL', Thermo Fischer Qtegra exports, as well as both text-image and file-per-line

[ii] pewlib: https://github.com/djdt/pewlib

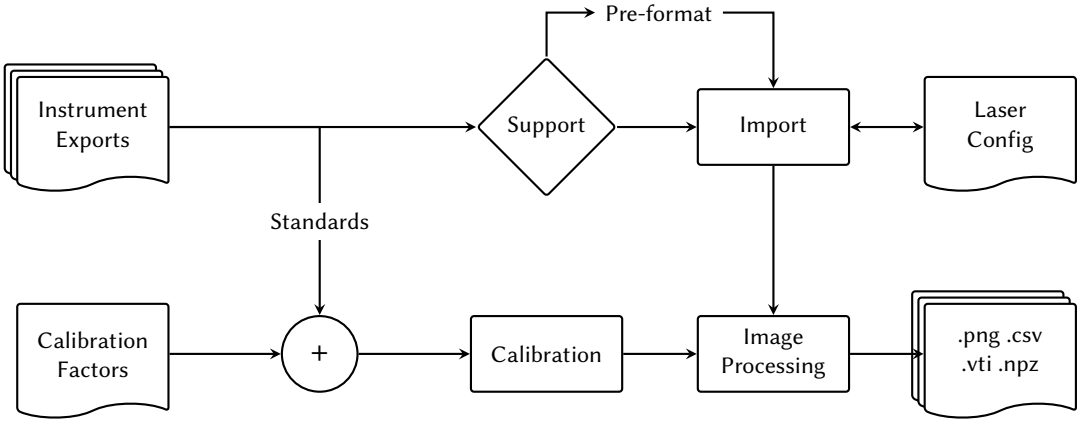

Figure 3.2. Typical workflows for import and analysis of LA–ICP–MS data using Pew².

exports for easy loading of data. Importing files also reads any available instrument parameters such as the MS acquisition time and applies them to the image configuration. Non-natively supported instruments can still be imported, however they require pre-formatting prior to import.

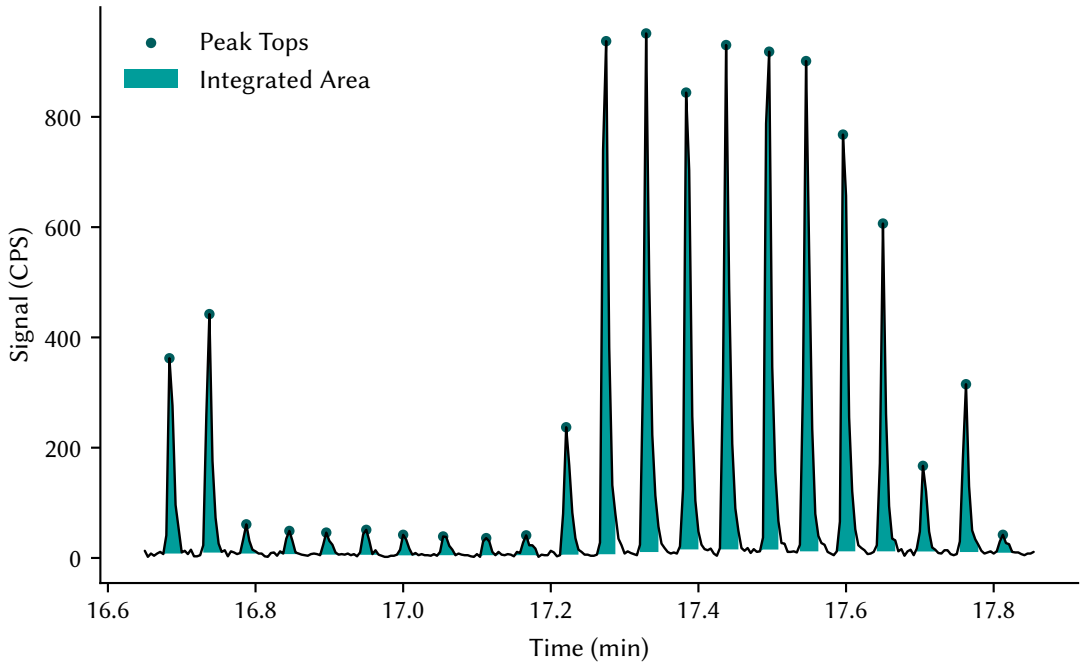

Figure 3.3. Integration of peaks following detection using continuous wavelet transformation. The highlighted area of each peak was used to produce pixels in the LA–ICP–MS image.

While the primary focus of Pew² is line-by-line collected data, importation of spot-wise data is also implemented. A variety of peak detection techniques such as simple or windowed thresholding and continuous wavelet transforms (Figure 3.3) have been incorporated for accurate peak detection even in situations where background signal is not uniform.[283] A single 'marker' element is used to guide

the integration of peaks and an image for each element is constructed using the peak height or area. However, this requires at least one element to be present across the entirety of the sample and for the positions of peaks for each element to be similar.

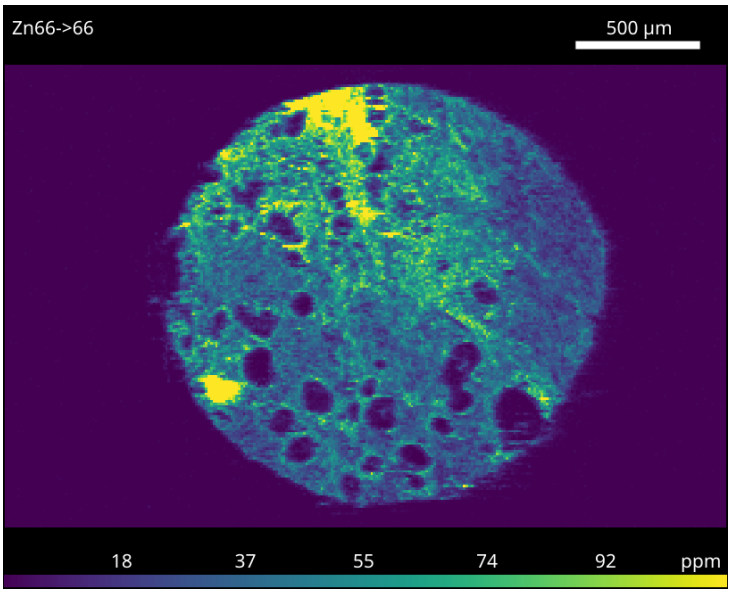

Figure 3.4. Image of ^{66}Zn imported into Pew².

As Agilent MassHunter is directly supported by Pew² the data for both the sample and standard may be imported by drag-and-drop of the batch folders into the main window. Data is read directly from the MassHunter binary files created on collection of each line. The correct acquisition time is automatically applied to the image using average difference of recorded acquisition event times (to the nearest µm). Following import, the laser spot-size and speed are entered manually to ensure the correct image aspect and correct sizing of the scale-bar (Figure 3.4). The calibration standards may be imported in a similar fashion before being loaded into the built-in standardisation tool.

3.3.3 Calibration

Like most MS based techniques, LA–ICP–MS data uses calibration factors for quantification. These factors are collected by ablating materials of known concentrations before, after or during the sampling of a specimen. Calibration factors are then calculated from a linear fit of the known concentrations to MS responses. Pew² allows direct input of externally calculated factors and provides an area-based standardisation tool, where the user can assign rectangular areas of an image to specific calibration values (todo Figure S1). Values are then used to calculate a line of best fit and relevant coefficients for assessing validity (Table 3.2). Weighting of the linear regression may also be used to increase accuracy in

Table 3.2. Calibration values and coefficients.

Element	Intercept	Gradient	r^2	$S_{y,x}$
^{55}Mn	7.06	29.20	0.9931	4.7
^{56}Fe	11.41	18.71	0.9959	24.6
^{63}Cu	4.01	2.04	0.9940	0.6
^{66}Zn	8.48	4.12	0.9915	4.5

$S_{y,x}$: Residual Error calculated as per eq. 3.1.

the lower end of the calibration range as signal deviations are typically non-uniform across a calibrated range.[284] These calibrations can then be saved and applied to other open images or exported for external use.

$$S_{y,x} = \sqrt{\frac{\sum y_i - \hat{y}_i}{n_y - 2}} \tag{3.1}$$

3.3.4 Data processing

Image processing is essential for researchers to better communicate their results. Removal of instrument noise and selection of ROIs often clarify and focus an image's meaning for easier interpretation by readers. Drift correction, filtering and calculator tools built into Pew² enable removal of instrument artefacts and improved image interpretability.

3.3.4.1 Filtering

Spikes in data, and regions of extremely low or high signal resulting from instrument noise may be removed by applying a local (mean or median) filter at the position of each spike. Spikes are identified by comparing pixel values to the mean or median of its surrounding values, if the value is above a user defined threshold, such as 3 times the standard deviation then it is replaced with the local mean (Listing A.1) or median (Listing A.2) value (Figure 3.5). The filtering threshold must be carefully selected to prevent alteration of valid signal. These features correct variation in raw signal, resulting in production of consistent and easily interpretable images.

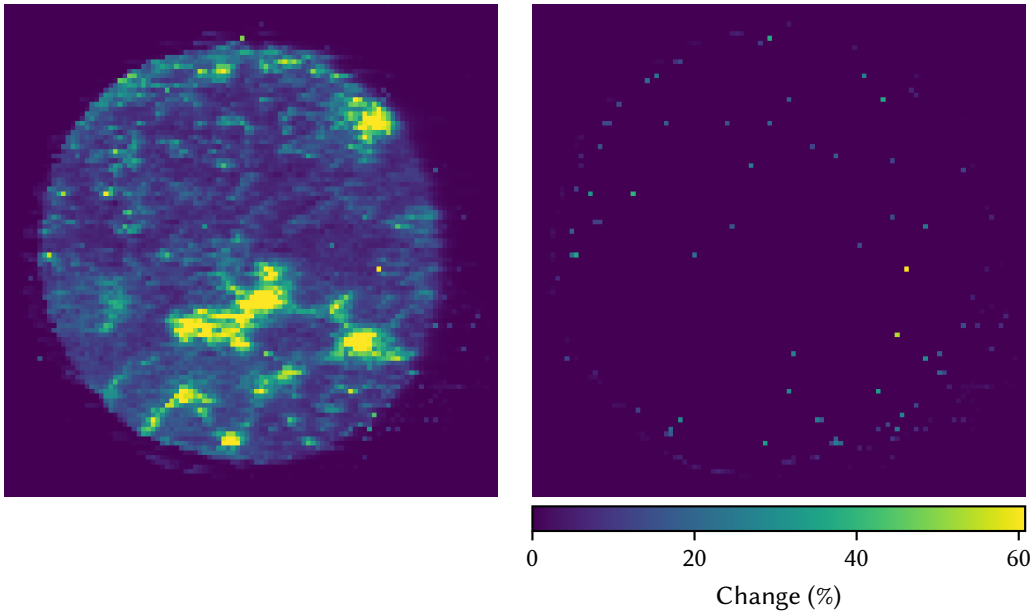

Figure 3.5. A rolling median filter is applied to an image of ^{56}Fe in a pancreatic cancer core to remove noise. The change in signal is limited to pixels with a median value greater than nine times the median of its neighbours.

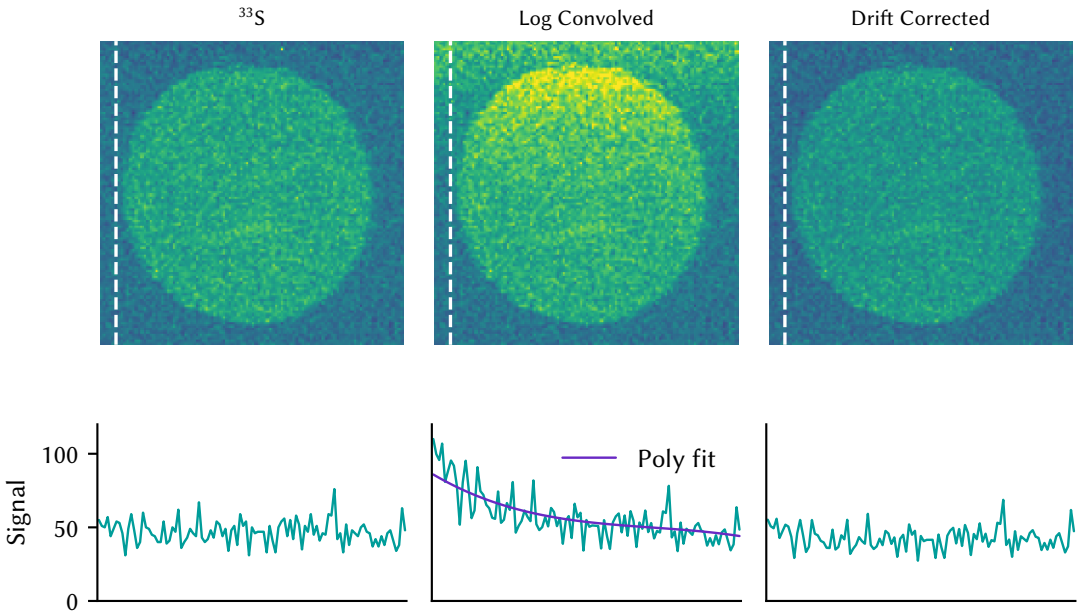

Figure 3.6. Simulated drift removal from an image of ^{33}S (left) with a logarithmic curve (center). The drift tool applied a polynomial fit to approximate the drift and remove it (right). Signal traces along dashed lines are displayed below the relevant images.

3.3.4.2 Drift correction

Changes in laser, plasma or MS conditions may cause signal drift and result in a distorted image. While drift should be minimised by using shorter runs and correctly 'warming up' the instruments, it can be mitigated when quantification is not required. The drift tool calculates a polynomial fit in the direction of acquisition in a user-defined slice of the background, which is then used to re-normalise the image (Figures 3.6 and A.2).

3.3.4.3 Segmentation

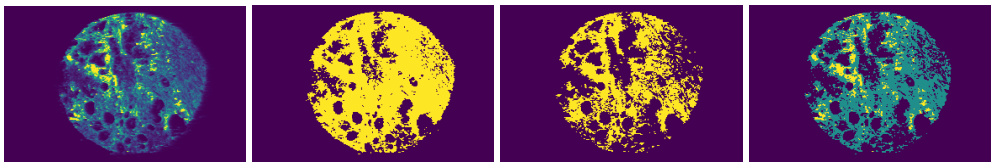

Figure 3.7. Unsupervised segmentation of ^{56}Fe. From left to right: ^{56}Fe, mean thresholding, Otsu's method, three-level k-means. The masks produced by each algorithm can be used for removal of background and image feature selection.

Segmentation is a fundamental imaging analysis tool used to isolate ROIs from the background. This can be performed either manually or automatically using image thresholding, as in Figure 3.7. Automatic, or unsupervised, methods have the advantage of removing biases than a user can introduce when manually selecting ROIs. Pew² has multiple image thresholding methods built in including manual selections, binary filters such as median and Otsu's method, as well as multiple level k-means thresholding (Figure 3.7). Binary filters are typically used to separate signal from the background, while multiple level filters allow specific area quantification in systems where the sample consists of multiple structural features, not all of which should be included in quantified data.[270]

3.3.4.4 Calculator

Construction of images as ratios of two or more elements is a useful analysis technique for normalisation and feature contrast.[206] Normalisation allows samples and ROIs where a non-uniform amount of material is ablated, such as those with different thickness, to be compared. Ratiometric analysis has also been used to perform internal standardisation of LA–ICP–MS data and analysis of isotopic ratios. Pew² greatly simplifies the way these types of images can be constructed; given an image with elements A and B a user only is required to enter A/B into the formula to produce an image of the ratio. The calculator

also implements several useful functions and can parse if-then-else statements, enabling thresholding of both images and calculations. By combining functions and operations a user can perform isotopic analysis, ratiometric quantification, background removal and other Boolean operations.

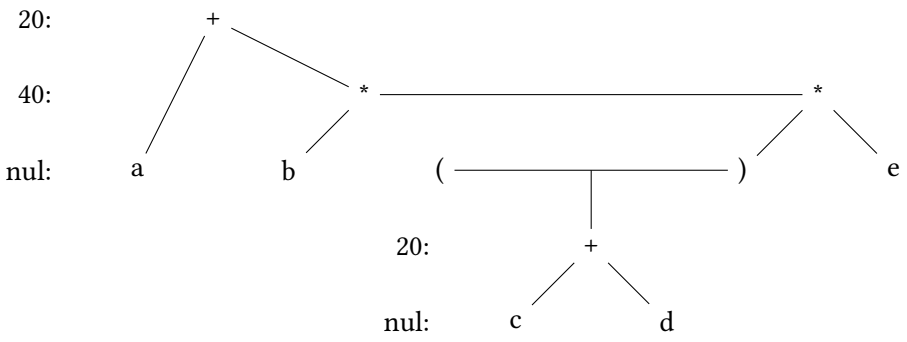

Figure 3.8. Top down precedence parsing of $a + b * (c + d) * e$ to $+\ a\ *\ *\ b\ +\ c\ d\ e$. Values on the left indicate the binding powers of each token.

The calculator uses top down operator precedence to interpret user input as a series of tokens.[285] A table of operator symbols and binding powers is used to make precedence decisions during parsing by recursive descent. The tree in Figure 3.8 demonstrates how a simple input is broken into multiple precedence levels during parsing. Once parsed, the input is easily reduced by recursion (Listing A.3) and the output is displayed by the calculator preview window. The default table includes simple mathematical operators, conditional logic and uni-, bi- and ternary input functions. Both ease of use and implementation results from the translation of inputs familiar to users to more easily reduced tokens.

3.3.4.5 Elemental overlays

It is often desirable to be able to view multiple elemental images at once, for visual assessment of the spatial relationship of elements. The image overlay tool in Pew² allows viewing of up to three elements simultaneously using RGB or CMYK colouring. The spatial overlap of Mn (red) and Zn (blue) and spatial difference of Fe (green) were able to be visualised using this tool Figure 3.9. A numerical representation of this overlap was then calculated in Pew² using Pearson's R correlation coefficients (eq. 3.2) using the pixel values of two images.

$$r = \frac{\sum (x_i - \bar{x})(y_i - \bar{y})}{\sigma_x \sigma_y} \tag{3.2}$$

Both the image and the values in Table 3.3 show a correlative spatial relationship between Mn and Zn. Other colocalisation coefficients may be calculated using the approach developed by Costes et al.[286]

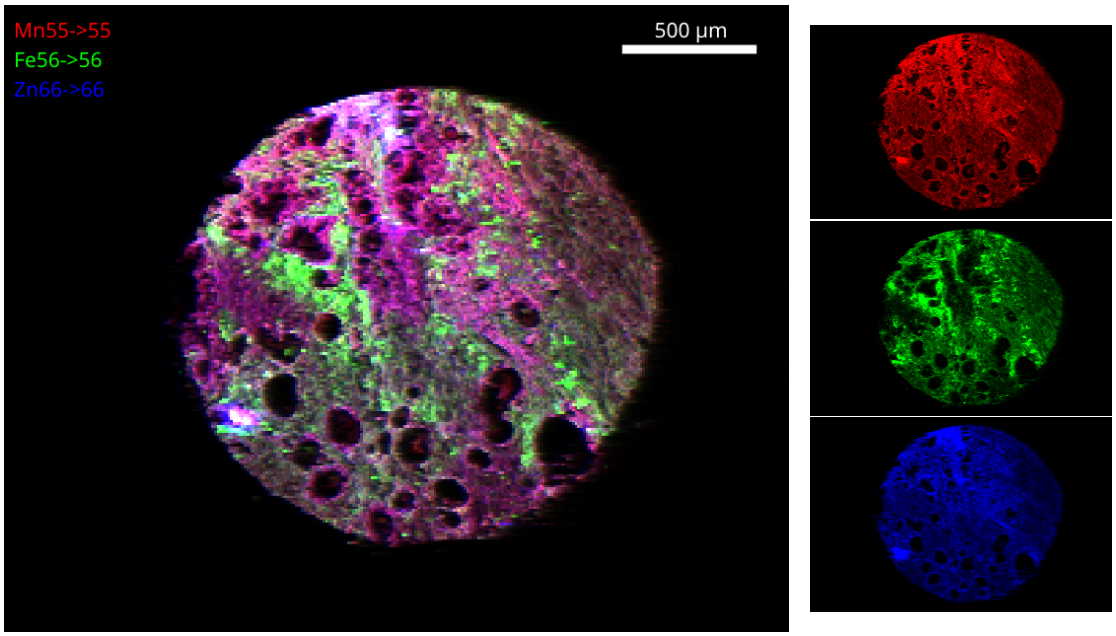

Figure 3.9. RGB overlay of ^{55}Mn, ^{56}Fe and ^{66}Zn. The colocalisation of Mn and Zn is clearly visible as magenta regions within the image.

Table 3.3. Pearson's R correlation coefficients of elements in the TMA core.

	^{55}Mn	^{56}Fe
^{66}Zn	0.80	0.26
^{56}Fe	0.37	–

3.3.5 Data export

While Pew² has some built in image processing capability, a large selection of field specific image analysis software is already available.[273,287] Image exports in '.csv' (text image), '.png' and '.vti' (VTK ImageData) formats maximise compatibility with these programs. However, these formats fail to store the laser configuration and calibration data of images which leads to unnecessary work in future reanalysis. To address this, a custom export using NumPy archives is used to compactly store the image data, configuration and calibrations, so they may be reapplied on load. Despite storing additional parameters these files are far smaller than comparable '.csv' text-images and maintain accessibility by only requiring the NumPy library for access.

3.4 Conclusion

Pew² is the first open-source, multiple-vendor compatible, imaging and analysis software specifically designed for LA–ICP–MS research. It was written with several design philosophies to minimise data bias, maximise analytical rigour and allow verification by third parties. The open nature of the program assists in ensuring its longevity and adoption. Features included in this software follow fast and simple workflows for the production of publication-ready, quantified, and processed images from raw instrument data.

Chapter 4

Imaging of Tumour Microarrays

Previous investigations into manganese have identified a correlation between its concentration and the inferred radioresistance of human tumours. In this chapter we address Aim 3 by revisiting this work using a semi-automated workflow and the improved tools developed and discussed in previous chapters. Transition metals were quantified in tissue arrays of testis, skin and pancreatic tumours, with Mn, Fe and Cu all found to correlate with inferred radioresistance. Variably radioresistant testis tumours are further investigated using elemental imaging and immunohistochemistry, but no further correlations were observed. Finally, phosphorus was evaluated as a potential marker for tissue density and was used for automated removal of stromal tissue areas.

4.1 Introduction

The radiosensitivity of a tumour is generally inferred from its type and location. Tumours such as pancreatic cancer (adenocarcinoma) are typically radioresistant, with radiation therapy providing no improvement in patient outcomes,[103] while others such as seminoma are nearly universally radiosensitive.[38] Despite these inferred resistances there also exists variation within tumour types; both melanoma cell lines and tumours are variably resistant to radiation.[104,105] Similarly, seminoma and NSGCTs are both germ cell tumours of the testis but have differing responses to radiotherapy.[117,118]

TMAs are often used to increase sample throughput, allowing examination of many samples in preclinical research for a more robust statistical base.[288] TMAs consist of cylindrical cores of tissue embedded in a paraffin block. Each core is between 1 and 2 mm and is usually sourced from a different patient. By incorporating many tissues in a small area, TMAs allow the efficient analysis of many samples.[10] This is highly advantageous in the context of LA–ICP–MS, where run times are based on

sample areas but when compared to raw tissue samples, use of TMAs do have some disadvantages. The small area contained within the core may not be representative of a complete sample, particularly in tumours where tissue heterogeneity is high.[289] It has been suggested that at least one 1 mm or three 0.6 mm cores are used to minimise the effect of tissue heterogenity.[290] Despite these effects the large increase in the number of samples able to be analysed can increase confidence in results when using TMAs.

H&E staining is routinely used in histopathology, as the combination of stains reveals the structure of tissue allowing diagnosis of a wide variety of conditions, including cancer.[250] The individual stains in an H&E correspond to different structural features, haematoxylin to cell nuclei and eosin to cell cytoplasm and the extracellular matrix. Diagnosis using H&E stained tissue is usually performed by human pathologists but there has also been much research in automating both the staining process and its interpretation. H&E staining is also used to complement other imaging techniques, using the revealed structural features to guide analysis.[291,292] This requires co-registration of the two images, converting both images to a similar coordinate system.

Registration of MSI and histological images can be performed manually or using an automated approach. Automated image registration is an iterative process to minimise a specific cost function, dependant on the difference in signal intensities of each image.[293] TMAs cores present a particular challenge for automated registration due to their similar shapes and relative lack of features and many different rotations could achieve a minimal cost. Co-registration of MSI data to H&E stained TMAs has been used previously to guide data extraction and analysis.[294] Both Neumann et al., Mascini et al.[292,295] used automated in-house tools, but little detail is provided about their registration methods or results. In all cases the individual TMA cores had to be annotated by a pathologist due to tissue heterogenity. Small errors in the registration of tissue to MSI data can normally be neglected due to the comparatively large pixel sizes used.[296] However, large deformations can be produced by processing, staining and imaging TMAs and can easily exceed several MSI pixels. Therefore TMA cores must be registered individually.

A recent paper compared inferred resistances and metal concentrations of several types tumours using TMAs. Investigations by Doble and Miklos[2] found that the distributions of Mn, and only Mn, correlated with the radiosensitivity of these tumours. However, this study lacked accurate quantification and was therefore unable to statistically compare the mean values of these distributions or compare cancerous and normal tissues.

In this chapter we test the hypothesis that concentrations of Mn, and no other transition metal, correlate with inferred tumour radioresistance. Here, the concentrations of transition metals in pancreas, skin and testis cancers are compared and the relationship between malignant and normal tissues investigated. Optimal methods for registering consecutive H&E and metal image slides are investigated, as well as methods for masking and segmenting tissue. Comparisons of seminoma and the more radioresistant NSGCTs will provide similar data within a single tissue type.

4.2 Materials and methods

Tissue arrays of melanoma (ME481c), pancreatic cancer (PA1001b), seminoma (TE802) and testis disease (TE803), all with core sizes of 1.5 mm, were purchased from US Biomax (Rockville, MD). Four consecutive 10 µm slices of all arrays slices were obtained (one H&E stain and three formalin-fixed paraffin-embedded (FFPE)) to allow both the measurement of endogenous metals and further imaging. All tissue arrays also contained both normal and tumour adjacent-normal tissue to act as controls.

4.2.1 Elemental imaging

Standards containing Mn, Fe, Cu and Zn were prepared as described in Chapter 2 and Lockwood et al.[221] Both P and S were also collected as potential internal standards, but neither was required due to the matrix-matching of the standards and samples. Samples provided as FFPE tissue were depariffinised in xylenes (two times 5 min; ChemSupply; Gillman, Australia) and washed two times in 100 % EMSURE®grade ethanol (Sigma; Castle Hill, Australia) for 5 min. These solvents were chosen for their low metal contents to minimise sample exposure to exogenous elements. Samples and standards were measured using an NWR193 Laser Ablation System operated at 40 Hz (Kenelec Scientific; Frenchs Forest, Australia) coupled to an Agilent Technologies 8900 triple quadrupole ICP–MS (Mulgrave, Australia) with Pt cones and x-lenses. The ICP–MS was operated with both quadrupoles at identical m/z and 3.2 mL min^{-1} H_2 gas. For all LA experiments the laser fluence was set at 0.1 J cm^{-2}, beam diameter to 35 µm, scan speed to 140 µm s^{-1} and ICP–MS scan time to 0.25 s.

4.2.2 Microscopy

Imaging of all H&E slides was performed with a Zeiss Axioscan Z1 (North Ryde, Australia). Fluorescent imaging of fluoresein isothiocyanate (FITC) tagged anti-CD30 in seminoma and NSGCT was performed

using a Zeiss Axioscan Z1. Slides were depariffinised as before and hydrated using an ethanol ladder (5 min in 100, 95, 75 and 0 %). Antigen retrieval was performed in a 10 mmol L^{-1} tris buffer containing 1 mmol L^{-1} ethylenediaminetetraacetic acid for 20 min in a pressure cooker. Slides were then washed for 5 min three times in tris-buffered saline (TBS) and blocked with normal blocking solution for 30 min. Primary staining was performed with Dako brand mouse anti-human CD30 antibody (Aglient Technologies; Mulgrave, Australia) diluted to 6.27 mg L^{-1} in normal blocking solution (0.3, 1 and 3 % triton, bovine serum albumin and normal goat serum in TBS). Slides were stained for 30 min at room temperature then washed three times in excess TBS. Secondary staining of FITC was performed overnight using goat anti-mouse from Bio-Rad (Gladesville, Australia). Once staining was complete slides were again washed three times with TBS and dehydrated using an ethanol ladder. Finally, slides were coverslipped using a 4',6-diamidino-2-phenylindole containing Fluoroshield mounting medium (Abcam; Melbourne, Australia).

Mitotic counts of select seminoma cores was performed on a Leica ICC50 W microscope. A total of five HPFs for each core (approximately 90 % coverage) was used.

4.2.3 Image registration and masking

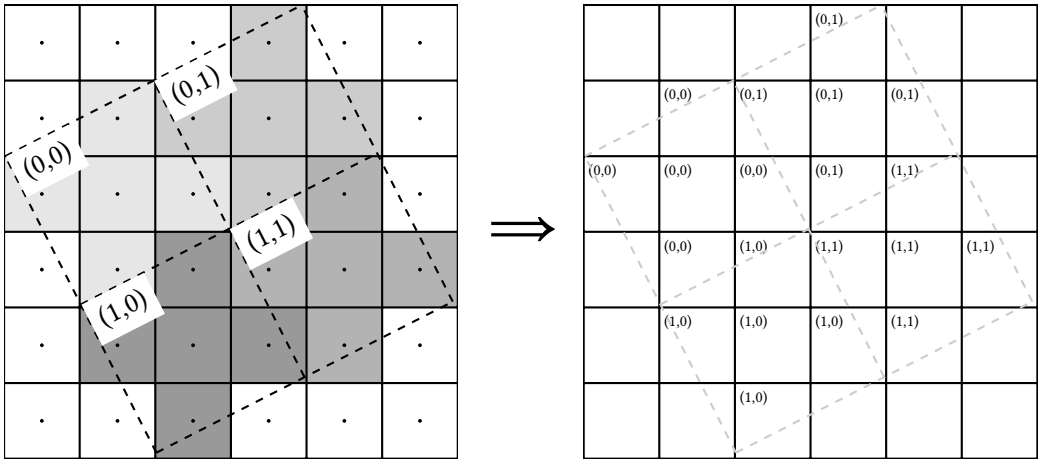

Figure 4.1. Registration of the micrograph and elemental images. A map is created from the centre of pixels in the micrograph to those in the elemental image.

Registration of microscope and LA–ICP–MS images was performed using a custom interactive python script. The script loads and displays both images using and allows manual registration via move-scale-rotate and affine transformations of the LA–ICP–MS image. Both images are loaded at the correct scaling by reading pixel-sizes from the image meta-data. Both file-paths, the microscope 'Scene' parameter and

affine coefficients of transformations are saved to a text file and can be read to immediately recreate the registration. To map pixels of the micrograph to corresponding LA–ICP–MS pixels the centres of each micrograph image pixel were first converted into µm coordinates using the image pixel size. These coordinates were then transformed by the stored affine transformation and converted to LA–ICP–MS pixel coordinates (Figure 4.1). Border regions and blank mosaic tiles were then removed from images to reduce noise and mismatching cores, such as those with folds or debris, were removed. Removal of bubbles had to be performed for the pancreatic cancer slide due to a poorly coverslipped H&E and was performed by thresholding the residual colour deconvolution channel. Once the two images were registered the weight masks were calculated using the process in Figure 4.2.

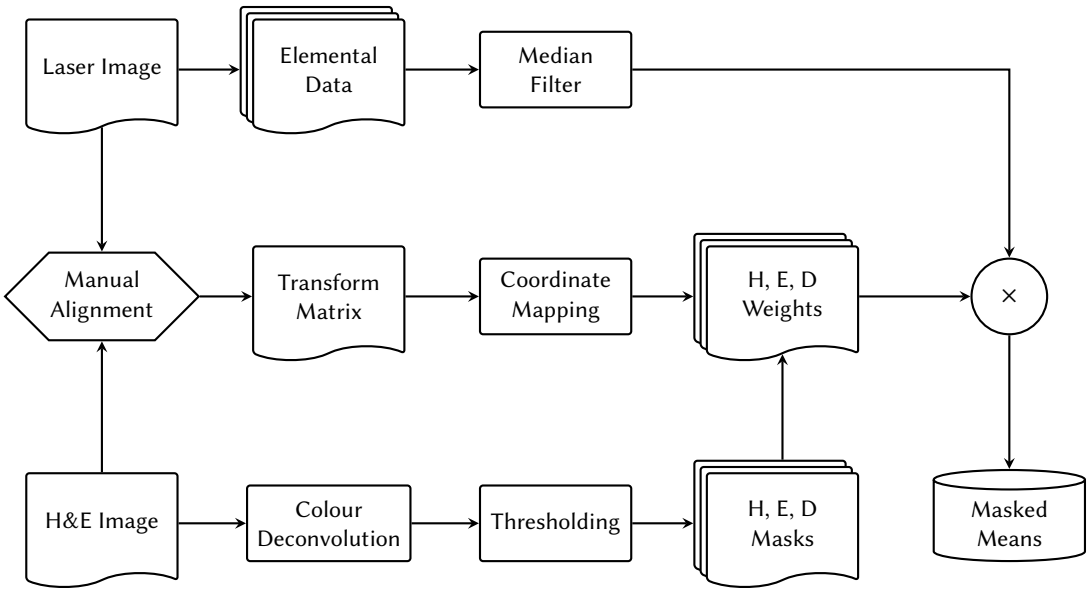

Figure 4.2. The process for calculating masked means.

4.3 Results and discussion

4.3.1 Image registration

When data is collected on two or more different instruments it must undergo transformation to a single coordinate system before any comparisons can be made. The difference in resolution (35 µm and 0.4 µm per pixel) and varying alignment of the LA–ICP–MS and H&E images made registration essential before comparative analysis could be performed. Registration of images had to be performed manually as the low resolution of the metal images greatly reduced the accuracy of traditional feature- and intensity-based algorithms. Additionally, individual cores required hand registration as cores in

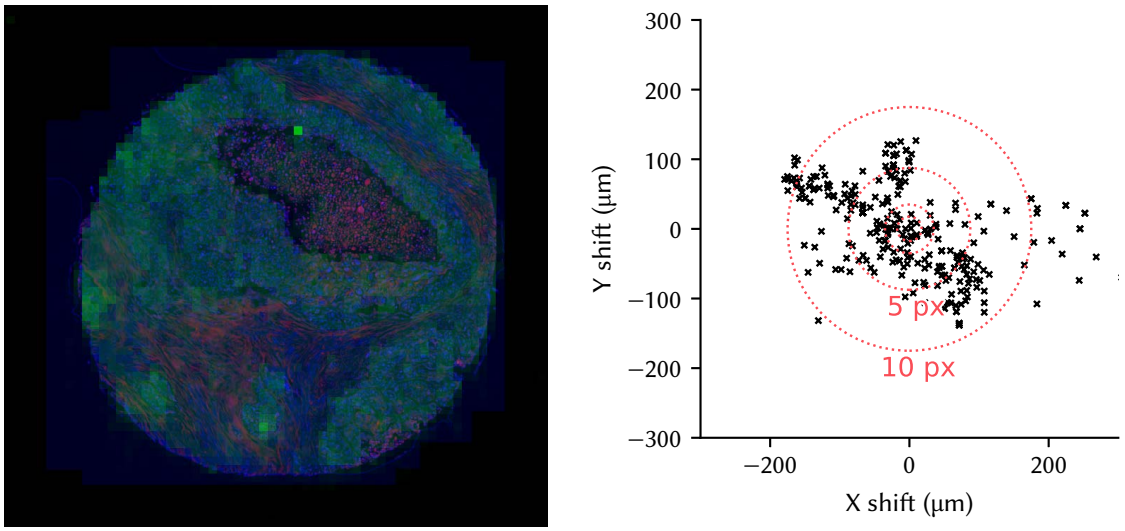

(a) Registration of a micrograph and LA–ICP–MS image of a pancreatic cancer core.

(b) Positional differences between registered cores.

Figure 4.3. Registration of an H&E micrograph and LA–ICP–MS image (a), haematoxylin and eosin channels are shown in blue and red while the metal image (^{55}Mn) is shown in green. Positional differences (from the mean value) that occurred during registration of cores are plotted in (b). Red lines correspond to a shift of 1, 2, 5 and 10 LA–ICP–MS pixels.

consecutive slides did not line up exactly (Figure 4.3a). These differences were due to cores moving during the FFPE process, dapariffinisation, staining and coverslipping and made manual registration for each core essential. The difference in each core position from the mean was calculated for each TMA and plotted in Figure 4.3b. More than half the cores had a positional difference from the mean of greater than five LA–ICP–MS pixels (175 µm), around one tenth of the core diameter. Once the two images were registered comparative analysis between the tissue staining and metals was undertaken.

4.3.2 Colour deconvolution

To maximise the utility of the H&E stain images in differentiating structural features the individual stains first require separation. Stains were separated from red-green-blue (RGB) images of the TMAs using the haematoxylin, eosin, 3,3'-diaminobenzidine (DAB) stain separation matrix described by Ruifrok and Johnston[297] (eq. 4.1). Deconvolution enabled quantification of both the haematoxylin and eosin stains as well any residual colour not accounted for by either stain. The residual colour typically comes from another stain, DAB, but also includes tissue that is pigmented prior to staining, such as the melanin in melanocytes.

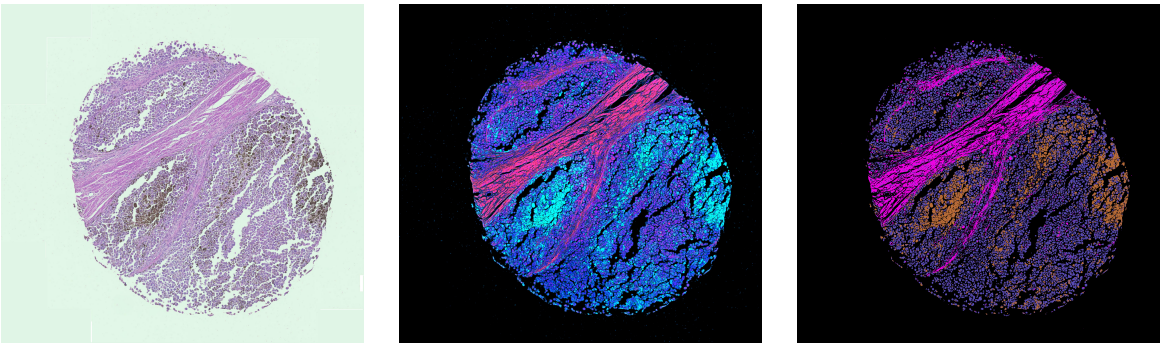

(a) H&E image of a melanoma core.

(b) Colour deconvolution of the core.

(c) Haematoxylin, eosin and 3,3'-diaminobenzidine (DAB) masks.

Figure 4.4. An RGB image of an H&E stained melanoma core. Colour deconvolution (b) and thresholding were used to create the haematoxylin, eosin and DAB stain masks seen in (c). Masks were used to restrict data analysis to specific structural regions of the core.

$$\begin{bmatrix} H \\ E \\ D \end{bmatrix} = \begin{bmatrix} 0.65 & 0.70 & 0.29 \\ 0.07 & 0.99 & 0.11 \\ 0.27 & 0.57 & 0.78 \end{bmatrix}^{-1} \begin{bmatrix} R \\ G \\ B \end{bmatrix} \tag{4.1}$$

Once the stains were separated, they could be used to remove the stroma and background from each image. Initially a masking approach using unsupervised segmentation algorithms including k-means, mean, median and Otsu's method were trialled, but were found to be inferior to the weighting method described below.[298] Each mask was created using a manually calculated threshold, and as each image was taken using the same camera and configuration only a single threshold needed to be used for all the TMAs. Figure 4.4 shows an RGB image of a melanoma core, its deconvolution and the masks created by thresholding the deconvoluted stains. These masks were used to restrict analysis of the data to structural features of the tissue, such as the parenchyma or stroma as well as removing background signal. Optimal segmentation of images was produced using the threshold values in eq. 4.2, where w is the weight pixel corresponding to pixels $i \ldots n$ in H, the deconvolved haematoxylin image.

$$w = \sum_{i=0}^{n} (H > 0.082) \tag{4.2}$$

To assess the correlation between metal concentrations and the inferred radioresistance of tissue types the mean metal concentrations were determined for each core. However, for metals to provide a protective effect they must be located at the site of radiation induced protein damage.[1] Weighted

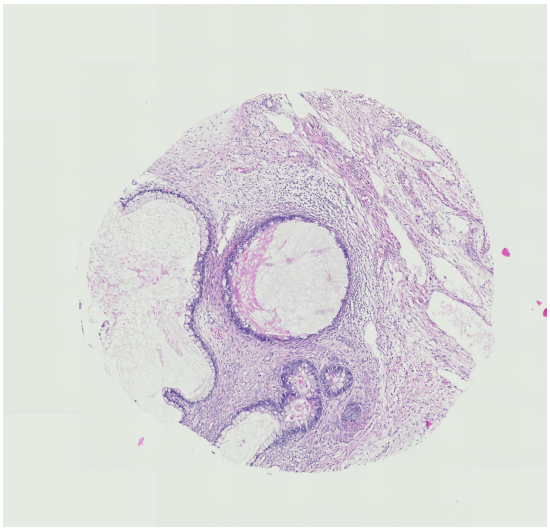

(a) H&E micrograph.

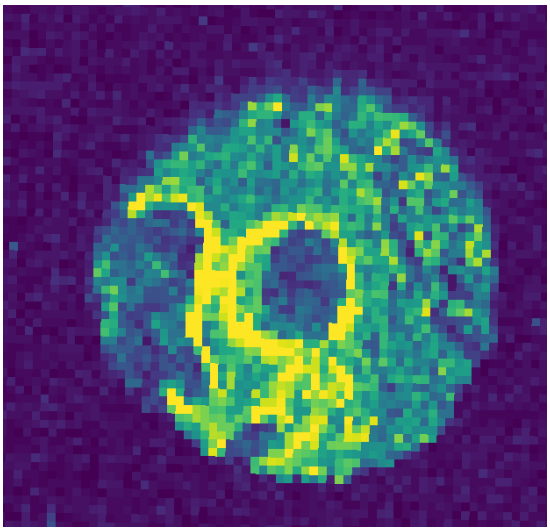

(b) LA–ICP–MS image of Mn.

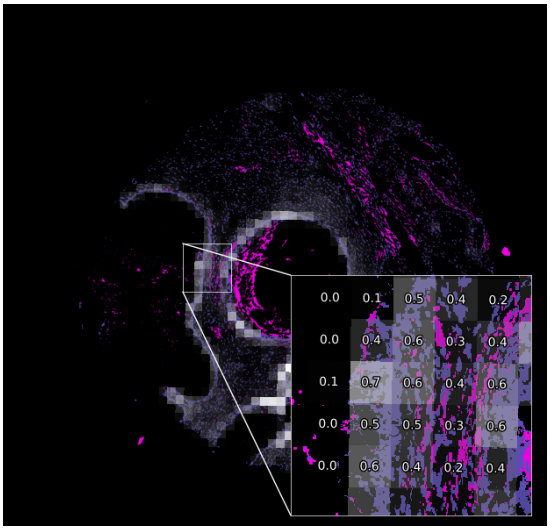

(c) Weights from the H&E.

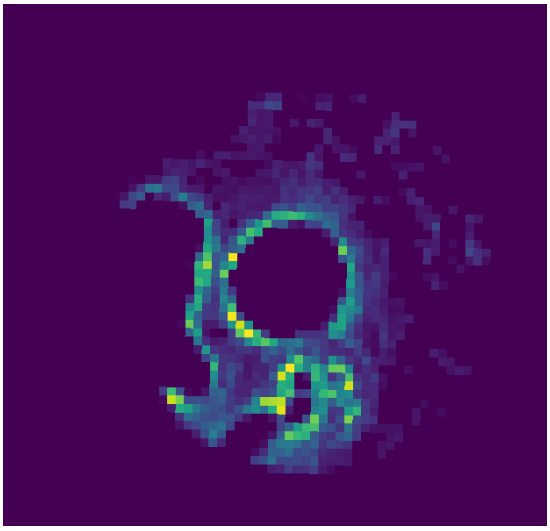

(d) Registered and weighted Mn image.

Figure 4.5. Weights created for a testis teratoma are used to exclude background and stroma from the Mn LA–ICP–MS image. Weight masks are created for cores using colour deconvolution and thresholding of the H&E.

masks were created as per eq. 4.2, Gaussian filtered with a σ of 0.5 and finally cleared of any values corresponding to lower than 5 % coverage of an LA–ICP–MS pixel. A completely masked pixel (1.0) contributed its full weight the core's mean while those with no coverage (0.0) were ignored. Use of the weights preserved the fidelity of the high resolution H&E images when applied to the lower resolution LA–ICP–MS images (Figure 4.5).

4.3.3 Malignant and normal tissues

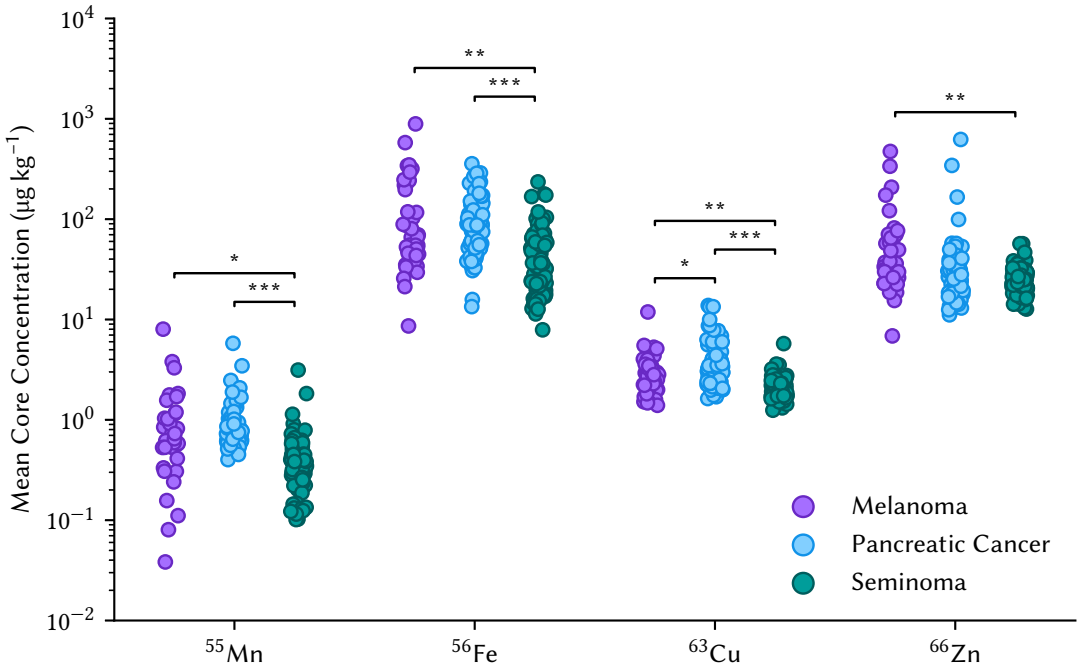

Figure 4.6. Mean metal concentrations of masked regions for each malignant TMA core, separated by tissue type. Statistics were performed using Student's or Welch's t-test, dependant on homoscedasticity (*, $p = 0.05$, **, $p = 0.01$, ***, $p = 0.001$).

Mean parenchyma concentrations of 35, 75 and 90 melanoma, pancreatic cancer and seminoma cores were determined using the weighted masks and are plotted in Figure 4.6. Concentrations of all the metals increased with the inferred radioresistance of tumours and a significant difference between radiosensitive seminoma and both melanoma and pancreatic cancer was seen for Mn, Fe and Cu. However as both Fe and Cu are known radiosensitisers and producers of ROS, Mn is the only likely candidate for metal-complex related radioresistance.[142,143,299] This is in partial agreement with previous research, where only Mn was found to be higher in radioresistant tumours.[2] The calculated values in Table 4.1 match the inferred resistance and variability of resistance of each tumour type; melanoma is variably resistant, pancreatic cancer uniformly resistant and seminoma uniformly sensitive.

Table 4.1. Relevant figures and statistics for Mn in the TMAs. Tests for population and distribution similarity were performed between malignant and normal cores.

Organ	Type	Mean ($\mu g\,g^{-1}$)	Std. ($\mu g\,g^{-1}$)	No. Cores	p Pop.[a]	p Dist.[b]
Skin	Melanoma	1.1	1.4	35	0.76 [c]	0.75 [c]
	Normal	0.9	0.5	8		
Pancreas	Adenocarcinoma	1.0	0.8	75	0.0013	0.000 62
	Normal	1.7	1.1	20		
Testis	Seminoma	0.4	0.4	92	0.034	0.000 62
	NSGCT	0.23	0.17	25	0.56	0.34
	Normal	0.26	0.11	23		

[a] Student's or Welch's t-test, dependant on homoscedasticity.
[b] two-sample Kolmogorov-Smirnov.
[c] significance limited by sample size.

Previous experiments in bacteria have shown the ratio of Fe and Mn to be a better indicator of gamma resistance than Mn concentrations alone.[125] Figure 4.7b shows that no significant relationship was observed between Mn/Fe and the inferred resistances. This was expected given that both metals were increased in radioresistant tumours and indicates that Mn/Fe ratios are not a good indicator of radioresistance in tumours.

Comparison of malignant and normal tissues (Figure 4.8) was performed to determine if the radioresistant tumours had an increased Mn uptake. Counter to the Mn-complex hypothesis, Mn was significantly lower in normal tissues than in radiosensitive seminoma and significantly higher in normal pancreas than in radioresistant pancreatic cancer (Table 4.1). Concentrations of Mn in the normal and tumour adjacent normal tissues also correlated with inferred radioresistance (Figure 4.7a). This means that the measured tumours do not have increased metal scavenging capabilities; any metal-complex related radioresistance must rely on the metals normally present within tissues. Metal concentrations were more variable in the malignant cores (RSDs 30 to 134 %) than in the normal tissue (RSDs 21 to 65 %). Distributions of Mn, Zn in pancreas and all metals in testis were different in malignant and normal tissues (two-sample Kolmogorov-Smirnov, $p < 0.05$). No significant differences were observed for any metal within skin. This variability caused a few seminoma cores to have Mn concentrations far outside the normal tissue range, possibly indicating increased Mn uptake.

All melanoma cores with high Mn were highly melanotic and melanin content (taken as the mean of the DAB channel from the colour-deconvolved H&E) weakly correlated with the concentration of Mn

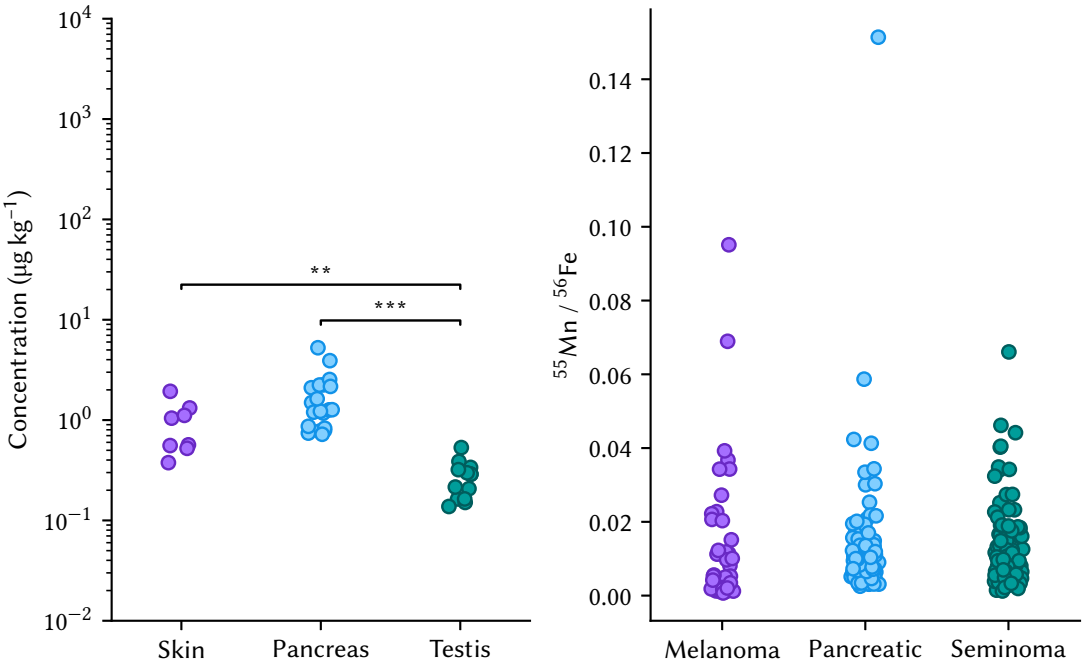

(a) Mean Mn concentrations in normal tissues.

(b) Mn/Fe ratios in malignant tissues.

Figure 4.7. Concentrations in normal tissues (a) correlated with inferred resistance of cancers. There was no relationship between radioresistance and ratios of Mn/Fe (b). Statistics were performed using Student's or Welch's t-test, dependant on homoscedasticity (*, $p = 0.05$, ***, $p = 0.001$).

($r^2 = 0.3910$). Both the correlation and increase in Mn are explained by melanin's ability to chelate metal ions. While melanin has been shown to provide protection against radiation,[36] studies in epithelial and melanoma cell lines showed that melanin alone does not have an effect on radiosensitivity.[108,109] Both of these studies cultured cells in alpha minimum essential medium, a media that is devoid of transition metal containing inorganic salts. A future study that supplements and quantifies both melanin and metal concentrations would be needed to determine if their interaction is required for radioprotection.

Outliers in seminoma have previously been attributed to anaplastic variants.[2] Mitotic counts were performed for the 10 % of the TMA, covering cores with the highest Mn concentrations and those labelled as 'cataplastic' by the vendor. Three cores were found to have a mitotic counts greater than 3 / HPF, the cut-off for anaplastic classification but only one of these had a high Mn concentration. Outlying Mn core concentrations can therefore not be accounted for by anaplastic variants of seminoma. This was not unexpected as both classical and anaplastic seminoma have similar response to therapy, including radiotherapy.[114,115]

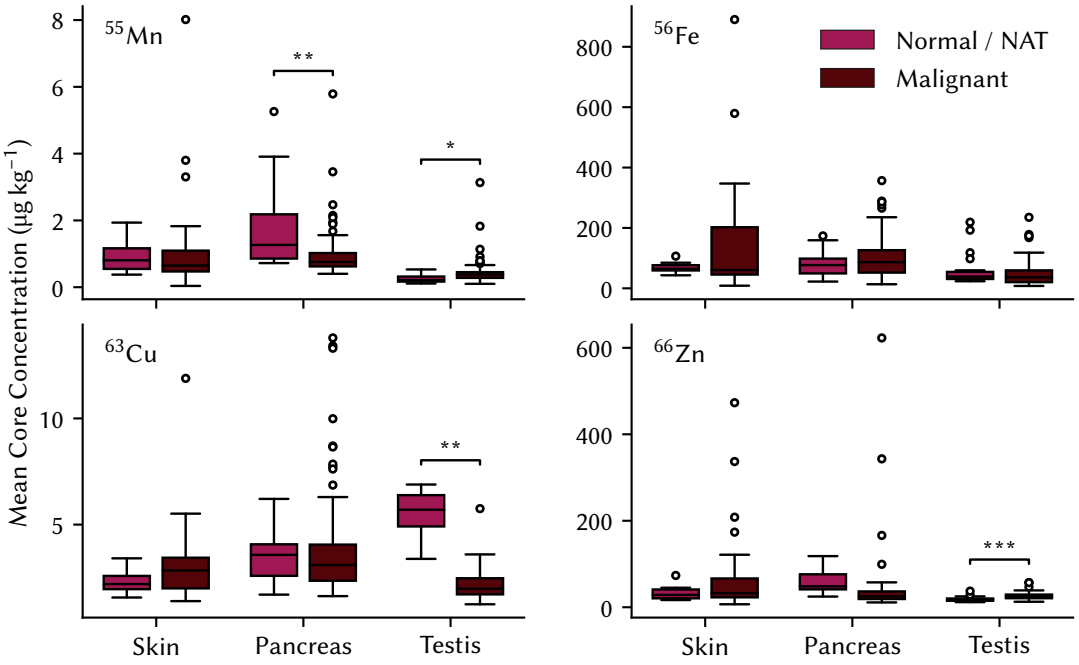

Figure 4.8. Mean concentrations of Mn, Fe, Cu and Zn in malignant and normal tissue cores. Statistics were performed using Student's or Welch's t-test, dependant on homoscedasticity (*, $p = 0.05$, **, $p = 0.01$, ***, $p = 0.001$).

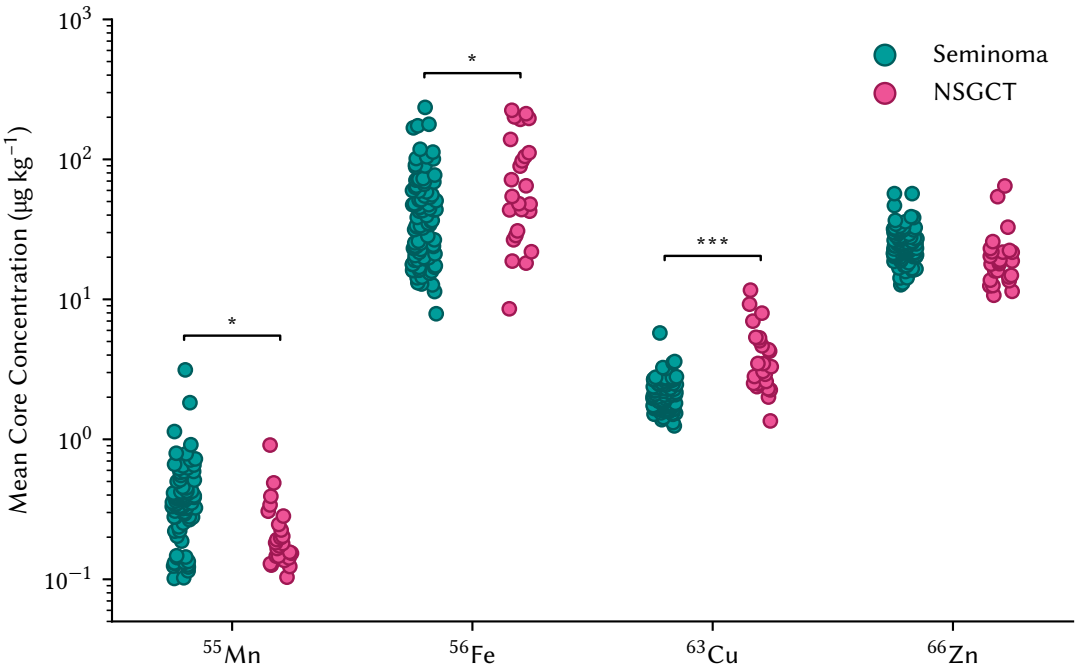

Figure 4.9. Metal concentrations in seminoma and NSGCT. Only Cu correlated with inferred radioresistance. Statistics were performed using Student's or Welch's t-test, dependant on homoscedasticity (*, $p = 0.05$, **, $p = 0.01$, ***, $p = 0.001$).

4.3.4 Testis tumours

Natural concentrations of metals vary in different tissue and thus have the potential to affect the interpretation of analyses. These biases could be removed by analysing two tumours with varying radiosensitivities that are situated in the same tissue. In this study seminoma were compared to NSGCTs, germ-cell testis tumours with a known worse prognosis and lower radiosensitivity.[117,118] While it was hypothesised that the NSGCTs would have high Mn concentrations the opposite was observed (Figure 4.9). Mean Mn was $0.23 \pm 0.17\,\mu g\,kg^{-1}$ in the 25 NSGCT cores compared to $0.4 \pm 0.4\,\mu g\,kg^{-1}$ in the 90 seminoma and the distribution of Mn in NSGCTs matched that of normal testicular tissue.. Cu was the only element that correlated with inferred resistances, however Cu ions are known to cause radiosensitisation in bacteria.[299,300]

Pathologies provided by the TMA supplier were confirmed using immunohistochemistry targeting CD30, a tumour necrosis factor that is expressed in NSGCTs but absent in seminoma.[9] Fluorescent signals of FITC-tagged anti-CD30 correlated with the provided pathologies ($p = 0.00007$) but did not correlate with concentrations of any transition metal (Figure 4.10). Given the decreased Mn concentrations in the confirmed NSGCTs it appears that complexes of Mn are not responsible for the variable radioresistance of testis tumours.

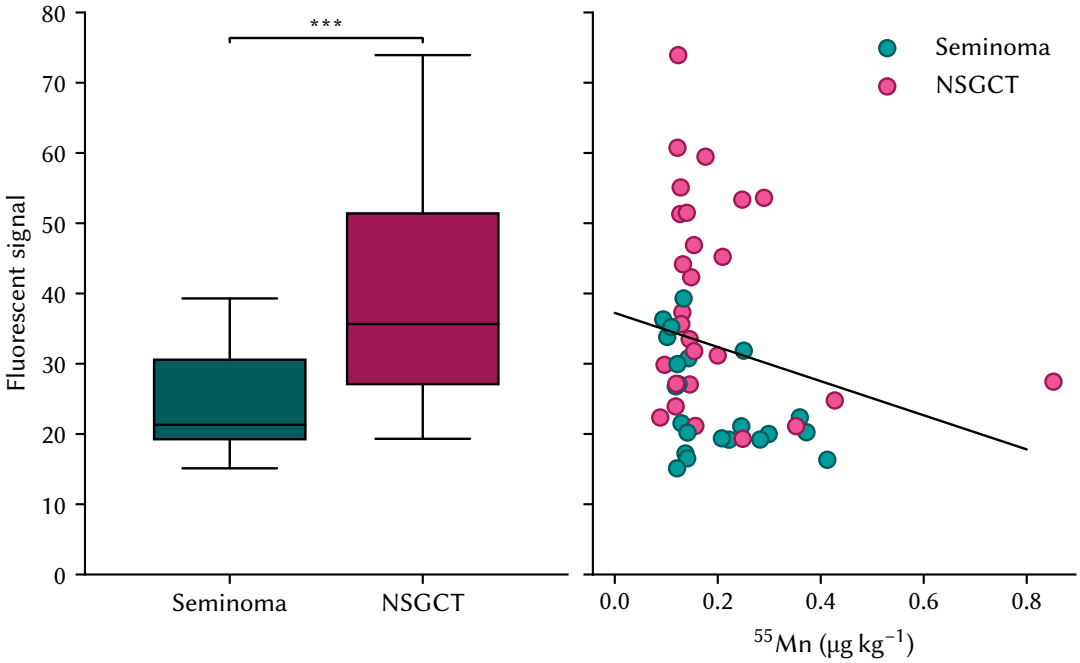

Figure 4.10. Mean fluorescent intensities where higher in NSGCT than seminoma. While intensities did confirm the pathologies, they did not correlate with Mn concentrations (Welch's t-test, $p = 0.001$).

4.3.5 Phosphorus colocalisation and masking

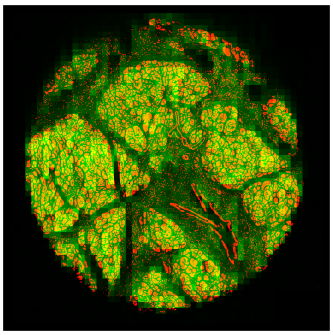

(a) Normal pancreas.

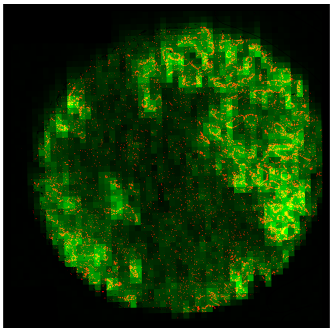

(b) Pancreatic cancer.

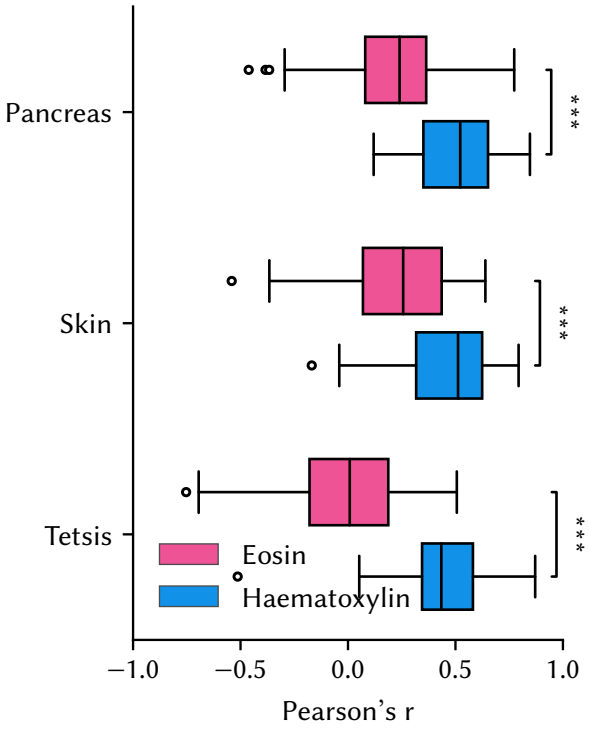

(c) Colocalisation of P with haematoxylin and eosin stains. (Student's / Welch's t-test, $p = 0.001$)

Figure 4.11. Concentrations of P (green) were colocalised with haematoxylin stain (red) in both normal (a) and tumorous (b) cores. This correlation was demonstrated in all tissues using Pearson's correlation coefficients (c). The same correlation was not seen with eosin.

Haematoxylin binds to negatively charged molecules such as nucleic acids and selectively stains cell nuclei. Haematoxylin should therefore colocalise with P due to the abundance of phospholipids in nuclear and cell membranes. Pearson correlation coefficients used to investigate the correlation between metal distributions and the H&E stains (Figure 4.11). As expected there was a strong colocalisation between haematoxylin and P for all tissue types, with mean correlations of 0.45, 0.50 and 0.47 for testis, pancreas and skin respectively. This colocalisation was not observed with eosin, which stains cytoplasm and the extracellular matrix. Colocalisation of P and haematoxylin raises the possibility of using P as a masking element for quantification in heterogeneously structured tissue.

While phosphorus has been used previously to remove signal backgrounds[301] and indicate cell density[302] in LA–ICP–MS images, its potential for use as a tissue masking element remains unexplored. Use of P would significantly simplify the masking process as it could be collected simultaneously with other elements, so no complex image registration process would be required. This process was tested

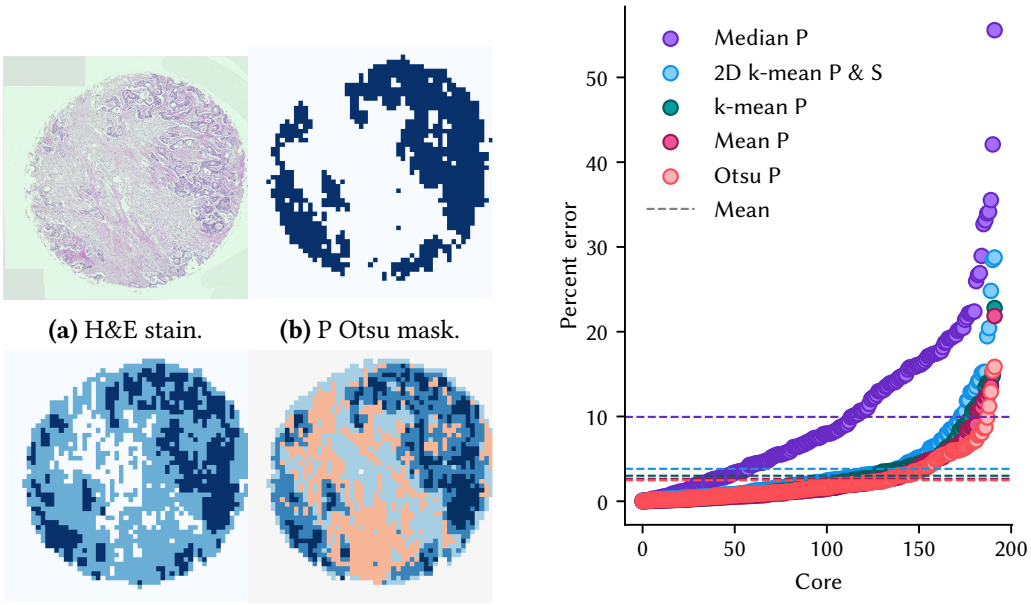

(a) H&E stain. **(b)** P Otsu mask.

(c) P *k*-means labels. **(d)** P & S 2d-*k*-means labels.

(e) Differences of P masking methods from the H&E registration method.

Figure 4.12. Masks produced from the P elemental image using different thresholding methods. The Otsu's mask performed most similarly to H&E registration and colour deconvolution.

on the TMA means using mean, median, Otsu's and multi-level optimal *k*-means clustering.[298] Mean, Otsu thresholding and three level *k*-means clustering (Figure 4.12) were able to successfully separate the parenchyma from stroma and background signal in cores containing at least 25 % parenchyma. Means of Mn from the mean and *k*-means, mean and Otsu masked regions differed by those from the H&E masks by (3 ± 4), (3 ± 3) and (2 ± 2) %, with a maximum difference of 23, 22 and 16 % respectively, shown in Figure 4.12. One issue that may arise when using mean thresholding is the amount of background present in an image. Cropping out background changes the mean value and thus the mask created. It is therefore recommended that the relative and thus more robust Otsu and multi-level *k*-means methods be used. Analysis of core means using the Otsu or *k*-means masks only affected the significance between melanoma and seminoma in ^{66}Zn (0.0071 to 0.074; Figure A.1). These results show that thresholding using P can create robust tissue masks that closely mimic the haematoxylin stained regions of tissue, excluding stroma.

4.4 Conclusion

Image registration and masking was used to calculate transition metal concentrations in TMA core parenchyma. Concentrations of Mn, Fe and Cu correlated with inferred radioresistance however, this correlation was echoed in normal tissues. No metal was found to be higher in radioresistant tumours when compared to normal or tumour-adjacent tissues, ruling out the possibility that radioresistant tumours have an increased metal scavenging capacity. Higher metal variability was seen in malignant cores but without additional information about patient treatment and outcomes it is difficult to draw any conclusions about those with high concentrations. There was no significant difference in the Mn/Fe ratio between the radiosensitive and -resistant tissues. Pathologies of seminoma and NSGCT were confirmed using IHC but the level of staining did not correlate with the concentration of any metal. Only Cu (a known radiosensitiser) correlated with inferred resistance in the variably radioresistant testis tumours, the correlation of Mn was inverse. Locations of haematoxylin stained tissue correlated closely with P elemental maps and P could be used as a masking element for parenchyma, removing the need for complicated image registration.

Chapter 5

Elemental Contents of Brain Tumours Treated Using Radiotherapy

The two most common primary brain tumours, glioblastoma and meningioma, have vastly different responses to treatment and thus patient outcomes. While meningioma are generally considered radiosensitive, glioblastoma are inherently radioresistant and increase in resistance following treatment with radiation. In this chapter the metal contents of brain tumours from patients who have undergone treatment were interrogated and compared to both inferred radioresistance and known patient outcomes.

5.1 Introduction

Glioblastoma and meningioma are the most common forms of primary and intra-cranial tumours. Glioblastoma are highly aggressive and both their location and inherent radioresistance makes treatment extremely difficult. Standard treatment involves tumour resection and both chemo- and radiotherapy however, recurrence of the tumour following radiotherapy is common and the median survival time after diagnosis is only 14.6 months.[101] In contrast, 90 % of meningioma are benign and many are actively monitored in place of treatment. Treatment of meningioma involves surgical removal of the tumour and radiotherapy in cases where the location of the tumour makes complete resection difficult.[91] When combined with surgery, radiotherapy increases the five year PFS of grade I meningioma from 38 to 91 %.[102] 'Atypical' (grade II and III) meningioma have a high recurrence rate and are therefore surgically resected and treated with radiotherapy.[92] However, treatment is complicated by the increased radioresistance of atypical meningioma.

One of the most challenging factors in treating glioblastoma is the increased chemo- and radio-resistance of recurrent tumours. Glioblastoma are highly heterogeneous and small resistant cell populations can become dominant through the selective pressures of therapy.[303] Recurrent glioblastoma are enriched in DNA repair enzyme O^6-methylguanine-DNA methyltransferase[304,305] and prominin-1 (CD133) expressing cells,[46,306] indicating increased CSC characteristics. Radioresistant CD133-positive cells have also been found in atypical meningioma, providing a source of CSCs for tumour regenesis.[307] High expression of DNA repair enzymes[46] and ROS scavengers[49] in CSCs cause an inherent radioresistance that further promotes the creation of radioresistant populations after treatment.

It has recently been hypothesised that the radioresistance observed in glioblastoma could be caused by ROS scavenging Mn based complexes.[2] Mn_2^+ is a catalytic scavenger of $O_2 \cdot -$ and the increased radioresistance of both glioblastoma and atypical meningioma may therefore be due to increased Mn contents within CSCs. This hypothesis could be tested by measuring Mn in tumour biopsies with known medical histories. Tumours from atypical meningioma and post-treatment glioblastoma should contain significantly more Mn than their typical and untreated counterparts. Additionally, distributions of Mn should change following treatment, due to the increased presence of CSCs and populations derived from them.

5.2 Materials and methods

Standards containing Mn, Fe, Cu and Zn were prepared as described in Chapter 2 and Lockwood et al.[221] Both P and S were also collected as potential internal standards, but neither was required due to the matrix-matching of the standards and samples. Samples of 16 (11 grade I; 4 grade II) meningioma and 10 glioblastoma from patients who had undergone treatment were provided by the University Hospital Münster Institute of Neuropathology, along with patient histories. Samples provided frozen were defrosted and used as is while those provided as FFPE tissue were depariffinised in xylenes (ChemSupply; Gillman, Australia) and washed in absolute ethanol (Sigma; Castle Hill, Australia). Tumorous regions of each sample were identified by a pathologist using an H&E stained, consecutive slice. Areas were transferred by overlapping the H&E and P elemental image in GNU image manipulation program and creating masks of tumour, stroma and necrotic regions with the same dimensions as the elemental image.

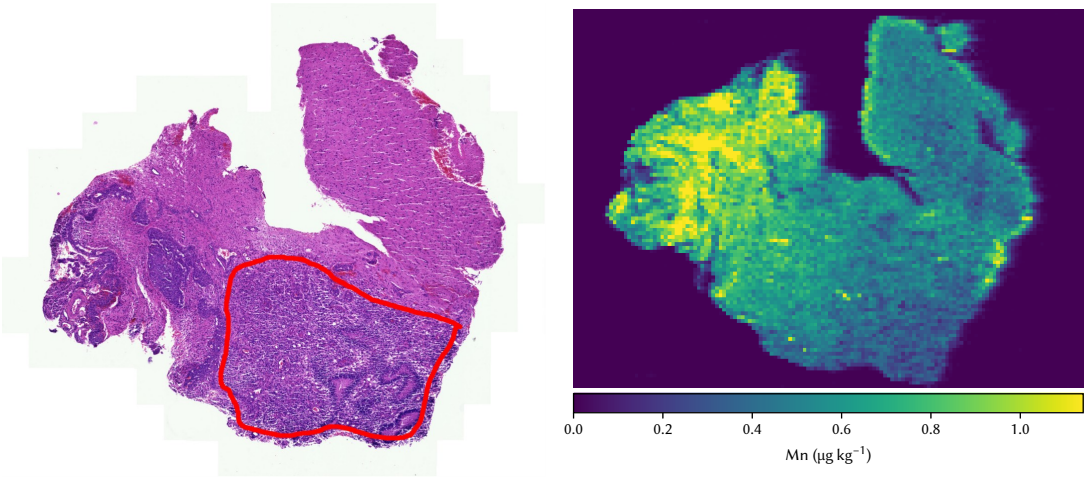

Figure 5.1. A meningioma H&E with the tumorous regions labelled and the corresponding Mn elemental image. Pathologist marked ROIs were used to guide analysis of the metal images.

Samples and standards were measured using an NWR193 Laser Ablation System operated at 40 Hz (Kenelec Scientific; Frenchs Forest, Australia) coupled to an Agilent Technologies 8900 triple quadrupole ICP–MS (Mulgrave, Australia). Hydrogen (3.2 mL min^{-1}) was used as a reaction gas to remove polyatomic interferences. For all normal resolution experiments the laser fluence was set at 0.4 J cm^{-2}, beam diameter to 35 µm, scan speed to 140 µm s^{-1} and ICP–MS scan time to 0.25 s. Calibration was performed using spiked gelatine standards prepared as described in Chapter 2 and Lockwood et al.[221] and run before and after each sample. Linearity of the 52 gelatine standards run during analysis ranged from 0.9944 to 0.9996, 0.9871 to 0.9995, 0.9943 to 0.9994 and 0.9911 to 0.9996 for Mn, Fe, Cu and Zn respectively.

5.3 Results and discussion

Tumorous ROIs within each sample slice were identified by a pathologist using H&E stained consecutive slices. The ROIs (as shown in Figure 5.1) were then used to guide data analysis and exclude normal, stromal and necrotic regions. Background was identified as regions less than the mean plus three standard deviations of the P gas blank (first five seconds of each image) and also excluded.

Following the Mn complex hypothesis it would be expected that radiosensitive meningioma (grade I) would contain lower levels of manganese than the radioresistant glioblastoma. Data in Figure 5.2 shows that only Cu was significantly different between the two sample types. This is similar to previous studies, where Cu was found to accumulate in glioblastoma but not in meningioma. This accumulation was not seen for Zn in either tumour type.[308] Serum levels of Cu are raised in glioblastoma patients

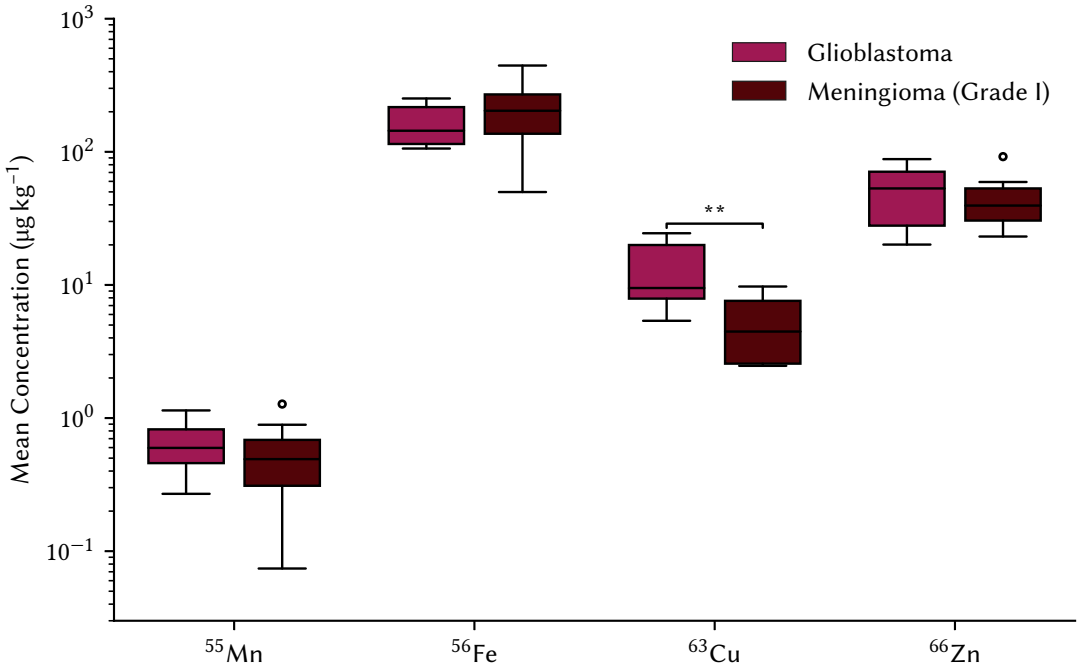

Figure 5.2. Transition metal concentrations in glioblastoma and grade I meningioma. Only Cu was found to have a significant difference in concentration. Statistics were performed using Student's t-test (**, $p = 0.01$).

and reducing levels has been shown to significantly improve PFS and reduce angiogenesis-related factors.[309,310] Angiogenesis (the formation of new blood vessels) is a hallmark of glioblastoma and its inhibition has been highlighted as a potential treatment strategy.[311]

Both Cu and Zn have been shown to be lower in tumours than the surrounding normal tissues even when raised in patient serum levels.[312] In the absence of matched normal and tumour samples the stroma surrounding tumours was used. Each sample containing both regions identified as tumour and stroma were plotted in Figure 5.3 and a paired-samples t-test was performed. In glioblastoma, only Zn concentrations were significantly different, slightly raised in tumorous tissue. This could be due to the increase cell density of tumours, however no other metal was found to be significantly raised. There has been little study of Mn in brain tumours but what does exist has not shown significant differences between normal and tumorous tissues.[313]

Grade II or 'atypical' meningioma are more aggressive and radioresistance than grade I.[92] While Mn was generally higher in grade II (median of 1.07 µg kg^{-1} versus 0.49 µg kg^{-1} for grade I), this difference did not achieve significance (Figure 5.4). Analysis was limited by the relatively small number of grade II samples (four) and a larger sample size may be able to achieve significance. Atypical meningioma represent only 10 % of total meningioma cases, although not all patients will receive radiotherapy.

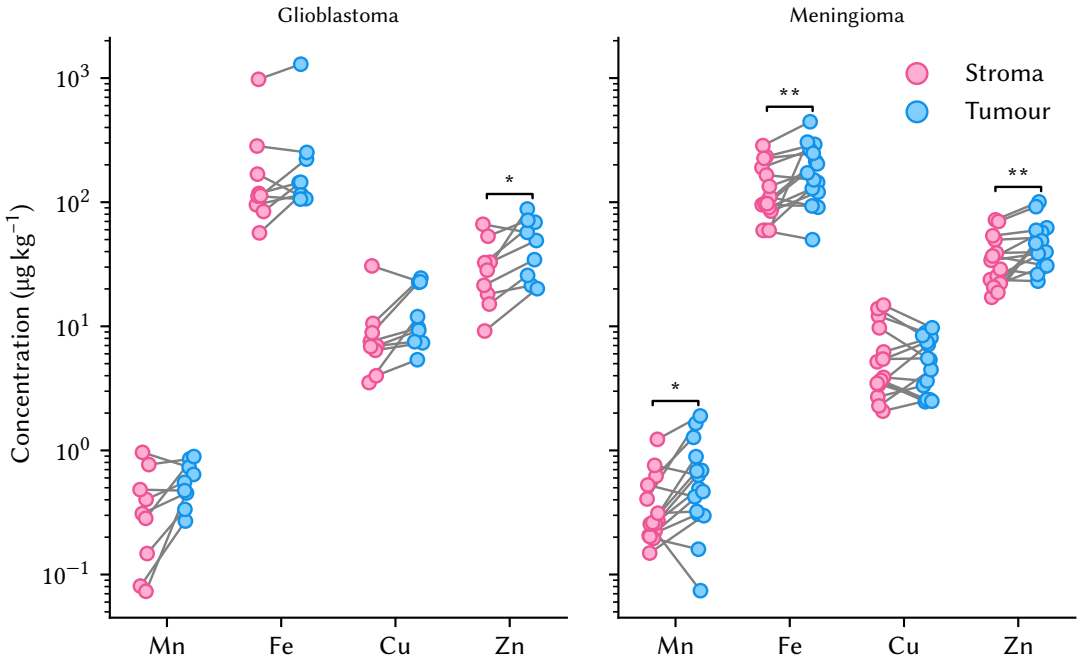

Figure 5.3. Concentrations of metals in sample with regions of both tumour and stroma (pairs shown linked by lines). Metal levels were generally higher in tumour than stroma. Statistics were performed using Student's t-test for paired samples (*, $p = 0.05$; **, $p = 0.01$).

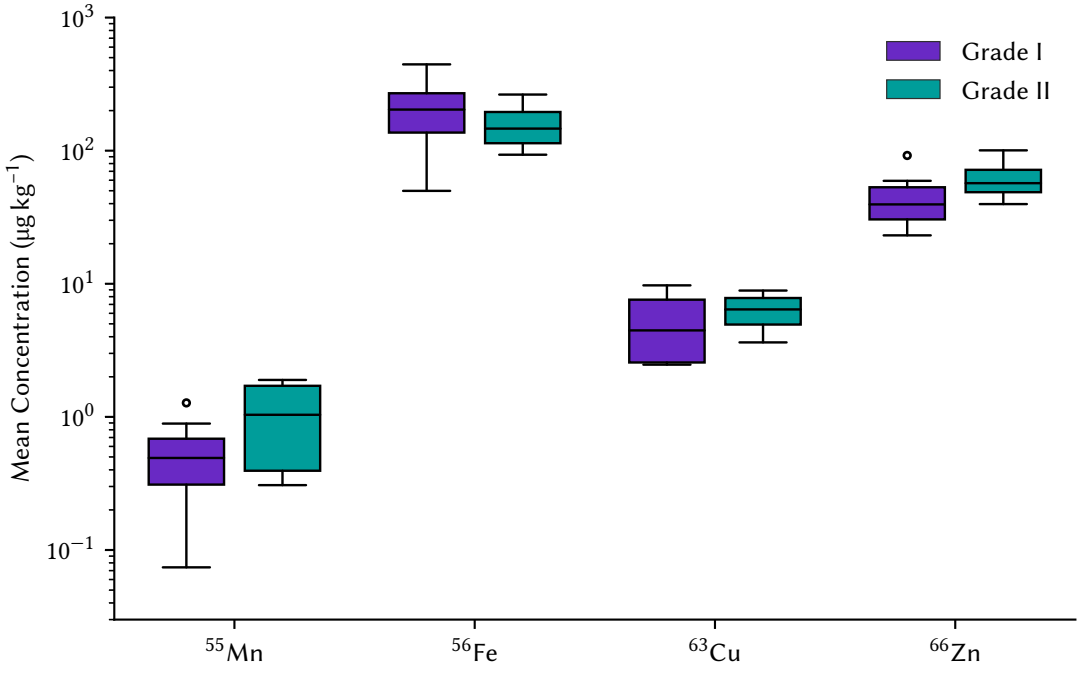

Figure 5.4. Transition metal concentrations in grade I and grade II (atypical) meningioma. No significance difference in concentrations was detected.

There was no significant difference in any of the other metal concentrations between the two grades of meningioma.

Statistical analysis of the elemental concentrations and patient information was performed to determine any correlations between the two. Pearson correlation coefficients were used to interrogate numerical information such as patient age, PFS and overall survival whilst categorical information: sex, Simpson and WHO grading, recurrence, death and whether radiotherapy or adjunctive therapies were administered, was investigated using analysis of variance (ANOVA). Relationship between Zn and patient sex ($p = 0.02$) as well as Cu and WHO grade ($p = 0.0056$) where discovered. Zn concentrations are typically lower in women and this most likely accounts for the difference in tumour Zn.[314] The correlation between grading and copper as was shown previously in Figure 5.2 as glioblastoma are considered WHO grade IV. There were no significant correlations ($p < 0.05$) between Mn, Fe, Cu or Zn and any of the other patient data.

5.4 Conclusion

When comparing glioblastoma to benign (WHO grade I) meningioma, only Cu was found to be significantly elevated. This confirms previous research that observed increased serum Cu in glioblastoma patients and could be a factor in tumour angiogenesis. Several metals were found to be higher in pathologist identified areas of tumour when compared to surrounding tissue. Mn, Fe and Zn were increased in meningioma, while only Zn was significantly higher in glioblastoma. Concentrations of Mn were increased in WHO grade II meningioma, but did not achieve significance and further studies with a larger sample size would be needed to increase statical power. Tumour Zn was found to be increased in males, in agreement with typical serum levels. No other correlations were observed between metal concentrations and any other patient data.

Chapter 6

Single Particle Software and Applications

Most of the work demonstrating the radioprotective nature of manganese has been performed using cell models. The uptake of manganese into cells is usually determined using acid digestion and important information about the distribution of manganese and cell-to-cell variations is lost. This is particularly apparent when analysing heterogeneous cell populations such as cancers. Single-cell inductively coupled plasma mass spectrometry has emerged as a powerful solution to both of these problems, yet quantification of manganese is difficult due to its high background, and there is a lack of truly transparent analysis software. In this chapter a novel open-source, Python-based solution is presented and demonstrated via analysis of Ti nano-materials in water, C in algal cells and C in a solid matrix using laser-ablation. Improved thresholding techniques are implemented with the goal of improving the quantification of elements with high backgrounds, addressing aim Aim 4.

6.1 Introduction

The characterisation of discrete nano- and micro-structures has become increasingly relevant in industry and several disciplines including medicine, life- and environmental science. The properties of NPs can be tuned for specific applications by controlling their size, composition and structure. In the field of medical sciences, NP properties provided new perspectives and inspired strategies for diagnostics and treatments.[315–319] However, the generation, application and discharge of engineered and incidental nanomaterials have also raised environmental and health concerns.[320,321]

The characterisation of nanomaterials requires techniques capable of counting discrete particles whilst characterising their elemental composition, mass and size. Here, spICP–MS has emerged as an elegant technique combining rapid particle counting, high sensitivity and robustness to characterise

nano- and micro-particulate matter in aqueous suspensions.[226] The working principle of spICP–MS is based on the delivery of individual NPs into an Ar-based plasma where they disintegrate into atoms, which are subsequently ionised and extracted into the mass spectrometer as spatially secluded ion clouds. Best signal-to-noise ratios are achieved by reducing signal integration times and collecting several data points for each ion cloud. A minimum integration time of 100 µs is recommended. Determination of the size, mass and number concentrations of detected particles is possible via calibration with reference materials.[322]

The concepts of spICP–MS are also applicable for the determination of elements in cells.[323] scICP–MS is of interest in various medical and environmental scenarios where the up- and down-regulation of elements trigger certain biological traits or pathologies. Another interesting direction in the field of particle characterisation is the hyphenation of spICP–MS with secondary instrumentation. The coupling with laser-ablation enables spatial investigations of particles among ionic species in solids and is used to study their fate and impact.[259,324] Furthermore, it was recently shown that LA–spICP–MS can sample intact NPs from biological tissues to investigate translocation, sizes and spatial abundances.[325–327] NPs are also incorporated into LA–ICP–MS workflows to improve detection capabilities, as shown in the field of immunohistochemistry.[259,328] However, hyphenated spICP–MS may produce transient data sets with drifting background signals and require dynamic models for signal thresholding.[329]

The acquisition of NPs and cells via sp or scICP–MS generates large data sets that often exceed 10e6 data points, making manual analysis inefficient and requiring dedicated processing algorithms to reduce data into a manageable form. These algorithms must be able to detect NP events in the presence of background noise, integrate and calibrate detections, and perform statistical analysis.[235,330,331] Commercial sp software packages for data analysis and visualisation are available from various ICP–MS vendors, as reviewed by Meermann and Nischwitz.[332] Vendor packages are usually integrated into the processing software and enable on-site and real-time analysis. However, the underlying processing algorithms are often only partially transparent and access to meta data is limited. These factors complicate the comparison of data sets from different vendors and limit user modifications, which are often required for the characterisation of uncommon materials, cells and other research endeavours.

Python is an open-source general-purpose programming language with wide adoption in the fields of data science, imaging, analytics and automation.[333] Popular libraries such as NumPy extend Python and facilitate the efficient creation, access and manipulation of data.[282] As such, Python has become popular amongst natural scientists, who often require fit for purpose software solutions for large data sets

with unconventional structures. Its widespread application and popularity in the scientific community makes Python a good choice for spICP–MS data analysis as code accessibility and extensibility are often required to implement new or adapt existing sp routines.

In this work, we present an open-source Python-based platform for efficient and interactive analysis of sp and scICP–MS data sets. The integration of processing, filtering and calibration algorithms into an interactive GUI are detailed. Different calibration and filtering methods are demonstrated by the exemplary analysis of particles in surface water and soil as well as by targeting single cells.

6.2 Materials and methods

6.2.1 Instrumentation

spICP–MS experiments were performed on an 8900 series ICP-MS/MS system operated with MassHunter software (Agilent Technologies) and equipped with Pt cones and s-lenses. A concentric nebuliser and Scott double pass spray chamber cooled to 2 °C was used for aerosol generation. Liquid solutions were introduced via a peristaltic pump. The PA factor and detector dead-time of the instrument were determined by analysing diluted element standards for ICP–MS. The instrumental performance was tuned daily by analysing a 1 µg L^{-1} Li, Y, Tl, Ce and Ba standard. For spICP–MS analysis, the quadrupole mass analyser was operated with a dwell time of 0.1 ms. LA experiments were performed using a New Wave Research NWR-193 excimer laser (Kennelec Scientific; Mitcham, Australia).

6.2.2 Chemicals and consumables

Spherical Au NP standards (NanoXact, 99.99 % purity) with diameters of 15 and 50 nm and dispersed in 2 mmol L^{-1} sodium citrate solution were purchased from nanoComposix (San Diego, CA) and stored at 4 °C. Before analysis, solutions were warmed to room temperature and sonicated for two minutes to re-suspend precipitated NPs. Standards were diluted in milli-Q water obtained from an Arium® Pro Vf system (Sartorius; Goettingen, Germany) to sp working concentrations in tubes made of polypropylene. Certified ionic Au and Ti were purchased at 10 mg L^{-1} in 2 % HNO_3 from High Purity Standards (Thornleigh, Australia) and diluted to 1 µg L^{-1} to determine elemental responses. To investigate thresholding and applicability of the different filters, an ionic 1 mg L^{-1} Au standard was analysed while altering the 'Plate bias' tuning parameter to generate different signal background levels.

6.2.3 Application 1: spICP–MS analysis

For the demonstration of the data processing platform for mass, size and concentration calibrations, a freshwater sample was obtained from the Merlynston Creek in Melbourne, Australia (coordinates: −37.691027, 144.936998) in December 2019 and analysed using spICP–MS/MS to detect and characterise TiO_2 NPs. Syringe filters (0.45 µm; Tisch Scientific; North Bend, OH) were used to remove larger particulate matter. Triple quadrupole ICP–MS using O_2 as reaction gas was required to remove spectral interferences and allowed the selective analysis of Ti by mass shifting $^{48}Ti \rightarrow {}^{48}Ti^{16}O$.

6.2.4 Application 2: LA–spICP–MS analysis

An acid washed sand sample was mixed with charcoal to simulate the presence of C containing matter in soil. The mix was spiked with 3.0 ± 0.1 µm polystyrene beads (10 % solids, 1.05 g cm^{-3}; Sigma Aldrich; Castle Hill, Australia), mixed again and pressed into pellets, which were then analysed via LA–spICP–MS using a spot size of 100 µm and a scan speed of 400 µm s^{-1}. The isotope ^{12}C was monitored in single particle mode according to a previously published method.[323] A blank soil sample was prepared without plastics and analysed but no sp signal spikes were visible. Calibration was performed by analysing dried droplets of a 3 µm polystyrene standard on microscope glass slides.

6.2.5 Application 3: scICP–MS analysis

A cell culture of Symbiodiniaceae unicellular algae was analysed and calibrated via sp and scICP–MS according to a protocol by González de Vega et al.[323] The isotope ^{12}C was targeted and analysed via a mass shift ($^{12}C \rightarrow {}^{12}C^{16}O$) using O_2 as reaction gas. The sc signal spikes were calibrated using 4.0 ± 0.1 µm polystyrene beads (10 % solids, 1.05 g cm^{-3}; Sigma Aldrich) as reference particles.

6.2.6 Data processing

The following section describes mathematical operations implemented in the program for signal filtering, processing and calibration. The developed software converts inputs into SI units and outputs to user defined units. Raw data may be loaded from CSV or text files consisting of either a single column of signal values or two columns of acquisition times and values. For the latter, dwell times are determined automatically. The mean of the raw data (μ_b) is the basis for threshold calculation and data filtering and is calculated across all data points, or a specified window. A Poisson filter was integrated into the

software and sets thresholds based on considerations by Currie[334] who described counting statistics for radioactive decay. The concept was later adopted for spICP–MS.[235,330,331] The Poisson filtering algorithm takes two inputs, the limit of criticality (L_c) and LOD (L_d), which are calculated from the input signal using Currie's expressions for paired observations shown as eqs. 6.1 and 6.2.[335] Contiguous regions above the L_c containing at least one point above the L_d are background subtracted and integrated to produce a single particle signal, as shown in Listing 6.1. At count rates of less than five counts the correction term ϵ is used to avoid underestimation of the limits. The value of ϵ is pre-set to 0.5 but may be modified manually.[334]

Listing 6.1. Sums contiguous regions above `limit_accumulation` with at least one point above `limit_detection`. Error handling code removed for readability.

```
def accumulate_detections(
    y: np.ndarray, limit_accumulation: float, limit_detection: float,
) -> Tuple[np.ndarray, np.ndarray, np.ndarray]:

                                        get start and end positions of regions above accumulation limit
                                                    diff labels starts of regions with 1, ends with -1
    diff = np.diff((y > limit_accumulation).astype(np.int8), prepend=0)
    starts = np.flatnonzero(diff == 1)
    ends = np.flatnonzero(diff == -1)
    regions = np.stack((starts, ends), axis=1)                  stack into pairs of (start, end)

                                                remove regions without a max value above detection limit
    detections = np.logical_or.reduceat(y > limit_detection, regions.ravel())[::2]
    regions = regions[detections]

    sums = np.add.reduceat(y, regions.ravel())[::2]                                  sum regions

    labels = np.zeros(y.size, dtype=np.int16)                  create a label array of detections

    ix = np.arange(1, regions.shape[0] + 1)                                set start to +i, ends to -i
    labels[regions[:, 0]] = ix
    labels[regions[:, 1]] = -ix
    labels = np.cumsum(labels)                                                  cumsum to label regions

    return sums, labels, regions
```

$$L_c = 2.33\sqrt{\mu_b + \epsilon} \tag{6.1}$$

$$L_d = 2.71 + 4.65\sqrt{\mu_b + \epsilon} \tag{6.2}$$

Gaussian data filters determine the L_d according to eq. 6.3, where x is a coefficient that may be selected to adjust thresholds. In this case the same recognition and accumulation algorithms are used with L_c set to L_d. Gaussian filters use the standard deviation (σ) and either the mean or median of the signal to define the L_d.

$$L_d = \mu_b + x\sigma \tag{6.3}$$

The L_d is subsequently used to define the mass and size detection limits L_m and L_s. The L_m of a particle may be determined via the transport efficiency (η), ionic response (s), dwell time (t), flow rate (V) and mass fraction (f) according to eq. 6.4. The L_s is derived from the L_m according to eq. 6.5, assuming a spherical particle with density ρ.

$$L_m = \frac{\eta t L_d V}{s f} \tag{6.4}$$

$$L_s = \sqrt[3]{\frac{6L_d}{\pi\rho}} \tag{6.5}$$

An alternative approach to determine the L_m considers the mass response (R), where the mean signal of a target element ($\overline{I_D}$) in a standard particle with either known mass m or known density ρ and diameter $\oslash$ is determined according to eqs. 6.6 and 6.7.

$$R = \frac{mf}{\overline{I_D}} = \frac{4\pi\rho f}{3\overline{I_D}}\left(\frac{\oslash}{2}\right)^3 \tag{6.6}$$

$$L_m = \frac{\eta t L_d V}{s f} \tag{6.7}$$

The ionic background concentration (c_i) is determined from the mean of all non-detection regions in the input ($\overline{I_{ND}}$) according to eq. 6.8

$$c_i = \frac{\overline{I_{ND}}}{s} \tag{6.8}$$

For the calibration of the NP signal data array, η may be determined and entered manually[336] or calculated automatically using a reference material. The number of detected reference particles (N) over a certain acquisition time (T) can be used to determine η according to eqs. 6.9 and 6.10, if the particulate mass concentration (c_p), density and diameter are known. Alternatively, η may be calculated using the signal (I_d) and mass of the standard particle via eqs. 6.9 and 6.11 if the ionic response, density, diameter and mass fraction of the standard particle are available.

$$m = \frac{4\pi\rho f}{3}\left(\frac{\varnothing}{2}\right)^3 \tag{6.9}$$

$$\eta = \frac{mN}{c_p VT} \tag{6.10}$$

$$\eta = \frac{msf}{tI_d V} \tag{6.11}$$

The particle number concentration (PNC), (c_N) is determined using eq. 6.12 when η is calculated. The detection of single particles is governed by Poisson statistics and the standard deviation is therefore estimated using the square root of the particle count.[330]

$$c_N = \frac{N}{\eta t V} \tag{6.12}$$

The calibration of detection intensities into masses is possible via transport efficiency according to eq. 6.13. Alternatively, the particle mass can be calculated according to eq. 6.14 by considering the mass response factor determined from a standard particle.

$$m = \frac{\eta t I_d V}{sf} \tag{6.13}$$

$$m = \frac{RI_d}{f} \tag{6.14}$$

The particle masses can further be calibrated into particle sizes or into the total particulate concentration using eqs. 6.15 and 6.16.

$$\oslash = \sqrt[3]{\frac{6m}{\pi rho}} \tag{6.15}$$

$$c_p = \frac{\sum m}{\eta V T} \tag{6.16}$$

Signal, mass and size distributions are visualised together with figures of merit in histograms and may be automatically fitted with a normal or log-normal function. The fitting is performed by minimising the fit difference using a Nelder–Mead simplex method.[337]

Any processing step for the analysis of particles is also applicable for the characterisation of cells, where masses, sizes and cell counts can be performed accordingly.[323] The intracellular concentration (c_c) can be determined using the molecular weight of the analyte (M) according to eq. 6.17 but requires knowledge of the mean cell size.

$$c_c = \frac{9m}{2000\pi \oslash^3 M} \tag{6.17}$$

6.3 Results and discussion

6.3.1 Signal thresholding and NP recognition

In this work, we present an open-source Python-based data processing platform that aims to provide transparent analysis of sp/scICP–MS and hyphenated spICP–MS data sets. An interactive GUI was implemented in Qt5 using the PySide2 library, and NumPy was used for the rapid generation and manipulation of large data arrays. The library 'bottleneck' was used to further accelerate windowed calculations. An executable version of the program is provided for Windows 10 users and requires no previous Python installation or expertise. The GUI simplifies operation of the program by compartmentalising inputs and outputs into four tabs: options, sample inputs, reference inputs, and results.

Gaussian distribution models are fundamental in the analysis and modelling of data in analytical chemistry and are commonly used for estimating limits of analysis. The LOD is often defined by the 3σ criteria, where an analyte signal is distinguished from random noise if it is greater than three standard deviations of the baseline. The 3σ criteria describes a 99.73 % confidence interval and leads to 0.27 % falsely detected signals, which is problematic in spICP–MS analyses. For example, applying a 3σ criterion to a normally distributed baseline signal of one million data points (equivalent to a 100 s analysis with a

0.1 ms dwell time) returns approximately 2700 data points which fall outside the 3σ criterion and are therefore falsely associated with NPs. Furthermore, while Gaussian models may sufficiently predict the signal distribution at high counting rates, the small dwell times and low ionic background levels often occurring in spICP–MS can be better modelled with a Poisson distribution. Therefore, adapted concepts including Gaussian filters with higher thresholds (e.g. 5σ) or Poisson filters can be found in the literature.[235,236]

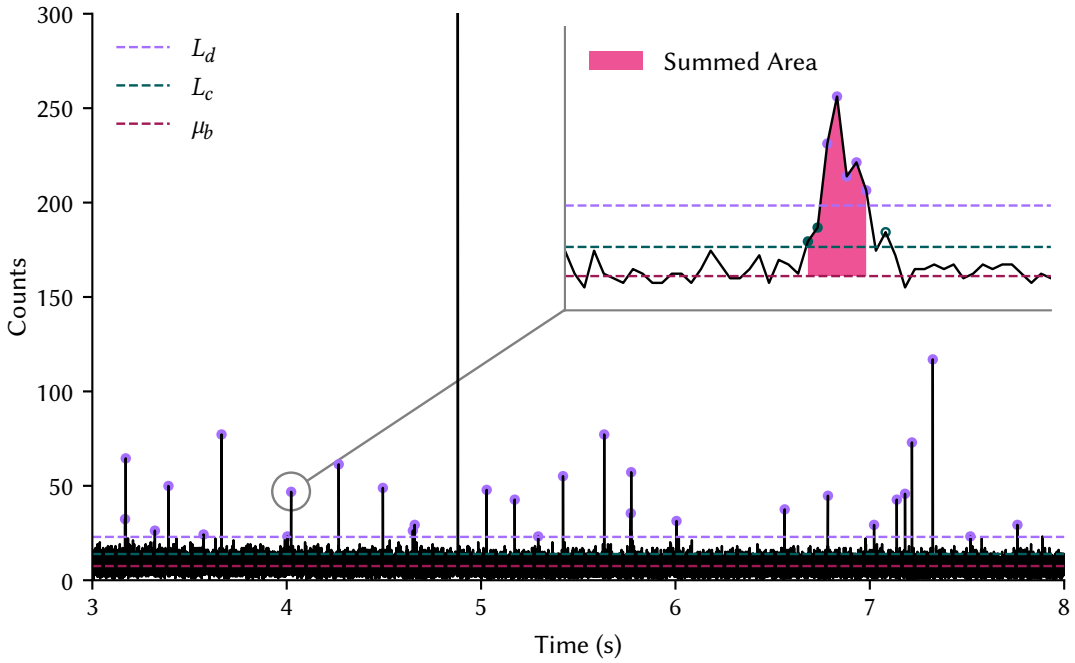

Figure 6.1. Poisson filtering used the signal mean (μ_b) to determine the L_d and L_c. Signals above the L_d were recognised as NPs and continuous regions above the L_c with at least one point above the L_d were accumulated to produce a single NP signal.

In our software, detection events are distinguished from the background using thresholds defined by either Gaussian or Poisson statistics. Two Gaussian filters were implemented to predict the L_d based on the mean or median signal value. The latter was useful for the analysis of NP dispersions with high PNCs and large particle sizes, which increased the mean of the data set and led to an overestimation of the threshold. The Poisson filter was implemented as previously described, with the thresholds L_c and L_d calculated from the signal mean. Figure 6.1 shows the exemplary application of a Poisson filter for the filtering of small NP signal events. Values in contiguous regions above the L_c with at least one point above the L_d were summed as shown and saved in a data array for further analysis. This procedure supports the application of both rapid mass analysers recording several data points per NP and slower analysers recording only one point per NP.

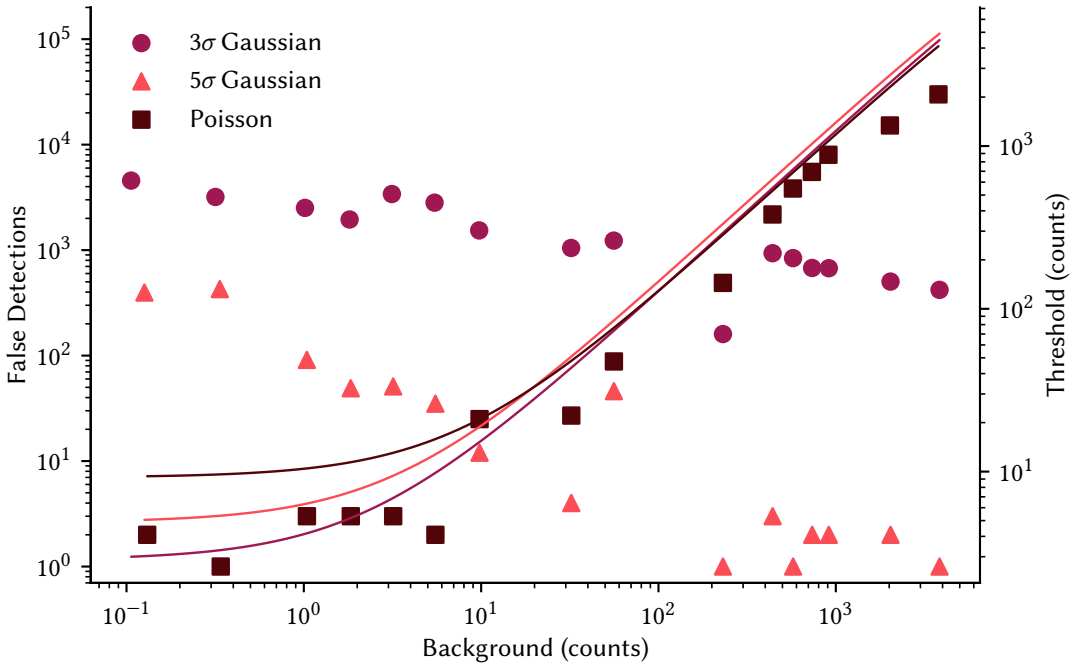

Figure 6.2. Comparison of the number of false detections produced by different filters. The threshold set by a 3σ Gaussian filter falsely detected a large number of NPs across all background signals. Use of 5σ and Poisson filters set thresholds that avoided false detections at high and low backgrounds respectively.

Accuracy and performance of the Gaussian and Poisson filters were dependent on the nature of the noise present in the signal background, as demonstrated by the analysis of an ionic Au standard in Figure 6.2. The standard was analysed using a 0.1 ms dwell time for 40 s, generating 400000 data points and three different filters were applied for NP detection: 3σ Gaussian, 5σ Gaussian and Poisson. As expected, the Poisson filter had the highest threshold (L_d) at low background signals leading to efficient filtering at low counting rates but performed worse than the Gaussian filters at higher counting rates. The 3σ Gaussian filter resulted in the false detection of a significant number of signals across low and high background signals. Increasing the threshold to 5σ mitigated the misidentification of NPs at high count rates. The background dependent applicability of filters suggests a case-to-case decision whether Poisson and Gaussian (5σ) are adequate for thresholding. While the developed software allows manual selection of filters, two methods for automatically selecting a threshold were implemented. A conservative approach applies the filter with the highest threshold while the other approach switches between Poisson and Gaussian filters depending on the mean input signal. For the latter, a Poisson filter is used for mean values below 50 counts. Above this value the Poisson distribution transits into a normal distribution and a Gaussian filter is selected (Figure 6.2).

The accuracy and precision of determined PNCs depended on many factors, including the particle flux into the plasma, the dwell time and total acquisition time. Under the prerequisite that particles do not interact with each other and are homogeneously distributed in a sample, their introduction into the plasma is randomised and the coincidental detection of two or more particles can be described with Poisson statistics.[226] If the coincidental detection of particles is unlikely (at low PNC and dwell times), the standard deviation of the particle count can be estimated via its square root.[330]

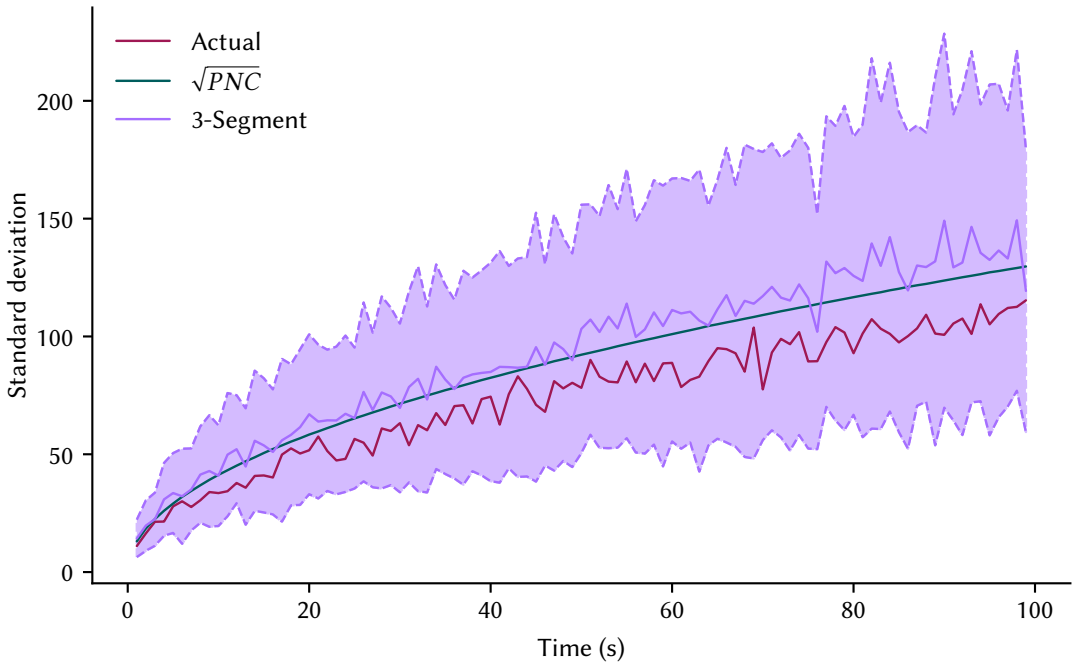

Figure 6.3. Calculation of the standard deviation of the PNC using simulated data.

Simulations were used to test the accuracy of two different methods of calculating the standard deviation of the PNC, the square root of the PNC and the standard deviation of the particle counts split across three segments of the acquisition. The rate of particles was modelled by fitting a Gamma distribution ($k = 1.4$) to data produced by a 15 nm Au reference particle. The model was then used to simulate 100 experiments with total acquisition times of 1 to 99 s (10000 total experiments) with the results shown in Figure 6.3. The square root of the PNC overestimated the standard deviation by 18 ± 8 %, likely due to the particle rate not being truly Poisson in nature. The three segment method had a large variation between simulations and made the three segment method unreliable.

6.3.2 Calibration of masses, sizes and concentrations

Calibration of detected NP events is performed to obtain the PNC, the sizes and masses of NPs, and to investigate statistical distributions within one or across multiple samples. Different calibration methods can be selected in "Options". Their applicability depends on the availability of both predetermined parameters and reference materials. Three distinct pathways were implemented for manual input of calibration parameters and for automated calculation of relevant parameters (mass response or transport efficiency) from reference materials. Manual input requires the previous determination of multiple parameters: the sensitivity, determined by analysis of an ionic standard; the uptake rate, calculated by weighing the introduced liquid; and the transport efficiency, which may be approximated by three approaches as described by Pace et al.[336] The dwell time is automatically determined if the loaded data file contained acquisition times but may also be entered manually. A reference material with known particle sizes or concentrations may be analysed to calculate the transport efficiency. The mass response of the reference material is also able to calibrate data according to eq. 6.14 and consequently values for uptake rate, ionic response and transport efficiency are not required. While this allows to determine masses and sizes, it does not grant access to the PNC or ionic background unless the ionic response and transport efficiency are provided additionally.

The "Sample" tab was designed to load and visualise raw spICP–MS data. Upon load, the program performs the previously described NP detection algorithms and plots raw signals, limits and detections. A trim function was implemented to remove unwanted data regions from the beginning and/or end of acquisitions. While statistics on raw data are readily available after loading the file, data may be calibrated by entering sample specific parameters. Input of common chemical formulas automatically fills the density, molar mass and molar ratio of a particle. In cases where the chemical formula is not available or applicable, these parameters may be entered manually.

The "Reference" tab is only available when selecting a calibration method requiring a reference material and allows loading of calibration data. This tab functions similarly to the "Sample" tab, loading, detecting and displaying the raw reference data. Information on the diameter or particulate concentration of reference particles is entered here to calculate the transport efficiency or mass response. If both diameter and particulate concentration are entered, the latter is used to calculate the transport efficiency.

The "Results" tab lists the calibrated data arrays and visualises the signal distribution of the detected NPs. The signal mean, median and the detection limits are determined and listed automatically. If calibrated, the mass and size distributions and figures of merit are also available. Furthermore, the number of detected NPs, PNC, particulate mass concentration and the ionic background are determined depending on the calibration pathway chosen. Histograms are further statistically analysed, labelled, visualised and may be fitted with either a normal or log-normal curve. Data and figures can be exported, and a batch dialog allows the application of the processing method to any number of other sample files and the subsequent export of results. The following three applications are of current interest in environmental sciences and were selected to showcase integrated algorithms, calibration pathways and specific software features.

6.4 Application 1: analysis of TiO_2 NPs in surface water

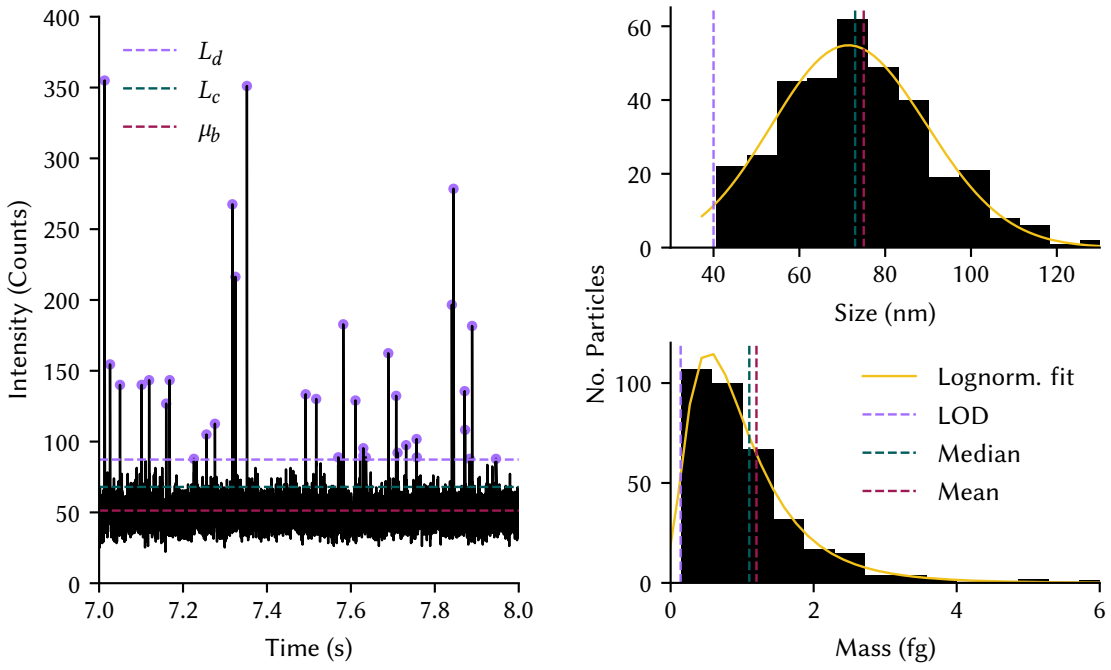

(a) NP detection

(b) Size and mass histograms

Figure 6.4. TiO_2 NPs in freshwater from obtained from the metropolitan Melbourne area. A Poisson filter was used for signal thresholding and NP recognition. Histograms show the LOD, mean and median particle size and mass.

The occurrence of incidental and engineered NPs is raising concerns and is particularly pronounced in urban areas with significant anthropogenic pressures.[320,321] TiO_2 NPs in particular have been frequently reported in surface waters within the catchments of major cities.[338–341] The toxicological impact of NPs

depends on their abundance, size, transport and their direct environment.[342,343] spICP–MS provides an elegant solution for the characterisation of these NPs in the environment by allowing efficient and high throughput analyses. As a demonstration of the developed data processing platform, freshwater was sourced from the Melbourne area, analysed using spICP–MS/MS and subsequently processed via the 'manual' calibration pathway. An ionic Ti standard was analysed to determine the response and uptake rate. The transport efficiency was determined by analysing a 50 nm Au particle dispersion. Figure 6.4a shows the data filtering and NP recognition utilising a Poisson filter. The signal histogram was translated into mass and size distributions using eqs. 6.13 and 6.15, as shown in Figure 6.4b. Signal, mass and size distributions were further fitted and analysed. Mean mass and size were 1.20 fg and 75.0 nm per particle and the mass and size detection limits were 0.14 fg and 40.0 nm, respectively. The PNC, particulate mass concentration and the ionic background concentration were determined to be $2.53 \pm 0.10 \times 10^9\,\mathrm{L}^{-1}$, $3.12\,\mu\mathrm{g\,L}^{-1}$ and $36 \pm 7\,\mu\mathrm{g\,L}^{-1}$, respectively.

6.5 Application 2: LA–spICP–MS of micro-plastic particles

The discharge and distribution of micro-plastic particles into the environment is a major and current issue that has caused global concern and triggered various research initiatives to investigate the fate and behaviour of these particles in environmental and biological systems.[344–347] A recent advance in the analysis of micro-plastics was the application of spICP–MS targeting C isotopes to determine PNCs, size and mass distributions.[323,348,349] spICP–MS was shown to be effective at describing C masses and sizes of individual micro-plastic particles, even in complex matrices like seawater.[323] LA may be combined with spICP–MS to sample and transport intact particulate matter from solid matrices for elemental single particle analysis.[325] It was previously shown that this strategy may be used to investigate and image NPs in biological tissues[326,327] raising the question as to whether LA–spICP–MS is also applicable for the investigation of intact micro-plastics in solid matrices. This would enable the study of micro-plastic occurrences in soil samples as well as their sedimentation and precipitation from water bodies. However, a common prerequisite for the application of thresholding filters is a stable baseline. While this is usually the case when analysing homogeneous NP dispersions, samples investigated via LA–spICP–MS often have heterogeneous background distributions for the element of interest.

In this study, a soil sample was mixed with 3 µm polystyrene-based micro-plastics and charcoal was added to simulate a heterogeneous C background. LA–spICP–MS was employed to analyse plastics

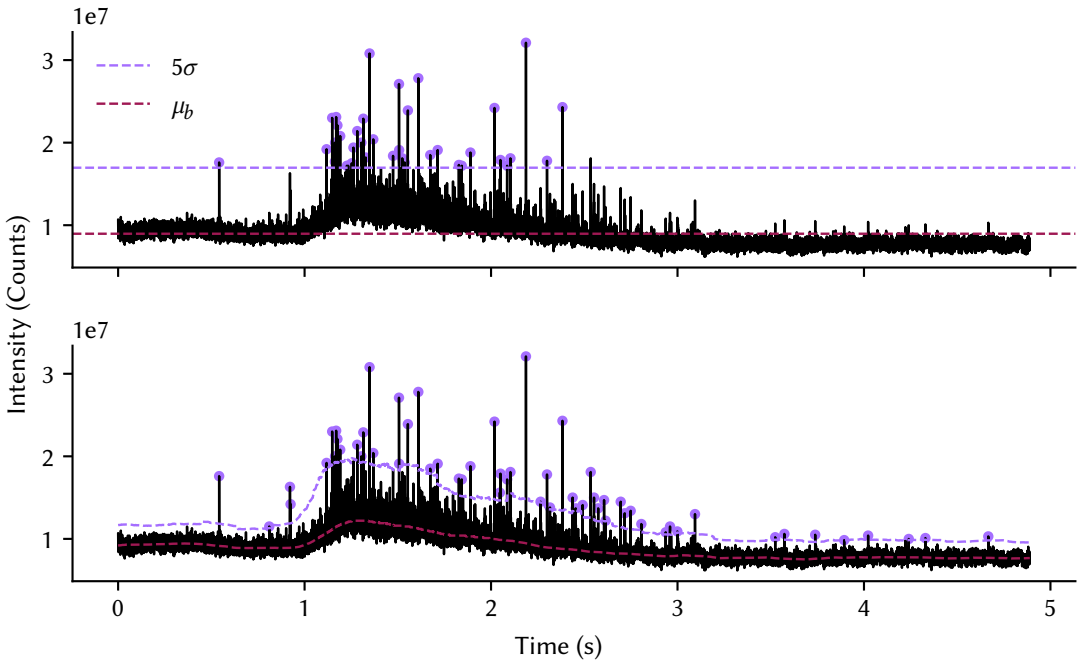

Figure 6.5. LA and spICP–MS targeting ^{12}C was used to analyse micro-plastics embedded in a soil matrix. The heterogeneous distribution of C in the matrix led to a variable baseline. Static Gaussian filters (top) could not reliably distinguish NP events from the background and a dynamic filter (bottom) was required.

and a selected scan line is shown in Figure 6.5. The high ^{12}C baseline required a 5σ Gaussian filter for micro-plastic recognition. A static filter was not adequate to distinguish individual signal pulses from the variable background and led to incorrect mean particle sizes. Accurate micro-plastic identification and characterisation was achieved by accounting for the drifting baseline using a dynamic filter. Here, a window size of 2000 data points was employed to determine local thresholds using a rolling 5σ Gaussian median filter. This filter calculated the median value and standard deviation for every data point using data located only within the defined window and thus followed the variances in the baseline. The appropriate window size depended on baseline drift rate, the number and intensity of detections. Generally, small windows were more influenced by the single-event detections and limits of analysis were overestimated. However, large windows were not able to compensate spontaneous baseline fluctuations. The application of a dynamic filter allowed accurate analysis of micro-plastics and determined mean and median sizes of 3.1 µm and 3.0 ± 0.8 µm, respectively with a theoretical value of 3.0 ± 0.1 µm.

6.6 Application 3: carbon fixation in algae

The previous application has demonstrated that spICP–MS is not restricted to the analysis of nano-scaled particles but may be extended to the characterisation of micro-particles. Individual cells may be perceived as micro-scaled C-based particles that can be analysed individually using scICP–MS. This is useful for investigating the elemental fingerprint of cells and to correlating it to phenotypic traits and pathologies.[323,350] Therefore, scICP–MS can be used to study the cellular uptake of elements of interest in medical and environmental studies.[351]

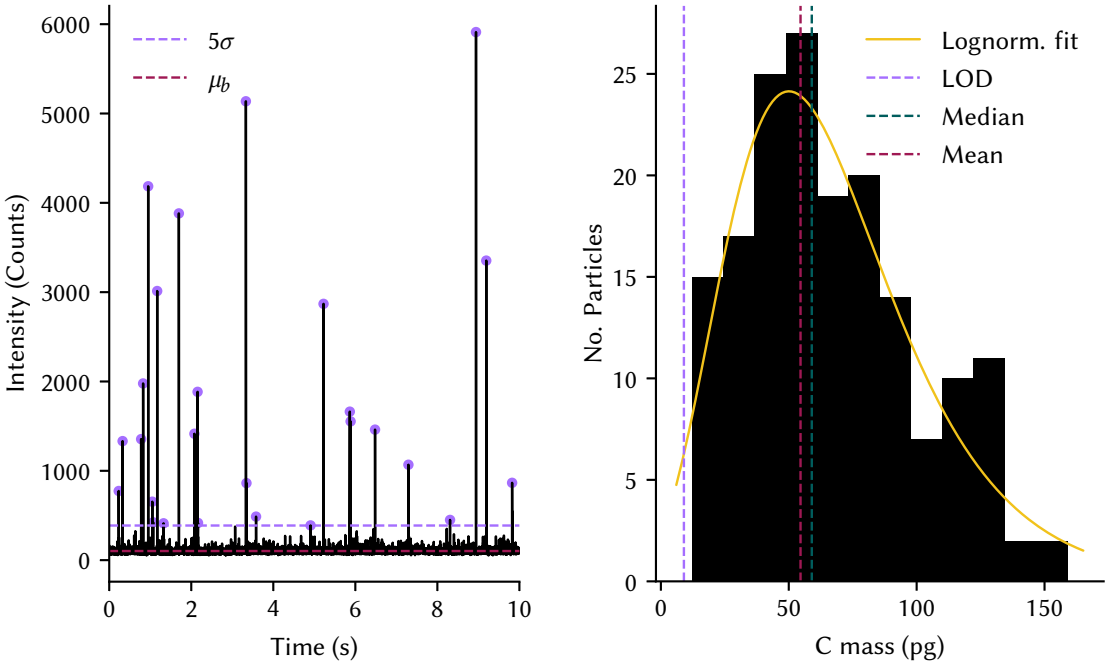

(a) Cell detection **(b)** Mass histogram

Figure 6.6. Carbon analysis across individual algal cells. $^{12}C^{16}O$ signals of individual cells were calibrated using 4 µm polystyrene reference beads.

This concept is, for example, useful to describe unicellular algae which fix carbon from the atmosphere and which can be regarded as a major natural sink for anthropogenic CO_2. Techniques used for spICP–MS analysis of micro-plastics via C isotopes were readily transferable to the C mass calibration of individual cells. Figure 6.6 shows the analysis and calibration of ^{12}C (via $^{12}C^{16}O$) in individual algae in seawater. The C mass per cell was calculated by analysing a matrix-matched polystyrene-based standard with a particle size of 4 µm. In both the sample and standard a 5σ Gaussian (mean) filter was used to distinguish the signals of individual cells from the background. The known average mass of the standard particle was used to estimate the mass response (2108 ag), which was then used to translate

the C signal histogram of the cells into the mass histogram shown in Figure 6.6b. In this case, 1021pm32 cells were counted and the mean and median C mass per cell was 54.6 pg and 59.0 ± 30.0 pg, respectively. The mass detection limit was 9.0 pg. If the cellular mass fraction of C is known, the mass distribution may further be translated into a size distribution as shown recently.[323] The mass response method does not determine cellular number concentrations or ionic background concentrations. While this may be achieved by selecting the 'Reference' method, it requires further parameters such as the ionic response and uptake rate.

6.7 Conclusion

An open-source Python-based data processing platform was developed for the efficient analysis and calibration of sp and scICP–MS data sets. Different filtering methods are available for reliable signal thresholding and detection of single events among dynamic, static, low and high background levels. Signals resolved with several data points are integrated and saved for statistical analysis and calibration. Three calibration pathways are available, offering versatile calibration options via different parameters and references. Results and relevant parameters are calculated and visualised and may be accessed and exported together with statistical parameters. Furthermore, the processing methods can be applied for batch analyses. The analysis of TiO_2 NPs in surface water, the LA sampling of micro-plastic particles in soils and the C mass calibration across individual cells were demonstrated. The developed software is designed for simple and interactive analysis of spICP–MS data. The open-source nature of the software improves traceability and offers possibilities for code modification.

Chapter 7

Radioresistance in a Breast Cancer Cell Model

While there is abundant data on the radioprotective properties of manganese in bacteria and yeast, very little work has been performed in human cell models. Here I address this gap and Aim 4 using a breast cancer cell model and a cheap, open-source UV irradiation device. Inorganic manganese was not found to provide protection against UV-C radiation at any non-toxic concentrations. Finally, single-cell techniques were applied to study manganese concentrations, highlighting the need for population based investigatory tools.

7.1 Introduction

The initial discovery of the ability for Mn^{2+} to catalytically remove $O_2^{\bullet -}$ in place of SOD was made in the bacterium *L. plantarum*.[120] Bacteria grown in Mn enriched media actively accumulated Mn^{2+} and were more resistant to oxygen toxicity than those grown in normal media. The *L. plantarum* could also survive in aerobic conditions despite lacking SODs, enzymes usually responsible for removing $O_2^{\bullet -}$ formed by aerobic respiration. Work by Daly[125] demonstrated that *D. radiodurans*, an extremophile capable of surviving exposure to large amounts of radiation (50 000 Gy), also used Mn^{2+} in place of SOD. Filtered digests of the bacterium was enriched in Mn, mostly bound to small molecules and peptides. The filtrate also provided protection from ionising radiation to proteins, radiosensitive bacteria and human Jurkat-T cells.[126] Injection of a Mn^{2+}-decapeptide derived from the *D. radiodurans* filtrate provided protection to mice from exposure to 100 Gy.[130]

In the presence of certain anions Mn^{2+} can form a redox cycling complex and, in milli-molar concentration, replace cellular SOD by catalytically removing $O_2^{\bullet -}$ (eqs. 7.1 to 7.3).

$$Mn_2{}^{+} + O_2^{\bullet -} \rightleftharpoons MnOO^{+}{-}L \tag{7.1}$$

$$L + MnOO^{+}{-}L \rightleftharpoons [MnOO{-}L{-}L]^{-1} \tag{7.2}$$

$$(MnOO^{+}{-}L)_2 \xrightarrow{H^{+}} 2\,Mn_2{}^{+}{-}L + H_2O_2 + O_2 \tag{7.3}$$

Initially it was thought that either phosphate could stabilise the $MnOO^{+}$ intermediate (eq. 7.2) but only *ortho*-phosphate can do so catalytically as *pyro*-phosphate dissociates H_2O_2, forming Mn^{3+}.[82,121] This makes a Mn-HPO_4-anion complex the most likely prospect from in vivo removal of $O_2^{\bullet -}$. While phosphate alone can form this complex, other ions such as amino acids and peptides can significantly improve its protective effect.[131] Complexes containing the aromatic and sulphur containing amino acids provided the best protection and a histadine/methanine hexapeptide increased the required radiation dose to deactivate glutamine synthetase from 2 to 112 kGy. Despite the effective anti-oxidative nature of this complex it is almost completely absent in aerobic organisms. Tight regulation of $HPO_4{}^{3+}$ concentrations is required, making it a more difficult system to implement than normal enzymatic SOD.[131]

Mn is both an essential nutrient and toxic heavy metal, with chronic exposure having effects to the liver, kidney and central nervous system (CNS).[352] Both acute and chronic exposure have significant behavioural effects indicating uptake into the CNS.[353] Previous work on antioxidant Mn-complexes in bacteria exposes these organisms to mmol L^{-1} levels of Mn,[135] concentrations that are toxic to human cells. Acute exposure of kidney, liver and CNS cell lines caused 50 % inactivation at 650, 250 and 50 µmol L^{-1} respectively.[352] A similar effect was seen in the breast cancer cell line MDA-MB-231, where only 100 µmol L^{-1} $MnCl_2$ was required to restrict cell growth.[354]

Exposure of cells to UV radiation damages DNA and generates a range of ROS, including $O_2^{\bullet -}$.[355,356] These mechanisms are dependant on the wavelength of UV with UV-A (UVA), UV-B and UV-C (UVC) all inducing differing mechanisms for cell apoptosis.[357,358] UV induced damage to DNA is predominantly caused by singlet oxygen and $^{\bullet}OH$, with $O_2^{\bullet -}$ having little effect.[359] As shorter wavelengths are more effective at generating $O_2^{\bullet -}$ and less effective at generating singlet oxygen,[360,361] the ability of complexes to protect proteins from oxidation could be studied using UVA and UVC light.[28,362] This has already been proven by Krisko and Radman[363] who found that the dose of UVC and gamma radiation required

to induce cell death was always coincident. UVC radiation could be used to study the protective effects of Mn-complexes during exposure to gamma-radiation.

Early spectroscopy work by Mulay et al.[364] demonstrated that Mn content in malignant breast is higher than non-cancerous breast tissue. Serum from patients with breast cancer also contains significantly higher Mn.[365,366] These results are thought to be caused by over-expression of Mn-SOD, which has been observed in triple-negative MDA-MB-231 cells.[367,368] Although Weydert et al.[369] observed the opposite effect, with over-expression inhibiting growth. There has been little research into the role that inorganic Mn may play in breast cancer cells.[354] demonstrated that the addition of $MnCl_2$ promoted the proliferation and invasive behaviour of MDA-MB-231 cells and Mn is required for cancer metastasis.[370]

When studying the effects of metal ions in vitro one important, but often overlooked, factor is the metal buffering capacity of serum. Proteins in serum can bind to metals and reduce the availability of 'free' ions to orders of magnitude below the total concentration. The median lethal dose (LD_{50}) of Zn^{2+} was reduced from 154.4 µmol L^{-1} to 82.8 µmol L^{-1} by reducing fetal calf serum (FCS) content from 10 % to 1 %.[371] Cells are grown in media containing only 5 to 20 % FCS which can lead to over-estimation of effects of metal ions when extrapolated to in vivo conditions.

7.2 Materials and methods

Metals contents of the cell media formulations (Minimum Essential Media, Dulbecco's Modified Eagle Medium (DMEM), Iscove's Modified Dulbecco's Medium) and FCS were determined via solution-nebulisation ICP–MS, as in Table 7.1.

7.2.1 Cell culture

Normal and radioresistant triple-negative breast cancer cell lines (MDA-MB-231) were obtained from St. George Hospital. All cell lines were grown in high-glucose DMEM (Thermo Fisher; Goodwood, Australia) supplemented with 10 % FCS (Thermo Fischer) and cultured in a humidified incubator at 37 °C with 5 % CO_2. All treatments were performed in DMEM with 1 % FCS unless specified otherwise. Manganese and phosphate spiked media were created using $MnCl_2$ (99.995 % metal-basis purity) purchased from Sigma Aldrich, and $NaH_2PO_4 \cdot 2\,H_2O$ / Na_2HPO_4 from Univar (Ingleburn, Australia).

7.2.2 Viability assays

Prior to any assay, cells were washed three times with TBS to remove any residual metals. Cell viability assays were performed on a Tecan infinite M1000Pro plate reader (Männedorf, Switzerland) following four hours incubation with alamarBlue© (Thermo Fischer) added to complete media. Fluorescence reading were taken using an excitation at 560 nm, emission at 590 nm and optimal gain.

7.2.3 Cell digests

Cells were seeded onto 24-well plates and cultured for 24 h in normal conditions. Media was then exchanged for the required treatment and the cells incubated for the required treatment time. Following treatment, cells were washed three times with TBS, sealed and digested overnight in 50 µL of concentrated trace-element nitric acid (Choice Analytical; Thornleight, Australia). Digests were diluted to 1 mL using milli-Q water, transferred to micro-centrifuge tubes and quantified.

Quantification was performed using solution-nebulisation on an Agilent Technologies 7700 series ICP–MS (Mulgrave, Australia). Samples were introduced using a peristaltic pump, using a separate 50 µg L^{-1} solution of Rh as an internal standard. Mixed element calibration standards and Rh used for quantification were purchased from Choice Analytical.

7.2.4 UV exposure challenges

UV exposure challenges were performed with a lab-built device consisting of three driver boards, each with four UV light-emitting diodes (LEDs), and an STM32 micro-controller based control board (Figures A.4 and A.5). The device used Vishay VLMU1610-365-135 UVA and Lumex SML-LXF3535UVCC10 UVC LEDs (Mouser Electronics; Kowloon, Hong Kong) with a flux at 30 mA of 35 mW and 2.7 mW respectively. A small C program controlled rates of irradiation (10 W m^{-2} UVA; 0.7 W m^{-2} UVC) by varying LED current in the range of 0 to 30 mA. To protect users the LEDs were housed in a UV resistant polycarbonate box. The micro-controller source code, schematics and PCB design files are available online. [i]

Cells were seeded into 12 well plates at a density of 0.1×10^6 and cultured for 24 h in normal media. Media was exchanged for a 24 h treatment and finally 1 % FCS media for 24 h before exposure. Following exposure cells were allowed to recover for 24 h before assaying, to ensure the measurement of any delayed apoptotic effects.

[i] 12 well UV source code and schematics: https://github.com/djdt/stm_uv12

7.2.5 scICP-MS experiments

Single cell quantification was performed on a 7900 series ICP–MS (Agilent technologies) system equipped with a 1.1 mm torch, pt cones and s-lenses, using the parameters in Table A.2. Solutions were introduced via a peristaltic pump at 0.33 mL min^{-1} and a concentric nebuliser and Scott double pass spray chamber cooled to 2 °C was used for aerosol generation. Transport efficiency was determined using an 8 µm polystyrene micro particle standard as per González de Vega et al.[323]

Cells were prepared for analysis as per Meyer et al.[372] Briefly, cells were washed with PBS, detached using TrypLE™ (Thermo Fischer) and spun down to form a cell pellet. The pellet was then reconstituted in ice cold deionised water at a target concentration of 1×10^5 to 2×10^5 mL^{-1} and analysed within five minutes.

7.3 Results and discussion

Metal concentrations in the growth media and FCS were determined using ICP–MS to ensure that endogenous levels wouldn't impact $MnCl_2$ treatments. Trace levels of Mn, Fe and Zn were detected in all growth media formulations and low µmol L^{-1} concentrations in FCS, as listed in Table 7.1. Concentrations of transition metals in FCS varied by 8.2 to 23.0 % over the three measured batches. Normal growth media (DMEM with 10 % FCS) would contain 0.08 µmol L^{-1} Mn, well below the lowest treatment level.

Table 7.1. Metal concentrations in various media formations and FCS batches (µmol L^{-1}).

	Mn	Fe	Cu	Zn
MEM	0.0785	0.174	nd	0.227
DMEM	0.009 57	0.203	0.004 04	0.119
IMDM	0.002 38	0.0593	0.0200	0.0284
FCS Batch 1	0.709	50.8	2.34	48.8
FCS Batch 2	0.792	41.7	2.13	45.1
FCS Batch 3	0.648	46.4	3.24	53.1

nd: not detected.

Even if low levels of Mn protect against free radicals, higher concentrations are toxic. The optimal $MnCl_2$ treatment conditions were determined before starting experiments in reducing ROS. The MDA-MB-231 cells were treated with 0 to 10 mmol L^{-1} $MnCl_2$ spiked in treatment media for 24 h. The

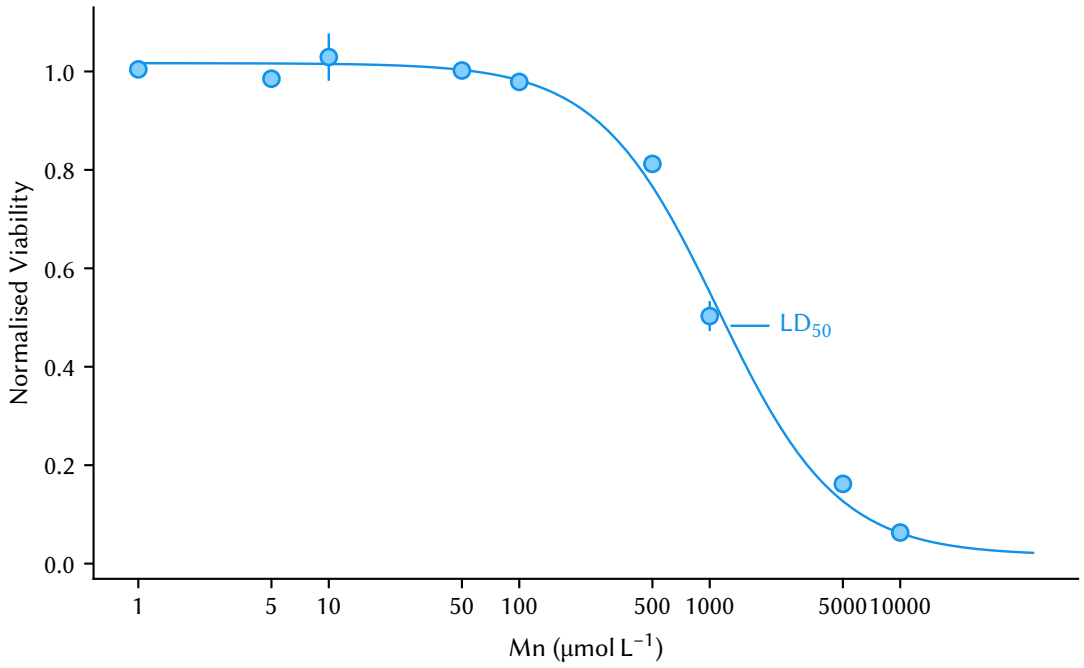

Figure 7.1. Cell viability when exposed to $MnCl_2$. Media with 1 % FCS was used to limit metal buffering.

concentration of FCS greatly affected the $MnCl_2$ toxicity, and switching from 10 % to 1 % FCS caused the LD_{50} to decrease by an order of magnitude (Figure 7.1). While no data exists for the binding of Mn^{2+} by serum proteins, metal buffering has been previously observed for Zn^{2+}, another divalent transition metal.[371] The LD_{50} in 1 % FCS was determined to be 1.2 mmol L^{-1} by fitting cell viability to a sigmoid function. A maximum treatment level of 100 µmol L^{-1} was chosen for all future experiments to prevent Mn toxicity.

Both the uptake of 'free' Mn^{2+} and buffering by serum proteins take time, during which the Mn will be unavailable. To provide protection from protein damage it must be present within cells at a suitable concentration during irradiation. To mimic the ROS removal of 1 µmol L^{-1} CuZn-SOD a concentration of 91 µmol L^{-1} Mn-complex is required.[82] Uptake of Mn from the spiked media increased logarithmically with time (Figure 7.2). Assuming spherical cells with a diameter of 20 µm,[373] the intracellular concentrations of Mn were calculated to be approximately 11 µmol L^{-1} after treatment with 100 µmol L^{-1} Mn for 24 h. This provides enough Mn to form complexes mimicking a 120 nmol L^{-1} of CuZn-SOD, whereas concentrations required for normal growth are at least 1 µmol L^{-1}, 3 to 30 µmol L^{-1} in human tissue.[82,374] The phosphate and ligands required to form the Mn-complexes is found in sufficient abundance in normal media.[130] A typical DMEM formulation will contain 0.91 and 44 mmol L^{-1} of orthophosphate and carbonate respectively.

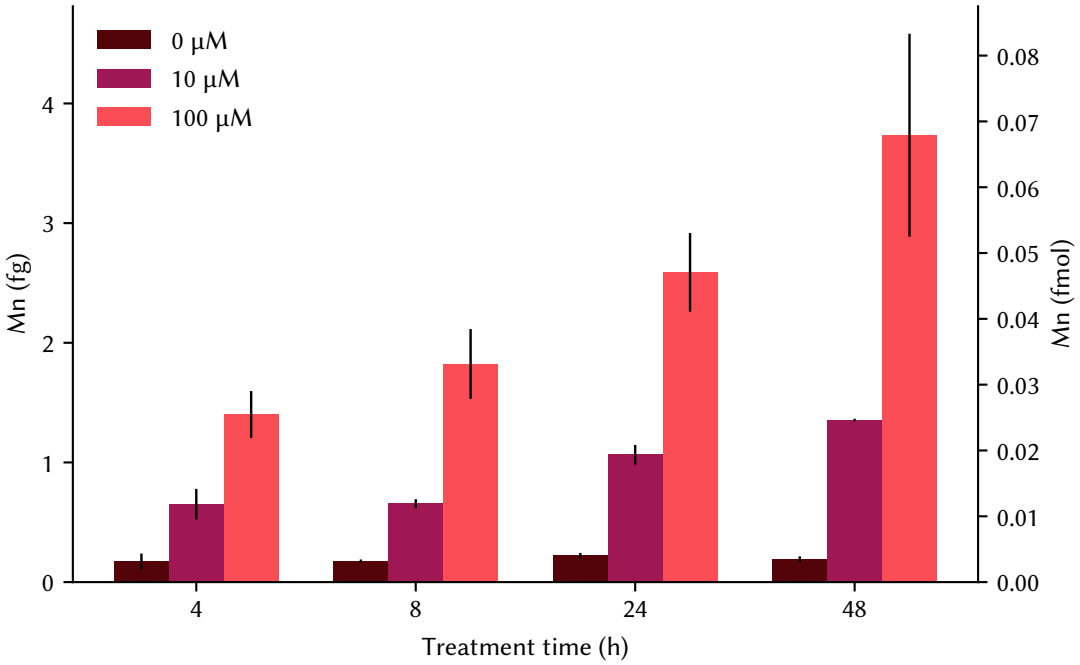

Figure 7.2. Manganese uptake as determined by bulk cell digestion and solution-nebulisation ICP–MS.

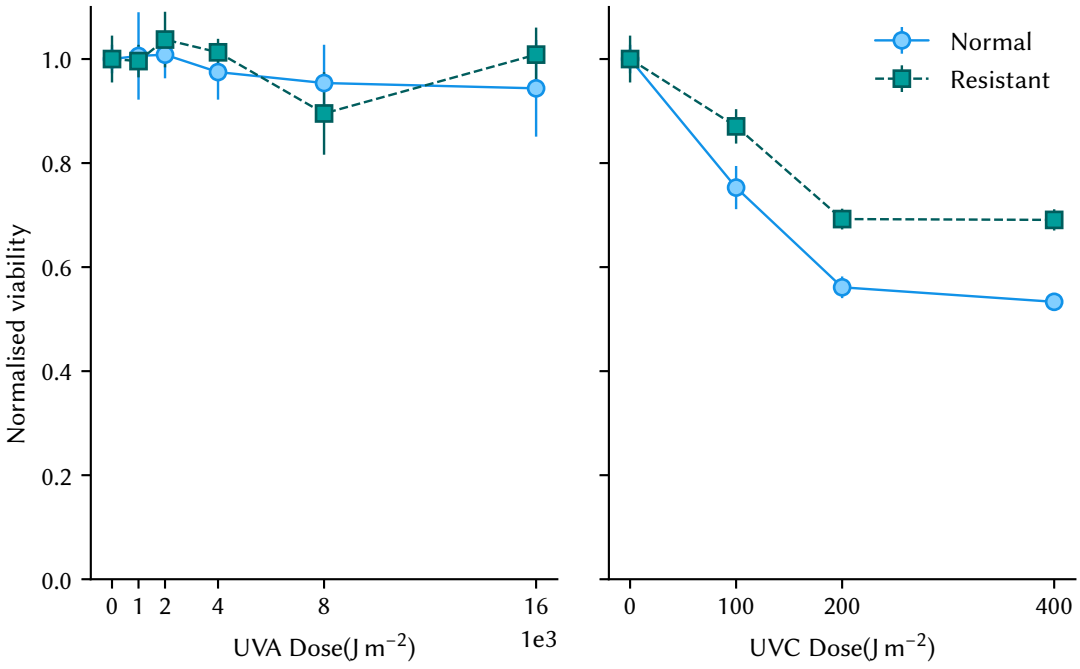

Figure 7.3. Viability of cells following UVA (left) and UVC (right) exposure. Treatments of up to 16×10^3 J m^{-2} UVA showed no toxicity for either MDA-MB-231 cell lines. Higher viability following UVC exposure was seen in the radioresistant cell line.

The appropriate UVA and UVC dose for treatment was established by successively increasing doses until a significant reduction in viability was achieved (Figure 7.4). Irradiation with UVA was terminated due to excessive treatment times with no observed decrease in cell viability. Previous studies have used doses in the 100 to 1000 kJ m^{-2} range[357,362] and the amount of UVA radiation produced by the LEDs was insufficient for the required treatments. Treatment with UVC achieved a 40 % decrease in viability at 200 J m^{-2} and levelled off at greater doses. Resistant cells had significantly higher viability ($p = 0.011$, repeated measures ANOVA) for the UVC treatments, suggesting an increased ability to resist oxidative stress.

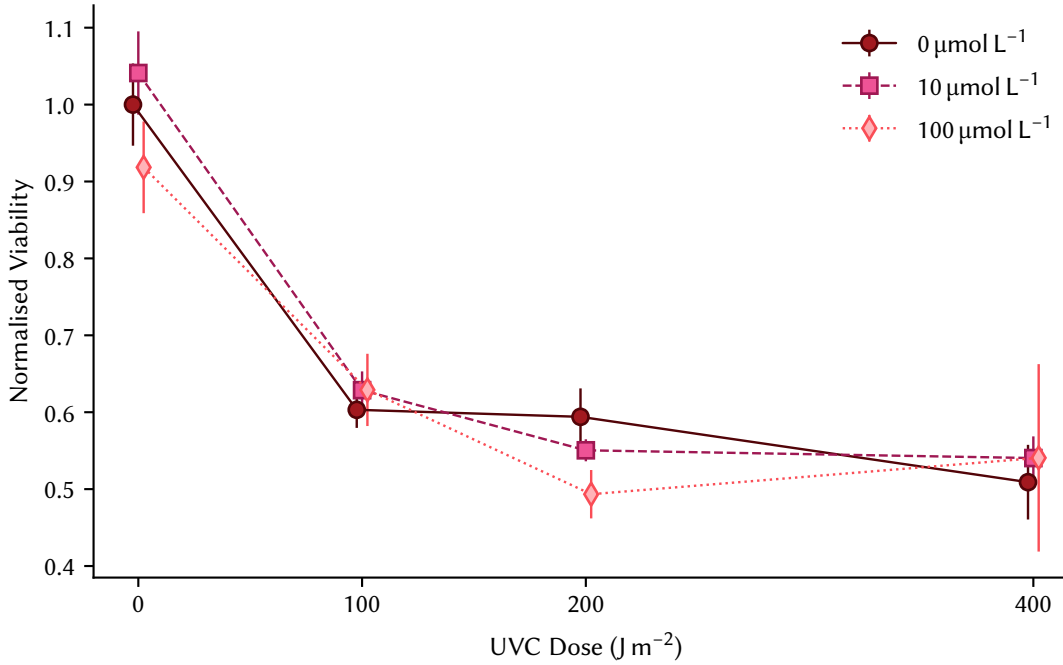

Figure 7.4. Viability of MDA-MB-231 cells following combined $MnCl_2$ and UVC treatments. Manganese treatments had no significant effect on the UVC treatment lethality.

Once the optimal treatment and challenge conditions had been determined, a set of 12 experiments were used to assess the potential for manganese to increase cell resistance to oxidative stress. Neither the low (10 µmol L^{-1}) nor high (100 µmol L^{-1}) treatments (Figure 7.4) provided any measurable improvement in cell viability.

The majority of existing studies that have shown an improved resistance to radiation following treatment with $MnCl_2$ have been performed in bacterial models, specifically in bacteria that specialise in scavenging Mn.[125,126] Experiments on mammalian cells have required inoculation with specifically extracted[126] or designed[130,131] complexes to achieve radioresistance. Both the current and previous

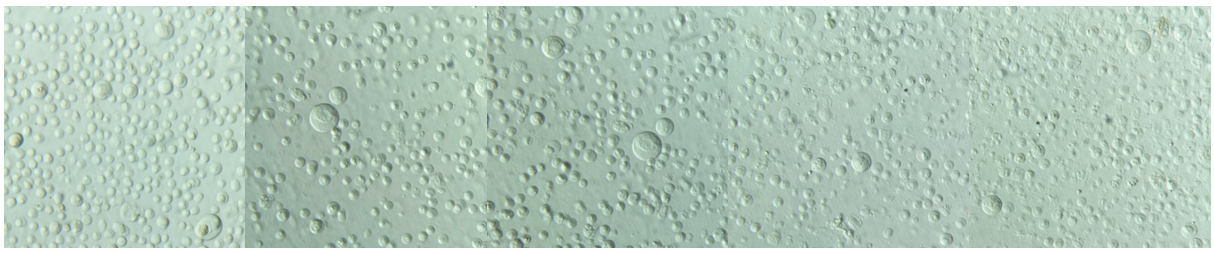

(a) 10 min **(b)** 15 min **(c)** 20 min **(d)** 25 min **(e)** 30 min

Figure 7.5. MDA-MB-231 cells were resuspended in deionised water. Lysis of the cells began after 15 min.

results suggest that the formation of sufficiently protective Mn-complexes is hard to achieve in human cells.

7.3.1 Manganese concentrations via scICP-MS

One major disadvantage of determining intracellular elemental concentrations using bulk digests is the introduction of error via cell counting. Manual counting using a hemacytometer remains the most popular method of counting cells and while accurate, the reproducibility of this method is poor.[375] Additionally, any information about the distribution of elements is lost during the digestion. scICP–MS can be used to simultaneously perform a cell count and determine intracellular concentrations along with their distribution.

Human cell lines have been prepared for scICP–MS analysis using multiple methods. Wang et al.[231] fixed cells before analysis using ice-cold methanol, a process that permeabilises cells. However, as permeabilisation could lead to the loss of cell contents alternative fixation methods such as paraformaldehyde or glutraldehyde would be preferred. A simple method was proposed by Meyer et al.[372] where cells were simply diluted in deionised water and analysed. If cells are left in a hypotonic solution for too long then water will be transported via osmosis into the cells, causing them to lyse and lose their contents. MDA-MB-231 cells were resuspended in deionised water and observed using a microscope to determine the time required for cells to lyse. The images in Figure 7.5 show mono-dispersed cells with no significant cell lysis before 15 min, leaving sufficient time for scICP–MS analysis.

Optimal ICP conditions were determined using *Microcystis aeruginosa* cyanobacteria as a model organism due to their resilience and ease of culture. The transport efficiency was determined using a 3 µm polystyrene micro-plastic standard, similar in size and density to *M. aeruginosa* cells (3 to 5 µm). The mean cell size was measured as 3.4 ± 0.9 µm using the calibrated C signal, likely an underestimation

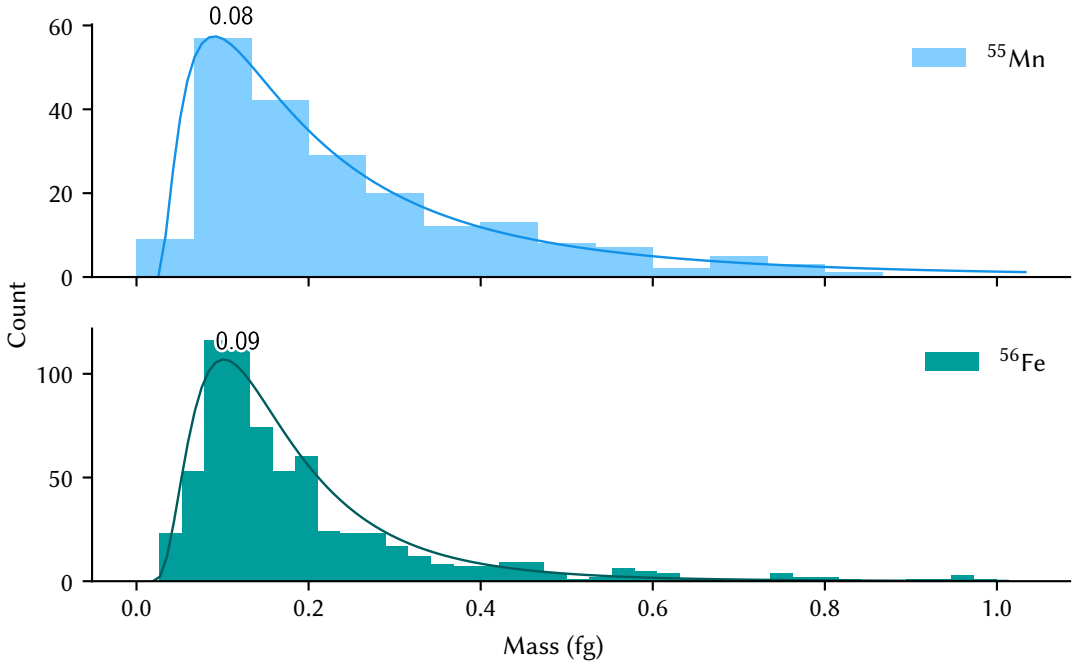

Figure 7.6. Distributions of Mn and Fe in cyanobacteria determined via scICP–MS. A similar distribution of metals was observed.

due to the high water content and heterogeneous make-up of algal cells. Natural abundances of Mn and Fe in the cyanobacteria were then determined using the tuned conditions and are displayed in Figure 7.6. Both elements had a similar log-normal distribution with modes of 0.08 and 0.09 fg for Mn and Fe respectively. The mean mass per cell was of Mn and Fe (0.4 ± 0.7) and (1 ± 2) fg and limits of detection were 0.06 and 0.04 fg. The large difference between distribution mode and mean is most likely caused by intense signals produced by residual colonies of *M. aeruginosa*. Colonies could be further broken up by vigorously shaking or sonicating the *M. aeruginosa* solution, but this was not performed as it may cause damage to the cells.

The scICP–MS mean concentrations of the 24 h treatments were significantly higher than those of the acid digestion in Table 7.2. This was due to the large number of high signal outliers, most likely clusters of cells as seen in the cyanobacterial samples. Using a more robust metric, the median of the scICP–MS data, the recoveries of the were 182, 80 and 106 % of the acid digest. Due to the relatively low natural abundance of Mn in the cells, the untreated sample was unable to be fully separated from the background. This can be seen in Figure 7.7 as an incomplete (or cut-off) log-normal distribution that is very close to the LOD and the PNC, and likely impacted the mean and median mass. Even though samples were diluted by eye, the PNC of the treated samples were within 30 % of the expected. In an

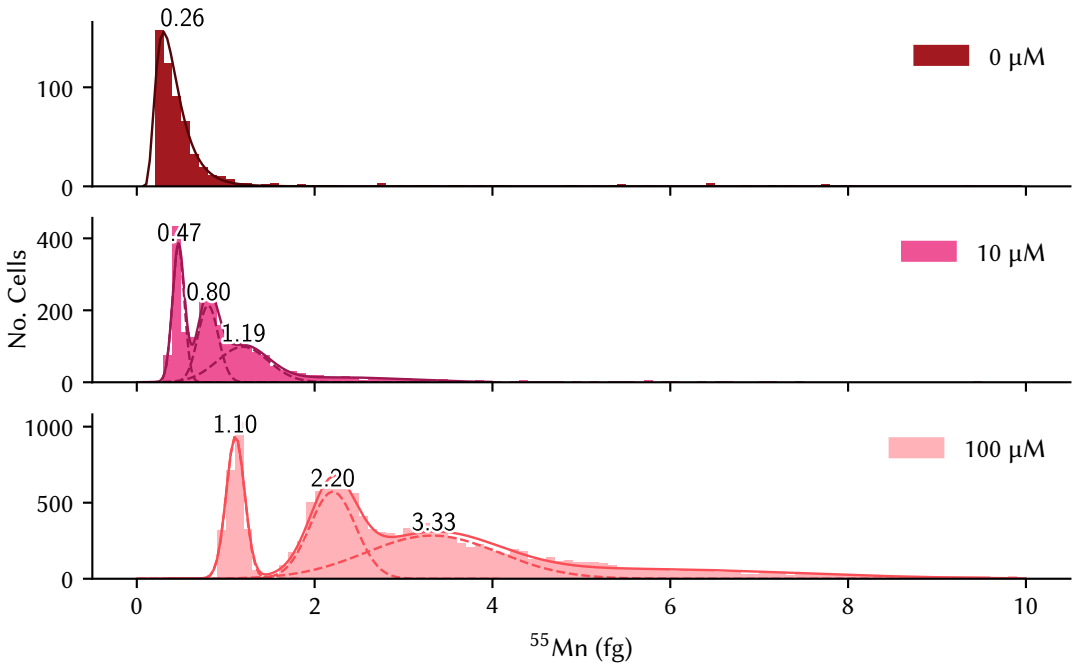

Figure 7.7. Distributions of Mn in MDA-MB-231 cells treated with 0, 10 and 100 µmol L^{-1} $MnCl_2$ for 24 h. Multi-modal distributions were detected in higher level treatments. Distributions were estimated using a Bayesian Gaussian mixture model.

attempt to improve LODs a triple-quadruple MS and O_2 reaction gas were used. Measurements of $^{55}Mn \rightarrow {}^{55}Mn$ and $^{55}Mn \rightarrow {}^{55}Mn^{16}O$ did not improve the LOD. The failure to separate the untreated sample from the background accounts for the differences in masses observed between the digest and scICP–MS.

Table 7.2. Concentrations of Mn in MDA-MB-231 cells treated with 0, 10 and 100 µmol L^{-1} $MnCl_2$ for 24 h as determined by digestion and scICP–MS.

$MnCl_2$ (µmol L^{-1})	Digest		scICP–MS		
	mean	±	mean	±	median
0	0.22	± 0.02	0.7	± 1.1	0.40
10	1.06	± 0.08	1	± 5	0.95
100	2.6	± 0.3	4	± 8	2.7

The distribution of Mn in untreated cells was log-normal, and multi-modal in both the 10 and 100 µmol L^{-1} treatments (Figure 7.7). Multi-modal distributions of Mn have been observed previously in human cancer and normal cell lines.[232] There are two hypotheses to explain the multiple distributions observed. The first was that distributions are subpopulations of cells with varying ability to uptake Mn from the media. Tumour cells are well known to be heterogeneous and cell-to-cell variations

and subpopulations has been previously observed in MDA-MB-231 cell lines.[376] Cell heterogenity would impact the survival of cells following irradiation and with those with highest Mn surviving and repopulating with increased resistance. Tumours of the breast have been shown to increase radioresistance following treatment and this extends to cell lines as well.[377]

The second hypothesis is that the multi-modal distribution was caused by increased cell adhesion in the treated samples, with each distribution caused by single-cell events containing clusters of one, two, three or more cells. Mn^{2+} is a powerful activator of integrins, the proteins that mediate cell-cell adhesion.[378] Multi-modal distributions were only observed in treated samples as the untreated sample was absent of the divalent cations required by integrins to initiate binding and as each sample was diluted with deionised water, all cations must have been present within the cells. Studies of divalent-cations (Ca^{2+}, Mg^{2+} and Mn^{2+} in particular) using scICP–MS will have to consider this factor when preparing samples and analysing data. A future study could determine if fixing or the addition of dissociation enzyme such as trypsin can reduce cell-to-cell binding.

7.4 Conclusion

An MDA-MB-231 cell model was successfully used to test the protective effects of Mn on cells exposed to UV radiation. Toxicity of $MnCl_2$ was determined, with an LD_{50} of 1.2 mmol L^{-1} in 1 % FCS and no significant toxicity observed in 24 h at concentrations below 100 µmol L^{-1}. The concentration of FCS drastically affected toxicity, with the LD_{50} and order of magnitude higher in 10 % FCS. Uptake of Mn from media increased with both time and concentration. Similar viability was observed after UVC challenges for cells treated with 0, 10 and 100 µmol L^{-1} $MnCl_2$; Mn was not protective against UVC radiation. Median concentrations of Mn determined using scICP–MS correlated with the concentration determined using traditional acid digestion. Untreated cells were unable to be separated from background noise using scICP–MS, leading to an overestimation of concentration. The observation of cell subpopulations demonstrated the capabilities of scICP–MS when investigating populations of cells and would have been missed if quantification was performed using digestion alone. ICP–MS is still emerging as a single-cell analysis technique but it has great potential for quantifying cell-to-cell variations.

Conclusions and Future Work

Novel mould-formed gelatine standards were produced with controllable thickness, improved surface characteristics and superior analytical figures of merit. The endogenous background of the gelatine was reduced using metal chelators, but remained high for certain elements. Polymer standards have the potential to offer true 'zero' background levels, but still require significant work. Additives and cross-linking of polymers could be used to control their physical characteristics and match the ablation patterns of gelatine and tissue. Use of spiked gelatine to create a height map was impossible due to imperfections introduced during moulding and dehydration. Techniques to control the drying of gelatine are already implemented in the food sciences and could be applied to improve surface characteristics of the gelatine further.[219]

Open-source LA–ICP–MS imaging software was created and demonstrated throughout the thesis. Improvements over existing software include native compatibility with existing ICP–MS vendors, speed, ease-of-use and the ability to export to a variety of formats. The open-source nature of the program ensures user extensibility and long term support. Maintenance of the software will have to continue, with addition of new file formats as they are introduced by vendors. Live imaging, direct capture and display of the sample being ablated, is possible and would be a useful addition to the software. Simultaneous display of other image formats such as micrographs would aid in region selection of samples.

Transition metals were quantified in TMAs and brain tumour sections and compared with inferred radioresistance. A correlation was seen between Mn concentrations and radioresistance in the TMAs but not in brain tumours. Radioresistance in testis tumours did not correlate with Mn, with NSGCTs concentrations lower when compared to seminoma. Concentrations of Mn were not raised in any radioresistant tumours when compared to normal tissue. Current work has been limited to a few representative tumours and a larger sample set with a greater range of types would improve our understanding of the relationship between endogenous metals and radioresistance. Statistical power

was also limited in brain sections due to the number of samples available and could be increased using a larger sample set. Samples of tumour and tumour-adjacent normal tissue from the same patient would remove inter-sample variances and help explore the differences in metal uptake between normal and tumorous tissues. Phosphorous masking has been shown as a potential tool in the automation of analysis but further work is required to improve and validate the masks. Use of large sample sets and computer learning approaches could be applied. Laser ablation imaging lacks the ability to discriminate between organic and inorganic sources of Mn. Up-regulation of Mn-SOD remains a potential source of the increased Mn observed and could be excluded using matrix-assisted laser desorption/ionisation imaging.[379]

Open-source ICP–MS software for single-particle and -cell analyses was created with multiple methods of filtration and calibration. The software's GUI guides users through the analysis of sp and sc data, and is fast enough to process the large data sets produced by these experiments in seconds. scICP–MS is emerging as an excellent tool for quantifying endogenous elements in individual cells, providing information about cell-to-cell variations in element concentrations and uptake. Future experiments could make use of scICP–MS to quantify the metal-tags used in mass cytometry, and thus cancer markers, with increased sensitivity.

Breast cancer cells were successfully used to model the radioprotective effects of inorganic Mn^{2+} using UVC radiation. While UVC is a reasonable analogue to gamma irradiation it would be worthwhile to repeat these experiments using a gamma radiation source such as ^{60}Co. Future studies could correlate the effects of UVC and gamma irradiation in breast cancer cells by measuring produced ROS and cell viability.[34] The protection of Mn-Pi-complexes has been shown to heavily depend on the ligands available.[131] Perhaps those that are naturally abundant in human cells and cell media are not sufficiently protective and thus require supplementation before irradiation.

Bibliography

References for Chapter 1

(1) Daly, M. J.; Gaidamakova, E. K.; Matrosova, V. Y.; Vasilenko, A.; Zhai, M.; Leapman, R. D.; Lai, B.; Ravel, B.; Li, S.-M. W.; Kemner, K. M.; Fredrickson, J. K. Protein Oxidation Implicated as the Primary Determinant of Bacterial Radioresistance. *PLoS Biology* **2007**, *5*, ed. by Petsko, G. A., e92.

(2) Doble, P. A.; Miklos, G. L. G. Distributions of manganese in diverse human cancers provide insights into tumour radioresistance. *Metallomics* **2018**, DOI: 10.1039/c8mt00110c.

(3) World Health Organisation, *World health statistics 2018: monitoring health for the SDGs*; World Health Organisation: 2018.

(4) Hart, I. R.; Saini, A. Biology of tumour metastasis. *The Lancet* **1992**, *339*, 1453–1457.

(5) Ferlay, J.; Soerjomataram, I.; Dikshit, R.; Eser, S.; Mathers, C.; Rebelo, M.; Parkin, D. M.; Forman, D.; Bray, F. Cancer incidence and mortality worldwide: Sources, methods and major patterns in GLOBOCAN 2012. *International Journal of Cancer* **2014**, *136*, E359–E386.

(6) Vineis, P.; Wild, C. P. Global cancer patterns: causes and prevention. *The Lancet* **2014**, *383*, 549–557.

(7) Bishop, D. P.; Cole, N.; Zhang, T.; Doble, P. A.; Hare, D. J. A guide to integrating immunohistochemistry and chemical imaging. *Chemical Society Reviews* **2018**, *47*, 3770–3787.

(8) Sjöström, M.; Lundstedt, D.; Hartman, L.; Holmberg, E.; Killander, F.; Kovács, A.; Malmström, P.; Niméus, E.; Rönnerman, E. W.; Fernö, M.; Karlsson, P. Response to Radiotherapy After Breast-Conserving Surgery in Different Breast Cancer Subtypes in the Swedish Breast Cancer Group 91 Radiotherapy Randomized Clinical Trial. *Journal of Clinical Oncology* **2017**, *35*, 3222–3229.

(9) Berney, D. M.; Lee, A.; Randle, S. J.; Jordan, S.; Shamash, J.; Oliver, R. T. D. The frequency of intratubular embryonal carcinoma: implications for the pathogenesis of germ cell tumours. *Histopathology* **2004**, *45*, 155–161.

(10) Wilson, L.; Heraty, L.; Ashford, B.; Coelho, S.; Frangi, A.; Pozo, J.; Ince, P.; Highley, J. Tissue microarray (TMA) use in post mortem neuropathology. *Journal of Neuroscience Methods* **2021**, *347*, 108963.

(11) Atun, R. et al. Expanding global access to radiotherapy. *The Lancet Oncology* **2015**, *16*, 1153–1186.

(12) Wong, K.; Delaney, G. P.; Barton, M. B. Evidence-based optimal number of radiotherapy fractions for cancer: A useful tool to estimate radiotherapy demand. *Radiotherapy and Oncology* **2016**, *119*, 145–149.

(13) Paganetti, H.; Bortfeld, T. In *New Technologies in Radiation Oncology*; Springer-Verlag: 2006, pp 345–363.

(14) Jäkel, O. In *New Technologies in Radiation Oncology*; Springer-Verlag: 2006, pp 365–377.

(15) Riley, P. A. Free Radicals in Biology: Oxidative Stress and the Effects of Ionizing Radiation. *International Journal of Radiation Biology* **1994**, *65*, 27–33.

(16) Von Sonntag, C.; Schuchmann, H.-P. The Elucidation of Peroxyl Radical Reactions in Aqueous Solution with the Help of Radiation-Chemical Methods. *Angewandte Chemie International Edition in English* **1991**, *30*, 1229–1253.

(17) Nikjoo, H.; Uehara, S.; Wilson, W. E.; Ho, M. Track structure in radiation biology: theory and applications. *International Journal of Radiation Biology* **1998**, *73*, 355–364.

(18) Rothkamm, K.; Lobrich, M. Evidence for a lack of DNA double-strand break repair in human cells exposed to very low x-ray doses. *Proceedings of the National Academy of Sciences* **2003**, *100*, 5057–5062.

(19) Kelley, K.; Knisely, J.; Symons, M.; Ruggieri, R. Radioresistance of Brain Tumors. *Cancers* **2016**, *8*, 42.

(20) Kastan, M. B.; Bartek, J. Cell-cycle checkpoints and cancer. *Nature* **2004**, *432*, 316–323.

(21) Ciccia, A.; Elledge, S. J. The DNA Damage Response: Making It Safe to Play with Knives. *Molecular Cell* **2010**, *40*, 179–204.

(22) Goldstein, M.; Kastan, M. B. The DNA Damage Response: Implications for Tumor Responses to Radiation and Chemotherapy. *Annual Review of Medicine* **2015**, *66*, 129–143.

(23) Von Sonntag, C., *Free-Radical-Induced DNA Damage and Its Repair*; Springer Berlin Heidelberg: 2006.

(24) Gray, L. H.; Conger, A. D.; Ebert, M.; Hornsey, S.; Scott, O. C. A. The Concentration of Oxygen Dissolved in Tissues at the Time of Irradiation as a Factor in Radiotherapy. *The British Journal of Radiology* **1953**, *26*, 638–648.

(25) Hodgkiss, R.; Roberts, I.; Watts, M.; Woodcock, M. Rapid-mixing Studies of Radiosensitivity with Thiol-depleted Mammalian Cells. *International Journal of Radiation Biology and Related Studies in Physics, Chemistry and Medicine* **1987**, *52*, 735–744.

(26) Ewing, D. The oxygen fixation hypothesis: a reevaluation. *American journal of clinical oncology* **1998**, *21*, 355–361.

(27) Funk, R. K.; Stockham, A. L.; Laack, N. N. I. In *Clinical Cardio-Oncology*; Elsevier: 2016, pp 39–60.

(28) Daly, M. J. Death by protein damage in irradiated cells. *DNA Repair* **2012**, *11*, 12–21.

(29) Imlay, J. A. Pathways of Oxidative Damage. *Annual Review of Microbiology* **2003**, *57*, 395–418.

(30) Keyer, K.; Imlay, J. A. Superoxide accelerates DNA damage by elevating free-iron levels. *Proceedings of the National Academy of Sciences* **1996**, *93*, 13635–13640.

(31) Lukianova, O. A.; David, S. S. A role for iron–sulfur clusters in DNA repair. *Current Opinion in Chemical Biology* **2005**, *9*, 145–151.

(32) Boal, A. K.; Yavin, E.; Barton, J. K. DNA repair glycosylases with a [4Fe–4S] cluster: A redox cofactor for DNA-mediated charge transport? *Journal of Inorganic Biochemistry* **2007**, *101*, 1913–1921.

(33) O'Brien, E.; Holt, M. E.; Thompson, M. K.; Salay, L. E.; Ehlinger, A. C.; Chazin, W. J.; Barton, J. K. The [4Fe4S] cluster of human DNA primase functions as a redox switch using DNA charge transport. *Science* **2017**, *355*, eaag1789.

(34) Krisko, A.; Radman, M. Protein damage and death by radiation in Escherichia coli and Deinococcus radiodurans. *Proceedings of the National Academy of Sciences* **2010**, *107*, 14373–14377.

(35) Strom, T.; Hoffe, S. E.; Fulp, W.; Frakes, J.; Coppola, D.; Springett, G. M.; Malafa, M. P.; Harris, C. L.; Eschrich, S. A.; Torres-Roca, J. F.; Shridhar, R. Radiosensitivity index predicts for survival with adjuvant radiation in resectable pancreatic cancer. *Radiotherapy and Oncology* **2015**, *117*, 159–164.

(36) Brożyna, A. A.; Jóźwicki, W.; Roszkowski, K.; Filipiak, J.; Slominski, A. T. Melanin content in melanoma metastases affects the outcome of radiotherapy. *Oncotarget* **2016**, *7*, 17844–17853.

(37) Peters, L. J.; Withers, H. R.; Thames, H. D.; Fletcher, G. H. Keynote address—the problem: Tumor radioresistance in clinical radiotherapy. *International Journal of Radiation Oncology*Biology*Physics* **1982**, *8*, 101–108.

(38) Classen, J.; Schmidberger, H.; Meisner, C.; Souchon, R.; Sautter-Bihl, M.-L.; Sauer, R.; Weinknecht, S.; Köhrmann, K.-U.; Bamberg, M. Radiotherapy for Stages IIA/B Testicular Seminoma: Final Report of a Prospective Multicenter Clinical Trial. *Journal of Clinical Oncology* **2003**, *21*, 1101–1106.

(39) Fertil, B.; Malaise, E. Intrinsic radiosensitivity of human cell lines is correlated with radioresponsiveness of human tumors: Analysis of 101 published survival curves. *International Journal of Radiation Oncology*Biology*Physics* **1985**, *11*, 1699–1707.

(40) Scott, J. G. et al. A genome-based model for adjusting radiotherapy dose (GARD): a retrospective, cohort-based study. *The Lancet Oncology* **2017**, *18*, 202–211.

(41) Lacombe, J.; Azria, D.; Mange, A.; Solassol, J. Proteomic approaches to identify biomarkers predictive of radiotherapy outcomes. *Expert Review of Proteomics* **2013**, *10*, 33–42.

(42) Armitage, E. G.; Barbas, C. Metabolomics in cancer biomarker discovery: Current trends and future perspectives. *Journal of Pharmaceutical and Biomedical Analysis* **2014**, *87*, 1–11.

(43) Gatenby, R. Perspective: Finding cancers first principles. *Nature* **2012**, *491*, S55–S55.

(44) Navin, N. et al. Inferring tumor progression from genomic heterogeneity. *Genome Research* **2009**, *20*, 68–80.

(45) Dewhirst, M. W.; Cao, Y.; Moeller, B. Cycling hypoxia and free radicals regulate angiogenesis and radiotherapy response. *Nature Reviews Cancer* **2008**, *8*, 425–437.

(46) Bao, S.; Wu, Q.; McLendon, R. E.; Hao, Y.; Shi, Q.; Hjelmeland, A. B.; Dewhirst, M. W.; Bigner, D. D.; Rich, J. N. Glioma stem cells promote radioresistance by preferential activation of the DNA damage response. *Nature* **2006**, *444*, 756–760.

(47) Zhang, M.; Atkinson, R. L.; Rosen, J. M. Selective targeting of radiation-resistant tumor-initiating cells. *Proceedings of the National Academy of Sciences* **2010**, *107*, 3522–3527.

(48) Viale, A.; Franco, F. D.; Orleth, A.; Cambiaghi, V.; Giuliani, V.; Bossi, D.; Ronchini, C.; Ronzoni, S.; Muradore, I.; Monestiroli, S.; Gobbi, A.; Alcalay, M.; Minucci, S.; Pelicci, P. G. Cell-cycle restriction limits DNA damage and maintains self-renewal of leukaemia stem cells. *Nature* **2009**, *457*, 51–56.

(49) Diehn, M. et al. Association of reactive oxygen species levels and radioresistance in cancer stem cells. *Nature* **2009**, *458*, 780–783.

(50) De Sousa e Melo, F.; Kurtova, A. V.; Harnoss, J. M.; Kljavin, N.; Hoeck, J. D.; Hung, J.; Anderson, J. E.; Storm, E. E.; Modrusan, Z.; Koeppen, H.; Dijkgraaf, G. J. P.; Piskol, R.; de Sauvage, F. J. A distinct role for Lgr5+ stem cells in primary and metastatic colon cancer. *Nature* **2017**, *543*, 676–680.

(51) Shackleton, M.; Quintana, E.; Fearon, E. R.; Morrison, S. J. Heterogeneity in Cancer: Cancer Stem Cells versus Clonal Evolution. *Cell* **2009**, *138*, 822–829.

(52) Bhatia, R. Persistence of malignant hematopoietic progenitors in chronic myelogenous leukemia patients in complete cytogenetic remission following imatinib mesylate treatment. *Blood* **2003**, *101*, 4701–4707.

(53) Quintana, E.; Shackleton, M.; Sabel, M. S.; Fullen, D. R.; Johnson, T. M.; Morrison, S. J. Efficient tumour formation by single human melanoma cells. *Nature* **2008**, *456*, 593–598.

(54) Brown, J. M. In *Methods in Enzymology*; Elsevier: 2007, pp 295–321.

(55) Thomlinson, R. H.; Gray, L. H. The histological structure of some human lung cancers and the possible implications for radiotherapy. *British journal of cancer* **1955**, *9*, 539–549.

(56) Grimes, D. R.; Kelly, C.; Bloch, K.; Partridge, M. A method for estimating the oxygen consumption rate in multicellular tumour spheroids. *Journal of The Royal Society Interface* **2014**, *11*, 20131124–20131124.

(57) Chaplin, D. J.; Olive, P. L.; Durand, R. E. Intermittent blood flow in a murine tumor: radiobiological effects. *Cancer research* **1987**, *47*, 597–601.

(58) Brown, J. M. Evidence for acutely hypoxic cells in mouse tumours, and a possible mechanism of reoxygenation. *The British Journal of Radiology* **1979**, *52*, 650–656.

(59) Chandel, N. S.; McClintock, D. S.; Feliciano, C. E.; Wood, T. M.; Melendez, J. A.; Rodriguez, A. M.; Schumacker, P. T. Reactive Oxygen Species Generated at Mitochondrial Complex III Stabilize Hypoxia-inducible Factor-1α during Hypoxia. *Journal of Biological Chemistry* **2000**, *275*, 25130–25138.

(60) Moeller, B. J.; Cao, Y.; Li, C. Y.; Dewhirst, M. W. Radiation activates HIF-1 to regulate vascular radiosensitivity in tumors. *Cancer Cell* **2004**, *5*, 429–441.

(61) Magnon, C.; Opolon, P.; Ricard, M.; Connault, E.; Ardouin, P.; Galaup, A.; Métivier, D.; Bidart, J.-M.; Germain, S.; Perricaudet, M.; Schlumberger, M. Radiation and inhibition of angiogenesis by canstatin synergize to induce HIF-1α–mediated tumor apoptotic switch. *Journal of Clinical Investigation* **2007**, *117*, 1844–1855.

(62) Lagadec, C.; Dekmezian, C.; Bauché, L.; Pajonk, F. Oxygen Levels Do Not Determine Radiation Survival of Breast Cancer Stem Cells. *PLoS ONE* **2012**, *7*, ed. by Tan, M., e34545.

(63) Szatrowski, T. P.; Nathan, C. F. Production of large amounts of hydrogen peroxide by human tumor cells. *Cancer research* **1991**, *51*, 794–798.

(64) Westman, N. G.; Marklund, S. L. Copper- and Zinc-containing Superoxide Dismutase and Manganese-containing Superoxide Dismutase in Human Tissues and Human Malignant Tumors. *Cancer Research* **1981**, *41*, 2962–2966.

(65) Cobbs, C. S.; Levi, D. S.; Aldape, K.; Israel, M. A. Manganese superoxide dismutase expression in human central nervous system tumors. *Cancer research* **1996**, *56*, 3192–3195.

(66) Landriscina, M.; Remiddi, F.; Ria, F.; Palazzotti, B.; Leo, M. D.; Iacoangeli, M.; Rosselli, R.; Scerrati, M.; Galeotti, T. The level of MnSOD is directly correlated with grade of brain tumours of neuroepithelial origin. *British Journal of Cancer* **1996**, *74*, 1877–1885.

(67) Nishida, S.; Akai, F.; Iwasaki, H.; Hosokawa, K.; Kusunoki, T.; Suzuki, K.; Taniguchl, N.; Hashimoto, S.; Tamura, T. T. Manganese superoxide dismutase content and localization in human thyroid tumours. *The Journal of Pathology* **1993**, *169*, 341–345.

(68) Janssen, A.; Bosman, C.; Sier, C.; Griffioen, G.; Kubben, F.; Lamers, C.; van Krieken, J.; van de Velde, C.; Verspaget, H. Superoxide dismutases in relation to the overall survival of colorectal cancer patients. *British Journal of Cancer* **1998**, *78*, 1051–1057.

(69) Suresh, A.; Tung, F.; Moreb, J.; Zucali, J. R. Role of manganese superoxide dismutase in radioprotection using gene transfer studies. *Cancer Gene Therapy* **1994**, *1*, 85–90.

(70) Kinnula, V. L.; Torkkeli, T.; Kristo, P.; Sormunen, R.; Soini, Y.; Pääkkö, P.; Ollikainen, T.; Kahlos, K.; Hirvonen, A.; Knuutila, S. Ultrastructural and Chromosomal Studies on Manganese Superoxide Dismutase in Malignant Mesothelioma. *American Journal of Respiratory Cell and Molecular Biology* **2004**, *31*, 147–153.

(71) Marklund, S. L.; Westman, N. G.; Lundgren, E.; Roos, G. Copper- and Zinc-containing Superoxide Dismutase, Manganese-containing Superoxide Dismutase, Catalase, and Glutathione Peroxidase in Normal and Neoplastic Human Cell Lines and Normal Human Tissues. *Cancer Research* **1982**, *42*, 1955–1961.

(72) Tsai, M.-H.; Cook, J. A.; Chandramouli, G. V.; DeGraff, W.; Yan, H.; Zhao, S.; Coleman, C. N.; Mitchell, J. B.; Chuang, E. Y. Gene Expression Profiling of Breast, Prostate, and Glioma Cells following Single versus Fractionated Doses of Radiation. *Cancer Research* **2007**, *67*, 3845–3852.

(73) Amundson, S. A.; Do, K. T.; Vinikoor, L. C.; Lee, R. A.; Koch-Paiz, C. A.; Ahn, J.; Reimers, M.; Chen, Y.; Scudiero, D. A.; Weinstein, J. N.; Trent, J. M.; Bittner, M. L.; Meltzer, P. S.; Fornace, A. J. Integrating Global Gene Expression and Radiation Survival Parameters across the 60 Cell Lines of the National Cancer Institute Anticancer Drug Screen. *Cancer Research* **2008**, *68*, 415–424.

(74) Wood, R. D.; Mitchell, M.; Sgouros, J.; Lindahl, T. Human DNA Repair Genes. *Science* **2001**, *291*, 1284–1289.

(75) Tusher, V. G.; Tibshirani, R.; Chu, G. Significance analysis of microarrays applied to the ionizing radiation response. *Proceedings of the National Academy of Sciences* **2001**, *98*, 5116–5121.

(76) Helland, Å.; Johnsen, H.; Frøyland, C.; Landmark, H. B.; Saetersdal, A. B.; Holmen, M. M.; Gjertsen, T.; Nesland, J. M.; Ottestad, W.; Jeffrey, S. S.; Ottestad, L. O.; Rodningen, O. K.; Sherlock, G.; Børresen-Dale, A.-L. Radiation-induced effects on gene expression: An in vivo study on breast cancer. *Radiotherapy and Oncology* **2006**, *80*, 230–235.

(77) Fu, Z.-c.; Wang, F.-m.; Cai, J.-m. Gene Expression Changes in Residual Advanced Cervical Cancer after Radiotherapy: Indicators of Poor Prognosis and Radioresistance? *Medical Science Monitor* **2015**, *21*, 1276–1287.

(78) Navin, N.; Kendall, J.; Troge, J.; Andrews, P.; Rodgers, L.; McIndoo, J.; Cook, K.; Stepansky, A.; Levy, D.; Esposito, D.; Muthuswamy, L.; Krasnitz, A.; McCombie, W. R.; Hicks, J.; Wigler, M. Tumour evolution inferred by single-cell sequencing. *Nature* **2011**, *472*, 90–94.

(79) Tamano, H.; Enomoto, S.; Oku, N.; Takeda, A. Preferential uptake of zinc, manganese, and rubidium in rat brain tumor. *Nuclear Medicine and Biology* **2002**, *29*, 505–508.

(80) Stephens, T.; Adams, K.; Peacock, J. Radiosensitivity of the B16 Melanoma Is Not Significantly Influenced by Melanin Content. *International Journal of Radiation Biology and Related Studies in Physics, Chemistry and Medicine* **1985**, *49*, 169–175.

(81) Zou, Z.-W.; Liu, T.; Li, Y.; Chen, P.; Peng, X.; Ma, C.; Zhang, W.-J.; Li, P.-D. Melatonin suppresses thyroid cancer growth and overcomes radioresistance via inhibition of p65 phosphorylation and induction of ROS. *Redox Biology* **2018**, *16*, 226–236.

(82) Barnese, K.; Gralla, E. B.; Valentine, J. S.; Cabelli, D. E. Biologically relevant mechanism for catalytic superoxide removal by simple manganese compounds. *Proceedings of the National Academy of Sciences* **2012**, *109*, 6892–6897.

(83) Koutcher, J. A.; Alfieri, A. A.; Barnett, D. C.; Cowburn, D. C.; Kornblith, A. B.; Kim, J. H. Changes in 31 P Nuclear Magnetic Resonance with Tumor Growth in Radioresistant and Radiosensitive Tumors. *Radiation Research* **1990**, *121*, 312.

(84) Ng, T. C.; Evanochko, W. T.; Hiramoto, R. N.; Ghanta, V. K.; Lilly, M. B.; Lawson, A. J.; Corbett, T. H.; Durant, J. R.; Glickson, J. D. 31P NMR spectroscopy of in vivo tumors. *Journal of Magnetic Resonance (1969)* **1982**, *49*, 271–286.

(85) Bobko, A. A.; Eubank, T. D.; Driesschaert, B.; Dhimitruka, I.; Evans, J.; Mohammad, R.; Tchekneva, E. E.; Dikov, M. M.; Khramtsov, V. V. Interstitial Inorganic Phosphate as a Tumor Microenvironment Marker for Tumor Progression. *Scientific Reports* **2017**, *7*, DOI: 10.1038/srep41233.

(86) Bredholt, G.; Mannelqvist, M.; Stefansson, I. M.; Birkeland, E.; Bø, T. H.; Øyan, A. M.; Trovik, J.; Kalland, K.-H.; Jonassen, I.; Salvesen, H. B.; Wik, E.; Akslen, L. A. Tumor necrosis is an important hallmark of aggressive endometrial cancer and associates with hypoxia, angiogenesis and inflammation responses. *Oncotarget* **2015**, *6*, DOI: 10.18632/oncotarget.5344.

(87) Edinger, A. L.; Thompson, C. B. Death by design: apoptosis, necrosis and autophagy. *Current Opinion in Cell Biology* **2004**, *16*, 663–669.

(88) Sambade, M. J.; Peters, E. C.; Thomas, N. E.; Kaufmann, W. K.; Kimple, R. J.; Shields, J. M. Melanoma cells show a heterogeneous range of sensitivity to ionizing radiation and are radiosensitized by inhibition of B-RAF with PLX-4032. *Radiotherapy and Oncology* **2011**, *98*, 394–399.

(89) Reddy, K.; Damek, D.; Gaspar, L. E.; Ney, D.; Waziri, A.; Lillehei, K.; Stuhr, K.; Kavanagh, B. D.; Chen, C. Phase II Trial of Hypofractionated IMRT With Temozolomide for Patients With Newly Diagnosed Glioblastoma Multiforme. *International Journal of Radiation Oncology*Biology*Physics* **2012**, *84*, 655–660.

(90) Perry, J. R. et al. A phase III randomized controlled trial of short-course radiotherapy with or without concomitant and adjuvant temozolomide in elderly patients with glioblastoma (CCTG CE.6, EORTC 26062-22061, TROG 08.02, NCT00482677). *Journal of Clinical Oncology* **2016**, *34*, LBA2–LBA2.

(91) Debus, J.; Wuendrich, M.; Pirzkall, A.; Hoess, A.; Schlegel, W.; Zuna, I.; Engenhart-Cabillic, R.; Wannenmacher, M. High Efficacy of Fractionated Stereotactic Radiotherapy of Large Base-of-Skull Meningiomas: Long-Term Results. *Journal of Clinical Oncology* **2001**, *19*, 3547–3553.

(92) Park, H. J.; Kang, H.-C.; Kim, I. H.; Park, S.-H.; Kim, D. G.; Park, C.-K.; Paek, S. H.; Jung, H.-W. The role of adjuvant radiotherapy in atypical meningioma. *Journal of Neuro-Oncology* **2013**, *115*, 241–247.

(93) Burmeister, B. H.; Smithers, B. M.; Burmeister, E.; Baumann, K.; Davis, S.; Krawitz, H.; Johnson, C.; Spry, N. A prospective phase II study of adjuvant postoperative radiation therapy following nodal surgery in malignant melanoma–Trans Tasman Radiation Oncology Group (TROG) Study 96.06. *Radiotherapy and Oncology* **2006**, *81*, 136–142.

(94) Stevens, G.; Thompson, J. F.; Firth, I.; O'Brien, C. J.; McCarthy, W. H.; Quinn, M. J. Locally advanced melanoma. *Cancer* **2000**, *88*, 88–94.

(95) Jones, W. G.; Fossa, S. D.; Mead, G. M.; Roberts, J. T.; Sokal, M.; Horwich, A.; Stenning, S. P. Randomized Trial of 30 Versus 20 Gy in the Adjuvant Treatment of Stage I Testicular Seminoma: A Report on Medical Research Council Trial TE18, European Organisation for the Research and Treatment of Cancer Trial 30942 (ISRCTN18525328). *Journal of Clinical Oncology* **2005**, *23*, 1200–1208.

(96) Oliver, R.; Mason, M.; Mead, G.; von der Maase, H.; Rustin, G.; Joffe, J.; de Wit, R.; Aass, N.; Graham, J.; Coleman, R.; Kirk, S.; Stenning, S. Radiotherapy versus single-dose carboplatin in adjuvant treatment of stage I seminoma: a randomised trial. *The Lancet* **2005**, *366*, 293–300.

(97) Ceha, H. M.; van Tienhoven, G.; Gouma, D. J.; Veenhof, C. H. N.; Schneider, C. J.; Rauws, E. A. J.; Phoa, S. S. K. S.; González, D. G. Feasibility and efficacy of high dose conformal radiotherapy for patients with locally advanced pancreatic carcinoma. *Cancer* **2000**, *89*, 2222–2229.

(98) Komaki, R.; Wadler, S.; Peters, T.; Byhardt, R. W.; Order, S.; Gallagher, M. J.; Herskovic, A.; Pederson, J. High-dose local irradiation plus prophylactic hepatic irradiation and chemotherapy for inoperable adenocarcinoma of the pancreas. A preliminary report of a multi-institutional trial (radiation therapy oncology group protocol 8801). *Cancer* **1992**, *69*, 2807–2812.

(99) Oliva, C. R.; Nozell, S. E.; Diers, A.; McClugage, S. G.; Sarkaria, J. N.; Markert, J. M.; Darley-Usmar, V. M.; Bailey, S. M.; Gillespie, G. Y.; Landar, A.; Griguer, C. E. Acquisition of Temozolomide Chemoresistance in Gliomas Leads to Remodeling of Mitochondrial Electron Transport Chain*. *Journal of Biological Chemistry* **2010**, *285*, 39759–39767.

(100) Qazi, M.; Vora, P.; Venugopal, C.; Sidhu, S.; Moffat, J.; Swanton, C.; Singh, S. Intratumoral heterogeneity: pathways to treatment resistance and relapse in human glioblastoma. *Annals of Oncology* **2017**, *28*, 1448–1456.

(101) Kazmi, F.; Soon, Y. Y.; Leong, Y. H.; Koh, W. Y.; Vellayappan, B. Re-irradiation for recurrent glioblastoma (GBM): a systematic review and meta-analysis. *Journal of Neuro-Oncology* **2018**, *142*, 79–90.

(102) Soyuer, S.; Chang, E. L.; Selek, U.; Shi, W.; Maor, M. H.; DeMonte, F. Radiotherapy after surgery for benign cerebral meningioma. *Radiotherapy and Oncology* **2004**, *71*, 85–90.

(103) Seshacharyulu, P.; Baine, M. J.; Souchek, J. J.; Menning, M.; Kaur, S.; Yan, Y.; Ouellette, M. M.; Jain, M.; Lin, C.; Batra, S. K. Biological determinants of radioresistance and their remediation in pancreatic cancer. *Biochimica et Biophysica Acta (BBA) - Reviews on Cancer* **2017**, *1868*, 69–92.

(104) Häkkinenm, A.-M.; Laasonen, A.; Linnainmaa, K.; Mattson, K.; Pyrhonen, S. Radiosensitivity of Mesothelioma Cell Lines. *Acta Oncologica* **1996**, *35*, 451–456.

(105) Rofstad, E. K. Radiation Biology of Malignant Melanoma. *Acta Radiologica: Oncology* **1986**, *25*, 1–10.

(106) Stevens, G.; McKay, M. J. Dispelling the myths surrounding radiotherapy for treatment of cutaneous melanoma. *The Lancet Oncology* **2006**, *7*, 575–583.

(107) Noonan, F. P.; Zaidi, M. R.; Wolnicka-Glubisz, A.; Anver, M. R.; Bahn, J.; Wielgus, A.; Cadet, J.; Douki, T.; Mouret, S.; Tucker, M. A.; Popratiloff, A.; Merlino, G.; Fabo, E. C. D. Melanoma induction by ultraviolet A but not ultraviolet B radiation requires melanin pigment. *Nature Communications* **2012**, *3*, DOI: 10.1038/ncomms1893.

(108) Grossi, G. F.; Durante, M.; Gialanella, G.; Pugliese, M.; Mosse, I. Effects of melanin on high- and low- linear energy transfer (LET) radiation response of human epithelial cells. *Radiation and Environmental Biophysics* **1998**, *37*, 63–67.

(109) Marshall, E.; Matthews, J.; Shaw, J.; Nixon, J.; Tumewu, P.; Finlay, G.; Holdaway, K.; Baguley, B. Radiosensitivity of new and established human melanoma cell lines: Comparison of [3H]thymidine incorporation and soft agar clonogenic assays. *European Journal of Cancer* **1994**, *30*, 1370–1376.

(110) Goldberg, H.; Klaassen, Z.; Chandrasekar, T.; Fleshner, N.; Hamilton, R. J.; Jewett, M. A. Germ Cell Testicular Tumors—Contemporary Diagnosis, Staging and Management of Localized and Advanced disease. *Urology* **2019**, *125*, 8–19.

(111) Bobba, V. S.; Mittal, B. B.; Hoover, S. V.; Kepka, A. Classical and anaplastic seminoma: difference in survival. *Radiology* **1988**, *167*, 849–852.

(112) Warde, P.; Specht, L.; Horwich, A.; Oliver, T.; Panzarella, T.; Gospodarowicz, M.; von der Maase, H. Prognostic Factors for Relapse in Stage I Seminoma Managed by Surveillance: A Pooled Analysis. *Journal of Clinical Oncology* **2002**, *20*, 4448–4452.

(113) Zengerling, F.; Kunath, F.; Jensen, K.; Ruf, C.; Schmidt, S.; Spek, A. Prognostic factors for tumor recurrence in patients with clinical stage I seminoma undergoing surveillance—A systematic review. *Urologic Oncology: Seminars and Original Investigations* **2018**, *36*, 448–458.

(114) Stutzman, R. E.; McLeod, D. G. Radiation Therapy: A Primary Treatment Modality for Seminoma. *Urologic Clinics of North America* **1980**, *7*, 757–764.

(115) Percarpio, B.; Clements, J. C.; McLeod, D. G.; Sorgen, S. D.; Cardinale, F. S. Anaplastic seminoma: An analysis of 77 patients. *Cancer* **1979**, *43*, 2510–2513.

(116) Suzuki, T.; Sasano, H.; Aoki, H.; Nagura, H.; Sasano, N.; Sano, T.; Saito, M.; Watanuki, T.; Kato, H.; Aizawa, S. Immunohistochemical comparison between anaplastic seminoma and typical seminoma. *Pathology International* **1993**, *43*, 751–757.

(117) Kersh, C. R.; Constable, W. C.; Hahn, S. S.; Spaulding, C. A.; Eisert, D. R.; Jenrette, J. M.; Marks, R. D.; Grayson, J. Primary malignant extragonadal germ cell tumors. An analysis of the effect of radiotherapy. *Cancer* **1990**, *65*, 2681–2685.

(118) Daugaard, G.; Petersen, P. M.; Rorth, M. Surveillance in stage I testicular cancer. *APMIS* **2003**, *111*, 76–85.

(119) Pierorazio, P. M.; Cheaib, J. G.; Patel, H. D.; Gupta, M.; Sharma, R.; Zhang, A.; Tema, G.; Bass, E. B. Comparative Effectiveness of Surveillance, Primary Chemotherapy, Radiotherapy and Retroperitoneal Lymph Node Dissection for the Management of Early Stage Testicular Germ Cell Tumors: A Systematic Review. *Journal of Urology* **2021**, *205*, 370–382.

(120) Archibald, F. S.; Fridovich, I. The scavenging of superoxide radical by manganous complexes: In vitro. *Archives of Biochemistry and Biophysics* **1982**, *214*, 452–463.

(121) Barnese, K.; Gralla, E. B.; Cabelli, D. E.; Valentine, J. S. Manganous Phosphate Acts as a Superoxide Dismutase. *Journal of the American Chemical Society* **2008**, *130*, 4604–4606.

(122) Stadtman, E. R.; Berlett, B. S.; Chock, P. B. Manganese-dependent disproportionation of hydrogen peroxide in bicarbonate buffer. *Proceedings of the National Academy of Sciences* **1990**, *87*, 384–388.

(123) Berlett, B. S.; Chock, P. B.; Yim, M. B.; Stadtman, E. R. Manganese(II) catalyzes the bicarbonate-dependent oxidation of amino acids by hydrogen peroxide and the amino acid-facilitated dismutation of hydrogen peroxide. *Proceedings of the National Academy of Sciences* **1990**, *87*, 389–393.

(124) Anjem, A.; Varghese, S.; Imlay, J. A. Manganese import is a key element of the OxyR response to hydrogen peroxide inEscherichia coli. *Molecular Microbiology* **2009**, *72*, 844–858.

(125) Daly, M. J. Accumulation of Mn(II) in Deinococcus radiodurans Facilitates Gamma-Radiation Resistance. *Science* **2004**, *306*, 1025–1028.

(126) Daly, M. J.; Gaidamakova, E. K.; Matrosova, V. Y.; Kiang, J. G.; Fukumoto, R.; Lee, D.-Y.; Wehr, N. B.; Viteri, G. A.; Berlett, B. S.; Levine, R. L. Small-Molecule Antioxidant Proteome-Shields in Deinococcus radiodurans. *PLoS ONE* **2010**, *5*, ed. by Otto, M., e12570.

(127) Stadtman, E. R.; Levine, R. L. Free radical-mediated oxidation of free amino acids and amino acid residues in proteins. *Amino Acids* **2003**, *25*, 207–218.

(128) Culotta, V. C.; Daly, M. J. Manganese Complexes: Diverse Metabolic Routes to Oxidative Stress Resistance in Prokaryotes and Yeast. *Antioxidants & Redox Signaling* **2013**, *19*, 933–944.

(129) Knobloch, B.; Linert, W.; Sigel, H. Metal ion-binding properties of (N3)-deprotonated uridine, thymidine, and related pyrimidine nucleosides in aqueous solution. *Proceedings of the National Academy of Sciences* **2005**, *102*, 7459–7464.

(130) Gupta, P.; Gayen, M.; Smith, J. T.; Gaidamakova, E. K.; Matrosova, V. Y.; Grichenko, O.; Knollmann-Ritschel, B.; Daly, M. J.; Kiang, J. G.; Maheshwari, R. K. MDP: A Deinococcus Mn2-Decapeptide Complex Protects Mice from Ionizing Radiation. *PLOS ONE* **2016**, *11*, ed. by Fornace, A. J., e0160575.

(131) Berlett, B. S.; Levine, R. L. Designing antioxidant peptides. *Redox Report* **2014**, *19*, 80–86.

(132) Wang, S.; Westmoreland, T. D. Correlation of Relaxivity with Coordination Number in Six-, Seven-, and Eight-Coordinate Mn(II) Complexes of Pendant-Arm Cyclen Derivatives. *Inorganic Chemistry* **2009**, *48*, 719–727.

(133) Marklund, S. L.; Westman, N. G.; Roos, G.; Carlsson, J.; Roos, G.; Carlsson, J. Radiation Resistance and the CuZn Superoxide Dismutase, Mn Superoxide Dismutase, Catalase, and Glutathione Peroxidase Activities of Seven Human Cell Lines. *Radiation Research* **1984**, *100*, 115.

(134) Marklund, S.; Beckman, G.; Stigbrand, T. A Comparison between the Common Type and a Rare Genetic Variant of Human Cupro-Zinc Superoxide Dismutase. *European Journal of Biochemistry* **1976**, *65*, 415–422.

(135) Sharma, A. et al. Across the tree of life, radiation resistance is governed by antioxidant Mn2, gauged by paramagnetic resonance. *Proceedings of the National Academy of Sciences* **2017**, *114*, E9253–E9260.

(136) Buxton, G. V.; Greenstock, C. L.; Helman, W. P.; Ross, A. B. Critical Review of rate constants for reactions of hydrated electrons, hydrogen atoms and hydroxyl radicals (·OH/·O- in Aqueous Solution. *Journal of Physical and Chemical Reference Data* **1988**, *17*, 513–886.

(137) Gray, B.; Carmichael, A. J. Kinetics of superoxide scavenging by dismutase enzymes and manganese mimics determined by electron spin resonance. *The Biochemical journal* **1992**, *281 (Pt 3)*, 795–802.

(138) Legrini, O.; Oliveros, E.; Braun, A. M. Photochemical processes for water treatment. *Chemical Reviews* **1993**, *93*, 671–698.

(139) Takeda, K.; Fujisawa, K.; Nojima, H.; Kato, R.; Ueki, R.; Sakugawa, H. Hydroxyl radical generation with a high power ultraviolet light emitting diode (UV-LED) and application for determination of hydroxyl radical reaction rate constants. *Journal of Photochemistry and Photobiology A: Chemistry* **2017**, *340*, 8–14.

(140) Gudkov, S. V.; Karp, O. E.; Garmash, S. A.; Ivanov, V. E.; Chernikov, A. V.; Manokhin, A. A.; Astashev, M. E.; Iaguzhinskiĭ, L. S.; Bruskov, V. I. Generation of reactive oxygen species in water under exposure of visible or infrared irradiation at absorption band of molecular oxygen. *Biofizika* **2012**, *57*, 5–13.

(141) Khodaveisi, J.; Banejad, H.; Afkhami, A.; Olyaie, E.; Lashgari, S.; Dashti, R. Synthesis of calcium peroxide nanoparticles as an innovative reagent for in situ chemical oxidation. *Journal of Hazardous Materials* **2011**, *192*, 1437–1440.

(142) Stadtman, E. R.; Berlett, B. S. Fenton chemistry. Amino acid oxidation. *Journal of Biological Chemistry* **1991**, *266*, 17201–17211.

(143) Thomas, C.; Mackey, M. M.; Diaz, A. A.; Cox, D. P. Hydroxyl radical is produced via the Fenton reaction in submitochondrial particles under oxidative stress: implications for diseases associated with iron accumulation. *Redox Report* **2009**, *14*, 102–108.

(144) McCord, J. M.; Fridovich, I. The reduction of cytochrome c by milk xanthine oxidase. *The Journal of biological chemistry* **1968**, *243*, 5753–5760.

(145) Marselli, B.; Garcia-Gomez, J.; Michaud, P.-A.; Rodrigo, M. A.; Comninellis, C. Electrogeneration of Hydroxyl Radicals on Boron-Doped Diamond Electrodes. *Journal of The Electrochemical Society* **2003**, *150*, D79.

(146) Chen, X.; Chen, G.; Gao, F.; Yue, P. L. High-Performance Ti/BDD Electrodes for Pollutant Oxidation. *Environmental Science & Technology* **2003**, *37*, 5021–5026.

(147) Michaud, P.-A.; Panizza, M.; Ouattara, L.; Diaco, T.; Foti, G.; Comninellis, C. Electrochemical oxidation of water on synthetic boron-doped diamond thin film anodes. *Journal of Applied Electrochemistry* **2003**, *33*, 151–154.

(148) Macpherson, J. V. A practical guide to using boron doped diamond in electrochemical research. *Physical Chemistry Chemical Physics* **2015**, *17*, 2935–2949.

(149) Jiang, Y.; Ni, P.; Chen, C.; Lu, Y.; Yang, P.; Kong, B.; Fisher, A.; Wang, X. Selective Electrochemical H2 O2 Production through Two-Electron Oxygen Electrochemistry. *Advanced Energy Materials* **2018**, 1801909.

(150) Yamanaka, I.; Onizawa, T.; Takenaka, S.; Otsuka, K. Direct and Continuous Production of Hydrogen Peroxide with 93 % Selectivity Using a Fuel-Cell System. *Angewandte Chemie International Edition* **2003**, *42*, 3653–3655.

(151) Yamanaka, I.; Hashimoto, T.; Ichihashi, R.; Otsuka, K. Direct synthesis of H2O2 acid solutions on carbon cathode prepared from activated carbon and vapor-growing-carbon-fiber by a H2/O2 fuel cell. *Electrochimica Acta* **2008**, *53*, 4824–4832.

(152) Iglesias, D.; Giuliani, A.; Melchionna, M.; Marchesan, S.; Criado, A.; Nasi, L.; Bevilacqua, M.; Tavagnacco, C.; Vizza, F.; Prato, M.; Fornasiero, P. N-Doped Graphitized Carbon Nanohorns as a Forefront Electrocatalyst in Highly Selective O 2 Reduction to H 2 O 2. *Chem* **2018**, *4*, 106–123.

(153) Choi, C. H.; Kim, M.; Kwon, H. C.; Cho, S. J.; Yun, S.; Kim, H.-T.; Mayrhofer, K. J. J.; Kim, H.; Choi, M. Tuning selectivity of electrochemical reactions by atomically dispersed platinum catalyst. *Nature Communications* **2016**, *7*, 10922.

(154) Amorati, R.; Valgimigli, L. Advantages and limitations of common testing methods for antioxidants. *Free Radical Research* **2015**, *49*, 633–649.

(155) Prior, R. L.; Wu, X.; Schaich, K. Standardized Methods for the Determination of Antioxidant Capacity and Phenolics in Foods and Dietary Supplements. *Journal of Agricultural and Food Chemistry* **2005**, *53*, 4290–4302.

(156) Li, S.; Timoshkin, I. V.; Maclean, M.; Macgregor, S. J.; Wilson, M. P.; Given, M. J.; Wang, T.; Anderson, J. G. Fluorescence detection of hydroxyl radicals in water produced by atmospheric pulsed discharges. *IEEE Transactions on Dielectrics and Electrical Insulation* **2015**, *22*, 1856–1865.

(157) Choi, H. S.; Kim, J. W.; Cha, Y.-N.; Kim, C. A Quantitative Nitroblue Tetrazolium Assay for Determining Intracellular Superoxide Anion Production in Phagocytic Cells. *Journal of Immunoassay and Immunochemistry* **2006**, *27*, 31–44.

(158) Sutherland, M. W.; Learmonth, B. A. The Tetrazolium Dyes MTS and XTT Provide New Quantitative Assays for Superoxide and Superoxide Dismutase. *Free Radical Research* **1997**, *27*, 283–289.

(159) Faulkner, K.; Fridovich, I. Luminol and lucigenin as detectors for O2ṡ-. *Free Radical Biology and Medicine* **1993**, *15*, 447–451.

(160) Oosthuizen, M. M.; Engelbrecht, M. E.; Lambrechts, H.; Greyling, D.; Levy, R. D. The effect of pH on chemiluminescence of different probes exposed to superoxide and singlet oxygen generators. *Journal of bioluminescence and chemiluminescence* **1997**, *12*, 277–284.

(161) Kawano, T.; Pinontoan, R.; Hosoya, H.; Muto, S. Monoamine-dependent Production of Reactive Oxygen Species Catalyzed by Pseudoperoxidase Activity of Human Hemoglobin. *Bioscience, Biotechnology, and Biochemistry* **2002**, *66*, 1224–1232.

(162) Rodríguez-López, J. N.; Lowe, D. J.; Hernández-Ruiz, J.; Hiner, A. N. P.; García-Cánovas, F.; Thorneley, R. N. F. Mechanism of Reaction of Hydrogen Peroxide with Horseradish Peroxidase: Identification of Intermediates in the Catalytic Cycle. *Journal of the American Chemical Society* **2001**, DOI: 10.1021/ja011853.

(163) Manning, P.; McNeil, C. J. Electrochemical and optical sensing of reactive oxygen species: pathway to an integrated intracellular and extracellular measurement platform. *Biochemical Society Transactions* **2011**, *39*, 1288–1292.

(164) Eddowes, M. J.; Hill, H. A. O. Novel method for the investigation of the electrochemistry of metalloproteins: cytochrome c. *Journal of the Chemical Society, Chemical Communications* **1977**, 771b.

(165) Manning, P.; McNeil, C. J.; Cooper, J. M.; Hillhouse, E. W. Direct, Real-Time Sensing of Free Radical Production by Activated Human Glioblastoma Cells. *Free Radical Biology and Medicine* **1998**, *24*, 1304–1309.

(166) Balamurugan, M.; Santharaman, P.; Madasamy, T.; Rajesh, S.; Sethy, N. K.; Bhargava, K.; Kotamraju, S.; Karunakaran, C. Recent trends in electrochemical biosensors of superoxide dismutases. *Biosensors and Bioelectronics* **2018**, *116*, 89–99.

(167) Lvovich, V.; Scheeline, A. Amperometric Sensors for Simultaneous Superoxide and Hydrogen Peroxide Detection. *Analytical Chemistry* **1997**, *69*, 454–462.

(168) Karyakin, A. A.; Puganova, E. A.; Budashov, I. A.; Kurochkin, I. N.; Karyakina, E. E.; Levchenko, V. A.; Matveyenko, V. N.; Varfolomeyev, S. D. Prussian Blue Based Nanoelectrode Arrays for H2O2Detection. *Analytical Chemistry* **2004**, *76*, 474–478.

(169) Zehavi, D.; Rabani, J. Oxidation of aqueous bromide ions by hydroxyl radicals. Pulse radiolytic investigation. *The Journal of Physical Chemistry* **1972**, *76*, 312–319.

(170) Klein, G. W.; Bhatia, K.; Madhavan, V.; Schuler, R. H. Reaction of hydroxyl radicals with benzoic acid. Isomer distribution in the radical intermediates. *The Journal of Physical Chemistry* **1975**, *79*, 1767–1774.

(171) Ungnade, H. E.; Lamb, R. W. The Absorption Spectra of Benzoic Acid and Esters. *Journal of the American Chemical Society* **1952**, *74*, 3789–3794.

(172) Miles, C. I.; Schenk, G. H. Fluorescence of acetylsalicylic acid in solution and its measurement in presence of salicylic acid. *Analytical Chemistry* **1970**, *42*, 656–659.

(173) Pou, S.; Huang, Y. I.; Bhan, A.; Bhadti, V. S.; Hosmane, R. S.; Wu, S. Y.; Cao, G. L.; Rosen, G. M. A Fluorophore-Containing Nitroxide as a Probe to Detect Superoxide and Hydroxyl Radical Generated by Stimulated Neutrophils. *Analytical Biochemistry* **1993**, *212*, 85–90.

(174) Zhou, M.; Diwu, Z.; Panchuk-Voloshina, N.; Haugland, R. P. A Stable Nonfluorescent Derivative of Resorufin for the Fluorometric Determination of Trace Hydrogen Peroxide: Applications in Detecting the Activity of Phagocyte NADPH Oxidase and Other Oxidases. *Analytical Biochemistry* **1997**, *253*, 162–168.

(175) Zepp, R. G.; Skurlatov, Y. I.; Ritmiller, L. F. Effects of aquatic humic substances on analysis for hydrogen peroxide using peroxidase-catalyzed oxidations of triarylmethanes orp-hydroxyphenylacetic acid. *Environmental Technology Letters* **1988**, *9*, 287–298.

(176) Keston, A. S.; Brandt, R. THE FLUOROMETRIC ANALYSIS OF ULTRAMICRO QUANTITIES OF HYDROGEN PEROXIDE. *Analytical biochemistry* **1965**, *11*, 1–5.

(177) Guilbault, G. G.; Brignac, P. J.; Zimmer, M. Homovanillic acid as a fluorometric substrate for oxidative enzymes. Analytical applications of the peroxidase, glucose oxidase, and xanthine oxidase systems. *Analytical Chemistry* **1968**, *40*, 190–196.

(178) Aandreae, W. A. A sensitive method for the estimation of hydrogen peroxide in biological materials. *Nature* **1955**, *175*, 859–860.

(179) Florence, T. M.; Stauber, J. L.; Mann, K. J. The reaction of copper-2,9-dimethyl-1,10-phenanthroline with hydrogen peroxide. *Journal of Inorganic Biochemistry* **1985**, *24*, 243–254.

(180) Frederiks, W. M.; Bosch, K. S.; Van den Munckhof, R. J. Extinction coefficient of polymerized diaminobenzidine complexed with cobalt as final reaction product of histochemical oxidase reactions. *Histochemistry and cell biology* **1995**, *104*, 473–477.

(181) Okimoto, Y.; Watanabe, A.; Niki, E.; Yamashita, T.; Noguchi, N. A novel fluorescent probe diphenyl-1-pyrenylphosphine to follow lipid peroxidation in cell membranes. *FEBS Letters* **2000**, *474*, 137–140.

(182) Zielonka, J.; Kalyanaraman, B. Hydroethidine- and MitoSOX-derived red fluorescence is not a reliable indicator of intracellular superoxide formation: Another inconvenient truth. *Free Radical Biology and Medicine* **2010**, *48*, 983–1001.

(183) Waldron, K. J.; Rutherford, J. C.; Ford, D.; Robinson, N. J. Metalloproteins and metal sensing. *Nature* **2009**, *460*, 823–830.

(184) Hare, D. J. et al. An iron–dopamine index predicts risk of parkinsonian neurodegeneration in the substantia nigra pars compacta. *Chemical Science* **2014**, *5*, 2160–2169.

(185) Managh, A. J.; Hutchinson, R. W.; Riquelme, P.; Broichhausen, C.; Wege, A. K.; Ritter, U.; Ahrens, N.; Koehl, G. E.; Walter, L.; Florian, C.; Schlitt, H. J.; Reid, H. J.; Geissler, E. K.; Sharp, B. L.; Hutchinson, J. A. Laser Ablation–Inductively Coupled Plasma Mass Spectrometry: An Emerging Technology for Detecting Rare Cells in Tissue Sections. *The Journal of Immunology* **2014**, *193*, 2600–2608.

(186) Austin, C.; Smith, T. M.; Bradman, A.; Hinde, K.; Joannes-Boyau, R.; Bishop, D.; Hare, D. J.; Doble, P.; Eskenazi, B.; Arora, M. Barium distributions in teeth reveal early-life dietary transitions in primates. *Nature* **2013**, *498*, 216–219.

(187) Hare, D. J.; New, E. J.; de Jonge, M. D.; McColl, G. Imaging metals in biology: balancing sensitivity, selectivity and spatial resolution. *Chemical Society Reviews* **2015**, *44*, 5941–5958.

(188) Gholap, D. S.; Izmer, A.; Samber, B. D.; van Elteren, J. T.; Šelih, V. S.; Evens, R.; Schamphelaere, K. D.; Janssen, C.; Balcaen, L.; Lindemann, I.; Vincze, L.; Vanhaecke, F. Comparison of laser ablation-inductively coupled plasma-mass spectrometry and micro-X-ray fluorescence spectrometry for elemental imaging in Daphnia magna. *Analytica Chimica Acta* **2010**, *664*, 19–26.

(189) Passarelli, M. K.; Winograd, N. Lipid imaging with time-of-flight secondary ion mass spectrometry (ToF-SIMS). *Biochimica et Biophysica Acta (BBA) - Molecular and Cell Biology of Lipids* **2011**, *1811*, 976–990.

(190) Gray, A. L. Solid sample introduction by laser ablation for inductively coupled plasma source mass spectrometry. *The Analyst* **1985**, *110*, 551.

(191) Wang, S.; Brown, R.; Gray, D. J. Application of Laser Ablation-ICPMS to the Spatially Resolved Micro-Analysis of Biological Tissue. *Applied Spectroscopy* **1994**, *48*, 1321–1325.

(192) Sylvester, P. J.; Jackson, S. E. A Brief History of Laser Ablation Inductively Coupled Plasma Mass Spectrometry (LA–ICP–MS). *Elements* **2016**, *12*, 307–310.

(193) Yoo, J. H.; Jeong, S. H.; Mao, X. L.; Greif, R.; Russo, R. E. Evidence for phase-explosion and generation of large particles during high power nanosecond laser ablation of silicon. *Applied Physics Letters* **2000**, *76*, 783–785.

(194) Fernández, B.; Claverie, F.; Pécheyran, C.; Donard, O. F. X.; Claverie, F. Direct analysis of solid samples by fs-LA-ICP-MS. *TrAC Trends in Analytical Chemistry* **2007**, *26*, 951–966.

(195) Lear, J.; Hare, D. J.; Fryer, F.; Adlard, P. A.; Finkelstein, D. I.; Doble, P. A. High-Resolution Elemental Bioimaging of Ca, Mn, Fe, Co, Cu, and Zn Employing LA-ICP-MS and Hydrogen Reaction Gas. *Analytical Chemistry* **2012**, *84*, 6707–6714.

(196) Van Elteren, J. T.; Šelih, V. S.; Šala, M.; Malderen, S. J. M. V.; Vanhaecke, F. Imaging Artifacts in Continuous Scanning 2D LA-ICPMS Imaging Due to Nonsynchronization Issues. *Analytical Chemistry* **2018**, *90*, 2896–2901.

(197) Bishop, D. P.; Clases, D.; Fryer, F.; Williams, E.; Wilkins, S.; Hare, D. J.; Cole, N.; Karst, U.; Doble, P. A. Elemental bio-imaging using laser ablation-triple quadrupole-ICP-MS. *Journal of Analytical Atomic Spectrometry* **2016**, *31*, 197–202.

(198) May, T. W.; Wiedmeyer, R. H. A table of polyatomic interferences in ICP-MS. *Atomic Spectroscopy* **1998**, *19*, 150–155.

(199) Giesen, C.; Mairinger, T.; Khoury, L.; Waentig, L.; Jakubowski, N.; Panne, U. Multiplexed Immunohistochemical Detection of Tumor Markers in Breast Cancer Tissue Using Laser Ablation Inductively Coupled Plasma Mass Spectrometry. *Analytical Chemistry* **2011**, *83*, 8177–8183.

(200) Giesen, C.; Wang, H. A. O.; Schapiro, D.; Zivanovic, N.; Jacobs, A.; Hattendorf, B.; Schüffler, P. J.; Grolimund, D.; Buhmann, J. M.; Brandt, S.; Varga, Z.; Wild, P. J.; Günther, D.; Bodenmiller, B. Highly multiplexed imaging of tumor tissues with subcellular resolution by mass cytometry. *Nature Methods* **2014**, *11*, 417–422.

(201) Weiskirchen, R.; Weiskirchen, S.; Kim, P.; Winkler, R. Software solutions for evaluation and visualization of laser ablation inductively coupled plasma mass spectrometry imaging (LA-ICP-MSI) data: a short overview. *Journal of Cheminformatics* **2019**, *11*, DOI: 10.1186/s13321-019-0338-7.

(202) Lockwood, T. E.; Westerhausen, M. T.; Doble, P. A. Pew2: Open-Source Imaging Software for Laser Ablation–Inductively Coupled Plasma–Mass Spectrometry. *Analytical Chemistry* **2021**, *93*, 10418–10423.

(203) López-Fernández, H.; de S. Pessôa, G.; Arruda, M. A. Z.; Capelo-Martínez, J. L.; Fdez-Riverola, F.; Glez-Peña, D.; Reboiro-Jato, M. LA-iMageS: a software for elemental distribution bioimaging using LA–ICP–MS data. *Journal of Cheminformatics* **2016**, *8*, DOI: 10.1186/s13321-016-0178-7.

(204) Feldmann, J.; Kindness, A.; Ek, P. Laser ablation of soft tissue using a cryogenically cooled ablation cell. *Journal of Analytical Atomic Spectrometry* **2002**, *17*, 813–818.

(205) Austin, C.; Hare, D.; Rawling, T.; McDonagh, A. M.; Doble, P. Quantification method for elemental bio-imaging by LA-ICP-MS using metal spiked PMMA films. *Journal of Analytical Atomic Spectrometry* **2010**, *25*, 722.

(206) Hare, D.; Burger, F.; Austin, C.; Fryer, F.; Grimm, R.; Reedy, B.; Scolyer, R. A.; Thompson, J. F.; Doble, P. Elemental bio-imaging of melanoma in lymph node biopsies. *The Analyst* **2009**, *134*, 450–453.

(207) Hare, D. J.; George, J. L.; Grimm, R.; Wilkins, S.; Adlard, P. A.; Cherny, R. A.; Bush, A. I.; Finkelstein, D. I.; Doble, P. Three-dimensional elemental bio-imaging of Fe, Zn, Cu, Mn and P in a 6-hydroxydopamine lesioned mouse brain. *Metallomics* **2010**, *2*, 745.

(208) Hare, D. J.; Lear, J.; Bishop, D.; Beavis, A.; Doble, P. A. Protocol for production of matrix-matched brain tissue standards for imaging by laser ablation-inductively coupled plasma-mass spectrometry. *Analytical Methods* **2013**, *5*, 1915.

(209) Reifschneider, O.; Wentker, K. S.; Strobel, K.; Schmidt, R.; Masthoff, M.; Sperling, M.; Faber, C.; Karst, U. Elemental Bioimaging of Thulium in Mouse Tissues by Laser Ablation-ICPMS as a Complementary Method to Heteronuclear Proton Magnetic Resonance Imaging for Cell Tracking Experiments. *Analytical Chemistry* **2015**, *87*, 4225–4230.

(210) Niehoff, A.-C.; Grünebaum, J.; Moosmann, A.; Mulac, D.; Söbbing, J.; Niehaus, R.; Buchholz, R.; Kröger, S.; Wiehe, A.; Wagner, S.; Sperling, M.; von Briesen, H.; Langer, K.; Karst, U. Quantitative bioimaging of platinum group elements in tumor spheroids. *Analytica Chimica Acta* **2016**, *938*, 106–113.

(211) Stärk, H.-J.; Wennrich, R. A new approach for calibration of laser ablation inductively coupled plasma mass spectrometry using thin layers of spiked agarose gels as references. *Analytical and Bioanalytical Chemistry* **2010**, *399*, 2211–2217.

(212) Šala, M.; Šelih, V. S.; van Elteren, J. T. Gelatin gels as multi-element calibration standards in LA-ICP-MS bioimaging: fabrication of homogeneous standards and microhomogeneity testing. *The Analyst* **2017**, *142*, 3356–3359.

(213) Hare, D.; Reedy, B.; Grimm, R.; Wilkins, S.; Volitakis, I.; George, J. L.; Cherny, R. A.; Bush, A. I.; Finkelstein, D. I.; Doble, P. Quantitative elemental bio-imaging of Mn, Fe, Cu and Zn in 6-hydroxydopamine induced Parkinsonism mouse models. *Metallomics* **2009**, *1*, 53–58.

(214) Arora, M.; Hare, D.; Austin, C.; Smith, D. R.; Doble, P. Spatial distribution of manganese in enamel and coronal dentine of human primary teeth. *Science of The Total Environment* **2011**, *409*, 1315–1319.

(215) Sela, H.; Karpas, Z.; Cohen, H.; Zakon, Y.; Zeiri, Y. Preparation of stable standards of biological tissues for laser ablation analysis. *International Journal of Mass Spectrometry* **2011**, *307*, 142–148.

(216) Matusch, A.; Depboylu, C.; Palm, C.; Wu, B.; Höglinger, G. U.; Schäfer, M. K. H.; Becker, J. S. Cerebral bioimaging of Cu, Fe, Zn, and Mn in the MPTP mouse model of Parkinson's disease using laser ablation inductively coupled plasma mass spectrometry (LA-ICP-MS). *Journal of the American Society for Mass Spectrometry* **2010**, *21*, 161–171.

(217) Fhlaithearta, S. N.; Fontanier, C.; Jorissen, F.; Mouret, A.; Dueñas-Bohórquez, A.; Anschutz, P.; Fricker, M. B.; Günther, D.; de Lange, G. J.; Reichart, G.-J. Manganese incorporation in living (stained) benthic foraminiferal shells: a bathymetric and in-sediment study in the Gulf of Lions (NW Mediterranean). *Biogeosciences* **2018**, *15*, 6315–6328.

(218) Costas-Rodríguez, M.; Acker, T. V.; Hastuti, A. A. M. B.; Devisscher, L.; Campenhout, S. V.; Vlierberghe, H. V.; Vanhaecke, F. Laser ablation-inductively coupled plasma-mass spectrometry for quantitative mapping of the copper distribution in liver tissue sections from mice with liver disease induced by common bile duct ligation. *Journal of Analytical Atomic Spectrometry* **2017**, *32*, 1805–1812.

(219) Schrieber, R.; Gareis, H., *Gelatine Handbook*; Wiley-VCH: 2007; 347 pp.

(220) Vecchione, R.; Pitingolo, G.; Falanga, A. P.; Guarnieri, D.; Netti, P. A. Confined Gelatin Dehydration as a Viable Route To Go Beyond Micromilling Resolution and Miniaturize Biological Assays. *ACS Applied Materials & Interfaces* **2016**, *8*, 12075–12081.

(221) Lockwood, T. E.; Westerhausen, M. T.; González de Vega, R.; Röhnelt, A.; Bishop, D. P.; Cole, N.; Doble, P. A.; Clases, D. Low background mould-prepared gelatine standards for reproducible quantification in elemental bio-imaging. *The Analyst* **2019**, *144*, 6881–6888.

(222) Becker, J. S.; Zoriy, M.; Matusch, A.; Wu, B.; Salber, D.; Palm, C.; Becker, J. S. Bioimaging of metals by laser ablation inductively coupled plasma mass spectrometry (LA-ICP-MS). *Mass Spectrometry Reviews* **2009**, *29*, n/a–n/a.

(223) Frick, D. A.; Günther, D. Fundamental studies on the ablation behaviour of carbon in LA-ICP-MS with respect to the suitability as internal standard. *Journal of Analytical Atomic Spectrometry* **2012**, *27*, 1294.

(224) Montalbetti, E.; Biscéré, T.; Ferrier-Pagès, C.; Houlbrèque, F.; Orlandi, I.; Forcella, M.; Galli, P.; Vai, M.; Seveso, D. Manganese Benefits Heat-Stressed Corals at the Cellular Level. *Frontiers in Marine Science* **2021**, *8*, DOI: 10.3389/fmars.2021.681119.

(225) Geertsen, V.; Barruet, E.; Gobeaux, F.; Lacour, J.-L.; Taché, O. Contribution to Accurate Spherical Gold Nanoparticle Size Determination by Single-Particle Inductively Coupled Mass Spectrometry: A Comparison with Small-Angle X-ray Scattering. *Analytical Chemistry* **2018**, *90*, 9742–9750.

(226) Meyer, S.; González de Vega, R.; Xu, X.; Du, Z.; Doble, P. A.; Clases, D. Characterization of Upconversion Nanoparticles by Single-Particle ICP-MS Employing a Quadrupole Mass Filter with Increased Bandpass. *Analytical Chemistry* **2020**, *92*, 15007–15016.

(227) Bandura, D. R.; Baranov, V. I.; Ornatsky, O. I.; Antonov, A.; Kinach, R.; Lou, X.; Pavlov, S.; Vorobiev, S.; Dick, J. E.; Tanner, S. D. Mass Cytometry: Technique for Real Time Single Cell Multitarget Immunoassay Based on Inductively Coupled Plasma Time-of-Flight Mass Spectrometry. *Analytical Chemistry* **2009**, *81*, 6813–6822.

(228) Ho, K.-S.; Chan, W.-T. Time-resolved ICP-MS measurement for single-cell analysis and on-line cytometry. *Journal of Analytical Atomic Spectrometry* **2010**, *25*, 1114.

(229) Groombridge, A. S.; Miyashita, S.-i.; Fujii, S.-i.; Nagasawa, K.; Okahashi, T.; Ohata, M.; Umemura, T.; Takatsu, A.; Inagaki, K.; Chiba, K. High Sensitive Elemental Analysis of Single Yeast Cells (Saccharomyces cerevisiae) by Time-Resolved Inductively-Coupled Plasma Mass Spectrometry Using a High Efficiency Cell Introduction System. *Analytical Sciences* **2013**, *29*, 597–603.

(230) Lau, W.-Y.; Chun, K.-H.; Chan, W.-T. Correlation of single-cell ICP-MS intensity distributions for the study of heterogeneous cellular responses to environmental stresses. *Journal of Analytical Atomic Spectrometry* **2017**, *32*, 807–815.

(231) Wang, H.; Wang, B.; Wang, M.; Zheng, L.; Chen, H.; Chai, Z.; Zhao, Y.; Feng, W. Time-resolved ICP-MS analysis of mineral element contents and distribution patterns in single cells. *The Analyst* **2015**, *140*, 523–531.

(232) Wang, H.; Wang, M.; Wang, B.; Zheng, L.; Chen, H.; Chai, Z.; Feng, W. Interrogating the variation of element masses and distribution patterns in single cells using ICP-MS with a high efficiency cell introduction system. *Analytical and Bioanalytical Chemistry* **2016**, *409*, 1415–1423.

(233) Liu, Z.; Xue, A.; Chen, H.; Li, S. Quantitative determination of trace metals in single yeast cells by time-resolved ICP-MS using dissolved standards for calibration. *Applied Microbiology and Biotechnology* **2019**, *103*, 1475–1483.

(234) Löhr, K.; Borovinskaya, O.; Tourniaire, G.; Panne, U.; Jakubowski, N. Arraying of Single Cells for Quantitative High Throughput Laser Ablation ICP-TOF-MS. *Analytical Chemistry* **2019**, *91*, 11520–11528.

(235) Tanner, M. Shorter signals for improved signal to noise ratio, the influence of Poisson distribution. *Journal of Analytical Atomic Spectrometry* **2010**, *25*, 405.

(236) Laborda, F.; Gimenez-Ingalaturre, A. C.; Bolea, E.; Castillo, J. R. Single particle inductively coupled plasma mass spectrometry as screening tool for detection of particles. *Spectrochimica Acta Part B: Atomic Spectroscopy* **2019**, *159*, 105654.

(237) Lockwood, T. E.; González de Vega, R.; Clases, D. An interactive Python-based data processing platform for single particle and single cell ICP-MS. *Journal of Analytical Atomic Spectrometry* **2021**, DOI: 10.1039/d1ja00297j.

References for Chapter 2

(191) Wang, S.; Brown, R.; Gray, D. J. Application of Laser Ablation-ICPMS to the Spatially Resolved Micro-Analysis of Biological Tissue. *Applied Spectroscopy* **1994**, *48*, 1321–1325.

(195) Lear, J.; Hare, D. J.; Fryer, F.; Adlard, P. A.; Finkelstein, D. I.; Doble, P. A. High-Resolution Elemental Bioimaging of Ca, Mn, Fe, Co, Cu, and Zn Employing LA-ICP-MS and Hydrogen Reaction Gas. *Analytical Chemistry* **2012**, *84*, 6707–6714.

(205) Austin, C.; Hare, D.; Rawling, T.; McDonagh, A. M.; Doble, P. Quantification method for elemental bio-imaging by LA-ICP-MS using metal spiked PMMA films. *Journal of Analytical Atomic Spectrometry* **2010**, *25*, 722.

(206) Hare, D.; Burger, F.; Austin, C.; Fryer, F.; Grimm, R.; Reedy, B.; Scolyer, R. A.; Thompson, J. F.; Doble, P. Elemental bio-imaging of melanoma in lymph node biopsies. *The Analyst* **2009**, *134*, 450–453.

(208) Hare, D. J.; Lear, J.; Bishop, D.; Beavis, A.; Doble, P. A. Protocol for production of matrix-matched brain tissue standards for imaging by laser ablation-inductively coupled plasma-mass spectrometry. *Analytical Methods* **2013**, *5*, 1915.

(210) Niehoff, A.-C.; Grünebaum, J.; Moosmann, A.; Mulac, D.; Söbbing, J.; Niehaus, R.; Buchholz, R.; Kröger, S.; Wiehe, A.; Wagner, S.; Sperling, M.; von Briesen, H.; Langer, K.; Karst, U. Quantitative bioimaging of platinum group elements in tumor spheroids. *Analytica Chimica Acta* **2016**, *938*, 106–113.

(211) Stärk, H.-J.; Wennrich, R. A new approach for calibration of laser ablation inductively coupled plasma mass spectrometry using thin layers of spiked agarose gels as references. *Analytical and Bioanalytical Chemistry* **2010**, *399*, 2211–2217.

(212) Šala, M.; Šelih, V. S.; van Elteren, J. T. Gelatin gels as multi-element calibration standards in LA-ICP-MS bioimaging: fabrication of homogeneous standards and microhomogeneity testing. *The Analyst* **2017**, *142*, 3356–3359.

(214) Arora, M.; Hare, D.; Austin, C.; Smith, D. R.; Doble, P. Spatial distribution of manganese in enamel and coronal dentine of human primary teeth. *Science of The Total Environment* **2011**, *409*, 1315–1319.

(215) Sela, H.; Karpas, Z.; Cohen, H.; Zakon, Y.; Zeiri, Y. Preparation of stable standards of biological tissues for laser ablation analysis. *International Journal of Mass Spectrometry* **2011**, *307*, 142–148.

(219) Schrieber, R.; Gareis, H., *Gelatine Handbook*; Wiley-VCH: 2007; 347 pp.

(222) Becker, J. S.; Zoriy, M.; Matusch, A.; Wu, B.; Salber, D.; Palm, C.; Becker, J. S. Bioimaging of metals by laser ablation inductively coupled plasma mass spectrometry (LA-ICP-MS). *Mass Spectrometry Reviews* **2009**, *29*, n/a–n/a.

(238) Seuma, J.; Bunch, J.; Cox, A.; McLeod, C.; Bell, J.; Murray, C. Combination of immunohistochemistry and laser ablation ICP mass spectrometry for imaging of cancer biomarkers. *PROTEOMICS* **2008**, *8*, 3775–3784.

(239) Fernández, B.; Rodríguez-González, P.; Alonso, J. I. G.; Malherbe, J.; García-Fonseca, S.; Pereiro, R.; Sanz-Medel, A. On-line double isotope dilution laser ablation inductively coupled plasma mass spectrometry for the quantitative analysis of solid materials. *Analytica Chimica Acta* **2014**, *851*, 64–71.

(240) Clases, D.; González de Vega, R.; Adlard, P. A.; Doble, P. A. On-line reverse isotope dilution analysis for spatial quantification of elemental labels used in immunohistochemical assisted imaging mass spectrometry via LA-ICP-MS. *Journal of Analytical Atomic Spectrometry* **2019**, *34*, 407–412.

(241) Günther, D.; Hattendorf, B. Solid sample analysis using laser ablation inductively coupled plasma mass spectrometry. *TrAC Trends in Analytical Chemistry* **2005**, *24*, 255–265.

(242) Limbeck, A.; Galler, P.; Bonta, M.; Bauer, G.; Nischkauer, W.; Vanhaecke, F. Recent advances in quantitative LA-ICP-MS analysis: challenges and solutions in the life sciences and environmental chemistry. *Analytical and Bioanalytical Chemistry* **2015**, *407*, 6593–6617.

(243) Bonta, M.; Lohninger, H.; Marchetti-Deschmann, M.; Limbeck, A. Application of gold thin-films for internal standardization in LA-ICP-MS imaging experiments. *The Analyst* **2014**, *139*, 1521.

(244) Hare, D.; Austin, C.; Doble, P. Quantification strategies for elemental imaging of biological samples using laser ablation-inductively coupled plasma-mass spectrometry. *The Analyst* **2012**, *137*, 1527.

(245) Hare, D.; Austin, C.; Doble, P.; Arora, M. Elemental bio-imaging of trace elements in teeth using laser ablation-inductively coupled plasma-mass spectrometry. *Journal of Dentistry* **2011**, *39*, 397–403.

(246) Niehaus, R.; Sperling, M.; Karst, U. Study on aerosol characteristics and fractionation effects of organic standard materials for bioimaging by means of LA-ICP-MS. *Journal of Analytical Atomic Spectrometry* **2015**, *30*, 2056–2065.

(247) Rodríguez-Menéndez, S.; Fernández, B.; García, M.; Álvarez, L.; Fernández, M. L.; Sanz-Medel, A.; Coca-Prados, M.; Pereiro, R.; González-Iglesias, H. Quantitative study of zinc and metallothioneins in the human retina and RPE cells by mass spectrometry-based methodologies. *Talanta* **2018**, *178*, 222–230.

(248) González-Iglesias, H.; Petrash, C.; Rodríguez-Menéndez, S.; García, M.; Álvarez, L.; Cueto, L. F.-V.; Fernández, B.; Pereiro, R.; Sanz-Medel, A.; Coca-Prados, M. Quantitative distribution of Zn, Fe and Cu in the human lens and study of the Zn–metallothionein redox system in cultured lens epithelial cells by elemental MS. *Journal of Analytical Atomic Spectrometry* **2017**, *32*, 1746–1756.

(249) González de Vega, R.; Fernández-Sánchez, M. L.; Pisonero, J.; Eiró, N.; Vizoso, F. J.; Sanz-Medel, A. Quantitative bioimaging of Ca, Fe, Cu and Zn in breast cancer tissues by LA-ICP-MS. *Journal of Analytical Atomic Spectrometry* **2017**, *32*, 671–677.

(250) Reifschneider, O.; Wehe, C. A.; Diebold, K.; Becker, C.; Sperling, M.; Karst, U. Elemental bioimaging of haematoxylin and eosin-stained tissues by laser ablation ICP-MS. *Journal of Analytical Atomic Spectrometry* **2013**, *28*, 989.

(251) Hachmöller, O.; Aichler, M.; Schwamborn, K.; Lutz, L.; Werner, M.; Sperling, M.; Walch, A.; Karst, U. Element bioimaging of liver needle biopsy specimens from patients with Wilson's disease by laser ablation-inductively coupled plasma-mass spectrometry. *Journal of Trace Elements in Medicine and Biology* **2016**, *35*, 97–102.

(252) M-M, P.; Merle, U.; Weiskirchen, R.; Becker, J. S. Bioimaging of copper deposition in Wilsons diseases mouse liver by laser ablation inductively coupled plasma mass spectrometry imaging (LA-ICP-MSI). *International Journal of Mass Spectrometry* **2013**, *354-355*, 281–287.

(253) Dorph-Petersen, K.-A.; Nyengaard, J. R.; Gundersen, H. J. G. Tissue shrinkage and unbiased stereological estimation of particle number and size*. *Journal of Microscopy* **2001**, *204*, 232–246.

(254) Gholap, D.; Verhulst, J.; Ceelen, W.; Vanhaecke, F. Use of pneumatic nebulization and laser ablation–inductively coupled plasma–mass spectrometry to study the distribution and bioavailability of an intraperitoneally administered Pt-containing chemotherapeutic drug. *Analytical and Bioanalytical Chemistry* **2012**, *402*, 2121–2129.

(255) Birka, M.; Wentker, K. S.; Lusmöller, E.; Arheilger, B.; Wehe, C. A.; Sperling, M.; Stadler, R.; Karst, U. Diagnosis of Nephrogenic Systemic Fibrosis by means of Elemental Bioimaging and Speciation Analysis. *Analytical Chemistry* **2015**, *87*, 3321–3328.

(256) Simons, C.; Mans, C.; Hanning, S.; Janßen, A.; Radtke, M.; Reinholz, U.; Ostermann, M.; Michaelis, M.; Wienold, J.; Alber, D.; Kreyenschmidt, M. Study on microscopic homogeneity of polymeric candidate reference materials BAM H001–BAM H010 by means of synchrotronμ-XRF and LA-ICP-MS. *Journal of Analytical Atomic Spectrometry* **2010**, *25*, 40–43.

(257) Hubicki, Z.; Koodynsk, D. In *Ion Exchange Technologies*; InTech: 2012.

(258) Clases, D.; González de Vega, R.; Bishop, D.; Doble, P. SEC-ICP-MS and on-line isotope dilution analysis for characterisation and quantification of immunochemical assays. *Analytical and Bioanalytical Chemistry* **2019**, *411*, 3553–3560.

References for Chapter 3

(190) Gray, A. L. Solid sample introduction by laser ablation for inductively coupled plasma source mass spectrometry. *The Analyst* **1985**, *110*, 551.

(201) Weiskirchen, R.; Weiskirchen, S.; Kim, P.; Winkler, R. Software solutions for evaluation and visualization of laser ablation inductively coupled plasma mass spectrometry imaging (LA-ICP-MSI) data: a short overview. *Journal of Cheminformatics* **2019**, *11*, DOI: 10.1186/s13321-019-0338-7.

(203) López-Fernández, H.; de S. Pessôa, G.; Arruda, M. A. Z.; Capelo-Martínez, J. L.; Fdez-Riverola, F.; Glez-Peña, D.; Reboiro-Jato, M. LA-iMageS: a software for elemental distribution bioimaging using LA–ICP–MS data. *Journal of Cheminformatics* **2016**, *8*, DOI: 10.1186/s13321-016-0178-7.

(206) Hare, D.; Burger, F.; Austin, C.; Fryer, F.; Grimm, R.; Reedy, B.; Scolyer, R. A.; Thompson, J. F.; Doble, P. Elemental bio-imaging of melanoma in lymph node biopsies. *The Analyst* **2009**, *134*, 450–453.

(221) Lockwood, T. E.; Westerhausen, M. T.; González de Vega, R.; Röhnelt, A.; Bishop, D. P.; Cole, N.; Doble, P. A.; Clases, D. Low background mould-prepared gelatine standards for reproducible quantification in elemental bio-imaging. *The Analyst* **2019**, *144*, 6881–6888.

(242) Limbeck, A.; Galler, P.; Bonta, M.; Bauer, G.; Nischkauer, W.; Vanhaecke, F. Recent advances in quantitative LA-ICP-MS analysis: challenges and solutions in the life sciences and environmental chemistry. *Analytical and Bioanalytical Chemistry* **2015**, *407*, 6593–6617.

(259) Doble, P. A.; González de Vega, R.; Bishop, D. P.; Hare, D. J.; Clases, D. Laser Ablation–Inductively Coupled Plasma–Mass Spectrometry Imaging in Biology. *Chemical Reviews* **2021**, acs.chemrev.0c01219.

(260) Pozebon, D.; Scheffler, G. L.; Dressler, V. L.; Nunes, M. A. G. Review of the applications of laser ablation inductively coupled plasma mass spectrometry (LA-ICP-MS) to the analysis of biological samples. *J. Anal. At. Spectrom.* **2014**, *29*, 2204–2228.

(261) Chew, D.; Drost, K.; Marsh, J. H.; Petrus, J. A. LA-ICP-MS imaging in the geosciences and its applications to geochronology. *Chemical Geology* **2021**, *559*, 119917.

(262) Li, X.; Liu, T.; Chang, C.; Lei, Y.; Mao, X. Analytical Methodologies for Agrometallomics: A Critical Review. *Journal of Agricultural and Food Chemistry* **2021**, *69*, 6100–6118.

(263) Van Malderen, S.; Vincze, L.; Vanhaecke, F. In *NAWLA19, North American Workshop on Laser Ablation 2019, Abstracts*, Austin, TX, 2019, pp 23–23.

(264) Paton, C.; Hellstrom, J.; Paul, B.; Woodhead, J.; Hergt, J. Iolite: Freeware for the visualisation and processing of mass spectrometric data. *Journal of Analytical Atomic Spectrometry* **2011**, *26*, 2508.

(265) Suzuki, T.; Sakata, S.; Makino, Y.; Obayashi, H.; Ohara, S.; Hattori, K.; Hirata, T. iQuant2: Software for Rapid and Quantitative Imaging Using Laser Ablation-ICP Mass Spectrometry. *Mass Spectrometry* **2018**, *7*, A0065–A0065.

(266) Uerlings, R.; Matusch, A.; Weiskirchen, R. Reconstruction of laser ablation inductively coupled plasma mass spectrometry (LA-ICP-MS) spatial distribution images in Microsoft Excel 2007. *International Journal of Mass Spectrometry* **2016**, *395*, 27–35.

(267) Osterholt, T.; Salber, D.; Matusch, A.; Becker, J. S.; Palm, C. IMAGENA: Image Generation and Analysis – An interactive software tool handling LA-ICP-MS data. *International Journal of Mass Spectrometry* **2011**, *307*, 232–239.

(268) Managh, A. J.; Reid, P. A new freeware tool for image processing and its application to high speed LA-ICP-MS imaging. *Journal of Analytical Atomic Spectrometry* **2019**, *34*, 1369–1373.

(269) Sforna, M. C.; Lugli, F. MapIT!: a simple and user-friendly MATLAB script to elaborate elemental distribution images from LA-ICP-MS data. *Journal of Analytical Atomic Spectrometry* **2017**, *32*, 1035–1043.

(270) Castellanos-García, L. J.; Gokhan Elci, S.; Vachet, R. W. Reconstruction, analysis, and segmentation of LA-ICP-MS imaging data using Python for the identification of sub-organ regions in tissues. *The Analyst* **2020**, *145*, 3705–3712.

(271) Bianga, J.; Bouslimani, A.; Bec, N.; Quenet, F.; Mounicou, S.; Szpunar, J.; Bouyssiere, B.; Lobinski, R.; Larroque, C. Complementarity of MALDI and LA ICP mass spectrometry for platinum anticancer imaging in human tumor. *Metallomics* **2014**, *6*, 1382–1386.

(272) Gundlach-Graham, A.; Günther, D. Toward faster and higher resolution LA–ICPMS imaging: on the co-evolution of LA cell design and ICPMS instrumentation. *Analytical and Bioanalytical Chemistry* **2016**, *408*, 2687–2695.

(273) Schindelin, J. et al. Fiji: an open-source platform for biological-image analysis. *Nature Methods* **2012**, *9*, 676–682.

(274) Chen, X. et al. Open is not enough. *Nature Physics* **2019**, *15*, 113–119.

(275) Alomari, H. W.; Ramasamy, V.; Kiper, J. D.; Potvin, G. A User Interface (UI) and User eXperience (UX) evaluation framework for cyberlearning environments in computer science and software engineering education. *Heliyon* **2020**, *6*, e03917.

(276) O'Donoghue, S. I.; Baldi, B. F.; Clark, S. J.; Darling, A. E.; Hogan, J. M.; Kaur, S.; Maier-Hein, L.; McCarthy, D. J.; Moore, W. J.; Stenau, E.; Swedlow, J. R.; Vuong, J.; Procter, J. B. Visualization of Biomedical Data. *Annual Review of Biomedical Data Science* **2018**, *1*, 275–304.

(277) Borland, D.; Ii, R. M. T. Rainbow Color Map (Still) Considered Harmful. *IEEE Computer Graphics and Applications* **2007**, *27*, 14–17.

(278) Borkin, M.; Gajos, K.; Peters, A.; Mitsouras, D.; Melchionna, S.; Rybicki, F.; Feldman, C.; Pfister, H. Evaluation of Artery Visualizations for Heart Disease Diagnosis. *IEEE Transactions on Visualization and Computer Graphics* **2011**, *17*, 2479–2488.

(279) Paul, B. et al. Visualising mouse neuroanatomy and function by metal distribution using laser ablation-inductively coupled plasma-mass spectrometry imaging. *Chemical Science* **2015**, *6*, 5383–5393.

(280) Aonishi, T.; Hirata, T.; Kuwatani, T.; Fujimoto, M.; Chang, Q.; Kimura, J.-I. A numerical inversion method for improving the spatial resolution of elemental imaging by laser ablation-inductively coupled plasma-mass spectrometry. *Journal of Analytical Atomic Spectrometry* **2018**, *33*, 2210–2218.

(281) Malderen, S. J. M. V.; Managh, A. J.; Sharp, B. L.; Vanhaecke, F. Recent developments in the design of rapid response cells for laser ablation-inductively coupled plasma-mass spectrometry and their impact on bioimaging applications. *Journal of Analytical Atomic Spectrometry* **2016**, *31*, 423–439.

(282) Harris, C. R. et al. Array programming with NumPy. *Nature* **2020**, *585*, 357–362.

(283) Wee, A.; Grayden, D. B.; Zhu, Y.; Petkovic-Duran, K.; Smith, D. A continuous wavelet transform algorithm for peak detection. *ELECTROPHORESIS* **2008**, *29*, 4215–4225.

(284) Almeida, A.; Castel-Branco, M.; Falcão, A. Linear regression for calibration lines revisited: weighting schemes for bioanalytical methods. *Journal of Chromatography B* **2002**, *774*, 215–222.

(285) Pratt, V. R. In *Proceedings of the 1st annual ACM SIGACT-SIGPLAN symposium on Principles of programming languages - POPL '73*, ACM Press: 1973.

(286) Costes, S. V.; Daelemans, D.; Cho, E. H.; Dobbin, Z.; Pavlakis, G.; Lockett, S. Automatic and Quantitative Measurement of Protein-Protein Colocalization in Live Cells. *Biophysical Journal* **2004**, *86*, 3993–4003.

(287) Eliceiri, K. W.; Berthold, M. R.; Goldberg, I. G.; Ibáñez, L.; Manjunath, B. S.; Martone, M. E.; Murphy, R. F.; Peng, H.; Plant, A. L.; Roysam, B.; Stuurman, N.; Swedlow, J. R.; Tomancak, P.; Carpenter, A. E. Biological imaging software tools. *Nature Methods* **2012**, *9*, 697–710.

References for Chapter 4

(1) Daly, M. J.; Gaidamakova, E. K.; Matrosova, V. Y.; Vasilenko, A.; Zhai, M.; Leapman, R. D.; Lai, B.; Ravel, B.; Li, S.-M. W.; Kemner, K. M.; Fredrickson, J. K. Protein Oxidation Implicated as the Primary Determinant of Bacterial Radioresistance. *PLoS Biology* **2007**, *5*, ed. by Petsko, G. A., e92.

(2) Doble, P. A.; Miklos, G. L. G. Distributions of manganese in diverse human cancers provide insights into tumour radioresistance. *Metallomics* **2018**, DOI: 10.1039/c8mt00110c.

(9) Berney, D. M.; Lee, A.; Randle, S. J.; Jordan, S.; Shamash, J.; Oliver, R. T. D. The frequency of intratubular embryonal carcinoma: implications for the pathogenesis of germ cell tumours. *Histopathology* **2004**, *45*, 155–161.

(10) Wilson, L.; Heraty, L.; Ashford, B.; Coelho, S.; Frangi, A.; Pozo, J.; Ince, P.; Highley, J. Tissue microarray (TMA) use in post mortem neuropathology. *Journal of Neuroscience Methods* **2021**, *347*, 108963.

(36) Brożyna, A. A.; Jóźwicki, W.; Roszkowski, K.; Filipiak, J.; Slominski, A. T. Melanin content in melanoma metastases affects the outcome of radiotherapy. *Oncotarget* **2016**, *7*, 17844–17853.

(38) Classen, J.; Schmidberger, H.; Meisner, C.; Souchon, R.; Sautter-Bihl, M.-L.; Sauer, R.; Weinknecht, S.; Köhrmann, K.-U.; Bamberg, M. Radiotherapy for Stages IIA/B Testicular Seminoma: Final Report of a Prospective Multicenter Clinical Trial. *Journal of Clinical Oncology* **2003**, *21*, 1101–1106.

(103) Seshacharyulu, P.; Baine, M. J.; Souchek, J. J.; Menning, M.; Kaur, S.; Yan, Y.; Ouellette, M. M.; Jain, M.; Lin, C.; Batra, S. K. Biological determinants of radioresistance and their remediation in pancreatic cancer. *Biochimica et Biophysica Acta (BBA) - Reviews on Cancer* **2017**, *1868*, 69–92.

(104) Häkkinenm, A.-M.; Laasonen, A.; Linnainmaa, K.; Mattson, K.; Pyrhonen, S. Radiosensitivity of Mesothelioma Cell Lines. *Acta Oncologica* **1996**, *35*, 451–456.

(105) Rofstad, E. K. Radiation Biology of Malignant Melanoma. *Acta Radiologica: Oncology* **1986**, *25*, 1–10.

(108) Grossi, G. F.; Durante, M.; Gialanella, G.; Pugliese, M.; Mosse, I. Effects of melanin on high- and low- linear energy transfer (LET) radiation response of human epithelial cells. *Radiation and Environmental Biophysics* **1998**, *37*, 63–67.

(109) Marshall, E.; Matthews, J.; Shaw, J.; Nixon, J.; Tumewu, P.; Finlay, G.; Holdaway, K.; Baguley, B. Radiosensitivity of new and established human melanoma cell lines: Comparison of [3H]thymidine incorporation and soft agar clonogenic assays. *European Journal of Cancer* **1994**, *30*, 1370–1376.

(114) Stutzman, R. E.; McLeod, D. G. Radiation Therapy: A Primary Treatment Modality for Seminoma. *Urologic Clinics of North America* **1980**, *7*, 757–764.

(115) Percarpio, B.; Clements, J. C.; McLeod, D. G.; Sorgen, S. D.; Cardinale, F. S. Anaplastic seminoma: An analysis of 77 patients. *Cancer* **1979**, *43*, 2510–2513.

(117) Kersh, C. R.; Constable, W. C.; Hahn, S. S.; Spaulding, C. A.; Eisert, D. R.; Jenrette, J. M.; Marks, R. D.; Grayson, J. Primary malignant extragonadal germ cell tumors. An analysis of the effect of radiotherapy. *Cancer* **1990**, *65*, 2681–2685.

(118) Daugaard, G.; Petersen, P. M.; Rorth, M. Surveillance in stage I testicular cancer. *APMIS* **2003**, *111*, 76–85.

(125) Daly, M. J. Accumulation of Mn(II) in Deinococcus radiodurans Facilitates Gamma-Radiation Resistance. *Science* **2004**, *306*, 1025–1028.

(142) Stadtman, E. R.; Berlett, B. S. Fenton chemistry. Amino acid oxidation. *Journal of Biological Chemistry* **1991**, *266*, 17201–17211.

(143) Thomas, C.; Mackey, M. M.; Diaz, A. A.; Cox, D. P. Hydroxyl radical is produced via the Fenton reaction in submitochondrial particles under oxidative stress: implications for diseases associated with iron accumulation. *Redox Report* **2009**, *14*, 102–108.

(221) Lockwood, T. E.; Westerhausen, M. T.; González de Vega, R.; Röhnelt, A.; Bishop, D. P.; Cole, N.; Doble, P. A.; Clases, D. Low background mould-prepared gelatine standards for reproducible quantification in elemental bio-imaging. *The Analyst* **2019**, *144*, 6881–6888.

(250) Reifschneider, O.; Wehe, C. A.; Diebold, K.; Becker, C.; Sperling, M.; Karst, U. Elemental bioimaging of haematoxylin and eosin-stained tissues by laser ablation ICP-MS. *Journal of Analytical Atomic Spectrometry* **2013**, *28*, 989.

(288) Gustavson, M. D.; Rimm, D. L.; Dolled-Filhart, M. Tissue microarrays: leaping the gap between research and clinical adoption. *Personalized Medicine* **2013**, *10*, 441–451.

(289) Munari, E. et al. PD-L1 expression heterogeneity in non-small cell lung cancer: evaluation of small biopsies reliability. *Oncotarget* **2017**, *8*, 90123–90131.

(290) Khoury, T.; Zirpoli, G.; Cohen, S. M.; Geradts, J.; Omilian, A.; Davis, W.; Bshara, W.; Miller, R.; Mathews, M. M.; Troester, M.; Palmer, J. R.; Ambrosone, C. B. Ki-67 Expression in Breast Cancer Tissue Microarrays. *American Journal of Clinical Pathology* **2017**, *148*, 108–118.

(291) Tian, S.; Hou, Z.; Zuo, X.; Xiong, W.; Huang, G. Automatic Registration of the Mass Spectrometry Imaging Data of Sagittal Brain Slices to the Reference Atlas. *Journal of the American Society for Mass Spectrometry* **2021**, DOI: 10.1021/jasms.1c00137.

(292) Neumann, J. M.; Niehaus, K.; Neumann, N.; Knobloch, H. C.; Bremmer, F.; Krafft, U.; Kellner, U.; Nyirády, P.; Szarvas, T.; Bednarz, H.; Reis, H. A new technological approach in diagnostic pathology: mass spectrometry imaging-based metabolomics for biomarker detection in urachal cancer. *Laboratory Investigation* **2021**, DOI: 10.1038/s41374-021-00612-7.

(293) Abdelmoula, W. M.; Škrášková, K.; Balluff, B.; Carreira, R. J.; Tolner, E. A.; Lelieveldt, B. P. F.; van der Maaten, L.; Morreau, H.; van den Maagdenberg, A. M. J. M.; Heeren, R. M. A.; McDonnell, L. A.; Dijkstra, J. Automatic Generic Registration of Mass Spectrometry Imaging Data to Histology Using Nonlinear Stochastic Embedding. *Analytical Chemistry* **2014**, *86*, 9204–9211.

(294) Buck, A.; Balluff, B.; Voss, A.; Langer, R.; Zitzelsberger, H.; Aichler, M.; Walch, A. How Suitable is Matrix-Assisted Laser Desorption/Ionization-Time-of-Flight for Metabolite Imaging from Clinical Formalin-Fixed and Paraffin-Embedded Tissue Samples in Comparison to Matrix-Assisted Laser Desorption/Ionization-Fourier Transform Ion Cyclotron Resonance Mass Spectrometry? *Analytical Chemistry* **2016**, *88*, 5281–5289.

(295) Mascini, N. E.; Teunissen, J.; Noorlag, R.; Willems, S. M.; Heeren, R. M. Tumor classification with MALDI-MSI data of tissue microarrays: A case study. *Methods* **2018**, *151*, 21–27.

(296) Ščupáková, K.; Balluff, B.; Tressler, C.; Adelaja, T.; Heeren, R. M.; Glunde, K.; Ertaylan, G. Cellular resolution in clinical MALDI mass spectrometry imaging: the latest advancements and current challenges. *Clinical Chemistry and Laboratory Medicine (CCLM)* **2019**, *58*, 914–929.

(297) Ruifrok, A. C.; Johnston, D. A. Quantification of histochemical staining by color deconvolution. *Analytical and quantitative cytology and histology* **2001**, *23*, 291–299, ppublish.

(298) Bishop, D. P.; Westerhausen, M. T.; Barthelemy, F.; Lockwood, T.; Cole, N.; Gibbs, E. M.; Crosbie, R. H.; Nelson, S. F.; Miceli, M. C.; Doble, P. A.; Wanagat, J. Quantitative immuno-mass spectrometry imaging of skeletal muscle dystrophin. *Scientific Reports* **2021**, *11*, DOI: 10.1038/s41598-020-80495-8.

(299) Selvaraj, S.; (Saha), K. C.; Chakraborty, A.; Bhattacharyya, S. N.; Saha, A. Influence of copper (II) ions and its derivatives on radiosensitivity of Escherichia coli. *Radiation Physics and Chemistry* **2007**, *76*, 1160–1164.

(300) Kirschner, I.; Citri, N.; Levitzki, A.; Anbar, M. The Effect of Copper on the Radiosensitivity of Bacteria. *International Journal of Radiation Biology and Related Studies in Physics, Chemistry and Medicine* **1970**, *17*, 81–85.

(301) Hare, D. J.; Kysenius, K.; Paul, B.; Knauer, B.; Hutchinson, R. W.; O'Connor, C.; Fryer, F.; Hennessey, T. P.; Bush, A. I.; Crouch, P. J.; Doble, P. A. Imaging Metals in Brain Tissue by Laser Ablation - Inductively Coupled Plasma - Mass Spectrometry (LA-ICP-MS). *Journal of Visualized Experiments* **2017**, DOI: 10.3791/55042.

(302) Pamphlett, R.; Satgunaseelan, L.; Jew, S. K.; Doble, P. A.; Bishop, D. P. Elemental bioimaging shows mercury and other toxic metals in normal breast tissue and in breast cancers. *PLOS ONE* **2020**, *15*, ed. by Hu, Y., e0228226.

References for Chapter 5

(2) Doble, P. A.; Miklos, G. L. G. Distributions of manganese in diverse human cancers provide insights into tumour radioresistance. *Metallomics* **2018**, DOI: 10.1039/c8mt00110c.

(46) Bao, S.; Wu, Q.; McLendon, R. E.; Hao, Y.; Shi, Q.; Hjelmeland, A. B.; Dewhirst, M. W.; Bigner, D. D.; Rich, J. N. Glioma stem cells promote radioresistance by preferential activation of the DNA damage response. *Nature* **2006**, *444*, 756–760.

(49) Diehn, M. et al. Association of reactive oxygen species levels and radioresistance in cancer stem cells. *Nature* **2009**, *458*, 780–783.

(91) Debus, J.; Wuendrich, M.; Pirzkall, A.; Hoess, A.; Schlegel, W.; Zuna, I.; Engenhart-Cabillic, R.; Wannenmacher, M. High Efficacy of Fractionated Stereotactic Radiotherapy of Large Base-of-Skull Meningiomas: Long-Term Results. *Journal of Clinical Oncology* **2001**, *19*, 3547–3553.

(92) Park, H. J.; Kang, H.-C.; Kim, I. H.; Park, S.-H.; Kim, D. G.; Park, C.-K.; Paek, S. H.; Jung, H.-W. The role of adjuvant radiotherapy in atypical meningioma. *Journal of Neuro-Oncology* **2013**, *115*, 241–247.

(101) Kazmi, F.; Soon, Y. Y.; Leong, Y. H.; Koh, W. Y.; Vellayappan, B. Re-irradiation for recurrent glioblastoma (GBM): a systematic review and meta-analysis. *Journal of Neuro-Oncology* **2018**, *142*, 79–90.

(102) Soyuer, S.; Chang, E. L.; Selek, U.; Shi, W.; Maor, M. H.; DeMonte, F. Radiotherapy after surgery for benign cerebral meningioma. *Radiotherapy and Oncology* **2004**, *71*, 85–90.

(221) Lockwood, T. E.; Westerhausen, M. T.; González de Vega, R.; Röhnelt, A.; Bishop, D. P.; Cole, N.; Doble, P. A.; Clases, D. Low background mould-prepared gelatine standards for reproducible quantification in elemental bio-imaging. *The Analyst* **2019**, *144*, 6881–6888.

(303) Rabé, M. et al. Identification of a transient state during the acquisition of temozolomide resistance in glioblastoma. *Cell Death & Disease* **2020**, *11*, DOI: 10.1038/s41419-019-2200-2.

(304) Wiewrodt, D.; Nagel, G.; Dreimüller, N.; Hundsberger, T.; Perneczky, A.; Kaina, B. MGMT in primary and recurrent human glioblastomas after radiation and chemotherapy and comparison with p53 status and clinical outcome. *International Journal of Cancer* **2007**, *122*, 1391–1399.

(305) Chien, C.-H.; Hsueh, W.-T.; Chuang, J.-Y.; Chang, K.-Y. Dissecting the mechanism of temozolomide resistance and its association with the regulatory roles of intracellular reactive oxygen species in glioblastoma. *Journal of Biomedical Science* **2021**, *28*, DOI: 10.1186/s12929-021-00717-7.

(306) Tamura, K.; Aoyagi, M.; Wakimoto, H.; Ando, N.; Nariai, T.; Yamamoto, M.; Ohno, K. Accumulation of CD133-positive glioma cells after high-dose irradiation by Gamma Knife surgery plus external beam radiation. *Journal of Neurosurgery* **2010**, *113*, 310–318.

(307) Hu, W.; Shen, F.; Chen, G.; Shen, G.; Liu, W.; Zhou, J. Possible Involvement of Brain Tumour Stem Cells in the Emergence of a Fast-Growing Malignant Meningioma after Surgical Resection and Radiotherapy of High-Grade Astrocytoma: Case Report and Preliminary Laboratory Investigation. *Journal of International Medical Research* **2009**, *37*, 240–246.

(308) Yoshida, D.; Ikeda, Y.; Nakazawa, S. Quantitative analysis of copper, zinc and copper/zinc ratio in selected human brain tumors. *Journal of Neuro-Oncology* **1993**, *16*, 109–115.

(309) Yoshida, D.; Ikeda, Y.; Nakazawa, S. Copper Chelation Inhibits Tumor Angiogenesis in the Experimental 9L Gliosarcoma Model. *Neurosurgery* **1995**, *37*, 287–293.

(310) Jazayeri, S.; Feli, A.; Bitaraf, M. A.; Dodaran, M. S.; Alikhani, M.; Hosseinzadeh-Attar, M. J. Effects of Copper Reduction on Angiogenesis-Related Factors in Recurrent Glioblastoma Cases. *Asian Pacific Journal of Cancer Prevention* **2016**, *17*, DOI: 10.22034/APJCP.2016.17.10.4609.

(311) Ahir, B. K.; Engelhard, H. H.; Lakka, S. S. Tumor Development and Angiogenesis in Adult Brain Tumor: Glioblastoma. *Molecular Neurobiology* **2020**, *57*, 2461–2478.

(312) Dehnhardt, M.; Zoriy, M. V.; Khan, Z.; Reifenberger, G.; Ekström, T. J.; Becker, J. S.; Zilles, K.; Bauer, A. Element distribution is altered in a zone surrounding human glioblastoma multiforme. *Journal of Trace Elements in Medicine and Biology* **2008**, *22*, 17–23.

(313) Andrási, E.; Suhajda, M.; Sáray, I.; Bezúr, L.; Ernyei, L.; Réffy, A. Concentration of elements in human brain: glioblastoma multiforme. *Science of The Total Environment* **1993**, *139-140*, 399–402.

(314) Arnaud, J.; Touvier, M.; Galan, P.; Andriollo-Sanchez, M.; Ruffieux, D.; Roussel, A.-M.; Hercberg, S.; Favier, A. Determinants of serum zinc concentrations in a population of French middle-age subjects (SU.VI.MAX cohort). *European Journal of Clinical Nutrition* **2010**, *64*, 1057–1064.

References for Chapter 6

(226) Meyer, S.; González de Vega, R.; Xu, X.; Du, Z.; Doble, P. A.; Clases, D. Characterization of Upconversion Nanoparticles by Single-Particle ICP-MS Employing a Quadrupole Mass Filter with Increased Bandpass. *Analytical Chemistry* **2020**, *92*, 15007–15016.

(235) Tanner, M. Shorter signals for improved signal to noise ratio, the influence of Poisson distribution. *Journal of Analytical Atomic Spectrometry* **2010**, *25*, 405.

(236) Laborda, F.; Gimenez-Ingalaturre, A. C.; Bolea, E.; Castillo, J. R. Single particle inductively coupled plasma mass spectrometry as screening tool for detection of particles. *Spectrochimica Acta Part B: Atomic Spectroscopy* **2019**, *159*, 105654.

(259) Doble, P. A.; González de Vega, R.; Bishop, D. P.; Hare, D. J.; Clases, D. Laser Ablation–Inductively Coupled Plasma–Mass Spectrometry Imaging in Biology. *Chemical Reviews* **2021**, acs.chemrev.0c01219.

(282) Harris, C. R. et al. Array programming with NumPy. *Nature* **2020**, *585*, 357–362.

(315) Gao, J.; Xu, B. Applications of nanomaterials inside cells. *Nano Today* **2009**, *4*, 37–51.

(316) Fernandez-Fernandez, A.; Manchanda, R.; McGoron, A. J. Theranostic Applications of Nanomaterials in Cancer: Drug Delivery, Image-Guided Therapy, and Multifunctional Platforms. *Applied Biochemistry and Biotechnology* **2011**, *165*, 1628–1651.

(317) Jeevanandam, J.; Barhoum, A.; Chan, Y. S.; Dufresne, A.; Danquah, M. K. Review on nanoparticles and nanostructured materials: history, sources, toxicity and regulations. *Beilstein Journal of Nanotechnology* **2018**, *9*, 1050–1074.

(318) Kolahalam, L. A.; Viswanath, I. K.; Diwakar, B. S.; Govindh, B.; Reddy, V.; Murthy, Y. Review on nanomaterials: Synthesis and applications. *Materials Today: Proceedings* **2019**, *18*, 2182–2190.

(319) Du, Z.; Gupta, A.; Clarke, C.; Cappadona, M.; Clases, D.; Liu, D.; Yang, Z.; Karan, S.; Price, W. S.; Xu, X. Porous Upconversion Nanostructures as Bimodal Biomedical Imaging Contrast Agents. *The Journal of Physical Chemistry C* **2020**, *124*, 12168–12174.

(320) Hochella, M. F.; Mogk, D. W.; Ranville, J.; Allen, I. C.; Luther, G. W.; Marr, L. C.; McGrail, B. P.; Murayama, M.; Qafoku, N. P.; Rosso, K. M.; Sahai, N.; Schroeder, P. A.; Vikesland, P.; Westerhoff, P.; Yang, Y. Natural, incidental, and engineered nanomaterials and their impacts on the Earth system. *Science* **2019**, *363*, DOI: 10.1126/science.aau8299.

(321) Malakar, A.; Kanel, S. R.; Ray, C.; Snow, D. D.; Nadagouda, M. N. Nanomaterials in the environment, human exposure pathway, and health effects: A review. *Science of The Total Environment* **2021**, *759*, 143470.

(322) Mozhayeva, D.; Engelhard, C. A critical review of single particle inductively coupled plasma mass spectrometry – A step towards an ideal method for nanomaterial characterization. *Journal of Analytical Atomic Spectrometry* **2020**, *35*, 1740–1783.

(323) González de Vega, R.; Goyen, S.; Lockwood, T. E.; Doble, P. A.; Camp, E. F.; Clases, D. Characterisation of microplastics and unicellular algae in seawater by targeting carbon via single particle and single cell ICP-MS. *Analytica Chimica Acta* **2021**, *1174*, 338737.

(324) Galbács, G.; Kéri, A.; Kohut, A.; Veres, M.; Geretovszky, Z. Nanoparticles in analytical laser and plasma spectroscopy – a review of recent developments in methodology and applications. *Journal of Analytical Atomic Spectrometry* **2021**, *36*, 1826–1872.

(325) Metarapi, D.; Šala, M.; Vogel-Mikuš, K.; Šelih, V. S.; van Elteren, J. T. Nanoparticle Analysis in Biomaterials Using Laser Ablation-Single Particle-Inductively Coupled Plasma Mass Spectrometry. *Analytical Chemistry* **2019**, *91*, 6200–6205.

(326) Metarapi, D.; van Elteren, J. T.; Šala, M.; Vogel-Mikuš, K.; Arčon, I.; Šelih, V. S.; Kolar, M.; Hočevar, S. B. Laser ablation-single-particle-inductively coupled plasma mass spectrometry as a multimodality bioimaging tool in nano-based omics. *Environmental Science: Nano* **2021**, *8*, 647–656.

(327) Nordhorn, I. D.; Dietrich, D.; Verlemann, C.; Vennemann, A.; Schmid, R.; Elinkmann, M.; Fuchs, J.; Sperling, M.; Wiemann, M.; Karst, U. Spatially and size-resolved analysis of gold nanoparticles in rat spleen after intratracheal instillation by laser ablation-inductively coupled plasma-mass spectrometry. *Metallomics* **2021**, *13*, DOI: 10.1093/mtomcs/mfab028.

(328) González de Vega, R.; Clases, D.; Fernández-Sánchez, M. L.; Eiró, N.; González, L. O.; Vizoso, F. J.; Doble, P. A.; Sanz-Medel, A. MMP-11 as a biomarker for metastatic breast cancer by immunohistochemical-assisted imaging mass spectrometry. *Analytical and Bioanalytical Chemistry* **2018**, *411*, 639–646.

(329) Metarapi, D.; van Elteren, J. T. Fundamentals of single particle analysis in biomatrices by laser ablation-inductively coupled plasma mass spectrometry. *Journal of Analytical Atomic Spectrometry* **2020**, *35*, 784–793.

(330) Laborda, F.; Jiménez-Lamana, J.; Bolea, E.; Castillo, J. R. Critical considerations for the determination of nanoparticle number concentrations, size and number size distributions by single particle ICP-MS. *Journal of Analytical Atomic Spectrometry* **2013**, *28*, 1220.

(331) Mozhayeva, D.; Engelhard, C. A quantitative nanoparticle extraction method for microsecond time resolved single-particle ICP-MS data in the presence of a high background. *Journal of Analytical Atomic Spectrometry* **2019**, *34*, 1571–1580.

(332) Meermann, B.; Nischwitz, V. ICP-MS for the analysis at the nanoscale – a tutorial review. *Journal of Analytical Atomic Spectrometry* **2018**, *33*, 1432–1468.

(333) Millman, K. J.; Aivazis, M. Python for Scientists and Engineers. *Computing in Science & Engineering* **2011**, *13*, 9–12.

(334) Currie, L. A. On the detection of rare, and moderately rare, nuclear events. *Journal of Radioanalytical and Nuclear Chemistry* **2008**, *276*, 285–297.

(335) Currie, L. A. Limits for qualitative detection and quantitative determination. Application to radiochemistry. *Analytical Chemistry* **1968**, *40*, 586–593.

(336) Pace, H. E.; Rogers, N. J.; Jarolimek, C.; Coleman, V. A.; Higgins, C. P.; Ranville, J. F. Determining Transport Efficiency for the Purpose of Counting and Sizing Nanoparticles via Single Particle Inductively Coupled Plasma Mass Spectrometry. *Analytical Chemistry* **2011**, *83*, 9361–9369.

(337) Nelder, J. A.; Mead, R. A Simplex Method for Function Minimization. *The Computer Journal* **1965**, *7*, 308–313.

(338) Praetorius, A.; Gundlach-Graham, A.; Goldberg, E.; Fabienke, W.; Navratilova, J.; Gondikas, A.; Kaegi, R.; Günther, D.; Hofmann, T.; von der Kammer, F. Single-particle multi-element fingerprinting (spMEF) using inductively-coupled plasma time-of-flight mass spectrometry (ICP-TOFMS) to identify engineered nanoparticles against the elevated natural background in soils. *Environmental Science: Nano* **2017**, *4*, 307–314.

(339) Loosli, F.; Wang, J.; Rothenberg, S.; Bizimis, M.; Winkler, C.; Borovinskaya, O.; Flamigni, L.; Baalousha, M. Sewage spills are a major source of titanium dioxide engineered (nano)-particle release into the environment. *Environmental Science: Nano* **2019**, *6*, 763–777.

(340) Sanchís, J.; Jiménez-Lamana, J.; Abad, E.; Szpunar, J.; Farré, M. Occurrence of Cerium-, Titanium-, and Silver-Bearing Nanoparticles in the Besòs and Ebro Rivers. *Environmental Science & Technology* **2020**, *54*, 3969–3978.

(341) Azimzada, A.; Jreije, I.; Hadioui, M.; Shaw, P.; Farner, J. M.; Wilkinson, K. J. Quantification and Characterization of Ti-, Ce-, and Ag-Nanoparticles in Global Surface Waters and Precipitation. *Environmental Science & Technology* **2021**, *55*, 9836–9844.

(342) Mansfield, C.; Alloy, M.; Hamilton, J.; Verbeck, G.; Newton, K.; Klaine, S.; Roberts, A. Photo-induced toxicity of titanium dioxide nanoparticles to Daphnia magna under natural sunlight. *Chemosphere* **2015**, *120*, 206–210.

(343) Wang, J.; Nie, Y.; Dai, H.; Wang, M.; Cheng, L.; Yang, Z.; Chen, S.; Zhao, G.; Wu, L.; Guang, S.; Xu, A. Parental exposure to TiO2 NPs promotes the multigenerational reproductive toxicity of Cd in Caenorhabditis elegans via bioaccumulation of Cd in germ cells. *Environmental Science: Nano* **2019**, *6*, 1332–1342.

(344) Thompson, R. C.; Olsen, Y.; Mitchell, R. P.; Davis, A.; Rowland, S. J.; John, A. W. G.; McGonigle, D.; Russell, A. E. Lost at Sea: Where Is All the Plastic? *Science* **2004**, *304*, 838–838.

(345) Moore, C. J. Synthetic polymers in the marine environment: A rapidly increasing, long-term threat. *Environmental Research* **2008**, *108*, 131–139.

(346) Shah, A. A.; Hasan, F.; Hameed, A.; Ahmed, S. Biological degradation of plastics: A comprehensive review. *Biotechnology Advances* **2008**, *26*, 246–265.

(347) Barnes, D. K. A.; Galgani, F.; Thompson, R. C.; Barlaz, M. Accumulation and fragmentation of plastic debris in global environments. *Philosophical Transactions of the Royal Society B* **2009**, *364*, 1985–1998.

(348) Bolea-Fernandez, E.; Rua-Ibarz, A.; Velimirovic, M.; Tirez, K.; Vanhaecke, F. Detection of microplastics using inductively coupled plasma-mass spectrometry (ICP-MS) operated in single-event mode. *Journal of Analytical Atomic Spectrometry* **2020**, *35*, 455–460.

(349) Laborda, F.; Trujillo, C.; Lobinski, R. Analysis of microplastics in consumer products by single particle-inductively coupled plasma mass spectrometry using the carbon-13 isotope. *Talanta* **2021**, *221*, 121486.

(350) Corte-Rodríguez, M.; Álvarez-Fernández, R.; García-Cancela, P.; Montes-Bayón, M.; Bettmer, J. Single cell ICP-MS using on line sample introduction systems: Current developments and remaining challenges. *TrAC Trends in Analytical Chemistry* **2020**, *132*, 116042.

(351) Gomez-Gomez, B.; Corte-Rodríguez, M.; Perez-Corona, M. T.; Bettmer, J.; Montes-Bayón, M.; Madrid, Y. Combined single cell and single particle ICP-TQ-MS analysis to quantitatively evaluate the uptake and biotransformation of tellurium nanoparticles in bacteria. *Analytica Chimica Acta* **2020**, *1128*, 116–128.

References for Chapter 7

(28) Daly, M. J. Death by protein damage in irradiated cells. *DNA Repair* **2012**, *11*, 12–21.

(34) Krisko, A.; Radman, M. Protein damage and death by radiation in Escherichia coli and Deinococcus radiodurans. *Proceedings of the National Academy of Sciences* **2010**, *107*, 14373–14377.

(82) Barnese, K.; Gralla, E. B.; Valentine, J. S.; Cabelli, D. E. Biologically relevant mechanism for catalytic superoxide removal by simple manganese compounds. *Proceedings of the National Academy of Sciences* **2012**, *109*, 6892–6897.

(120) Archibald, F. S.; Fridovich, I. The scavenging of superoxide radical by manganous complexes: In vitro. *Archives of Biochemistry and Biophysics* **1982**, *214*, 452–463.

(121) Barnese, K.; Gralla, E. B.; Cabelli, D. E.; Valentine, J. S. Manganous Phosphate Acts as a Superoxide Dismutase. *Journal of the American Chemical Society* **2008**, *130*, 4604–4606.

(125) Daly, M. J. Accumulation of Mn(II) in Deinococcus radiodurans Facilitates Gamma-Radiation Resistance. *Science* **2004**, *306*, 1025–1028.

(126) Daly, M. J.; Gaidamakova, E. K.; Matrosova, V. Y.; Kiang, J. G.; Fukumoto, R.; Lee, D.-Y.; Wehr, N. B.; Viteri, G. A.; Berlett, B. S.; Levine, R. L. Small-Molecule Antioxidant Proteome-Shields in Deinococcus radiodurans. *PLoS ONE* **2010**, *5*, ed. by Otto, M., e12570.

(130) Gupta, P.; Gayen, M.; Smith, J. T.; Gaidamakova, E. K.; Matrosova, V. Y.; Grichenko, O.; Knollmann-Ritschel, B.; Daly, M. J.; Kiang, J. G.; Maheshwari, R. K. MDP: A Deinococcus Mn2-Decapeptide Complex Protects Mice from Ionizing Radiation. *PLOS ONE* **2016**, *11*, ed. by Fornace, A. J., e0160575.

(131) Berlett, B. S.; Levine, R. L. Designing antioxidant peptides. *Redox Report* **2014**, *19*, 80–86.

(135) Sharma, A. et al. Across the tree of life, radiation resistance is governed by antioxidant Mn2, gauged by paramagnetic resonance. *Proceedings of the National Academy of Sciences* **2017**, *114*, E9253–E9260.

(219) Schrieber, R.; Gareis, H., *Gelatine Handbook*; Wiley-VCH: 2007; 347 pp.

(231) Wang, H.; Wang, B.; Wang, M.; Zheng, L.; Chen, H.; Chai, Z.; Zhao, Y.; Feng, W. Time-resolved ICP-MS analysis of mineral element contents and distribution patterns in single cells. *The Analyst* **2015**, *140*, 523–531.

(232) Wang, H.; Wang, M.; Wang, B.; Zheng, L.; Chen, H.; Chai, Z.; Feng, W. Interrogating the variation of element masses and distribution patterns in single cells using ICP-MS with a high efficiency cell introduction system. *Analytical and Bioanalytical Chemistry* **2016**, *409*, 1415–1423.

(323) González de Vega, R.; Goyen, S.; Lockwood, T. E.; Doble, P. A.; Camp, E. F.; Clases, D. Characterisation of microplastics and unicellular algae in seawater by targeting carbon via single particle and single cell ICP-MS. *Analytica Chimica Acta* **2021**, *1174*, 338737.

(352) Rovetta, F.; Catalani, S.; Steimberg, N.; Boniotti, J.; Gilberti, M. E.; Mariggiò, M. A.; Mazzoleni, G. Organ-specific manganese toxicity: a comparative in vitro study on five cellular models exposed to MnCl2. *Toxicology in Vitro* **2007**, *21*, 284–292.

(353) Peres, T. V.; Schettinger, M. R. C.; Chen, P.; Carvalho, F.; Avila, D. S.; Bowman, A. B.; Aschner, M. Manganese-induced neurotoxicity: a review of its behavioral consequences and neuroprotective strategies. *BMC Pharmacology and Toxicology* **2016**, *17*, DOI: 10.1186/s40360-016-0099-0.

(354) Luparello, C. Effect of Manganese Chloride and of Cotreatment with Cadmium Chloride on the In Vitro Proliferative, Motile and Invasive Behavior of MDA-MB231 Breast Cancer Cells. *Molecules* **2019**, *24*, 1205.

(355) Masaki, H.; Okano, Y.; Sakurai, H. Generation of active oxygen species from advanced glycation end-products (AGEs) during ultraviolet light A (UVA) irradiation and a possible mechanism for cell damaging. *Biochimica et Biophysica Acta (BBA) - General Subjects* **1999**, *1428*, 45–56.

(356) Aitken, G. R.; Henderson, J. R.; Chang, S.-C.; McNeil, C. J.; Birch-Machin, M. A. Direct monitoring of UV-induced free radical generation in HaCaT keratinocytes. *Clinical and Experimental Dermatology* **2007**, *32*, 722–727.

(357) Godar, D. E.; Lucas, A. D. Spectral dependence of UV-induced immediate and delayed apoptosis: the role of membrane and DNA damage. *Photochemistry and Photobiology* **1995**, *62*, 108–113.

(358) Takasawa, R.; Nakamura, H.; Mori, T.; Tanuma, S. Differential apoptotic pathways in human keratinocyte HaCaT cells exposed to UVB and UVC. *Apoptosis* **2005**, *10*, 1121–1130.

(359) Zhang, X.; Rosenstein, B. S.; Wang, Y.; Lebwohl, M.; Wei, H. Identification of Possible Reactive Oxygen Species Involved in Ultraviolet Radiation-Induced Oxidative DNA Damage. *Free Radical Biology and Medicine* **1997**, *23*, 980–985.

(360) Widel, M.; Krzywon, A.; Gajda, K.; Skonieczna, M.; Rzeszowska-Wolny, J. Induction of bystander effects by UVA, UVB, and UVC radiation in human fibroblasts and the implication of reactive oxygen species. *Free Radical Biology and Medicine* **2014**, *68*, 278–287.

(361) Barta, C.; Kálai, T.; Hideg, K.; Vass, I.; Hideg, É. Differences in the ROS-generating efficacy of various ultraviolet wavelengths in detached spinach leaves. *Functional Plant Biology* **2004**, *31*, 23.

(362) Alapetite, C. Use of the alkaline comet assay to detect DNA repair deficiencies in human fibroblasts exposed to UVC, UVB, UVA and gamma-rays. *International Journal of Radiation Biology* **1996**, *69*, 359–369.

(363) Krisko, A.; Radman, M. Biology of Extreme Radiation Resistance: The Way of Deinococcus radiodurans. *Cold Spring Harbor Perspectives in Biology* **2013**, *5*, a012765–a012765.

(364) Mulay, I. L.; Roy, R.; Knox, B. E.; Suhr, N. H.; Delaney, W. E. Trace-Metal Analysis of Cancerous and Non-cancerous Human Tissues. *JNCI: Journal of the National Cancer Institute* **1971**, *47*, 1–13.

(365) Choi, R.; Kim, M.-J.; Sohn, I.; Kim, S.; Kim, I.; Ryu, J.; Choi, H.; Kim, J.-M.; Lee, S.; Yu, J.; Kim, S.; Nam, S.; Lee, J.; Lee, S.-Y. Serum Trace Elements and Their Associations with Breast Cancer Subgroups in Korean Breast Cancer Patients. *Nutrients* **2018**, *11*, 37.

(366) Afridi, H. I.; Kazi, T. G.; Kazi, G. H.; Jamali, M. K.; Shar, G. Q. Essential Trace and Toxic Element Distribution in the Scalp Hair of Pakistani Myocardial Infarction Patients and Controls. *Biological Trace Element Research* **2006**, *113*, 19–34.

(367) Kumar, A. P.; Loo, S. Y.; Shin, S. W.; Tan, T. Z.; Eng, C. B.; Singh, R.; Putti, T. C.; Ong, C. W.; Salto-Tellez, M.; Goh, B. C.; Park, J. I.; Thiery, J. P.; Pervaiz, S.; Clement, M. V. Manganese Superoxide Dismutase Is a Promising Target for Enhancing Chemosensitivity of Basal-Like Breast Carcinoma. *Antioxidants & Redox Signaling* **2014**, *20*, 2326–2346.

(368) Kattan, Z.; Minig, V.; Leroy, P.; Dauça, M.; Becuwe, P. Role of manganese superoxide dismutase on growth and invasive properties of human estrogen-independent breast cancer cells. *Breast Cancer Research and Treatment* **2007**, *108*, 203–215.

(369) Weydert, C. J.; Waugh, T. A.; Ritchie, J. M.; Iyer, K. S.; Smith, J. L.; Li, L.; Spitz, D. R.; Oberley, L. W. Overexpression of manganese or copper–zinc superoxide dismutase inhibits breast cancer growth. *Free Radical Biology and Medicine* **2006**, *41*, 226–237.

(370) Lymburner, S.; McLeod, S.; Purtzki, M.; Roskelley, C.; Xu, Z. Zinc inhibits magnesium-dependent migration of human breast cancer MDA-MB-231 cells on fibronectin. *The Journal of Nutritional Biochemistry* **2013**, *24*, 1034–1040.

(371) Haase, H.; Hebel, S.; Engelhardt, G.; Rink, L. The biochemical effects of extracellular Zn2+and other metal ions are severely affected by their speciation in cell culture media. *Metallomics* **2015**, *7*, 102–111.

(372) Meyer, S.; López-Serrano, A.; Mitze, H.; Jakubowski, N.; Schwerdtle, T. Single-cell analysis by ICP-MS/MS as a fast tool for cellular bioavailability studies of arsenite. *Metallomics* **2018**, *10*, 73–76.

(373) Khetan, J.; Shahinuzzaman, M.; Barua, S.; Barua, D. Quantitative Analysis of the Correlation between Cell Size and Cellular Uptake of Particles. *Biophysical Journal* **2019**, *116*, 347–359.

(374) Barry Halliwell, J. M. C. G., *Free Radicals in Biology and Medicine*; Oxford University Press: 2015; 896 pp.

(375) Camacho-Fernández, C.; Hervás, D.; Rivas-Sendra, A.; Marín, M. P.; Seguí-Simarro, J. M. Comparison of six different methods to calculate cell densities. *Plant Methods* **2018**, *14*, DOI: 10.1186/s13007-018-0297-4.

(376) Shen, Y.; Schmidt, B. U. S.; Kubitschke, H.; Morawetz, E. W.; Wolf, B.; Käs, J. A.; Losert, W. Detecting heterogeneity in and between breast cancer cell lines. *Cancer Convergence* **2020**, *4*, DOI: 10.1186/s41236-020-0010-1.

(377) Gray, M.; Turnbull, A. K.; Ward, C.; Meehan, J.; Martínez-Pérez, C.; Bonello, M.; Pang, L. Y.; Langdon, S. P.; Kunkler, I. H.; Murray, A.; Argyle, D. Development and characterisation of acquired radioresistant breast cancer cell lines. *Radiation Oncology* **2019**, *14*, DOI: 10.1186/s13014-019-1268-2.

(378) Ye, F.; Kim, C.; Ginsberg, M. H. Reconstruction of integrin activation. *Blood* **2012**, *119*, 26–33.

(379) Feng, X.-P.; Yi, H.; Li, M.-Y.; Li, X.-H.; Yi, B.; Zhang, P.-F.; Li, C.; Peng, F.; Tang, C.-E.; Li, J.-L.; Chen, Z.-C.; Xiao, Z.-Q. Identification of Biomarkers for Predicting Nasopharyngeal Carcinoma Response to Radiotherapy by Proteomics. *Cancer Research* **2010**, *70*, 3450–3462.

Appendix

Table A.1. Links to software and tools created for this thesis.

Name	Description	Link
ckwrap	Python wrapper for Ckmeans.1d.dp, optimal k-means clustering.	https://github.com/djdt/ckwrap
ExTMA	Automated segmentation and extraction of tissue micro-arrays	https://github.com/djdt/extma
opdxread	Import and fitting of Bruker 1D profilometric data	https://github.com/djdt/opdxread
pewlib	Library for import, processing and export of LA–ICP–MS data	https://github.com/djdt/pewlib
Pew²	GUI import and visualisation of LA–ICP–MS data	https://github.com/djdt/pewpew
SPCal	GUI import and calculator for spICP–MS data	https://github.com/djdt/spcal
STM UV12	Code and PCB files for UV cell irradiator	https://github.com/djdt/stm_uv12

A.1 Appendix for Imaging of Tumour Microarrays

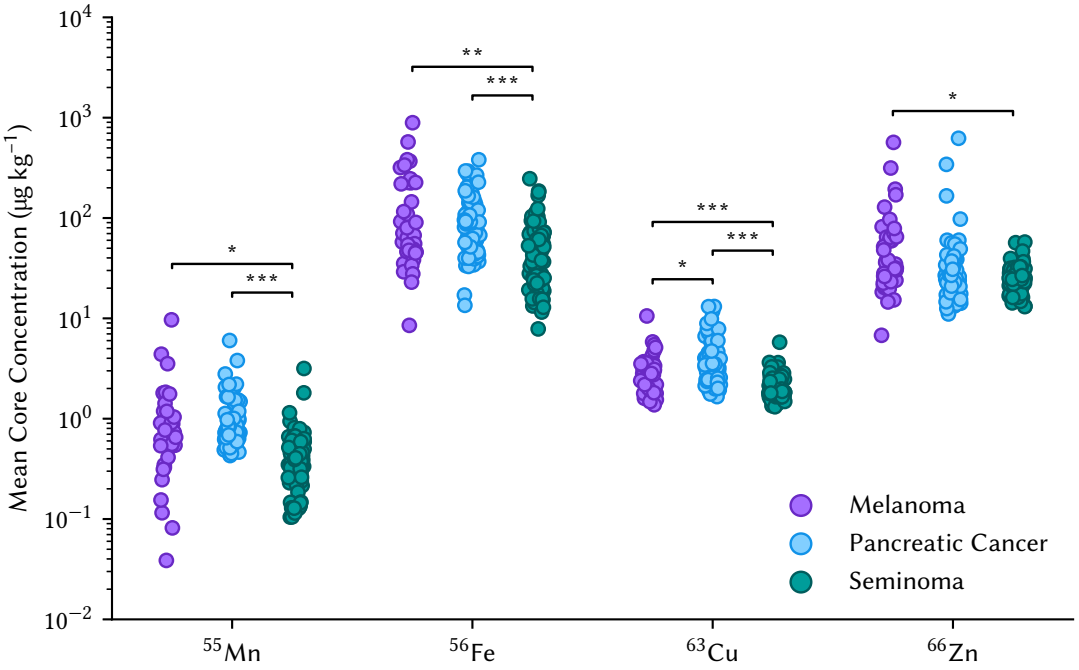

Figure A.1. Mean metal concentrations of Otsu P masked regions for each malignant TMA core, separated by tissue type. Statistics were performed using Student's or Welch's t-test, dependant on homoscedasticity (*, $p = 0.05$, **, $p = 0.01$, ***, $p = 0.001$).

A.2 Appendix for LA–ICP–MS Imaging Software

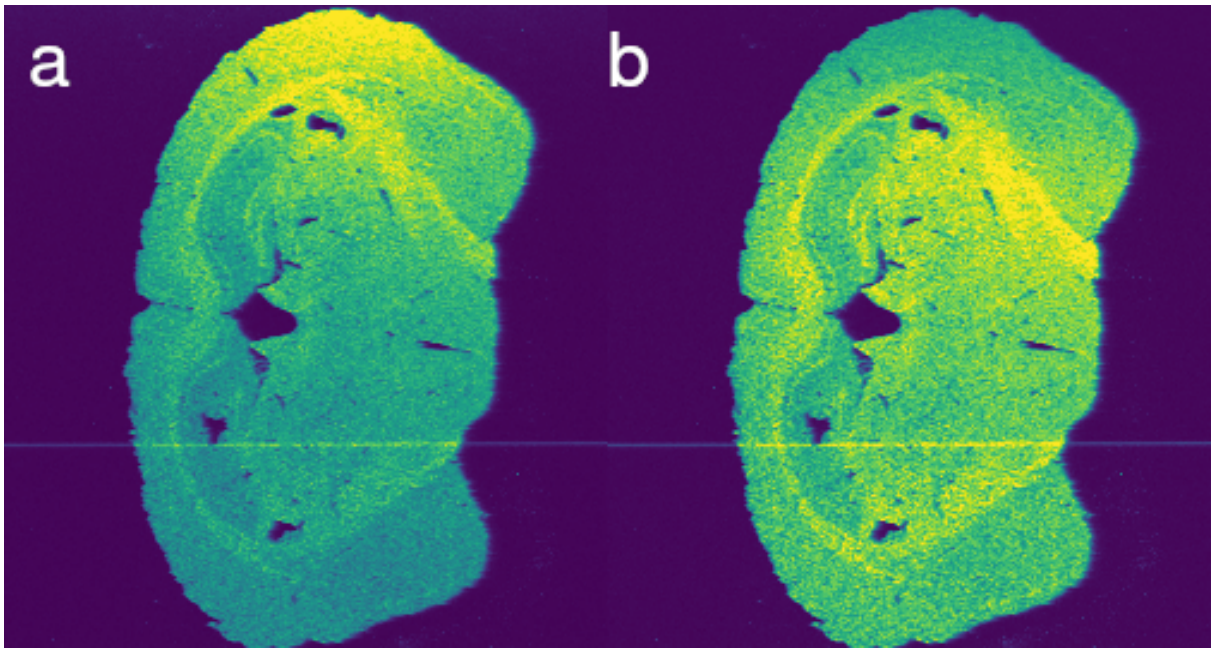

Figure A.2. Signal drift removed from an image of ^{31}P in a mouse brain using Pew². A polynomial fit to the background from image (a) was convolved from the entire image to remove the drift (b).

A.2.1 Code listings

Listing A.1. Calculates the rolling mean over an n-dimensional array and replaces outliers.

```
def rolling_mean(
    x: np.ndarray, block: Tuple[int, ...], threshold: float = 3.0
) -> np.ndarray:
                                                    prepare array by padding with nan to fit block size
    pads = [(b // 2, b // 2) for b in block]
    x_pad = np.pad(x, pads, constant_values=np.nan)
                                                    create block sized views into the array
    blocks = view_as_blocks(x_pad, block, tuple([1 for b in block]))

    axes = tuple(np.arange(x.ndim, x.ndim * 2))                    calculate means
    means = np.nanmean(blocks, axis=axes)

    nancenter = np.ones(block, dtype=np.float64)          calculate stds without central point
    nancenter[np.array(nancenter.shape) // 2] = np.nan
    stds = np.nanstd(blocks * nancenter, axis=axes)
```

```

    outliers = np.abs(x - means) > threshold * stds

    unpads = tuple([slice(p[0], -p[1]) for p in pads])                    remove padding
    x_pad[unpads][outliers] = np.nan

    means = np.nanmean(blocks, axis=axes)                    recalculate mean without outliers
                                                                  replace outliers with local mean
    return np.where(np.logical_and(outliers, ~np.isnan(means)), means, x)
```

Listing A.2. Calculates the rolling median over an n-dimensional array and replaces outliers.

```
def rolling_median(
    x: np.ndarray, block: Tuple[int, ...], threshold: float = 3.0
) -> np.ndarray:
                                                  prepare array by padding with nan to fit block size
    pads = [(b // 2, b // 2) for b in block]
    x_pad = np.pad(x, pads, constant_values=np.nan)
                                                              create block sized views into the array
    blocks = view_as_blocks(x_pad, block, tuple([1 for b in block]))

    axes = tuple(np.arange(x.ndim, x.ndim * 2))              calculate median and differences
    medians = np.nanmedian(blocks, axis=axes)

    unpads = tuple([slice(p[0], -p[1]) for p in pads])       remove the padding added earlier
    x_pad[unpads] = np.abs(x - medians)

    median_medians = np.nanmedian(blocks, axis=axes)    medians of differences from local median
    outliers = x_pad[unpads] > threshold * median_medians
                                                                replace outliers with local median
    return np.where(np.logical_and(outliers, ~np.isnan(medians)), medians, x)
```

Listing A.3. Reduction of parsed tokens is completed by recursively calling the 'reduceExpr' function until all tokens have been read. Error handling code has been removed to improve readability.

```
def reduceExpr(
    self,
    tokens: List[str],
```

```
    operations: Dict[str, Tuple[Callable, int]],
    variables: Dict[str, float]
) -> float:
    token = tokens.pop(0) #                                   take the first token

    if token in operations: #          token is operation, recursively call reduceExpr to get arguments
        op, nargs = operations[token]
        args = [reduceExpr(tokens, operations, variables) for _ in range(nargs)]
        return op(*args)
    elif token in variables: #                                token is a variable, return value
        return variables[token]
    else: #                                                       token is a simple number
        return float(token)
```

A.3 Appendix for Radioresistance in a Breast Cancer Cell Model

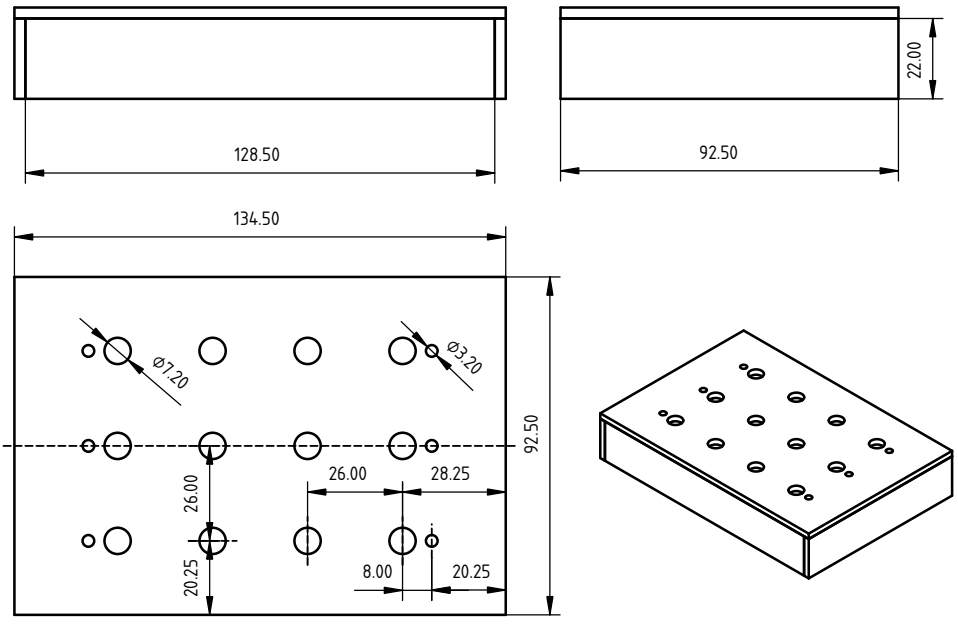

Figure A.3. CAD model of the protective shield for the UV irradiation device.

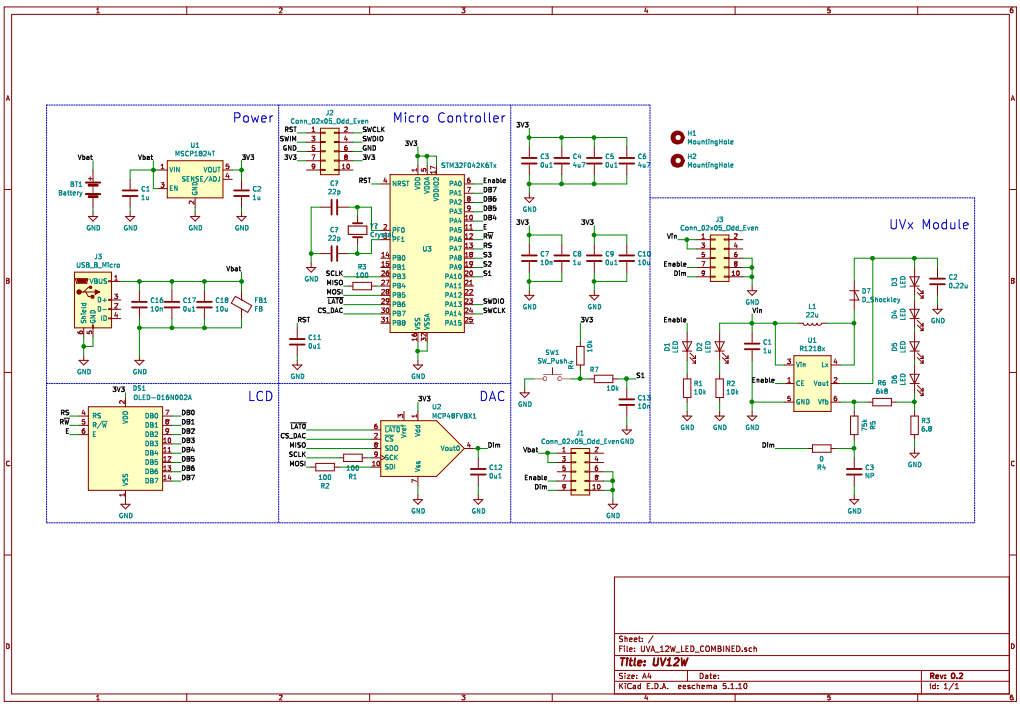

Figure A.4. Schematic for the control and LED board of the UV irradiation device.

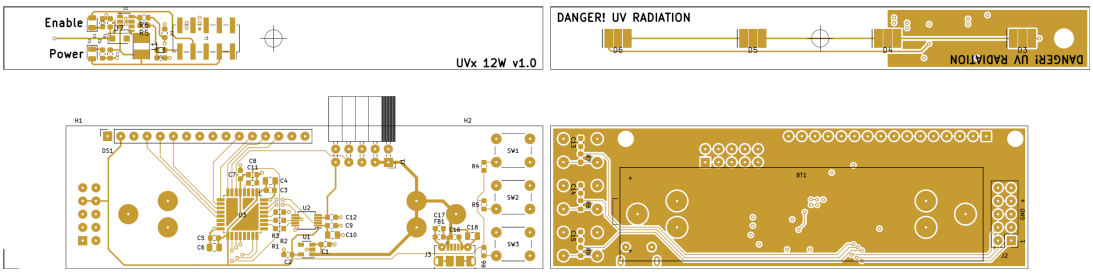

Figure A.5. PCBs for the UV irradiation device.

Table A.2. Instrument parameters used for single cell analyses.

	^{12}C	^{55}Mn	^{56}Fe
RF Power (W)		1550	
Sample depth (mm)		4.0	
Carrier gas (L min^{-1})		0.4	
Dilution gas (L min^{-1})		0.4	
Extract 1 (V)	-200	3.6	
Extract 2 (V)	2	-190	
Omega Bias (V)	-85	-100	
Omega Lens (V)	10.9	12.9	
Deflect (V)		8.0	
Cell gas (mL min^{-1})	–	–	3.0 H_2